Università degli studi di Genova

Doctoral thesis in Science and Technologies of

Chemistry and Materials

Curriculum: Chemical Science and Technologies

Cycle XXXIII

Thermal Barrier Coatings phase stability and in service degradation

Giacomo Roncallo

Tutors:

Prof. Gabriele Cacciamani

Dr. Erica Vacchieri

Summary

1 Introduction

This thesis work is the result of a collaboration between Ansaldo Energia's Materials Laboratory and the Department of Chemistry and Industrial Chemistry of the University of Genoa.

The study developed from the industrial need to better understand the degradation processes of the turbine blade thermal barriers coating already used in Ansaldo Energia gas turbines and to test new materials that could be used in the future.

The material mostly used as a protective coating is 7YSZ (ZrO_2 with 7 wt% of Y_2O_3) which has excellent characteristics and has been used inside turbines for land use and on aircraft engines since the 1960s.

The need to increase the operating temperature of the machines, with a consequent increase in efficiency, makes it necessary to modify this material, as it tends to degrade when it works at temperatures above 1300°C.

With cooling from high temperatures, the 7YSZ tends to modify its crystallographic structure until the formation of the monoclinic phase, extremely harmful because it is a source of mechanical fragility and an increase in thermal conductivity.

A new material has been proposed by Ansaldo Energia, consisting of a double layer, with the upper layer formed by 14YSZ (ZrO_2 with 14% of Y_2O_3), while the lower one remains 7YSZ for better compatibility with the metal substrate.

The new material is crystallographically stable but its properties must be characterized before being used in gas turbines. Starting from their precursor powders and reacting long exposure time at high temperature of sprayed material.

In addition, the TBC modifications due to interactions with CMAS (Calcium-Magresium-Alluminium-Silicates) have been investigated. Several tests have been performed for times up to 10000h and temperatures between 1100 and 1400°C. The samples have been examined mainly to evaluate the effect of the interaction on the formation of the monoclinic and other secondary phases, the modification of the microstructure and the variation of physical properties.

Finally, to better study the interaction phenomena between oxides, a multicomponent thermodynamic database (Al-Ca-Si-Mg-Si-Y-Zr-O) has been implemented using the CALPHAD method.

The thesis work has been divided into an experimental part, carried out at the Ansaldo Energia laboratories and a thermodynamic modeling part, conducted at the Department of Chemistry and Industrial Chemistry. The thermodynamic database for oxides has been also implemented through the experimental study of the MgO-Y_2O_3-ZrO_2 system at the University of Freiberg in Germany, in the group of Prof.Olga Fabrichnaya.

The experimental part focused on the analysis of thermal barrier specimens exposed at high temperature and examined with usual materials characterization techniques.

For this purpose, quantitative analysis of the detected phases has been carried out using Xray diffraction with quantification using the Rietveld method. The microstructural analyzes have been done using optical microscope and FEG-SEM (Field Emission Gun-Scanning Electron Microscope) equipped with EDS (Energy- dispersive detector) and EBSD (Electron Back Scattered Diffraction) to evaluate microstructure variations, phase compositions, grain shapes and dispersion of the phases within the sample.

Furthermore, thermal conductivity tests have been carried out, using thermography technique, thank to the collaboration with the group of Dr. Paolo Bison and Dr. Giovanni Ferrarini of the ITC-CNR of Padua.

At the same time, by means of thermodynamic modeling according to the CALPHAD method, the development of a thermodynamic database has been started. It includes the seven main oxides relevant to the CMAS-TBC interaction and our work was mainly focused on the definition of thermodynamic models for the description of the phases present in the system and the assessment of a series of pseudo-binary and pseudo-ternary subsystems .

The results obtained allow the definition of the critical conditions of the tested materials in service, to better understand their evolution and the degradation and to define the range of use.

The thesis is divided into seven chapters. After this brief introduction (**Chapter 1**), in a first introductory part, the general features of gas turbines characteristics of materials used in turbine blades with special attention to TBCs are presented (**Chapter 2**). The materials used for the experimental tests and the main methods of experimental investigation used in this thesis are then briefly described, as well as the principles of thermodynamic modeling according to the CALPHAD method (**Chapter 3**).

In the second part of this thesis the results obtained from both experimental and modeling work is reported. Chapters 4 and 5 are dedicated to the experimental results. In particular, in **Chapter 4** are reported the results of the analyzes and tests carried out on materials exposed at high temperatures. In this section, the transformations of 7YSZ and 14YSZ have been studied, considering thermodynamic and kinetic effects of fast cooling from 1400°C, which simulates the turning on and off of the turbine, and the characteristics of precursor powders exposed at high temperatures.

In Chapter 5 results obtained from the TBC-CMAS interaction tests, analyzed by X-ray, microscopy and thermography techniques are described.

In Chapter 6 the implementation of the thermodynamic database purposely built to simulate the interactions object of this study is presented and discussed . In particular, the models used for the different phases stable in the system are described and subsequently the results of the modeling of all the binary and ternary subsystems considered are systematically illustrated.

At the end of Chapters 4, 5 and 6 a discussion of the collected results is included. Finally, some more general concluding considerations are presented in the last chapter (**Chapter 7**).

2 Gas turbine and materials for high temperature components

2.1 *Gas turbine*

Gas turbines are used in diversified services from jet engines and simple mechanical drives (on land, sea and air) to sophisticated gas lasers and supersonic wind tunnels. Airborne applications are referred to as jets, turbojets, turbofans, and turboprops. Land and sea based applications are referred to as mechanical drive gas turbines [1].

In the strict sense, all gas turbines are gas generators. Their hot gases are expanded either through a turbine to generate shaft power or through a nozzle to create thrust. Some gas generators expand their hot gases only through a nozzle to produce thrust: these units are easily identified as jet engines (or turbojets). Other gas turbines expand some of the hot gas through a nozzle to create thrust and the rest of the gas is expanded through a turbine to drive a fan: these units are called turbofans. When a unit expands virtually all of its hot gases through the turbine driving the compressor and the attached propeller and no thrust is created from the gas exiting the exhaust nozzle: it is called a turboprop [2].

The mechanical drive gas turbines are available in three configurations: single spool-integral output shaft, single spool-split output shaft, and dual spool-split output shaft. In a single spool-integral output shaft unit the output shaft is an extension of the main shaft, which connects the compressor and turbine components. The output shaft may be an extension of the turbine shaft or it may be an extension of the compressor shaft. When the output drive shaft is an extension of the turbine component shaft it is referred to as a “hot end drive”. Likewise, when the output drive shaft is an extension of the compressor component shaft it is referred to as a “cold end drive”.

Aero-derivative and industrial gas turbines have demonstrated their suitability for heavy duty, continuous, base load operation in power generation, pump and compressor applications.

Main gas turbine components are compressor, combustor and turbine, reported in Figure 1.

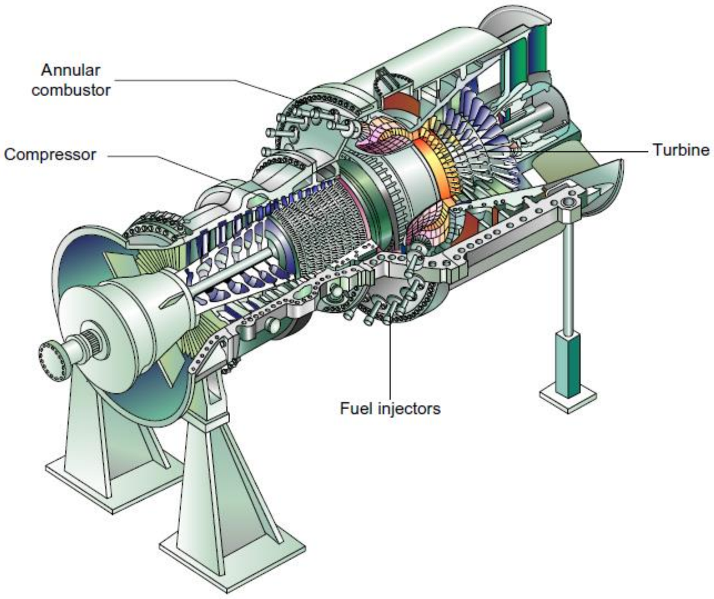

Figure 1 - Gas turbine components [1]

A compressor is a device that pressurizes a working fluid. The types of compressors fall into three categories: (1) the positive displacement compressors are used for low flow and high pressure (head), (2) centrifugal-flow compressors are medium flow and medium head, and (3) axial-flow compressors are high flow and low pressure. In gas turbines, the centrifugal-flow and axial flow compressors, which are continuous flow compressors, are the ones used for compressing the air. An axial-flow compressor compresses its working fluid by first accelerating the fluid and then diffusing it to obtain a pressure increase. The fluid is accelerated by a row of rotating airfoils or blades (the rotor) and diffused by a row of stationary blades (the stator). The diffusion in the stator converts the velocity increase gained in the rotor to a pressure increase. One rotor and one stator make up a stage in a compressor. A compressor usually consists of multiple stages. Centrifugal compressors are used in small gas turbines and are the driven units in most gas turbine compressor trains.

All gas turbine combustors perform the same function; they increase the temperature of the high-pressure gas. Combustor inlet temperature depends on engine pressure ratio, load, engine type, and whether or not the turbine is regenerative or non-regenerative especially at the low-pressure ratios. The new industrial turbine pressure ratios are between 17:1 and 35:1, which means that the combustor inlet temperatures range from 454°C to 649°C. The new aircraft engines have pressure ratios that are in excess of 40:1. Regenerative gas turbines have combustor inlet temperatures which range from 371°C to 593°C. Combustor exit temperatures range from 927°C to 1593°C. There are two types of combustors, diffusion combustors (most common) and Dry low NO_x (DLN) or dry low emission (DLE) combustors. The gas turbine diffusion combustor uses very little of its air (10%) in the combustion process. The rest of the air is used for cooling and mixing. The DLE approach is to burn most (at least

75%) of the fuel at cool and fuel-lean conditions to avoid any significant production of NO_x. The principal features of such a combustion system is the premixing of the fuel and air before the mixture enters the combustion chamber and leanness of the mixture strength in order to lower the flame temperature and reduce NO_x emission. Despite many design differences in combustors, all gas turbine combustion chambers have three features: (1) a recirculation zone, (2) a burning zone (with a recirculation zone that extends to the dilution region), and (3) a dilution zone.

There are two types of turbines used in gas turbines. These consist of the axial-flow type and the radial-inflow type. The radial-inflow turbine, or inward-flow radial turbine, has been in use for many years. Basically a centrifugal compressor with reversed flow and opposite rotation, the inward-flow radial turbine is used for smaller loads and over a smaller operational range than the axial turbine. The axial-flow turbine, like its counterpart the axial-flow compressor, has flow which enters and leaves in the axial direction. There are two types of axial turbines: (1) impulse type and (2) reaction type. The impulse turbine has its entire enthalpy drop in the nozzle; therefore, it has a very high velocity entering the rotor. The reaction turbine divides the enthalpy drop in the nozzle and the rotor. In addition, the first-stage blade is unshrouded and it has the cooling holes on the top of the blades; however, the second and third-stage blades are shrouded; the second-stage blades also do have cooling holes.

The first gas turbines were built at the beginning of the twentieth century, but the available materials imposed limited operating temperatures, which made their use less convenient.

The most important innovation happened when gas turbines were used in military aircraft engines: this led to an improvement in technology.

In the last sixty years the continuous engineering developments have allowed to increase the efficiency values with the use of materials resistant to ever higher temperatures.

The initial efficiency (in 1939) was 18%, and increased to 40% for single cycle turbines and to 55% for combined cycle turbines (in which hot fumes at 500-600 ° C leaving the first turbine are used in a water vapor cycle).

Gas turbines have a number of advantages such as:

- The production of large quantities of energy (between 0.5 MW and 340 MW) by means of relatively small plants;
- A large part of the components of the turbine is subject only to rotational movements, which reduces mechanical stresses and allows long life times and low maintenance costs;
- Gas turbines take a few minutes to reach maximum power (unlike steam turbines, which take a few hours instead).
- This feature is very advantageous for example in the field of electricity production, where, in recent times, flexibility in the production of energy during the day is often required;
- A great variety of fuels can be used, even natural gas is the most common;

- -air is the oxidizer normally used.

The gas turbine cycle is best depicted by the Brayton Cycle (Figure 2) [3]. The Brayton Cycle in its ideal form consists of two isobaric (constant pressure) processes and two isentropic (constant entropy) processes. The two isobaric processes consist of the combustor system of the gas turbine, while the two isentropic processes represent the compression (compressor) and the expansion (turbine expander) processes in the gas turbine. The gas turbine, as a continuous flow machine, is best described by the first law of thermodynamics.

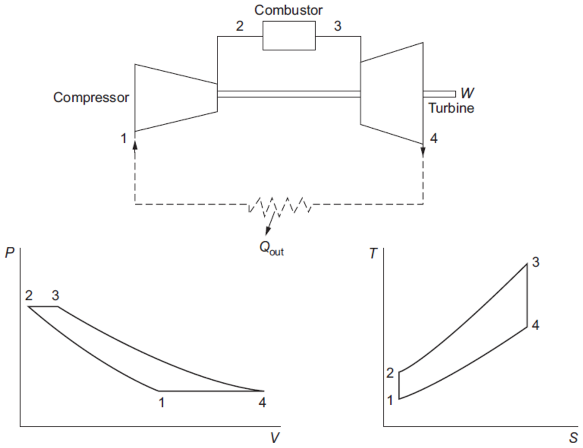

Figure 2 - The air-standard Brayton Cycle [1]

The overall adiabatic thermal cycle efficiency is

$$\eta_{cyc} = \frac{W_{cyc}}{Q_{2,3}}$$

Increasing the pressure ratio and the turbine firing temperature, the Brayton cycle’s adiabatic thermal efficiency rises.

Ansaldo Energia's gas turbines operate in an open cycle, (air is taken from the atmosphere at the beginning of the cycle and, at the end, is re-emitted into it).

The compressor, located on the same axis as the turbine, consists of a large number of stages (between 15 and 19), each of which is composed of a row of rotating blades alternating with a row of stationary blades. In this way the air is compressed when passing from one stage to another.

The combustion chamber is lined with refractory tiles, which have the task of protecting it from the flame that is created in the combustion reaction between the air and the fuel.

The air expands into the turbine through 4 stages of rotor blades and 4 stages of stator blades of gradually increasing size. The expansion of the gas rotates the blades while the temperature of the fumes decreases as it passes through the different stages. The blades rotate and transform the potential energy of the air into mechanical energy.

2.2 *Materials for high temperature components*

The increase in the efficiency of gas turbines is linked to an increase in temperature at which it can work. For this reason, the need arose to identify materials that could respond adequately to mechanical stress and that were chemically inert at high temperatures.

A material to work at high temperatures must have a resistance to mechanical degradation during a long period of time at high temperature (i.e. creep resistance) and the ability to withstand mechanical loads applied cyclically (i.e. fatigue resistance). The materials for these applications must also have a good tolerance to the heavy conditions of the working environments, in particular resistance to hot corrosion and oxidation.

To improve the performance of the materials, the metallic substrate is coated with two protective layers, one metallic and one ceramic, as reported in Figure 3.

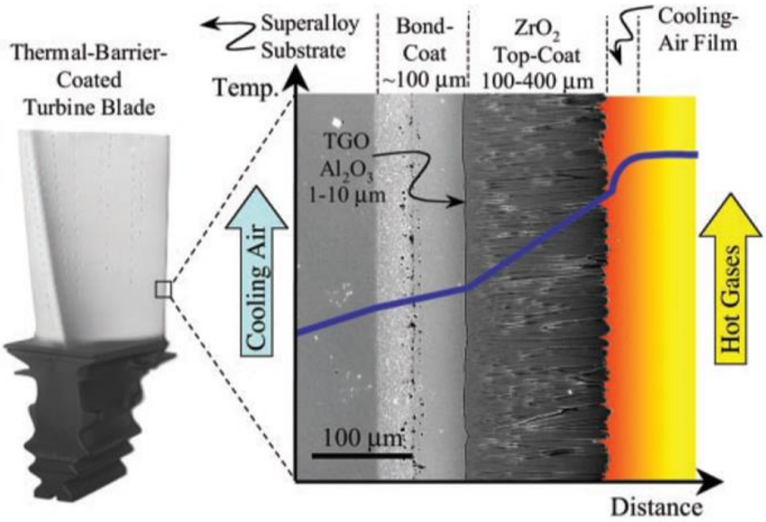

Figure 3 – Scheme of materials used in a blade of a gas turbine [4]

2.3 *Superalloys*

High temperature metallic materials must have their characteristics and properties even at operating temperatures. Among the characteristics they must have, there is the ability to withstand mechanical loads at an operating temperature close to their melting point.

In order to fall within the class of high temperature resistant materials, the operating temperature and melting point ratio must be greater than or equal to 0.6, a characteristic that is satisfied by nickel-based and cobalt-based alloys (defined as superalloys).

The graph shown in Figure 4 shows the best characteristics of these two alloys compared to those of other elements [5].

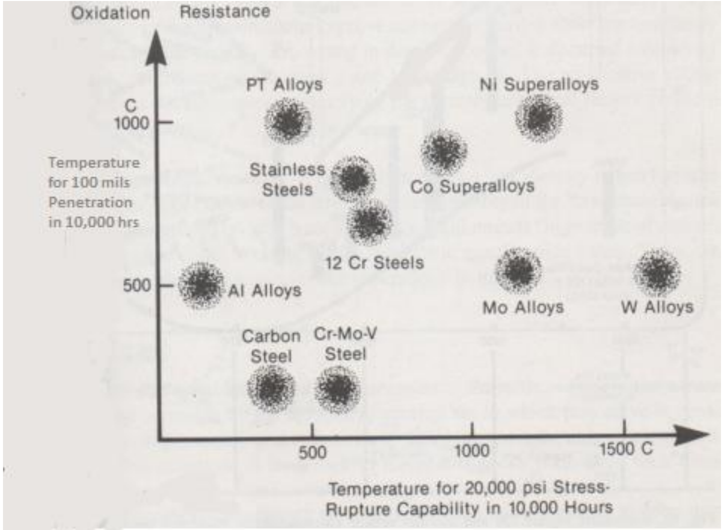

Figure 4 - Comparison between alloys on resistance to oxidation and "creep"/rupture [5]

The development of new component solidification techniques was also made necessary by the presence of increasingly complex geometries of the parts of the turbine. The machined superalloys were replaced by the solidified superalloys in castings, with the Investment Casting technique (lost wax), in order to obtain components of increasingly complex geometry to allow more and more intense cooling. The increasingly higher temperatures then led to an evolution of solidification techniques in castings with the introduction of directional solidification which allows the elimination of the grain edges normal to the main axis of the rotor components which coincides with the direction of the main stress (centrifugal force).

The best performances in terms of creep resistance at high temperatures are obtained with the complete elimination of the grain edges with monocrystalline solidification. This occurs because the grain boundary is the area richest in defects and therefore the one in which the creep crack develops and propagates.

For this reason the decrease in the presence of the grain edges, first with the passage to the casts and then with the directional and monocrystalline solidification techniques, has allowed to obtain better performances[6].

2.3.1 *Nickel based superalloys*

Nickel-based superalloys are the most used materials in the production of hot components of gas turbines. The choice of nickel as the basic element of materials for high temperatures is due to its high melting temperature and the good Ni solubility of many elements. In fact, nickel-based superalloys can contain up to 14 alloy elements, because the nickel has the 3*d* orbital not completely occupied and therefore can form solid solutions with different elements. A second factor that contributes to the choice of nickel as the basic element is its fcc structure which remains so from room temperature to the melting temperature, i.e. it does not undergo allotropic transformations that would cause expansion and contraction during component operation, as well as the variation of solubility of the added elements.

Even nickel-based alloys have an austenitic structure. This structure allows to have a low diffusion speed, which determines a high microstructural stability at high temperature, in which the characteristic of good resistance to creep must be sought, since the phenomenon is controlled by high temperature diffusion.

The austenitic alloy matrix confers a particular high temperature resistance, but this characteristic is increased with the addition of alloy elements.

In fact, chromium allows the formation of a layer of Cr_2O_3 by limiting the diffusion of the metal elements towards the outside and also prevents the penetration of oxygen, nitrogen and sulfur. At high temperature, then, nickel superalloys may be able to form an Al_2O_3 flake, depending on the aluminum content, which has passivating properties.

The best method of hardening of the alloy, which allows it to have better mechanical properties than the cobalt-based superalloy, is however the ability to form the γ′ phase which, precipitating during the production heat treatments in a manner consistent with the austenitic matrix , guarantees mechanical resistance at high temperature and creep.

This is an intermetallic phase with an approximate Ni_3Al composition in which aluminum can be replaced by titanium, niobium or tantalum, while nickel from cobalt. The Al-Ni state diagram is shown in Figure 5, together with a micrograph showing the γ/γ′ phases. The γ′ phase initially precipitates into spheroidal particles that, subsequently, thanks to specific heat treatments, are transformed into cuboidals.

The γ′ phase is a super reticle that has an AuCu3 type structure and has long-range order up to its melting temperature of 1385°C.

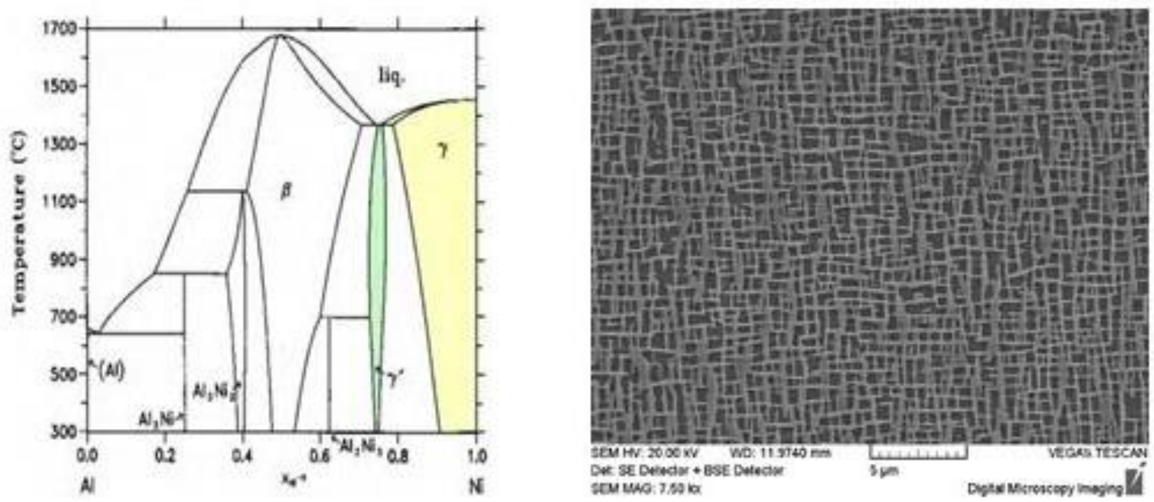

Figure 5 - Al-Ni phase diagram, underlined γ and γ ' phases (left). SEM-SE x7500 microstructure γ / γ '(dark phase γ, light phase γ') (right) [5]

The formation of carbides is due to the combination of carbon (contained between 0.02 and 0.2 wt%) with elements such as titanium, tantalum, chromium and tungsten. During service, MC type carbides have a tendency to decompose, generating carbides such as M23C6, M6C and M7C3 at the grain boundary. The carbides at the grain boundary have the purpose of strengthening and slowing down the viscous flow, while if they precipitate in the matrix they confer an increase in the hardness of the alloy. In cases where carbides form a continuous film on the grain boundary, the effect of improving creep performance is accompanied by a worsening of ductility; to avoid this phenomenon, the carbon alloy content is reduced. For this reason, the influence on mechanical properties is less than that of the γ 'phase.

2.3.2 *Cobalt based superalloys*

Cobalt-based superalloys are used more limited than nickel-based superalloys, but they play an important role in the gas turbine industry. In fact, they have higher thermal resistance, greater resistance to hot corrosion (probably because they contain a higher concentration of Cr than other alloys), greater resistance to thermal fatigue and better weldability than nickel-based superalloys. They also have the possibility of being melted and cast in air or argon, unlike other super alloys that require vacuum.

Cobalt-based superalloys are used in particular for the components of the first stator stages, which compared to the rotor blades are subjected to less mechanical stress, due to the absence of centrifugal forces and vibrations, but are directly exposed to gases at higher temperatures and undergo considerable thermal gradients on the walls. The higher thermal conductivity of these alloys improves their resistance to thermomechanical fatigue since it reduces the thermal gradients in the walls of the blades and consequently also the stresses of thermal origin.

These materials are not hardened by orderly precipitates, like nickel-based superalloys; they are characterized by a cubic austenitic matrix with centered faces, in which carbides are distributed.

The hardening by formation of intermetallic phases analogous to the phase γ' (Ni_3Al) does not occur because the existence of an intermetallic Co_3Al is denied by the Co-Al state diagram, as reported in Figure 6 [7].

Compared to nickel, cobalt has two fundamental advantages: it has a higher melting temperature and is lighter; this has led to carrying out studies to stabilize the γ ’phase for the cobalt-aluminum-tungsten ternary system[8], to have a hardening by precipitation of the phase also in Cobalt-based superalloys.

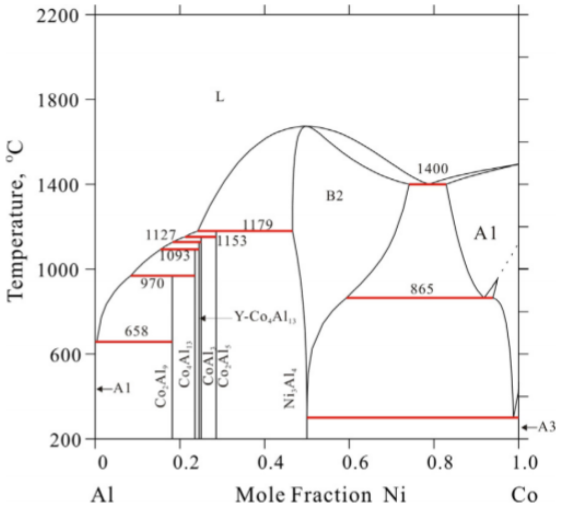

Figure 6 – Al-Co phase diagram, the γ’ phase is not thermodynamically stable [7]

Cobalt-based superalloys are mainly strengthened by the precipitation of incoherent cubic carbides with respect to the matrix. Therefore the carbon content in these alloys is substantially greater than the nickel-based superalloys (from 0.25 - 1.0 wt% C of the former against 0.05 - 0.20 wt% C of the latter).

The main carbides identifiable within the alloy microstructure are: M7C3, M23C6 and MC.

M7C3 and M23C6 are typically chromium carbides which also contain cobalt, tungsten or molybdenum to replace the former.

Carbides type M7C3 have a trigonal structure and are formed when a low chromium-carbon ratio is present. They are metastable carbides and turn into M23C6 carbides after aging. However, it is possible to find them in slowly cooled alloys, in which they dissolve during subsequent heat treatments.

In as cast alloys, in general, MC carbides have an FCC structure and are generally formed of tantalum and niobium. These are formed with a Chinese-script morphology within large grains.

MC carbides can decompose after a certain period at high temperature of use of the material; for alloys with high chromium contents, the decomposition reaction of MC carbides into M23C6 carbides is the most common.

In equilibrium conditions, the crystalline cobalt presents an allotropic transformation at 419°C, between a compact hexagonal lattice (cobalt ε), stable up to this temperature, and a cubic lattice with centered faces (cobalt γ), which remains up to the temperature of melting (1493°C).

The addition of elements in cobalt alloy alters the thermodynamic stability of the hcp or fcc structures, widening or restricting their fields of existence. Among the elements that stabilize the hcp structure are chromium and refractory elements. The elements that favor the fcc structure are mainly iron, nickel and manganese [9].

2.4 Metallic Coating

The need to use coatings for the turbine components is due to the increase in the gas inlet temperature. To increase the efficiency of the turbine, changes have been made in the compositions of the alloys used, but these variations have led to a decrease in resistance to oxidation and hot corrosion; therefore, metal coatings have been developed whose composition is optimized according to the operating environment. The main requirements that a metal coating must have are the ability to form a protective oxide scale (passivation), which is stable, adherent, of uniform thickness and with a slow growth kinetics. The coatings must have a microstructural stability, i.e. they must not have fragile phases and must have a limited diffusion through the interface with the base material. Furthermore, they must have a thermal expansion coefficient similar to that of the substrate.

The first coatings developed, the diffusion coatings, provide for an enrichment, through Chemical Vapor Deposition or Pack Cementation, of the external surface of the superalloy with corrosion-resistant elements (Al, Cr, Si); these technique allow to obtain a homogeneous microstructure, good resistance to thermomechanical fatigue and a high ductile-brittle transition temperature. Below this temperature, however, they are fragile and for this reason they are inadequate in the most demanding conditions. Overlay coatings were then developed which have a better compromise between environmental resistance, mechanical properties and microstructural stability. These coatings have a typical MCrAlY composition, where M represents Ni and / or Co [10–12].

Figure 7 shows various coatings compared according to their corrosion and oxidation resistance characteristics [13].

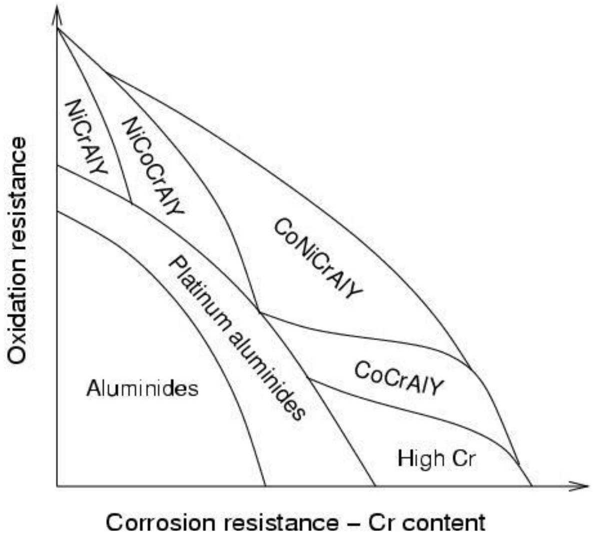

Figure 7 - Resistance to hot corrosion and oxidation of different types of coating [13]

Each element has a specific role and the characteristics of the coating depend on their balance:

- nickel gives ductility,
- chromium resistance to hot corrosion,
- aluminum guarantees resistance to oxidation,
- Yttrium further improves oxidation resistance by segregating the oxide flake at the grain edges.

The composition of the MCrAlY type coatings can be further optimized thanks to the addition of other elements, always in limited quantities, which has specific functions, such as tantalum iridium and rhenium.

Elements such as Mo and W, which are generally present in the composition of the superalloy, to improve the mechanical properties, are instead unwanted in the coatings, because they would worsen the resistance to oxidation, since they form volatile oxides.

The phases that form the metal coatings are mainly:

- Phase γ (fcc): has the same characteristics of the Ni base superalloy matrix, this phase increases the ductility of the coating, improving the resistance to thermomechanical fatigue. The γ phase can also contain Co, Cr and Y atoms;
- Phase β: it has NiAl composition, with structure bcc. It precipitates into the finely dispersed coating and represents the greater reserve of Al of the coating, containing on average 20 wt% of Al. With exposure to high temperatures the Al tends to spread both towards the base material and towards the overlying oxide scale the coating, the general depletion of Al inside the coating causes a decrease in the amount of phase β. Given the diffusion towards both

sides, the coating will have two emptying areas. Emptying β phase is therefore often used as an indicator of the life of the coating;

- Phase γ ’: this phase can be formed following the diffusion phenomena that occur in the coating. The morphology with which it occurs, however, is not the same as that in superalloys;
- Phase σ: phase with tetragonal structure, defined like tP30-CrFe[14]. This phase represents the main of the topologically close-packed (TCP) phases that are formed inside the coating and as in superalloys, the presence of this phase makes the material more fragile;
- α-Cr phase: the phase is cI2-W, or bcc structure. This phase has a high Cr content, in which low percentages of Ni, Co and Re are dissolved. [15]

Finally, the presence of finely dispersed oxides in the matrix also leads to improvements in the coating properties. In fact, these can act as a barrier for the movement of the dislocations and for the diffusion towards the outside of the elements that form the oxide scale such as alumina. They can also increase the yield strength (even at high temperatures) and the resistance to creep, while the coefficient of thermal expansion is significantly lowered.

Most of the coatings are currently applied using Vacuum plasma spray (VPS) and High Velocity Oxy Fuel (HVOF) techniques.

VPS is a process that has been improved for use in controlled environments. In order to obtain an inert working environment, the chamber where the spraying takes place is placed at a pressure of about 1 Pa, after being filled with the inert gas with which you want to work.

The coating is deposited by melting the powders using a plasma, which accelerates them towards the component to be coated. The plasma in this technique is produced through two electrodes that directly constitute the torch from which the plasma comes out (the gas that constitutes the plasma can be Argon or Nitrogen). The maximum temperatures reached with this technique are between 10000 and 15000°C, but higher temperatures can also be reached. For this reason, a water cooling system is also provided which prevents the electrodes from melting.

For an optimal process, the flow rate of the carrier gas of the powders and their size must be carefully evaluated. The powders cannot be too small (they could vaporize or float on the gas) or too large (they could only partially melt and bounce on the substrate or be deviated from the spraying path). Therefore sizes between 5 and 80 µm are used.

This process leads to the formation of highly dense and very homogeneous coatings, free of oxides within the microstructure. It is precisely the low oxygen content that provides the conditions for obtaining resistance to oxidation.

HVOF is a process based on the controlled combustion of a comburent and a fuel (propylene, ethane, propane, hydrogen or kerosene). Downstream of the combustion chamber there is a hole from which

the flue gases come out at supersonic speed and at a pressure higher than atmospheric pressure. Even the powders reach speeds close to those of the gases, allowing to obtain an excellent adhesion between the coating and the base material, a low content of oxides and a high density of the coating. The peculiar characteristics of this technique are therefore: the high speed that the particles assume (higher than they can have in a technique such as the plasma spray), the lower flame temperature (the maximum temperatures reached are below 3000 ° C), the possibility of operating without the vacuum and speed of the process. However, the lower temperature also determines a limit of this technique since high melting ceramic coatings cannot be deposited, such as for example zirconia-based thermal barriers. The quality of the coating obtained can be controlled by changing parameters such as the particle size of the powders, the distance at which the coating is sprayed, the fuel / comburent ratio and the temperature at which the substrate is located.
In Figure 8 is reported the schemes of VPS (on left) and HVOF (on right) techniques [16].

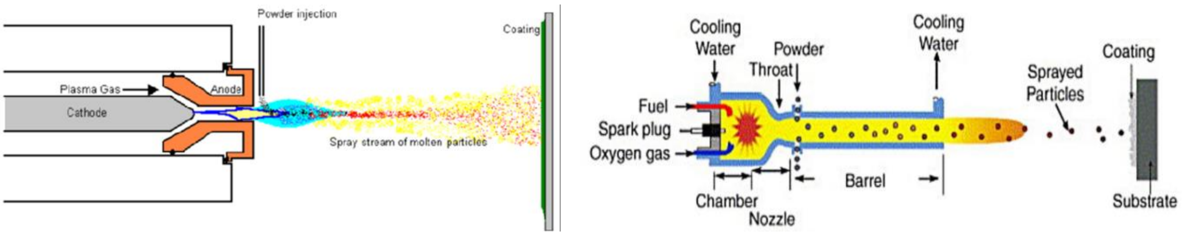

Figure 8 – Functioning scheme of the VPS (left) and HVOF (right) methods [16]

2.5 Thermal Barrier Coating

The use of TBCs (100 to 500 µm in thickness), along with internal cooling of the underlying superalloy component, provide major reductions in the surface temperature (100°C to 300°C) of the superalloy [17], as is reported in Figure 9. This has enabled modern gas-turbine engines to operate at gas temperatures well above the melting temperature of the superalloy (~1300°C), thereby improving engine efficiency and performance. The thermal barrier–coated component must withstand the most extreme temperature, temperature cycling, and stress conditions, and it is expected to last thousands of take-offs and landings in commercial jet engines and up to 30,000 hours of operation in industrial gas-turbine engines[1].

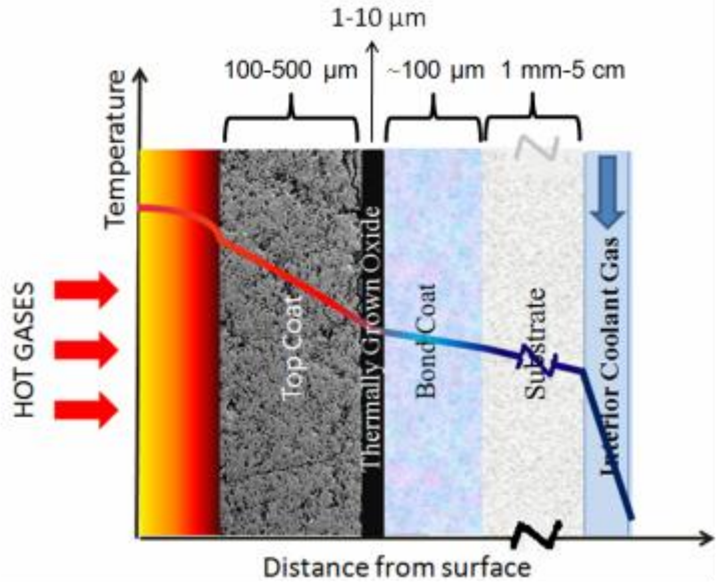

Figure 9 - Thermal gradient representation in a component [18]

The characteristics that the material used for TBC must have are:

- High melting point, as they are directly exposed to hot gases, whose temperatures can exceed 1300 ° C
- Low thermal conductivity, because the reduction in temperature through their thickness is inversely proportional to this property
- High coefficient of thermal expansion, which must be as much as close to of the metal substrate
- Microstructural stability with changes in temperature and in the presence of mechanical stress
- High resistance to hot corrosion and erosion.
- Ability to withstand the stresses and deformations imposed by the work
- Chemical compatibility with the substrate
- Resistance to thermal shock.[18]

The Ceramic top-coat is typically made of Y_2O_3-stabilized ZrO_2 (YSZ). In fact, YSZ has a suite of desirable properties that make it the best material for topcoats. It has one of the lowest thermal conductivities at elevated temperature of all ceramics (~2.3 Wm-1K-1 at 1000°C for a fully dense material) because of its high concentration of point defects (oxygen vacancies and substitutional solute atoms), which scatters heat-conducting phonons (lattice waves). YSZ also has a high thermal-expansion coefficient (~11 $\cdot 10^{-6}$ °C^{-1}), which helps alleviate stresses arising from the thermal expansion mismatch between the ceramic top-coat and the underlying metal (~14 $\cdot 10^{-6}$ °C^{-1}).

To further alleviate these stresses, microstructural features such as cracks and porosity are deliberately engineered into the top-coat, making it highly compliant (elastic modulus ~50 GPa) and “strain tolerant.” YSZ has a relatively low density (~6.4 g·cm·), which is important for parasitic-weight considerations in rotating engine components. It also has a hardness of ~14 GPa, which makes it resistant to erosion and foreign body impact. [4].

YSZ has a high melting point (~2700°C), making it suitable for high-temperature applications. Although ZrO_2 can be stabilized by a host of different oxides (MgO, CeO_2, Sc_2O_3, In_2O_3, CaO), Y_2O_3-stabilized ZrO_2 (YSZ) has been empirically found to be most suitable for TBC applications.

YSZ exists as three different polymorphs: monoclinic, tetragonal, and cubic, depending on the composition and the temperature in relation to the phase diagram, reported in Figure 10.

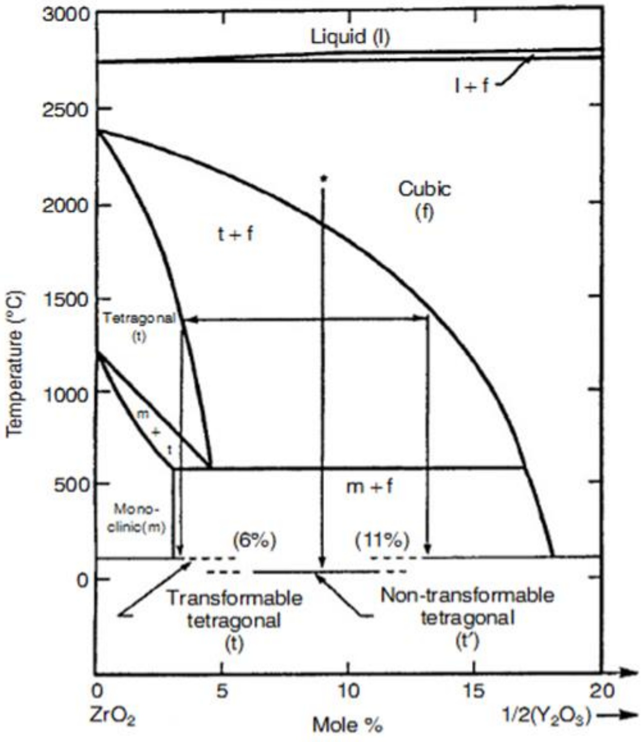

Figure 10 – Particular of ZrO_2-Y_2O_3 phase diagram (ZrO_2 rich) [19]

The materials most used as thermal barriers contain about 7-8 wt% of yttrium. In this case, the applied deposition method, stabilizes the tetragonal prime (t’) phase, a metastable structure of tetragonal phase. The new phase diagram, concerning the metastable phases is reported in Figure 11 [20].

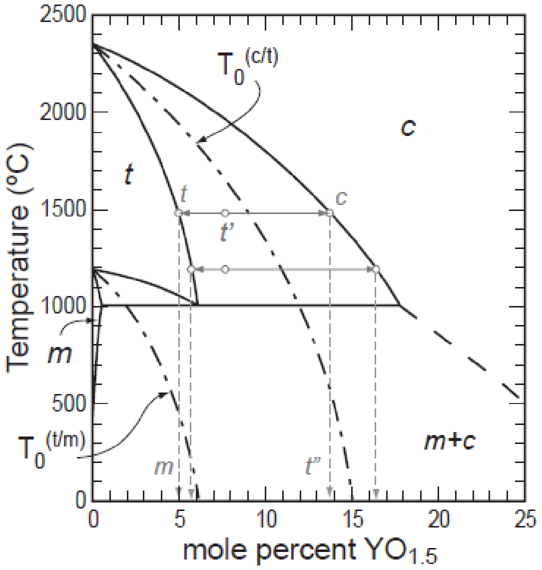

Figure 11 – ZrO_2-Y_2O_3 phase diagram where is reported the range of existenceof the metastable phases [20]

During service, the tetragonal prime phase observed at room temperature [21] evolves in other more stable structures following the sequence:

t'-YSZ → t-YSZ + c-YSZ → m-YSZ + c-YSZ [22]

where c is the cubic phase (with fluorite crystal structure), t is the stable tetragonal phase and m is the monoclinic phase [23,24].

This phenomenon is more evident when the TBC cools down after exposure at high temperature (over 1200-1250°C), because it has enough energy to form the monoclinic phase [25].

This transformation is highly dangerous for the integrity of the TBC because it causes a 4% increase in the unit cell volume, making the material more fragile[26].

The need to create new and more efficient gas turbines that can work at higher temperatures requires the development of materials with higher microstructural stability.

A number of new ceramic top coatings have been developed by doping Zirconia matrix with Rare Earth Oxides, to form ternary or quaternary oxides to solve the problematic of YSZ coatings.

In particular zirconate/hafnates with Gadolinium, Lanthanum, Samarium, Ytterbium and Neodymium have been studied in the last years. Rare-Earth (RE) Zirconates ($RE_2Zr_2O_7$) have attracted significant interest as a novel thermal protection layer because of their intrinsically lower thermal conductivities. The pyrochlore structure of many near equiatomic RE zirconates is also phase stable to higher temperatures than 7YSZ. They also have a higher melting temperature than 7YSZ, and a greater resistance to morphological evolution of their pore structure (sintering) [27].

The most promising materials that have been studied in the last twenty years are:

- Gadolinium Zirconate $Gd_2Zr_2O_7$, that has a low thermal conductivity, high phase stability and a slow kinetics of sintering in comparison to the 7YSZ [28].

- Lanthanum Zirconate $La_2Zr_2O_7$ coating because maintains the single cubic pyrochlore phase up to the melting temperature [29]
- Samarium Zirconate $Sm_2Zr_2O_7$ has the lowest thermal conductivity of the Rare Earth Zirconates and its pyrochlore structure is stable to 2200°C [27]
- hafnates or zirconates containing $YbO_{1.5}$, $GdO_{1.5}$, or $LaO_{1.5}$ which at high temperatures produce a protective layer of garnet and apatite [30].
- Neodymium Zirconate $Nd_2Zr_2O_7$ as new material for TBC obtaining good thermal conductivity results [31]

However, none of these materials replaced 7YSZ mainly due to the better compatibility of the latter with the metal substrate. For this reason, innovative materials have been tested many times as layers overlapping a traditional layer.

However, this multilayer structure can also lead to incompatibility between the individual thermal barrier layers, having different chemical compositions and crystallographic structures.

For these reasons, a new TBC formed by zirconia stabilized with yttria having higher Yttria content (~14wt%) has been studied to be used, combined by other materials, in the next generation gas turbines.

Moreover, to improve the high temperature behaviour while keeping a good compatibility with the metallic substrate, a double layer coating has been designed. This material consists in a first layer of zirconia 7wt% yttria (7YSZ) in contact with the metallic part followed by a second layer of zirconia 14wt% yttria (14YSZ), in contact with hot gas from combustion chamber[32].

Although there are various methods for depositing ceramic coatings on metal substrates, the two most important methods used for TBC deposition are:

- air-plasma-spray (APS)
- electron beam physical-vapor deposition (EB-PVD).

These two methods produce characteristic microstructures with certain desirable attributes that are discussed below.

Air-plasma–sprayed TBCs is based on many years of process development; APS TBCs have the following favourable microstructural characteristics (reported in Figure 12):

- “splat” grain morphology (1 to 5 µm thick, 200 to 400 µm diameter) with inter-“splat” boundaries and cracks parallel to the metal/ceramic interface for low thermal conductivity
- 15 to 25 vol% porosity for both low elastic modulus (high “strain tolerance”) and low thermal conductivity.

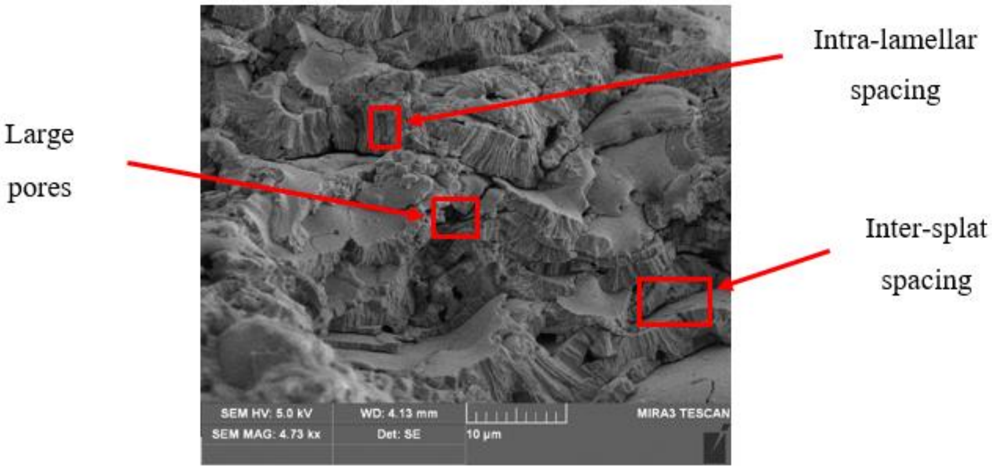

Figure 12 - **SEM/SE x4730 image as sprayed YSZ microstructure**

However, the undulating nature of the metal/ceramic interface, which is required for better interlocking adhesion, produces out-of-plane stresses responsible for in-service failure of APS TBCs. A typical APS top-coat is 300 µm thick, but in some industrial gas-turbine engines applications it can reach 600 µm in thickness. The orientation of the cracks and pores normal to the heat flow reduces the thermal conductivity of the top-coat from ~2.3 Wm^{-1}K^{-1} for a fully dense material to a more typical 0.8 to 1.7 Wm^{-1}K^{-1}[17] .Versatility and low production cost make APS TBCs commercially attractive. However, because of the proliferation of microstructural defects parallel to the interface and the roughness of the interface, APS TBCs generally have shorter thermal-cycling lives than EB-PVD TBCs. This makes APS TBC suitable only for less exacting applications in aircraft engines, such as combustors, fuel vaporizers, after-burner flame holders, and stator vanes.

In the last few years, new processes such as plasma spray-physical vapor deposition(PS-PVD) [33,34], solution precursor plasma spray(SPPS) [35,36] and suspension plasma spray (SPS) [37–39] have been developed to produce the YSZ TBCs with columnar or highly segmented microstructures, which should improve the strain tolerance and durability with reduced cost as compared to the EB-PVD process [40]. The modification of some spraying parameters allows the deposition of particular coatings defined as dense vertical cracks (DVC). DVC coating is a type of TBC that involves the insertion of artificial vertical cracks in the TBC, these cracks reduce the possibility of coating fracture since the cracks absorb the thermal expansion and shrinkage [41]. Air Plasma spray technology is shown in Figure 13.

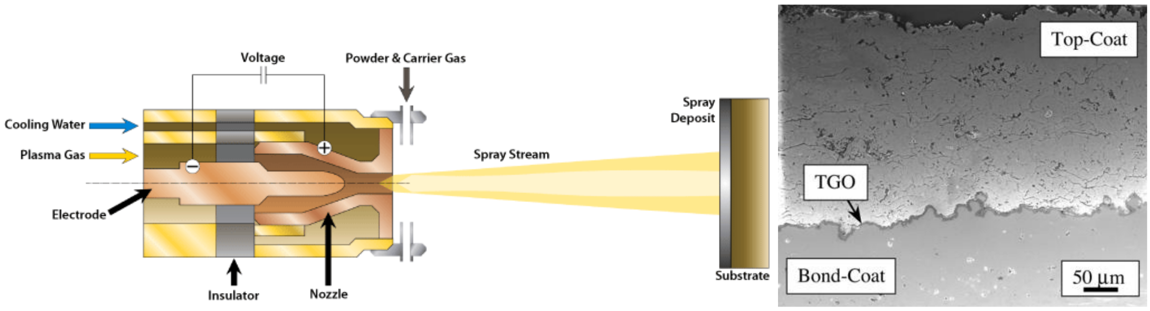

Figure 13 - Air Plasma spray technology (left); Cross-sectional SEM of an air-plasma-sprayed (APS) TBC (right) [4]

In **Electron-beam physical-vapor deposited TBCs**, in contrast to the APS case, the bond-coat surface can be smooth before deposition. Typically, EB-PVD top-coats (~125 µm thick) have the following microstructural features (shown in Figure 14):

- thin region of polycrystalline YSZ with equiaxed grains (size 0.5 to 1 µm) at and near the metal/ceramic interface;
- columnar YSZ grains (2 to 10 µm diameter) growing out of the equiaxed-grain region to the top-coat surface;
- nanometer-scale porosity within the columnar grains; and
- channels separating the columnar grains, normal to the metal/ceramic interface.

The disconnected columns impart "strain tolerance" to the TBC because they can separate at high temperatures, accommodating thermal expansion mismatch stresses. The porosity and the cracks help to reduce the thermal conductivity [~1.5 to 2 Wm^{-1}K^{-1}][17], but to a lesser extent than APS TBCs, because the channels are parallel to the direction of heat flow.

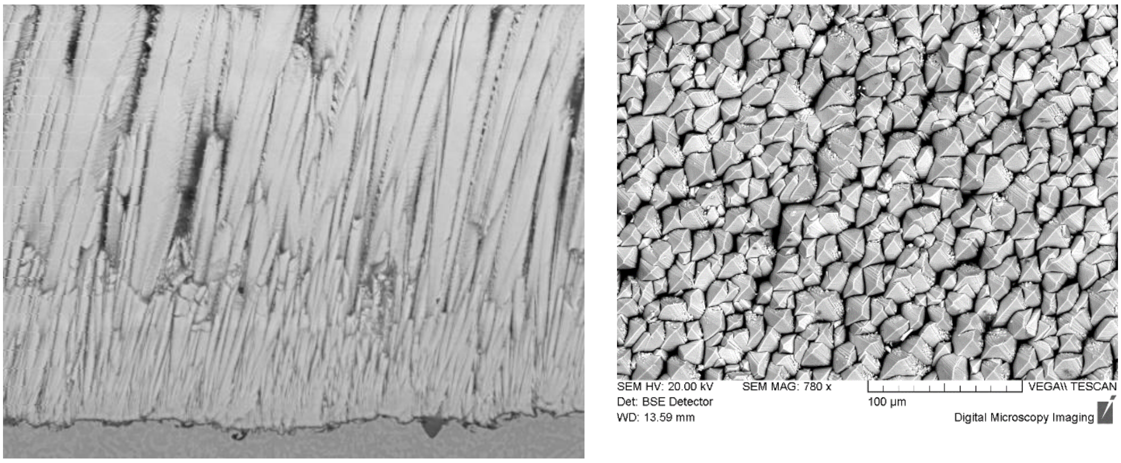

Figure 14 - SEM/BSE images on cross-section x2250 (left) and top surface x780 (right)

In conclusion, as regards the production of gas turbines in recent years, the plasma spray deposition method is clearly the most used. This is because the costs are more affordable than the EB PVD method, also considering the large components of these engines, which must be covered with a protective barrier.

2.5.1 *In service degradation: CMAS Corrosion*

During operation, the materials degrade due to the working conditions of the machine.

As described in the previous chapter, the classic thermal barriers (7YSZ) tend to degrade when the operating temperature exceeds 1300-1400°C, with the formation of the monoclinic phase.

Furthermore, engine shutdowns are a cause of stress for TBCs, also due to the growth of the alumina layer (TGO) at the interface between metal and ceramic material. For this reason, resistance to cyclic oxidation is a very important study factor to evaluate the goodness of the material [42,43].

The degradation of thermal-barrier coatings by molten deposits resulting from a combination of impurities introduced with the intake air and/or the fuel has been a concern since the introduction of these material systems in gas turbines [44].

Most elements in the earths crust and soil occur in minerals, with oxygen, silicon, aluminium, iron, magnesium and calcium being the most common chemical elements, giving the scope for corrosive mixture formation in a wide range of locations. Primary minerals break down during weathering and release oxides. Silicates are a really large and important group of minerals and account for over 40% of all common minerals and igneous rock. Silicates account for the bulk of the earths crust and most soils as both primary and secondary minerals. Alumino-silicates are a commonly occurring group, and usually occur as weathering products of volcanic ash. Allophane and imogolite are examples of Alumino-silicates that have very small particle sizes and high chemical reactivity. Calcite and Dolomite are the most abundant carbonate minerals in sedimentary rocks, and these have been identified as materials deposited in gas turbines during the Persian war, which subsequently led to the formation of CMAS [45], defined in this way because it mainly consists of CaO-MgO-Al_2O_3-SiO_2.

Particles of fine sand, fed with the air needed for combustion, deposit on the hot surfaces of the TBC as molten glasses of Calcium-Magnesium-Aluminum-Silicates (CMAS), which penetrate the TBC porous structure and subsequently solidify (Figure 15). The high temperature interaction of TBC with these molten compounds causes destabilization of the coating microstructure and properties [46].

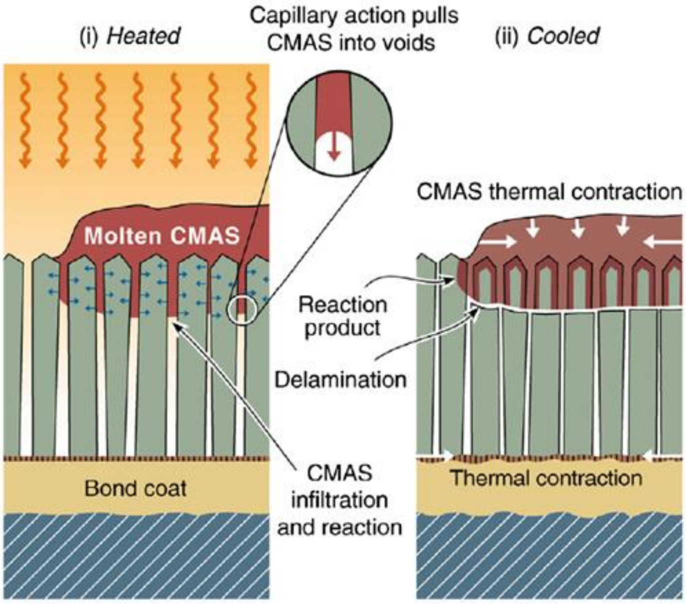

Figure 15 – Scheme of CMAS-TBC interaction [45]

The CMAS-TBC interaction can be physical, by solidifying and cracking the material during engine shut down, or chemical, by interacting with the oxides of the barrier.

In this case, the CMAS glass, penetrating in YSZ grain boundaries, if there is the necessary time, reacts with the elements of the thermal barrier and forms new secondary phases. When these these phases include yttrium the matrix is impoverished and the formation of monoclinic phase is favoured.

Incorporation of Calcium in YSZ can lead to an increase in volume or change in the distribution of stresses in the entire TBC system; this may lead to nucleation of cracks and their growth during thermal cycling. The upper reaction layer increases in thickness with temperature, from ~14 μm at 1240°C to ~21 μm at 1300°C and ~42 μm at 1400°C[47].

This phenomenon has been initially observed in aircraft turbines. In fact, it is very easy for some phenomena such as sandstorms or volcanic eruptions to cause an increase in dust that penetrates inside the motors and settles on the component coatings. For this reason, many studies have been made about the interactions between TB and CMAS with very short interaction times (in the order of a few hours) to simulate what happens in the aerospace field [48–54].

Ansaldo Energia has found sometimes CMAS deposits on ex-service components (Figure 16); if temperature is high enough, they produce TBC degradation through chemical interaction and spalling. An example of damage found on rotor blades is described below; it consisted in a local damage due to over heating of the metal with local loss of TBC. Examinations of detached fragments of TBC and of cross section of the blade near the failure zone have shown the presence of CMAS deposits, which interacted with TBC microstructure [55].

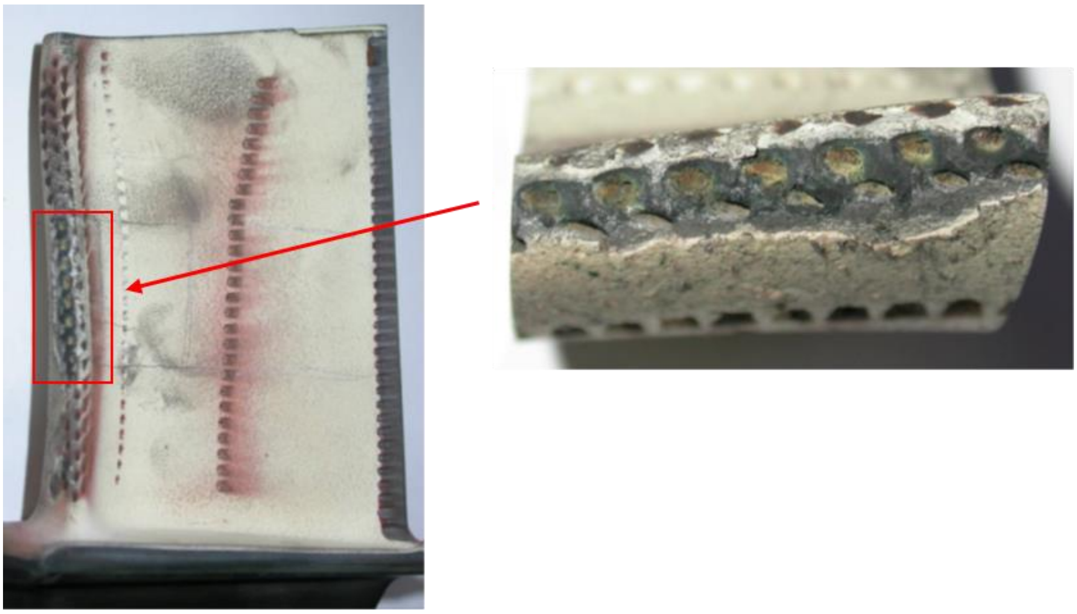

Figure 16 - Ex-service rotor blade with failure (left), particular of TBC detachment (right) [56]

The typical elements of CMAS mixture like Si, Ca, Mg and Al have been detected on a TBC fragment removed from the damaged area. Moreover, the presence of iron oxide, probably coming from the turbine, has been identified in large quantities. The EDS analysis of the blade surface is shown in Figure 17.

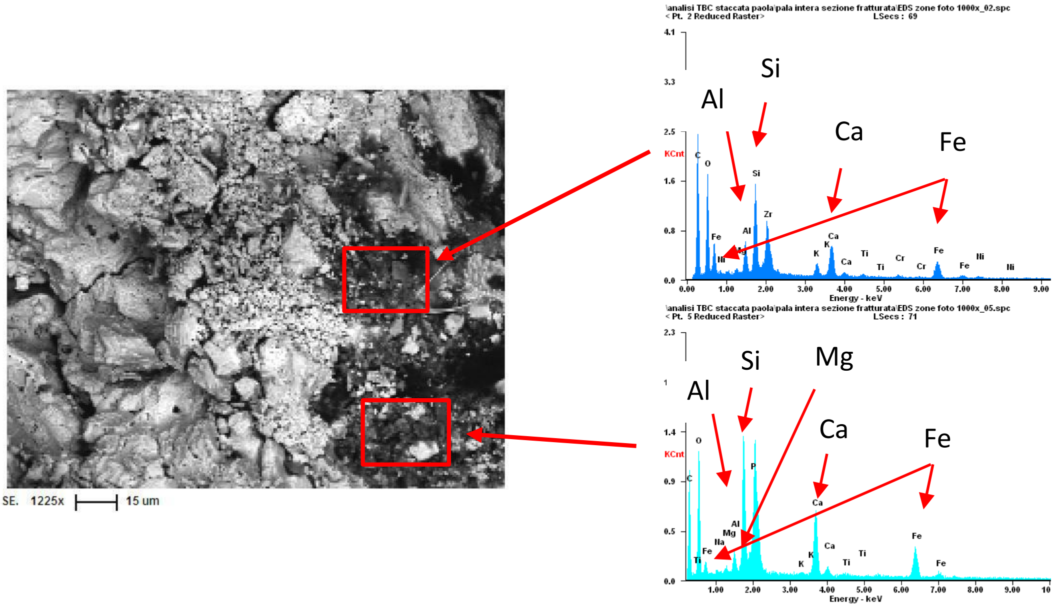

Figure 17 - SEM/SE x1125 and EDS spectra on fractured section of a fragment of TBC from the blade [56]

Close to the failure, TBC has been examined in cross section (Figure 18). It appeared damaged due to the presence of cracks and microstructural modifications too. This made necessary to improve the knowledge of the CMAS interaction mode.

The analysis of the chemical composition of the thermal barrier was carried out to verify the depth of interaction of the elements that form the corrosive mixture (Figure 19).

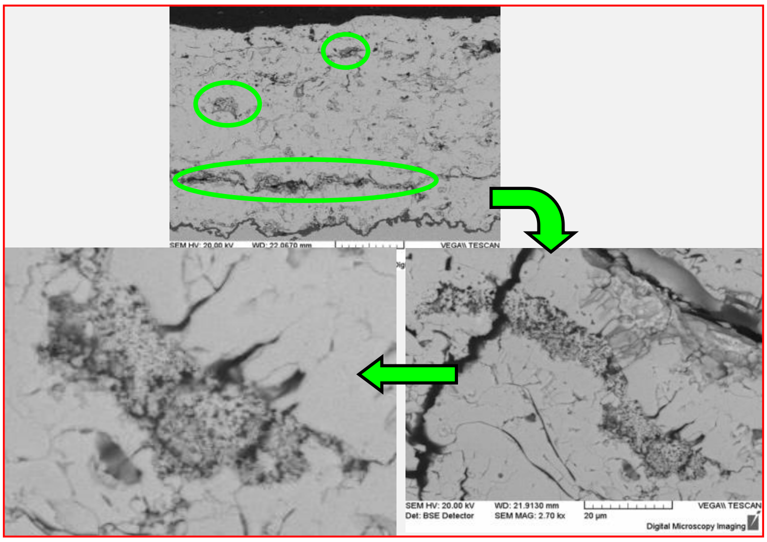

Figure 18 - CMAS induced degradation of TBC on ex-service components

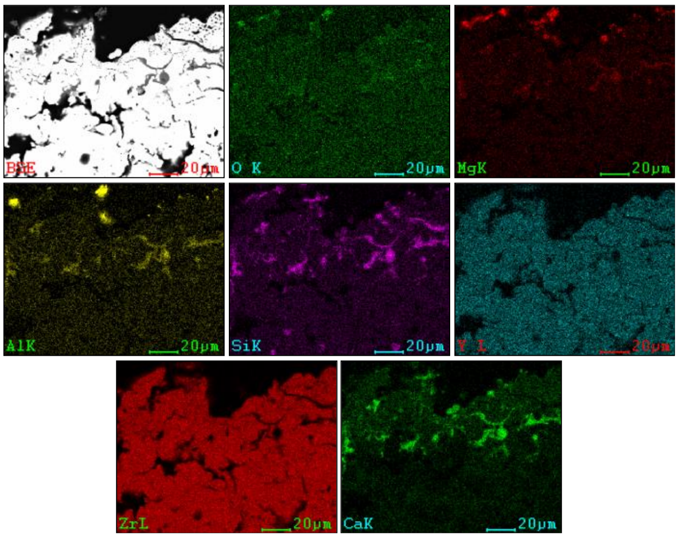

Figure 19 - SEM/BSE image and X ray maps on cross section 1200°C 1000h

In case of mixtures containing iron oxide, monoclinic Zirconia has been detected under the reaction layer (Figure 20), indicating TBC degradation because this transformation can lead to crack and delamination. The transformation is driven by the Y depletion observed under the reaction layer (Figure 21).

The presence of iron oxide in the mixture is not due, as in the case of other oxides, to the presence of this species in the air used as combustive agent. Indeed, the iron oxide is formed by the degradation of metal parts of the turbine itself which oxidize and release the species that mixes with the others coming from the outside.

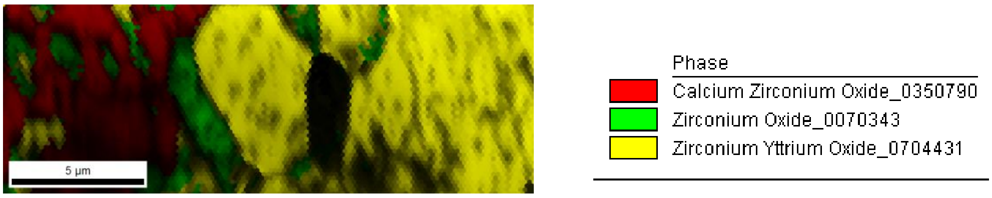

Figure 20 - Example of phase map obtained with monoclinic phase exposed for 1000h at 1200°C

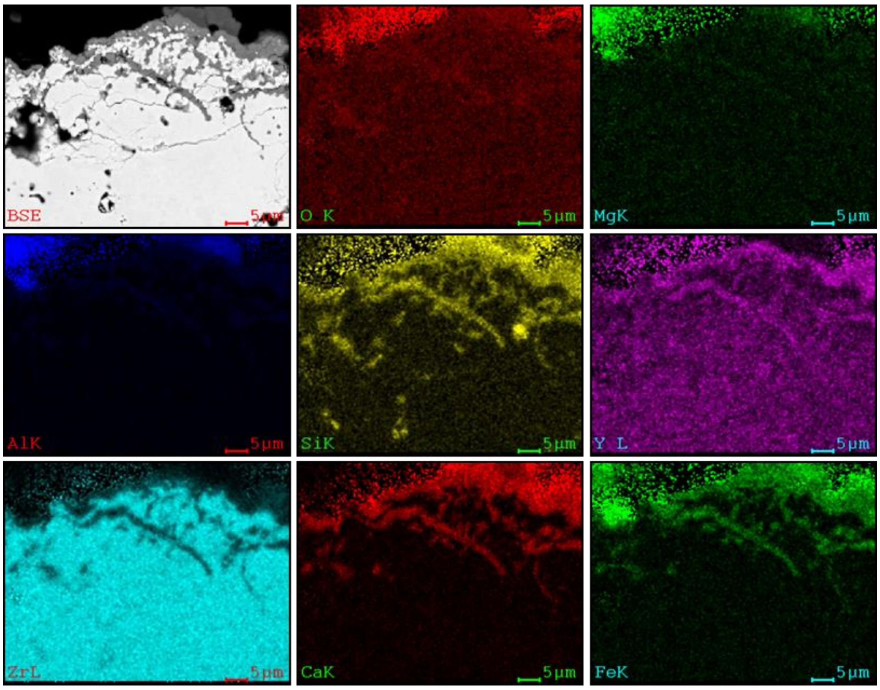

Figure 21 - EM/BSE image and X ray maps on cross section, 1250°C, 2000 h, CMAS with iron oxide

In this thesis many aspects of the degradation of thermal barriers have been studied experimentally. The results have been divided into two different chapters, to better analyse them. The first (defined "TBC intrinsic failure") focuses mainly on the degradation of the 7YSZ coating exposed to high temperature, while the second ("TBC extrinsic failure") studies different materials exposed with a CMAS deposit.

The intrinsic failure has been divided in different parts, since several factors have been studied.

In addition to the kinetic and thermodynamic factors of the thermal barrier degradation, the effect of the cooling rate has been also analyzed to simulate the turbine shutdowns and the initial conditions through the study of TBC powders.

The results, enriched by the thermodynamic study of the binary and ternary phase diagrams of the elements involved, allowed a thorough knowledge of the materials used, useful information on materials not yet mounted on the machines and a high level of knowledge of the degradation phenomena.

3 Materials and methods

3.1 Materials

In this work, different materials have been used to evaluate the evolution of TBC exposed to high temperatures.

Samples tested are powders obtained from supplier or massive TBCs, which are obtained from an unexercised components or from superalloy plates.

Regardless of the metal substrate, the massive material, before being exposed to high temperature, have been chemically detached with a solution HCl and H2O 1:1 under heating.

The performed tests are summarized below.

3.1.1 Materials for TBC high temperature evolution

3.1.1.1 Precursor powders effect

Phase analysis in massive TBC precursor powders is important for assessing the material's tendency to form harmful (monoclinic) phases after high temperature exposure.

This analysis anticipates the goodness of a material before it is deposited using the Plasma spray technique.

The powders analyzed in this work come from the same supplier and differ in the quantity of yttria. In fact, a 7YSZ powder and a 14YSZ powder (whose compositions are shown in Figure 22) has been exposed to high temperatures in a range between 1100 and 1400°C for times between 100 and 1000 h, reported in Table 1.

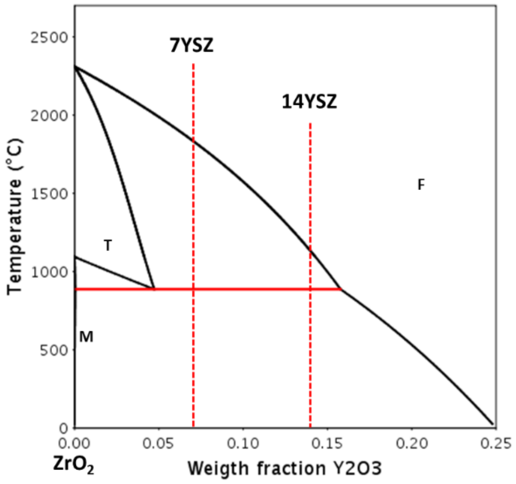

Figure 22 – Particular of phase diagram. The composition of 7YSZ and 14YSZ has been underlined

Table 1 - Scheme of powders samples tested

T (°C)	t (h)		
1100°C	100	300	1000
1200°C	100	300	1000
1300°C	100	300	1000
1400°C	100	300	1000

3.1.1.2 *Cooling rate effect*

In this work the evolution of the t→m transition as a function of the cooling rate starting from high temperature was studied for two different types of TBC have been tested.

The first one is defined dense vertical crack (DVC), while the second one is obtained by APS and it has a porous structure. For DVC coating the used powders are agglomerated and sintered, while the powders used for APS TBC are HOSP (hollow spheres, plasma spheroidized). In Figure 23, the microstructures by optical microscopy of the two studied materials are reported. Both the images have been obtained before the detachment of TBC from metallic substrate, therefore the metallic coating is visible.

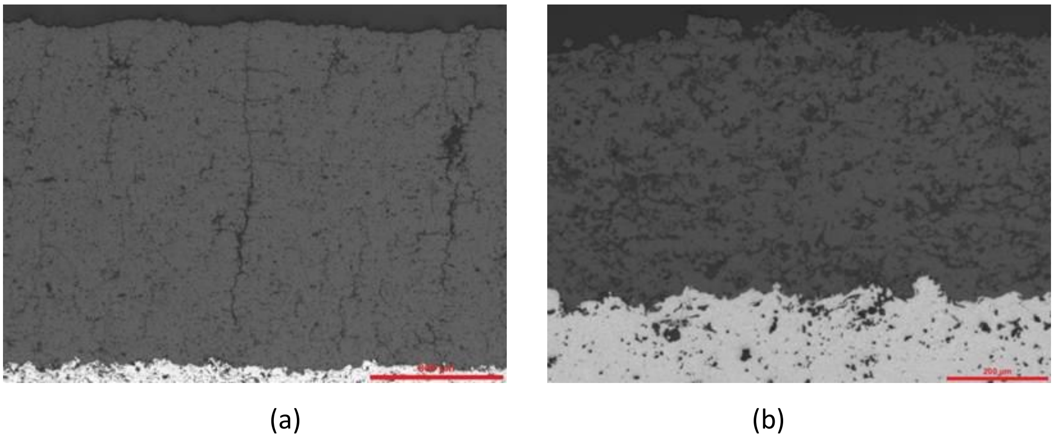
(a) (b)

Figure 23 - Optical microscope images (x100): DVC (a) and Porous (b) TBC

The free-standing samples have been exposed in tubular furnace at 1400 °C for 100 h. After exposure, the TBCs have undergone five different cooling rates. In addition to quenching in air and water, three treatments have been performed to simulate different cooling rates: 1 °C/min, 5°/min and 20 °C/min. After different cooling rates from 1400 °C, the samples have been annealed at low temperature as summarized in Table 2 for DVC material.

All the samples (DVC and porous materials) has been annealed at 250 °C for 24 hours. For DVC materials 168h at 250 °C and 24h at 400 °C annealing have been tested, too.

The different aging heat treatments have been defined in order to evaluate the effect of time at the same annealing temperature and the effect of an increase in temperature for a relatively short aging time.

Table 2 – Scheme of treatment of DVC TBC

	Testing conditions				
Cooling rate	1°/min	5°/min	20°/min	Air quenching	Water quenching
aging	+24h at 250°C	+24h at 250°	+24h at 250°	+24h at 250°	+24h at 250°
	168h at 250°C	168h at 250°C	168h at 250°C	168h at 250°C	168h at 250°C
	24h at 400°C	24h at 400°C		24h at 400°C	

3.1.1.3 Kinetics of zirconia phases

As already stated, during high temperature exposure, the tetragonal metastable structure tends to decompose into a cubic and tetragonal structure poor in Y_2O_3 and subsequently in monoclinic phase, contributing to the breakage of the coating.

The knowledge of the kinetics of the 7YSZ decomposition process, after high temperature exposure, allows to use the quantities of the various crystallographic species as an indicator of temperature.

To study this phenomenon, samples of a new component (microstructure shown in the Figure 23-b) have been tested between 1100 and 1400°C for different times. The scheme of samples studied are reported in Table 3.

Table 3 – Scheme of samples tested

T (°C)	**t (h)**								
1100°C	1	24	100	250	450	650	850	1000	1400
1200°C	1	10	100	200	300	1000			
1300°C	1	10	100	400					
1400°C	1	10	100	200	300	500			

3.1.1.4 Thermodynamic evolution of 7YSZ

The thermodynamic evolution of the 7YSZ has been studied through exposure in a high temperature oven for long times up to 10000h.

The materials and tests used are the same as those defined for the CMAS corrosion tests defined in the next paragraph, as the exposed samples without the presence of corrosive componentshave been also used as a comparison with those exposed with the deposits.

3.1.2 Materials for CMAS corrosion tests

For this kind of tests three different TBC systems have been tested: single layer zirconia stabilized with 7 wt% yttria (7YSZ), single layer zirconia stabilized with 14 wt% yttria (14YSZ), which composition is reported in Figure 22, and a double layer TBC formed by a 14YSZ layer superposed to a 7YSZ one (DL). The reason for the double layer is that this material combines the better phase stability at high temperature of 14YSZ with the better compatibility with the metallic substrate of 7YSZ. Notice that the TBC samples used in this work have different thickness: 7 and 14 are thinner (~250µm) while DL is thicker (~500µm).

The 14YSZ does not have the characteristics to be used as Thermal Barrier Coating, but it is important to evaluate the top layer behavior in the new double layer system

As for the microstructure, no significant difference can be appreciated between single and double layer materials (Figure 24): both show medium-large porosity and micro cracks, typical of the APS deposition.

Two different types of CMAS have been considered to investigate their interactions with the different TBC materials. Their compositions are reported in Table 4.

The first composition (STD) is generally studied in literature [57] while the second one (ANS), containing an appreciable amount of Fe_2O_3, has been derived from the analysis of operated blades and vanes from Ansaldo gas turbines (see paragraph 2.5.1).

Both compositions have been prepared in laboratory by mixing commercial oxides using a technical balance.

Table 4 – Composition of CMAS mixtures

CMAS	**Composition (wt%)**				
	SiO_2	**Al_2O_3**	**CaO**	**MgO**	**Fe_2O_3**
STD	48.4	12.0	32.9	6.8	
ANS	36.2	8.9	24.6	5.1	25.2

In Table 5 is summarised the nomenclature used in this work to identify samples: each name is composed by three symbols to describe the type of material, batch and CMAS used.

Table 5 – Scheme of nomenclature used in this work

TBC material	**Batch**	**CMAS Type**
7	A	STD
14	B	ANS
DL		NC

For each material, two different batches of powders have been studied to evaluate whether the difference of starting conditions affects phase transformations. In Table 6 the list of tested materials is summarized.

Table 6 – type of powder used to form TBCs tested in this work

Sample	Type of powder
7A	Stark_827
7B	Metco_204
14A	Stark_818
14B	IKH_14YSZ
DLA	Stark_(827+818)
DLB	IKH (8YSZ IKH+14YSZ IKH)

After the preparation of CMAS mixture, they have been suspended in water and sprayed using an airbrush on the external surface of the TBC samples kept at 50-70°C on a hotplate. The sprayed samples have been weighed in order to have a deposit of about 7 g/cm^2 (Figure 25-a). In the DL samples the surface on which the deposit is applied is the 14YSZ layer (external surface).

For each material, samples with CMAS (STD and ANS) and without CMAS (Not contaminated NC) have been put on a ceramic plate (Figure 25-b) and exposed in chamber furnaces at 1100, 1200, 1300 and 1400°C for different ageing times depending on the testing temperature, as summarized in Table 7. The temperatures have been chosen in order to cover a huge range of service conditions that TBCs can withstand during service, depending on the components where they are applied, on the operative profile of the gas turbine and on the thickness temperature profile. At high temperature, only two exposure times have been considered: 300 and 1000 h. Indeed, at these temperatures the interaction between TBCs and CMASs is facilitated by kinetic factors and it is not necessary to evaluate longer times.

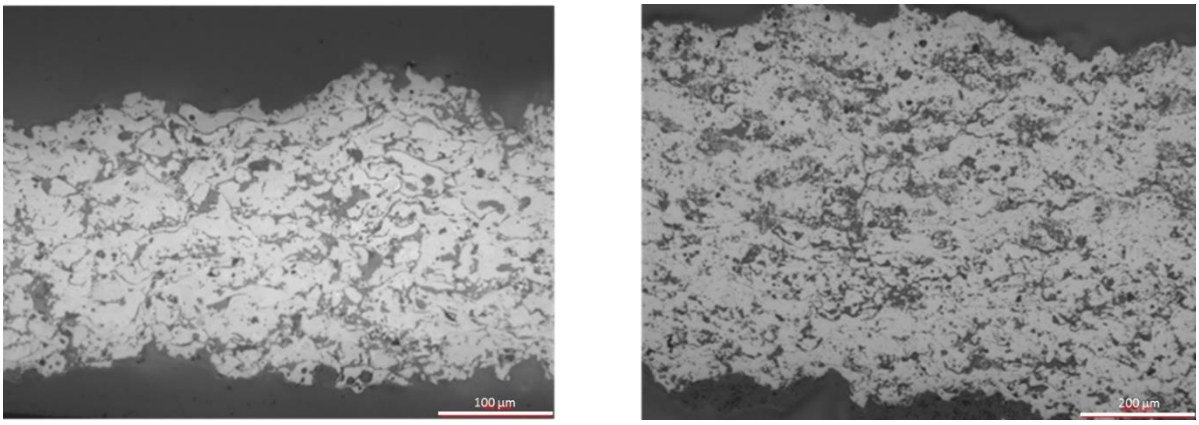

Figure 24 – Optical microscope images: 7YSZ sample on left, double layer sample on right


(a) (b)

Figure 25 – (a) CMAS deposition set-up and (b) samples on ceramic plate before high temperature exposure

Table 7 - High temperature test matrix on studied materials

	Testing conditions													
T (°C)	1100					1200					1300		1400	
time (h)	500	1000	3000	5000	10000	500	1000	3000	5000	10000	300	1000	300	1000

3.2 Methods

After exposure at high temperature, all samples described above have been analyzed by X-Ray diffraction (XRD) on both surfaces in order to identify the present phases. Then, they have been milled to produce powders and analyzed again by XRD to quantify the phases by Rietveld method.

Moreover, the sample have been mounted to perform microstructural analysis: the optical microscopy allowed to study the porosity and microstructure, the electronic microscopy to know composition and crystal structure of the phases.

The samples exposed with CMAS (and the corresponding specimens without the corrosive) have been studied by thermography to evaluate the variation of the physical properties (diffusivity) of the materials.

These techniques are briefly described in the chapters below. Finally, the CALPHAD method used for the study of the thermodynamic modeling of materials, described in chapter 6, is reported.

3.2.1 X-Ray diffraction

The samples have been analyzed on surface to identify the phases by X ray diffraction technique [58] and they have been milled to quantify the phases by Rietveld method [59].

The X-ray patterns, used as a reference during the quantification are taken from the ICSD database: [60] for t, [61] for t', [62] for c and [63] for m phase.

The diffractometer used is a PANalytical, Empyrean series 2 with linear high resolution Cu radiation; diffraction patterns were obtained within the 2theta 20–100 range in 0.007 theta steps using standard Bragg—Brentano geometry and a and PIXcel1D detector. Rietveld's refinement has been performed using the Panalytical Software High Score Plus.

XRD pattern and the Rietveld refinement was obtained following the Rietveld refinement guidelines formulated by the International Union of Crystallography Commission on powder diffraction[64].

The Rietveld method is a refinement technique able to optimize a structural model and consists in the minimization of the squared difference of the observed intensities with respect to the calculated ones. It relies on intensities calculated point by point and not on the integrated ones, this allows to preserve information deriving from the peak shape.

$$\Phi = \sum_{i=1}^{n} w_i \, (Y_i^{obs} - Y_i^{calc})^2$$

Where w_i is the weight associated to the i-th measure and, when the measured intensity is only affected by statistical errors, is defined as:

$$w_i = (Y_i^{obs})^{-1}$$

The Rietveld method uses the whole diffraction profile to determine by means of non-linear least squares the best structural and profile parameters which describe the experimental pattern.

Two agreement factor have been considerate to evaluate the goodness of phase quantifications.

R_{wp}factor is the square root of the minimization function scaled by the weighted intensities:

$$R_{wp} = (\frac{\sum_{i=1}^{n} w_i \, (Y_i^{obs} - Y_i^{calc})^2}{\sum_{i=1}^{n} w_i \; {Y_i^{obs}}^2})^{-1}$$

One of the most used agreement factors is goodness of fit, called also χ^2, and is defined as the ratio between square $R_{wp}$and squareR_{exp}.

$R_{exp}$is defined as:

$$R_{exp} = (\frac{N - P}{\sum_{i=1}^{n} w_i \; {Y_i^{obs}}^2})^{1/2}$$

with N – P equal to the difference between the number of experimental points and the number of refined parameters; it coincides with the number of degrees of freedom.

Finally, $\chi^2$is defined as:

$$\chi^2 = (\frac{R_{wp}}{R_{exp}})^2 = \frac{\sum_{i=1}^{n} w_i \, (Y_i^{obs} - Y_i^{calc})^2}{N - P}$$

3.2.2 Microscopy

3.2.2.1 Optical and electronic microscopy

In this work, the inverted optical microscope [65]Leica Reichert MEF4M has been used.

The micrographs of the samples are acquired from the state through a digital camera mounted on the microscope itself and connected to an image analysis system.

The samples have been analyzed by optical microscopy to evaluate the variation of morphology and porosity of TBC after severe test condition (normally high temperature). For this reason, generally, the samples observed with this technique have be cold mounted. In fact, to avoid the microstructural modification of the samples, which are very porous, a method of impregnation at room temperature under vacuum has been used.

The scanning electron microscope used in this work is a FEG SEM type Schottky MIRA 3 equipped with EDAX SDD Apollo-X detector.

The source to obtain the electron beam, unlike the SEM, exploits the emission by field effect: a strong negative potential is applied to a single crystal tip in W (tip). The applied potential and the favorable geometry cause a very intense electric field to arise, such as to bend the energy bands of the material and allow the electrons to escape by tunnel effect.

In this work, the electronic microscopy have been used to characterize the microstructure, define the elemental composition of the secondary phases and evaluate the compositional profile of some elements (in particular yttrium) in the thickness of the samples. Moreover, the detector EBSD, mounted on the instrument, also made it possible to evaluate crystallographic orientation and structure size of the TBC grains and the dispersion of the phases within the sample.

Since the instrument works with samples whose surface is conductive, the specimens have been hot mounted. This technique is important for improving the EDS measurement, even though the pressure exerted on the specimens during embedding can change the original porous structure.

3.2.2.2 EBSD detector

The EBSD technique is a useful tool for the acquisition of micro-textile data, for the characterization and crystallographic identification of unknown phases and for the evaluation of deformation in the crystal lattices [19].

This technique is based on the detection, on a phosphor screen (about 5 cm in diameter and about 2 cm away from the sample), of retro diffused electrons that go in diffraction with the surface of the sample. The sample must be oriented about 70 ° with respect to the horizontal plane of the SEM.
Figure 26 shows a schematic representation and an image of the microscope chamber with the EBSD detector inserted.

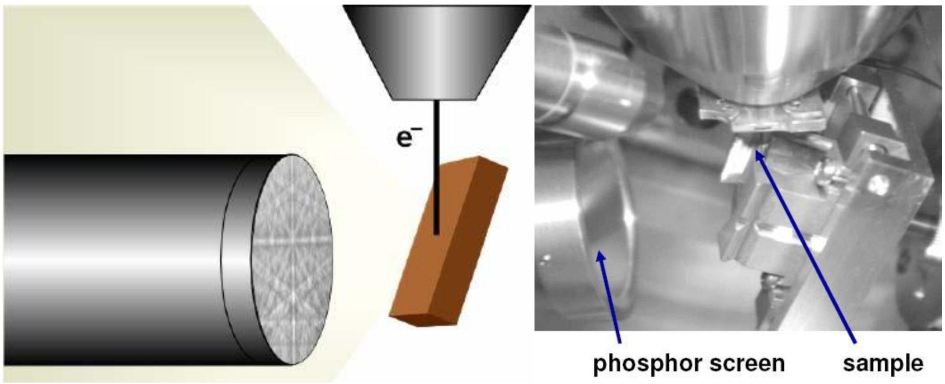

(a) *(b)*

Figure 26 - Schematic representation of the instrument (a) and image of the internal chamber of the SEM: arrangement of the sample and the phosphor screen with respect to the primary electron beam (b)

Diffraction occurs because Bragg's law is satisfied and the diffracted electrons create on the screen a pattern characterized by the presence of numerous bands; these patterns are called Kikuchi or EBSD patterns, represented in Figure 27.
The bands, formed by the intersection of the Kossel diffraction cones, represent the families of diffraction crystallographic planes and the width of the bands themselves is inversely proportional to the distance between the planes of the family, expressed as d in the Bragg law and to the voltage acceleration of primary electrons.

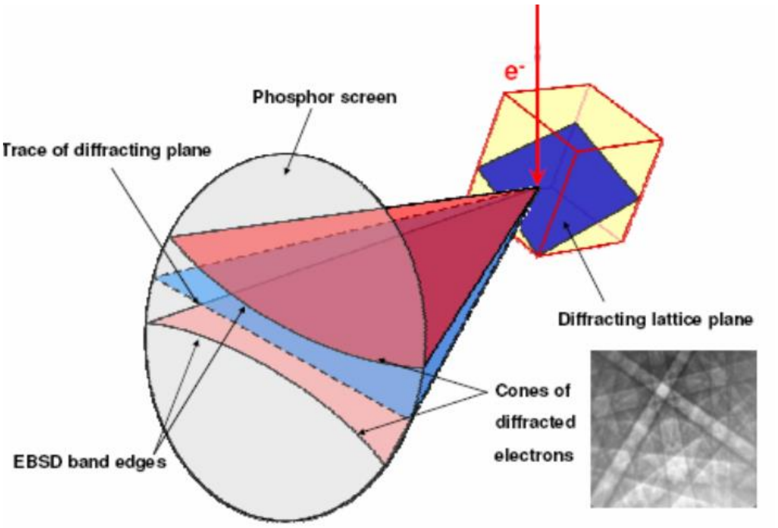

Figure 27 - Schematic representation of the electron diffraction in the crystal lattice of the sample and creation of the Kikuchi pattern on the phosphorus screen by intersection of the Kossel cones

The intersections of the bands are called axis zones, and represent the intersections of two crystallographic planes. The arrangement of the bands in the pattern highlights the elements of point symmetry of the crystal lattice in the study.

The data collected with the EBSD technique are processed through the use of dedicated software that allow you to obtain a very large number of processes and therefore display the results.

After acquiring the patterns over large areas for mapping, it is possible to reprocess the data and create different types of maps [66].

The samples subjected to these analyzes must be hot-embedded and cleaned with a particular technique that involves vibrating the surface of the samples in a silica suspension for at least 12 hours.

During this work, "Image quality" (IQ) maps were used to evaluate the structure of the mapped surface, "Inverse pole figure" (IPF) orientation maps, aimed at displaying the different grain dispositions and dimension, and, finally, maps “Phase” (PH), to identify the different secondary phases.

The technique does not distinguish the diffraction patterns of the cubic and tetragonal (t and t’) structures from each other as they are too similar, but it allows to highlight the monoclinic phase.

Therefore, this analysis is used to study the evolution of the grain size and the distribution of the monoclinic phase in the thickness of the samples.

3.3 Thermography

To measure the evolution of physical properties of TBC after test at high temperature for long exposure time, thermography has been exploited.

The Laser Flash method [67–69] is the most frequently used photo-thermal technique to measure thermal diffusivity. In particular, in many countries the laser flash method is currently considered a standard for thermal diffusivity measurement of solid materials[70]. This method consists of heating the front face of a sample (typically a small disk-shaped specimen) by a short laser pulse and detecting the temperature evolution on its rear surface.

The apparatus is described in Figure 28, where is reported the instrumentation used by the CNR of Padova and that of Ansaldo Energia.

The two techniques differ in the use of two different sources (laser for CNR, flash for Ansaldo) and for the use of a thermal imaging camera as a detector in the Ansaldo materials laboratory and a single point detector in CNR.

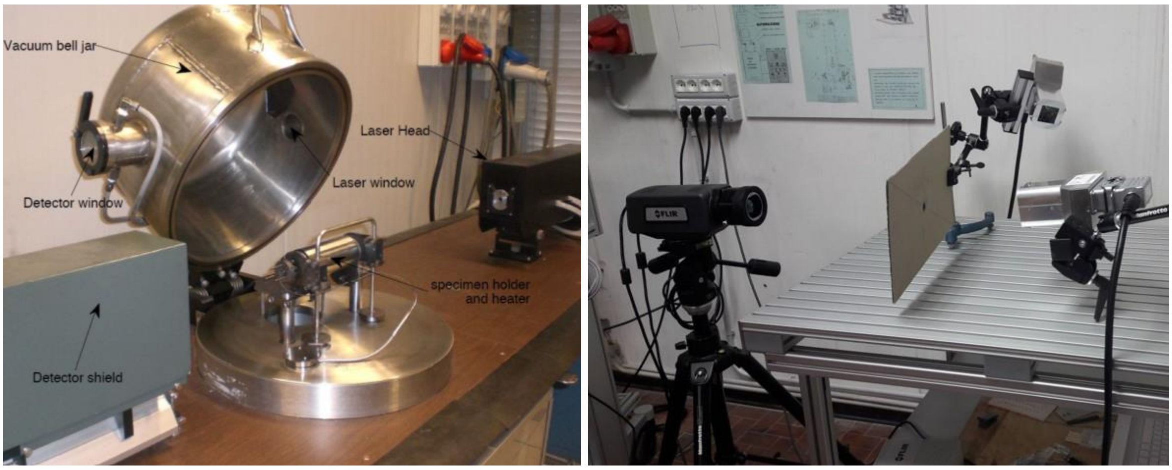

(a) *(b)*

Figure 28 - Instrumentation of thermography used by the CNR of Padova (a) and that of Ansaldo Energia (b)

The main advantages of this method are its simplicity and rapidity of measurement, and the possibility to measure the thermal diffusivity on a wide range of materials at different temperatures.

The mathematical model utilized to describe the heat conduction problem that arises in the Laser Flash experiment is the following (see Figure 29):

- a slab of thickness l
- heat flux prescribed on one side (z = 0) of the slab, consisting of a pulse of finite duration t_h
- heat exchange with the environment according to the linear Newton law on the heated side, adiabatic on the back side (z = l) where temperature is measured.

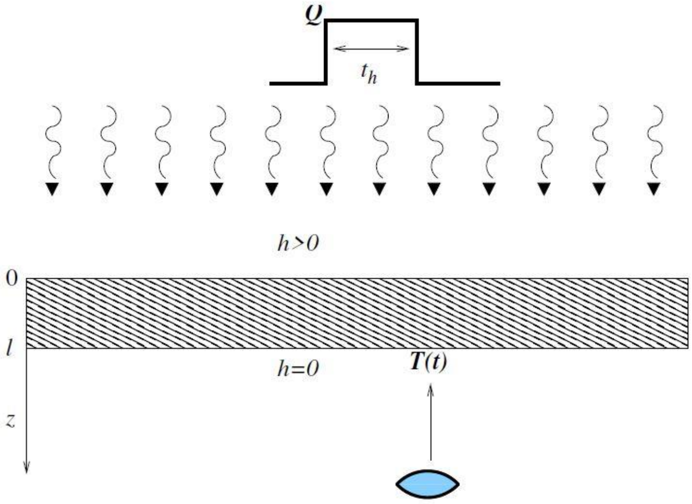

Figure 29 - Scheme of the thermography measurement

The solution for the temperature on the back side of the slab is given by:

$$T(t) = \frac{Q}{h}\sum_{i=1} \frac{2sin\mu_i}{\mu_i + sin\mu_i cos\mu_i}[\exp(\mu_1^2\frac{\alpha}{l^2}(t - t_h)) - \exp(\mu_1^2\frac{\alpha}{l^2})]$$

Where:

- Q is power of the pulse during the heating time [Wm^{-2}]
- h is heat exchange coefficient [$Wm^{-2}K^{-1}$]
- α is thermal diffusivity [m^2s^{-1}]
- l is specimen thickness [m]
- t is time [s]
- t_h is pulse duration [s]
- μ_i is i_{th} positive root of the transcendental equation $\mu \tan \mu = Bi$
- $Bi = \frac{hl}{\lambda}$ is dimensionless Biot number
- λ is thermal conductivity [$Wm^{-1}K^{-1}$]

The classical formula to obtain the thermal diffusivity from the flash experiment is due to Parker [71]:

$$\alpha = \frac{0.1388\, l^2}{t_{0.5}}$$

where $t_{0.5}$ is the time needed to the temperature to rise at half of its maximum value. This formula is valid in case of adiabatic conditions.

The measurements are carried out using two instrumental divers set ups, that are shown in Figure 30-a. Transmission measurements are obtained when the sample is placed between the source and the camera, while reflection measurements are carried out with the camera and the source placed on the same side respect to the sample.

In this work, using free standing TBC samples, the transmission measurement has been choose. The obtained heating profile, reported in Figure 30-b, is calculated with a curve though a matlab code provided by CNR.

The determination of the curve allowed the calculation of $t_{0.5}$ and consequently the diffusivity of the material.

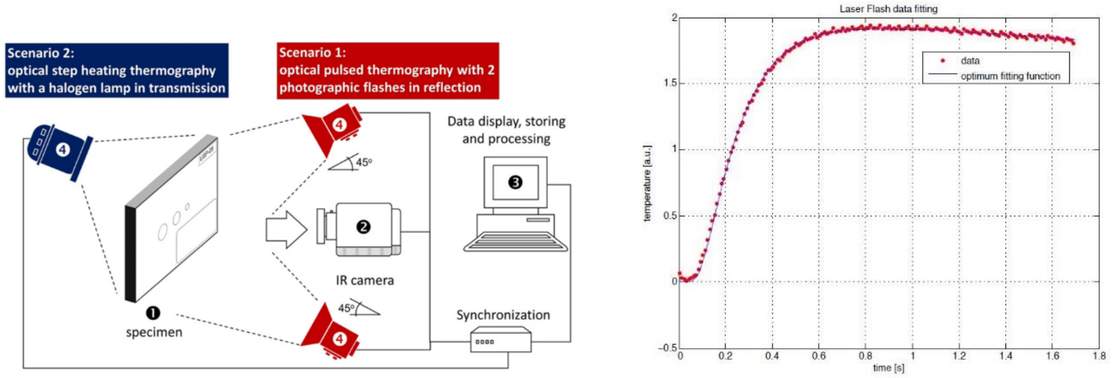

(a) (b)

Figure 30 – Scheme of instrumental divers set ups (a) and Example of registered heating profile (b)

3.4 CALPHAD method

The combination of thermodynamics and visualized phase diagrams can be an efficient tool to describe and analyze phase equilibira and transformations under both equilibium and non-equilibium conditions. The CALPHAD (CALculation of PHAse Diagram) approach is a method originally developed for the calculation of phase diagrams while now has become a powerful tool for materials design. It is Schematically summarized in Figure 31.

There are three main steps in the CALPHAD approach [72]:

1). The input data. Because CALPHAD is an approach strongly based on the experimental data, it is very important that all possible input data are collected before the work is started. These are mainly experimental data including the crystal structure information, stable and metastable phase equilibria, thermodynamic properties, such as enthalpy and Gibbs energy of phases and changes of these quantities during phase formation, structural transformations and change of temperatures, the absolute value of heat capacity and entropy, vapour pressure, various partial molar properties for multicomponent systems, etc. Moreover first principle calculations can offer very important data on the enthalpy of formation at ground state, which is comparable to the standard enthalpy of formation at 298.15K, when experimental data are not available. . All the original both experimental and theoretical data should be carefully evaluated so that the selected data are reasonable and consistent.

2). Thermodynamc models for phases. Appropriate thermodynamic models have to be adopted to describe the energetic behavior of phases. Reasonably, only models based on the structural and physical characteristics can truly reproduce the thermodynamic behavior of different phases. in any case the thermodynamic model includes a series of empirical parameters, which are optimized on the basis of the input experimental data. Some thermodynamic models have already been implemented in a form which reflects actual interactions between different atoms with good generalization. For example, by means of an appropriate sublattice model it is possible to describe both the substitutional solid solutions formed by atoms with similar properties, and the interstitial solid solution formed by atoms with largely different dimensions.

3). The optimisation process. Both the assessment of the model parameters and the calculation of the resulting phase diagram must be carried out by dedicated computer programs. Since L. Kaufman [73]developed the first software, several academic as well as commercial pieces of software have been developed, based on different mathematical methods and computer languages (e.g. Lukas program, Thermo-Calc, Fact-Sage, Pandat, etc.).

In the present work all the optimizations and calculations are carried out by the Thermo-Calc software package[74]. To derive the thermodynamic parameters of different phases, appropriate thermodynamic models have to be selected based on their structures.

In the following thermodynamic models adopted in this work are briefly introduced.

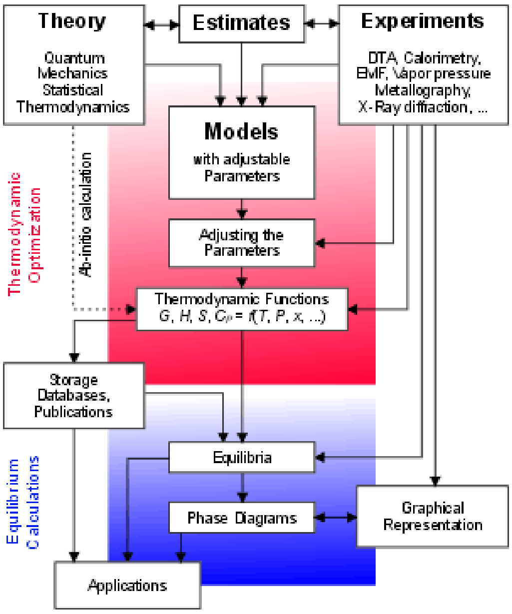

Figure 31 - The schematic diagram for the CALPHAD approach [75]

3.4.1 Pure elements

The Gibbs energy of an element or a stoichiometric substance at the ambient pressure can be expressed by:

$$G=A+BT+CTLnT+DT^2+ET^{-1}+\ldots$$

where A, B, C, D, E, … are the parameters which can be optimized from the experimental heat capacity, heat content and entropy data.

The equation above actually is valid only in a certain temperature range, and generally phases have different Gibbs energy functions in different temperature ranges. At the interval limits, the Gibbs energies are continuous. Because only the thermodynamic properties above room temperature (298.15 K) are of practical interest, it is supposed that the enthalpy of stable structure of any element at 298.15 K and 1 bar is equal to zero, and this assumption is set to be the reference state of elements. This reference state has already been widely accepted, and SGTE (Scientific Group Thermodata) has optimized the lattice stabilities of all elements with this principle.

3.4.2 Thermodynamic models for the solution phases

The solution formed by components which can substitute randomly is called substitutional solution. The thermodynamic properties of substitutional solution (gas, some liquid and solid solution phases) are referred to the ideal solution. The molar Gibbs energy of substitutional solution α phase is generally expressed by the following equation:

$$G_m^\alpha = \sum_i x_i \, {}^0G_i^\alpha + {}^M G_m^\alpha$$

where x_i means the mole fraction of component *i*. ${}^{0}G_i^{\alpha}$ is the Gibbs energy of component *i* with the same structure of α, and ${}^{M}G_i^{\alpha}$ is called the Gibbs energy of mixing which is composed of two parts:

$${}^{M}G_m^{\alpha} = -T\,{}^{M}S_m^{ideal} + {}^{E}G_m^{\alpha}$$

in which $-T^{M}S_m^{ideal}$ is the part from the contribution of ideal mixing, and ${}^{E}G_m^{\alpha}$ is the excess Gibbs energy. For the ideal mixing, because no any heat effect is produced, and thus only the entropy makes contribution to the Gibbs energy of mixing. ${}^{0}G_i^{\alpha}$ reflects how large the mixing behavior deviates from the ideal case, and how it varies with composition.

For example, the Gibbs energy of a solution phase which is composed of two components A and B can be formulated by:

$$G_m^{\alpha} = x_A\,{}^{0}G_A^{\alpha} + x_B\,{}^{0}G_B^{\alpha} + RT(x_A \ln x_A + x_B \ln x_B) + {}^{E}G_m^{\alpha}$$

$x_A\ {}^{0}G_A^{\alpha} + x_B\ {}^{0}G_B^{\alpha}$ is the part of Gibbs energy of mechanical mixing, and $RT(x_A ln\, x_A + x_B \ln x_B)$ is the part of Gibbs energy associated with the entropy of mixing. The sum of these two parts is the Gibbs energy function of ideal mixing. For the ideal case, the bond energies of A-A, A-B, and B-B are equal, and the atoms of A and B mix randomly without the production of heat. For the nonideal substitutional solution, ${}^{E}G_m^{\alpha}$ can be expressed by some polynomials, for example the Redlich-Kister polynomial [76]:

$${}^{E}G_m^{\alpha} = x_A x_B \sum_j I_j (x_A - x_B)^j$$

in which x_A and x_B are the mole fraction of atoms A and B, respectively, and the I_j is called the interaction parameter in the order of *j*. In case of *j*=0, the equation (3.5-5) is simplified to be:

$${}^{E}G_m^{\alpha} = X_A X_B I_0$$

Such case is called regular solution. In regular solution, the bond energies of A-A, A-B and B-B are not equal. Suppose ν is the energy to form a A-B or B-A atom bond by destroying a A-A and a B-B bonds (2 ν =2 $\varepsilon_{A\text{-}B}$- $\varepsilon_{A\text{-}A}$- $\varepsilon_{B\text{-}B}$, ε means the bond energy), N is the number of atoms, and Z is the coordination numbers of A and B, then the numbers of A-B and B-A bonds will be NZX_AX_B. Therefore, the excess Gibbs energy will be νNZX_AX_B, and the interaction parameter is:

$$I_0=\nu NZ$$

The I_0 is related to the solution status after the mixing of A and B atoms, and thus explicitly its physical meanings are described as follows:

(a). I_0=0. This means $\varepsilon_{A\text{-}B}=(\varepsilon_{A\text{-}A}+\varepsilon_{B\text{-}B})/2$, which corresponds to the ideal mixing. The atoms of A and B can substitute and arrange randomly.

(b). I_0>0. This means $\varepsilon_{A\text{-}B}>(\varepsilon_{A\text{-}A}+\varepsilon_{B\text{-}B})/2$, which corresponds to less stable A-B and B-A bonds than A-A and B-B bonds. Different kinds of atoms are repulsive to each other, and the same atoms can form clusters or order in some short range. In case of large positive I_0, the solution phase may separate into two isostructural compositions, which forms the miscibility gap.

(c). $I_0<0$. This means $\varepsilon_{A\text{-}B}<(\varepsilon_{A\text{-}A}+\varepsilon_{B\text{-}B})/2$, which corresponds to more stable A-B and B-A bonds than A-A and B-B bonds. The formation of A-B and B-A bonds is a spontaneous process, by decreasing the Gibbs energy of the system after mixing.

However, the regular solution model treats the solution by assuming the atoms always distribute randomly without the consideration of the influence of the different atoms surroundings. Actually, the atoms surroundings can make the thermodynamic properties of solution more complicated than those of regular mixing. To describe the more complicated cases, sometimes the sub-regular solution model (*j*=1) or the sub-sub-regular solution model (*j*=2) have to be used.

3.4.3 Compound energy formalism

The Compound Energy Formalism (CEF) was developed by M. Hillert et al. [77] in order to introduce a general approach able to describe ordered solution phases and compounds. It is called formalism because it includes a large variety of thermodynamic models.

The CEF formalism was developed with reference to the reciprocal quaternary ionic systems where cations can mix in the cation sublattice, anions can mix in the anion sublattice, but not viceversa [77]. It assumes that in crystals different atomic species occupy separate sublattices (forming stoichiometric compounds) or the same sublattice (forming phases with composition range). A certain sublattice can be occupied by the intrinsic atoms as well as anti-site atoms, interstitial atoms, vacancies and electrons. Then, according to CEF, within each sublattice, the substitutional model discussed before is applied. This generalized model can be used to describe different solution phases with substitutional and intersititial species, charged species, ordering behavior, etc. The construction of the sublattices should be exactly based on the structure information of phases, so that the model has a physical meaning.

The compound energy formalism applied in different cases is shortly reviewed in the following paragraphs.

3.4.3.1 General case

The model for a solution phase can be expressed with the formula $(A,B,\ldots)_k(C,D,\ldots)_l(\ldots)_{\ldots}$, in which A, B, C, D,... are the constituents, and k, l, … are called stoichiometric coefficients. The division on sublattices is made according to the phase structure and, in principle, there are no limitations on the number of sublattices. The Gibbs energy function of the generalized model is:

$$G_m = \sum\prod y_J^S\, G_{\mathrm{end}} + \mathrm{RT}\sum\sum n^S y_J^S \ln\left(y_J^S\right) + G_m$$

in which n^S is the stoichiometric coefficient of sublattice *S*, and y_J^S is the site fraction of constituent *J* in the sublattice *S*. ${}^0G_{end}$ is the Gibbs energy of the so-called end-members, which are the stoichiometric compounds formed by the constituents when each sublattice is occupied by only one species, e.g. A_kC_l…. The excess Gibbs energy ${}^{E}G_m$ is expressed by:

$$G_m = \prod y_J^S \sum y_B^t L_{A,B:C:D\ldots} + \prod \quad y_J^S \sum \sum y_B^t y_D^u L_{A,B:C,D:E\ldots} + \ldots$$

where commas in the subscripts separate different constituents in the same sublattice, while colons separate the different sublattices. In the first group of terms, the interaction parameter $L_{A,B:C:D\ldots}$ describes the interactions in a certain sublattice while each of the other sublattices is only occupied by a single constituent. In the second group of terms, the interaction parameter $L_{A,B:C,D:E\ldots}$ describes the interactions occurred in two sublattices at a same time while each of the other sublattices is only occupied by a single constituent, and this interaction parameter is called ''reciprocal parameter''. All these interaction parameters can be expanded as the Redlich-Kister polynomials.

3.4.3.2 Ionic crystals

For the ionic crystals, the constituents are charged ions: cations and anions are located in different sublattices. The model is given by the formula $(A^{+m}, B^{+n},\ldots)_a(C^{+i}, D^{+j},\ldots)_b(E^{-k}, F^{-l},\ldots)_c(\ldots)_{\ldots}$. Some of the end-members resulting from this model could be not electroneutral. As a consequence, in order to maintain the electroneutrality, the site fraction of constituents in certain sublattices are not always independent on the occupations in other sublattices. The equation (2-8) can be applied also for the Gibbs energy of ionic crystals: the only difference is that the constraint on the electroneutrality can affect the site fractions of constituents in sublattices.

3.4.3.3 Ionic melts

In an ionic liquid the long range order of a crystal disappears, and the atoms do loose their fixed lattice positions by reaching a disordered state. However, due to the interactions between the atoms with opposite charges, it can still be assumed that there is one cation and one anion sublattice in a short distance range. To maintain the electroneutrality of the phase, the assumption is made that the stoichiometric coefficients of the cation and anion sublattices are variable, what is consistent with the real structure of the ionic liquid. If we use the model A_PB_Q, in which A, B are the cation and anion sublattices, respectively, and P, Q the stoichiometric coefficients, these can be calculated as [78]:

$$P = \sum y(-\gamma_j)$$

$$Q = \sum y_i \gamma_i$$

where γ is the valence, and *y* is the site fraction of species in sublattices. Subscripts *i* and *j* represent the different components in sublattices. The Gibbs energy of two-sublattice ionic solution model is given by:

$$G_m = \sum_{\mathrm{ij}} y_i y_j G_{i:j} + \mathrm{PRT} \sum_i y_i \ln(y_i) + \mathrm{QRT} \sum_j y_j \ln(y_j) + G_m$$

where ${}^0G_{i:j}$ is the Gibbs energy of formation of the substance formed by cation species *i* and anion species *j*. $PRT \sum_i y_i \, ln(y_i)$ is the ideal entropy of mixing of the species in the cation sublattice, and $QRT \sum_j y_j \, ln(y_j)$ is the ideal entropy of mixing of the species in the anion sublattice. The excess Gibbs energy ${}^EG_m$ can be expressed by equation used in the general case:

$$G_m = \prod y_J^S \sum y_B^t L_{A,B:C:D\ldots} + \prod \quad y_J^S \sum \sum y_B^t y_D^u L_{A,B:C,D:E\ldots} + \ldots$$

3.4.3.4 The stoichiometric phases

A limiting case of the model $(A,B,\ldots)_k(C,D,\ldots)_l(\ldots)_{\ldots}$ is that each sublattice is occupied by a single species. This means that the different components occupy their own crystal sublattices, without mixing, giving rise to a stoichiometric compound. The Gibbs energy of such compound can be simply described by means of equation ($G=A+BT+CTLnT+DT^2+ET^{-1}+\ldots$) if there are enough thermodynamic data on heat capacity, enthalpy increment, or entropy. However, in the case that such thermodynamic data are not available, the Gibbs energy function can be simply expressed by Neumann-Kopp rule [79]:

$$G_m = \sum_i x_i G_i + A + \mathrm{BT}$$

where the x_i and ${}^0G_i$ are the mole fraction and Gibbs energy of component *i*, respectively. *A* and *B* are the parameters to be determined and can be thought as the enthalpy and entropy of formation of the compound from the components. In the case of lacking thermodynamic data, *A* and *B* can be optimized from phase equilibrium data.

4 Experimental results: TBC high temperature evolution

In this chapter, thermal barrier coating evolution due to high temperature operation have been studied.

Many tests have been planned to investigate phase evolution in the material, evaluate the kinetic and thermodynamic factors that govern phase transitions and lead to the degradation of TBC.

Furthermore, the effect of the cooling rate on the formation of the monoclinic phase and its possible inhibition by means of quenching has been studied.

This also allowed us to re-evaluate the ZrO_2-Y_2O_3 metastable phase diagram, by testing the t→m transition line and comparing it with the literature data [20,80,81].

Moreover, the phase transition observed in precursor powders exposed to high temperature has been investigated.

The mentioned tests have been conducted for different times in a temperature interval between 1100 and 1400 °C. The classic 7YSZ material has always been tested and only in the case of the powder study, the 14YSZ material has been also evaluated, mainly for comparison with the evolution of the standard material.

The information obtained from these different tests led to a complete evaluation of the degradation of the TBC exposed in conditions similar to those that can occur during operation in a gas turbine, discussed at the end of this chapter.

4.1 Precursor powders effect

The study of the evolution of TBC precursor powders is important to evaluate the quality of the massive material.

In fact, the simple exposure to high temperature of the powders and the evaluation of the quantity of harmful phases formed inside the specimen allows to estimate the quantity of monoclinic phase that will form inside the deposited material.

Furthermore, the study of the phase distribution in the powders must also be carried out on powders as delivered, since, by Ansaldo definition, the maximum quantity of monoclinic phase must not exceed 3% [82].

In this work precursor powders of 7YSZ and 14YSZ were examined, to compare the phase stability of the two materials.

Micrographs of 7YSZ powders obtained by electron microscopy are shown in Figure 32. The images show spherical shape and surface roughness of the particles. This kind of investigation allows to measure the particle size: difference in size favor a better packing during sintering.

Particle diameters are in a range of 42-110 micron, with a mean value of 73 micron.

Phase quantification in a batch of 7YSZ (see paragraph 3.1.1.1) is measured by X-Ray diffraction (see Figure 33), using Rietveld method.

All the polymorphic structures of zirconia are present in the powders, included the metastable t' structure. Phases quantifications, with the agreement factors calculated by the Rietveld technique, are reported in Table 8.

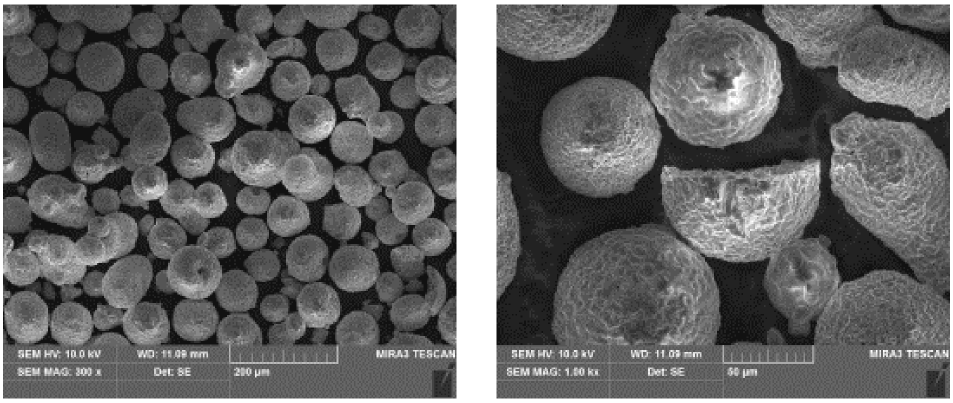

(a) (b)

Figure 32 – SEM-SE image x 300 (a) and x1000 (b): conformation of 7YSZ powders

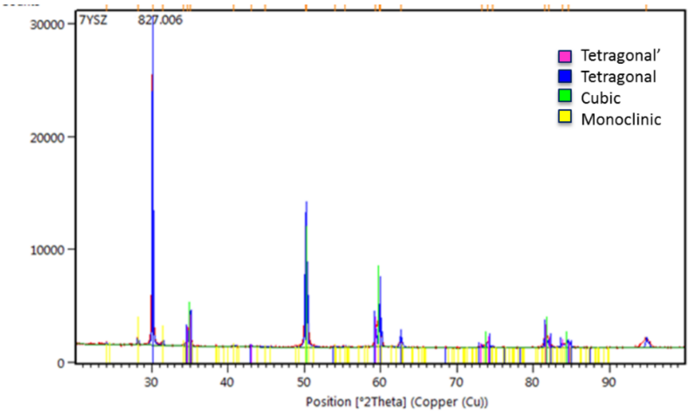

Figure 33 – X-Ray pattern and Rietveld quantification of 7YSZ powders

The subsequent analysis have been done on particles sectioned by incorporating them inside conductive resin so as to have a smooth surface suitable for SEM analysis with EBSD detector. A typical section of powders is shown in Figure 34.

Two types of particles are identified in this batch: one much smaller and more compact, almost already pre-sintered, and one larger and much more porous. The EBSD analysis of sections are shown in Figure 35 and Figure 36 for compact and porous particles, respectively. In the pre-sintered powders the analysis doesn't show the presence of monoclinic phase, while this technique does not permit to distinguish the tetragonal and cubic phases. Instead, the porous particles contain little islands of monoclinic phase, with lamellar structure typical of the martensitic transformation, shown by image quality and inverse pole figure maps (Figure 37). The EDS analysis of the monoclinic areas confirm the lower content of yttrium with respect to the other phases.

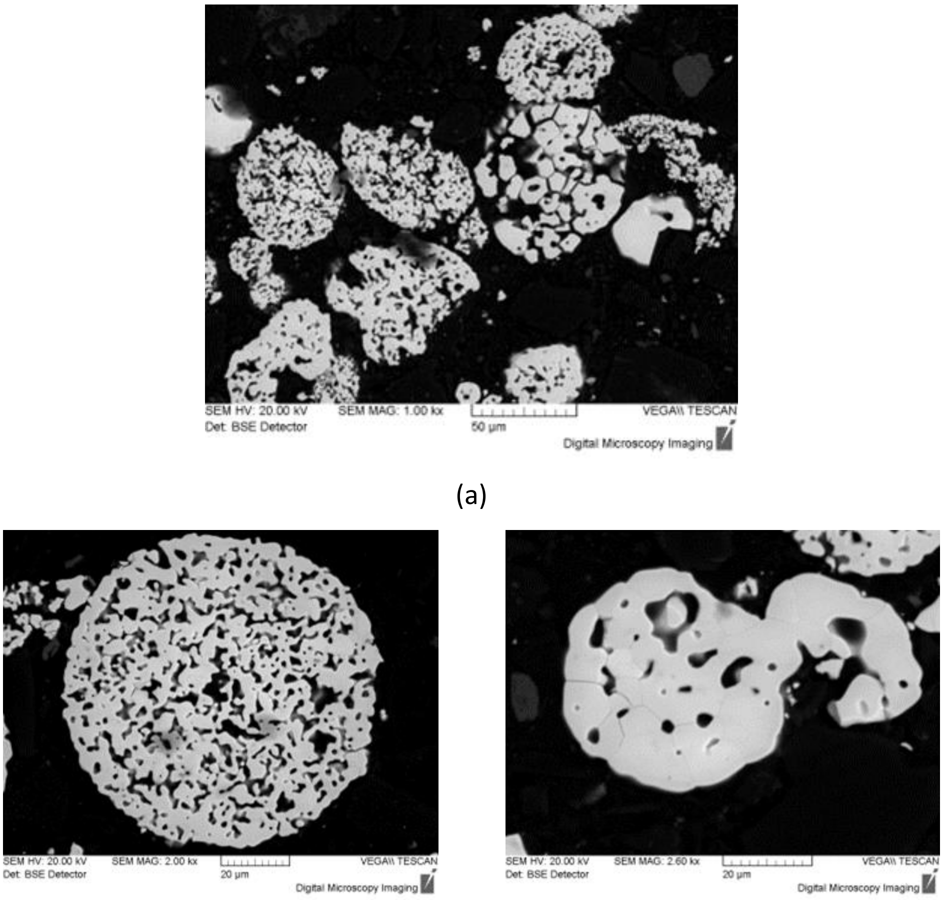

(a)

(b) (c)

Figure 34 – SEM-BSE image x1000: section of 7YSZ powders(a). Particular of two type of powders: porous (a) and compact (b) particles

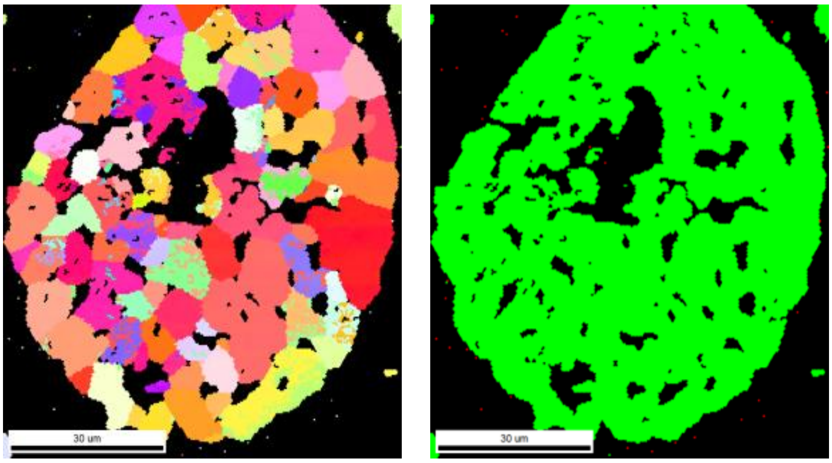

(a) (b)

Figure 35 – EBSD analysis of compact particle: IPF (a) and phase (b) maps. The color green correspond to cubic or tetragonal phase

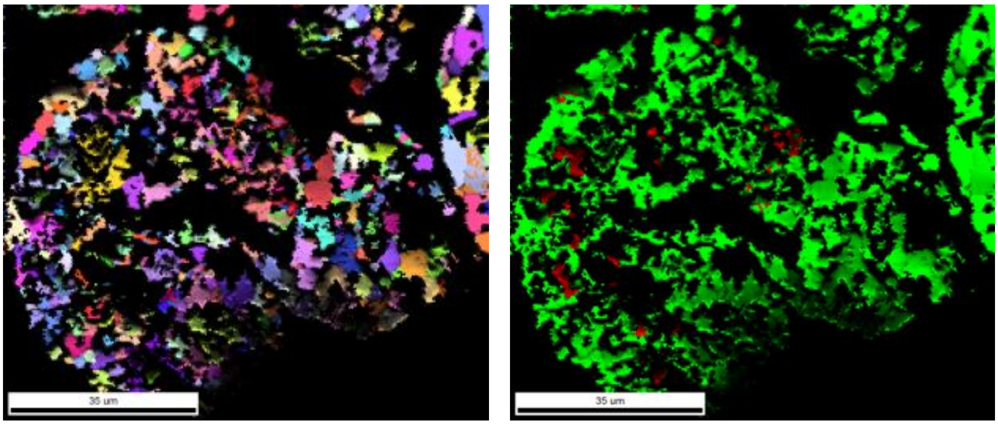

(a) (b)

Figure 36 - EBSD analysis of porous particle: IPF (a) and phase (b) maps. The color green correspond to cubic or tetragonal phase, while red is monoclinic phase

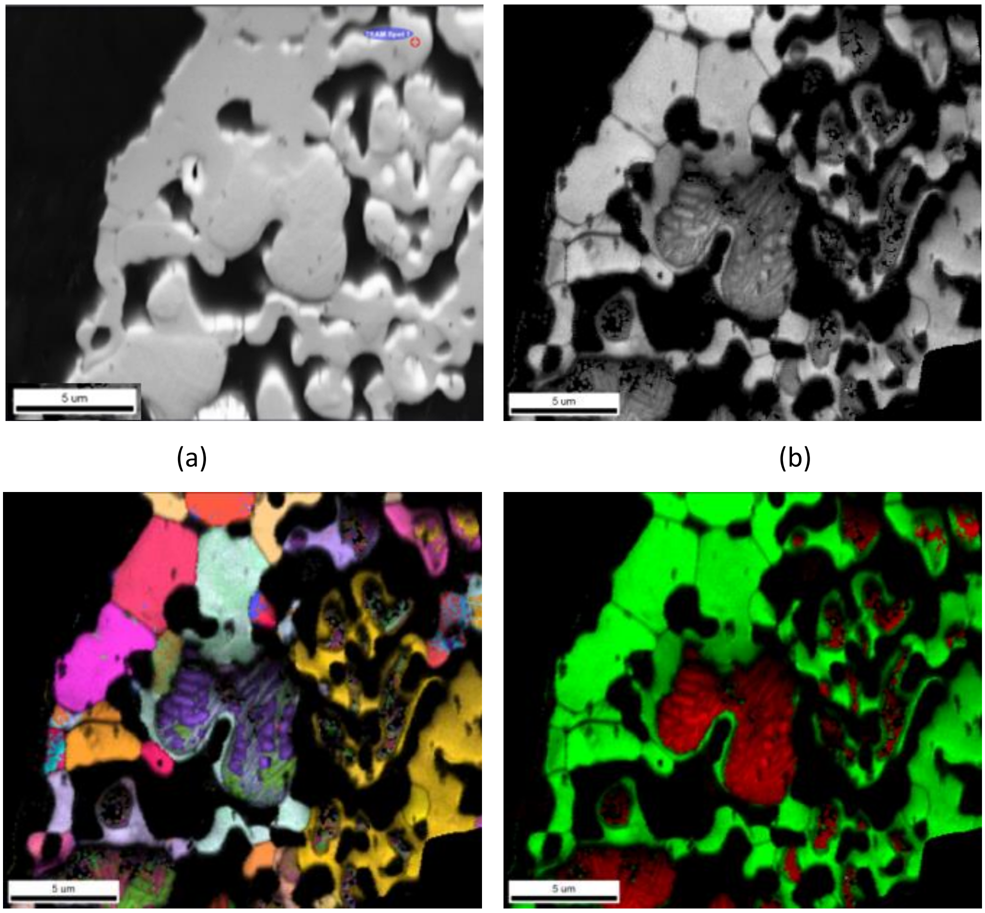

(a) (b)

(c) (d)

Figure 37 – EBSD analysis, particular of porous particle(a): Image quality (a) and IPF (b) maps underline the lamellar structure of monoclinic phase, identify with red color in phase map (d)

The same analysis have been performed on 14YSZ powders (see paraghraph 3.1.1.1). SEM images of the powders show spherical particles with a surface more porous than the 7YSZ lot.

The particles diameter are in a range of 24-136 mm, with a mean value of 75mm. Therefore, the mean value is similar to the one of 7YSZ batch, although in this case there are much smaller and larger particles than in the previous case.

The X-Ray analysis shows the presence of only two phases, cubic and monoclinic, while the tetragonal phases are not present, as predicted by the phase diagram of the system. Phase quantification is reported in Table 8 and it shows that the amount of m phase in 14YSZ is about two times the one observed in 7YSZ (14% vs 8%).

The analysis of the powder sections performed by SEM with EBSD shows the presence of only one type of powders, porous particles, as reported in Figure 40.

The EBSD investigation of the sections has given results similar to those obtained on the same type of powder of batch 7YSZ (Figure 41). Indeed, little islands of monoclinic phase have been individuated, with the same lamellar structure, as shown in Figure 42.

The m phase areas, in both powder batches, are easy to be identified, when the sample is tilted for EBSD analysis: in fact the different phase hardness results in a three-dimensional appearance of the monocline areas (Figure 37-a and Figure 42-a).

Probably, the absence of compact particles that in 7YSZ were present and free of m phase, is the cause of a greater overall quantity of this phase in 14YSZ.

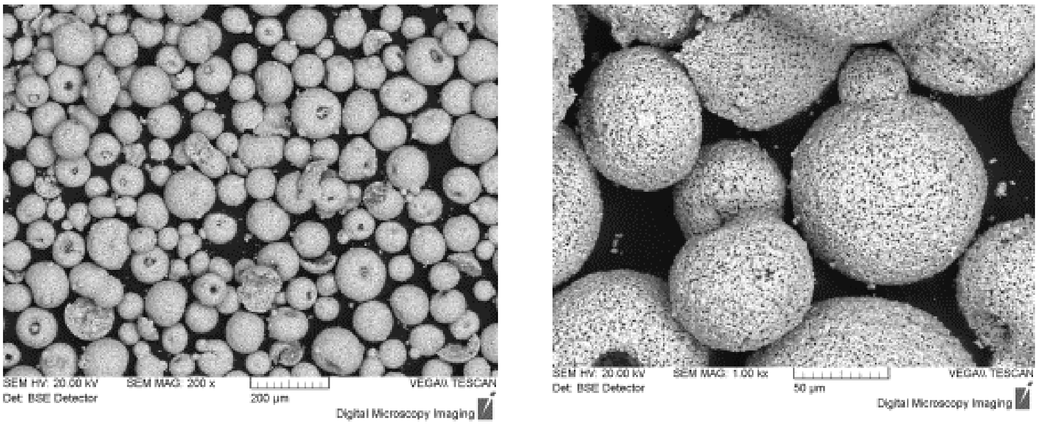

(a) (b)

Figure 38 - SEM-SE image x 200 (left) and x1000 (right): conformation of 14YSZ powders

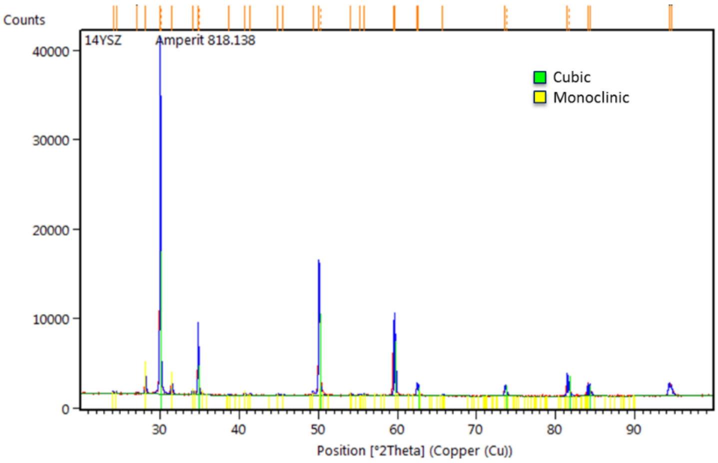

Figure 39 - X-Ray pattern and Rietveld quantification of 14YSZ powders

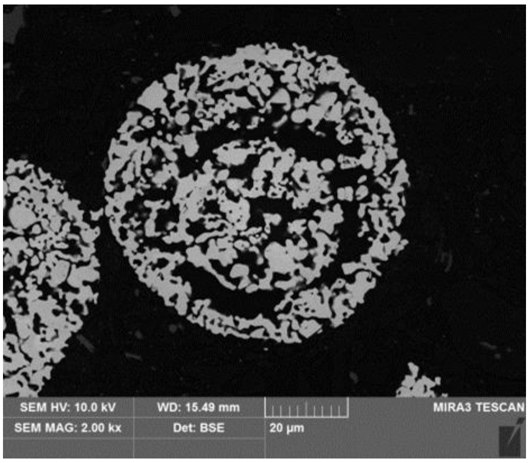

Figure 40 - SEM-BSE image x2000: section of 14YSZ powders

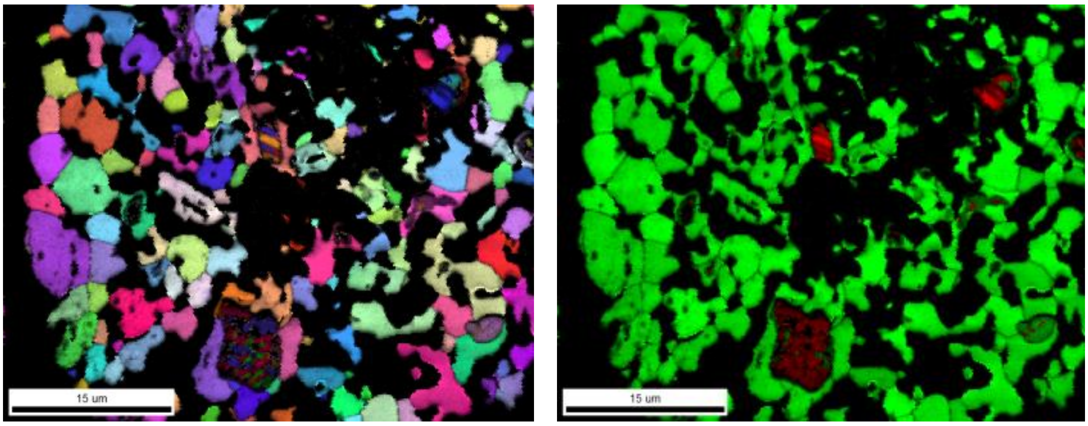

(a)

(b)

Figure 41 - EBSD analysis of porous particle: IPF (a) and phase (b) maps. The color green correspond to cubic or tetragonal phase, while red is monoclinic phase

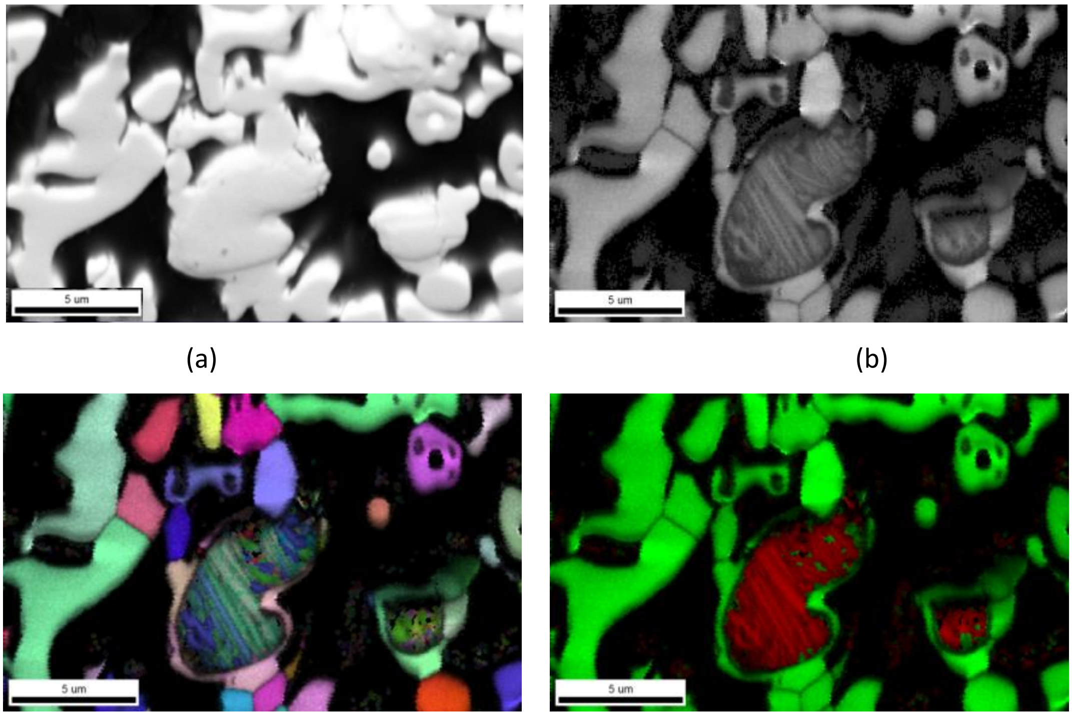

(a) (b)

(c) (d)

Figure 42 - EBSD analysis, particular of porous particle(a): Image quality (a) and IPF (b) maps underline the lamellar structure of monoclinic phase, identify with red color in phase map (d)

To evaluate the effect of temperature on the 7YSZ and 14YSZ powders, the two batches have been exposed at high temperature, between 1100 and 1400°C, for three exposure times: 100, 300 and 1000h.

The Rietveld quantification of the phases is reported in Table 8 for annealed powders as well as for as delivered powders (X-Ray pattern Figure 33 and Figure 39). To evaluate the goodness of the Rietveld quantifications agreement factors are reported in the last column.

The trend of each phase, namely cubic, tetragonal, tetragonal prime and monoclinic, are reported as a function of time and temperature in Figure 43, Figure 44, Figure 45 and Figure 46, respectively.

The cubic phase (Figure 43) shows a tendency to increase with temperature. The difference between high (1300-1400°C) and low (1100-1200°C) is more evident already 100 h, while after 1000 h this trend tends to slightly decrease. The c amount at 1100°C remains almost constant at each exposure time, similar to the starting quantity, while it increases strongly towards 40-50% for samples exposed at 1300 and 1400°C since the first aging time. Only the samples at 1200°C show a significant evolution of the c amount with exposure time.

Table 8 – Phase quantification with Rietveld method for samples of 7YSZ and 14YSZ powders with agreement factors

	T (°C)	T (h)	Phases (wt%)				Agreement factors	
Material			t’	t	c	m	R_{wp}	X^2
7YSZ powdres	0	0	67	12	13	8	4,4	3,1
	1100	100	61	25	9	5	5.4	4.8
		300	62	21	12	6	5.5	5.0
		1000	61	18	14	7	5.5	3.2
	1200	100	64	16	11	7	4.6	3.2
		300	50	22	19	9	4.8	3.5
		1000	27	43	24	6	6.3	4.7
	1300	100	21	29	41	9	4.6	3.3
		300	15	29	42	14	4.5	3.2
		1000	8	16	48	27	6.5	5.0
	1400	100	17	30	45	9	4.7	3.6
		300	11	21	47	21	4.0	2.5
		1000	5	15	46	34	5.9	4.1
14YSZ powders	0	0	/	/	86	14	3.9	2.6
	1100	100	/	/	89	11	5.3	4.7
		300	/	/	89	11	3.5	4.2
		1000	/	/	91	9	6.7	4.9
	1200	100	/	/	91	9	5.6	5.4
		300	/	/	90	10	6.0	6.3
		1000	/	/	91	9	10.2	12.7
	1300	100	/	/	90	10	6.1	6.4
		300	/	/	91	9	6.9	8.4
		1000	/	/	91	9	9.4	8.7
	1400	100	/	/	92	8	6.5	7.2
		300	/	/	91	9	4.3	3.1
		1000	/	/	93	7	5.9	3.7

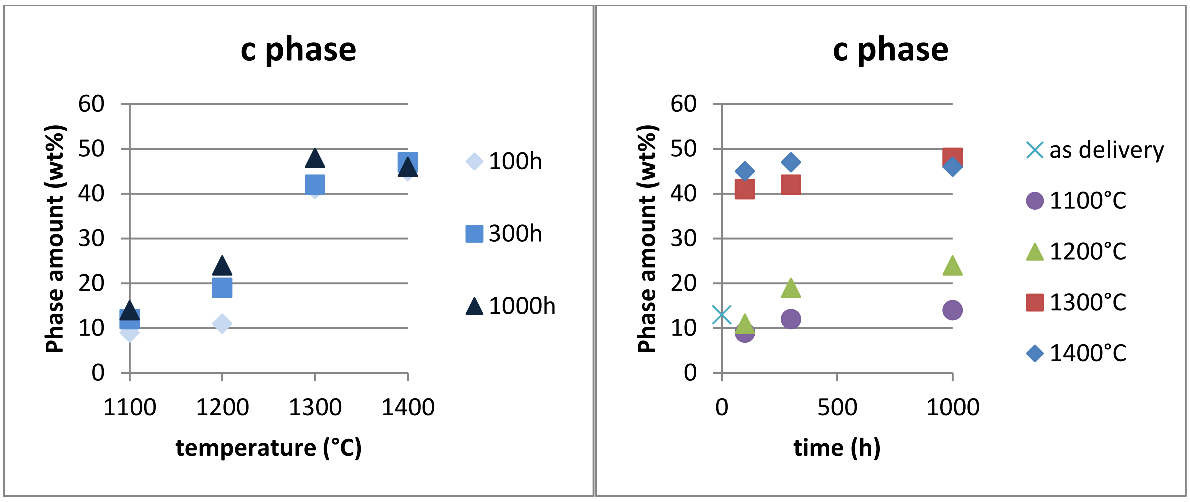

Figure 43 – Effect of time and temperature for cubic phase, measured in samples of 7YSZ powder tested at high temperature

The tetragonal phase (Figure 44) remains almost constant with the variation of the temperature, but the scatter range increases at higher temperature. At each temperature, the phase tends to increase with respect to the starting condition after 100 and 300 h, almost doubling the quantity, while after 1000 h all samples (except for the sample exposed at 1200°C) converge towards the same value (around 18-19%).

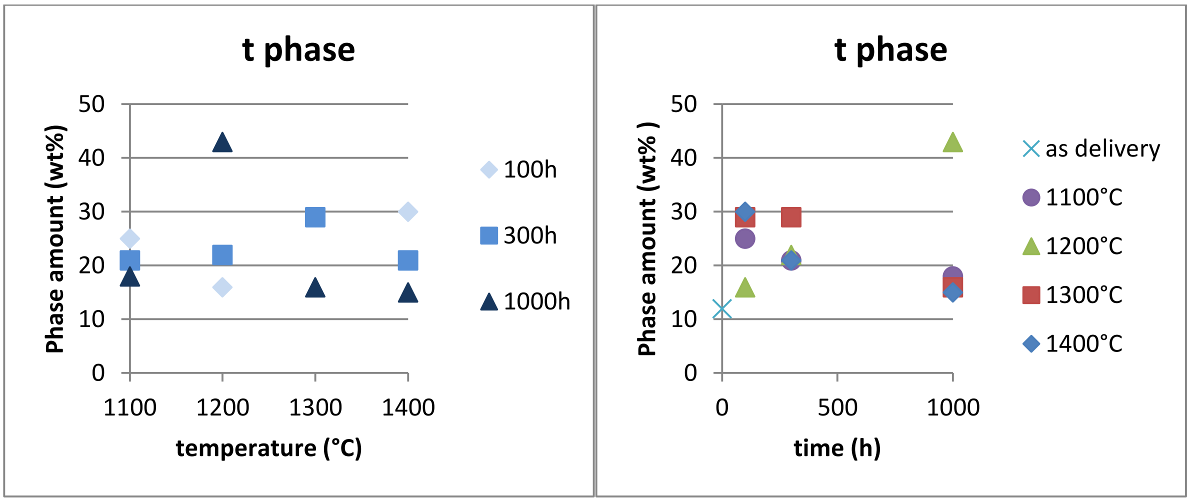

Figure 44 - Effect of time and temperature for tetragonal phase, measured in samples of 7YSZ powder tested at high temperature

The trend of tetragonal prime phase (Figure 45) is opposite to c phase. The phase tends to decreases with the temperature and already after 100h at the highest temperatures (1300 and 1400°C) the amount of the phase is very low with respect to the starting condition. At the lowest temperature (1100°C) t' quantity does not change also after 1000h, while a decrease is observed at 1200°C.

This trend, compared to the others, suggests that the cubic phase is formed from tetragonal prime phase.

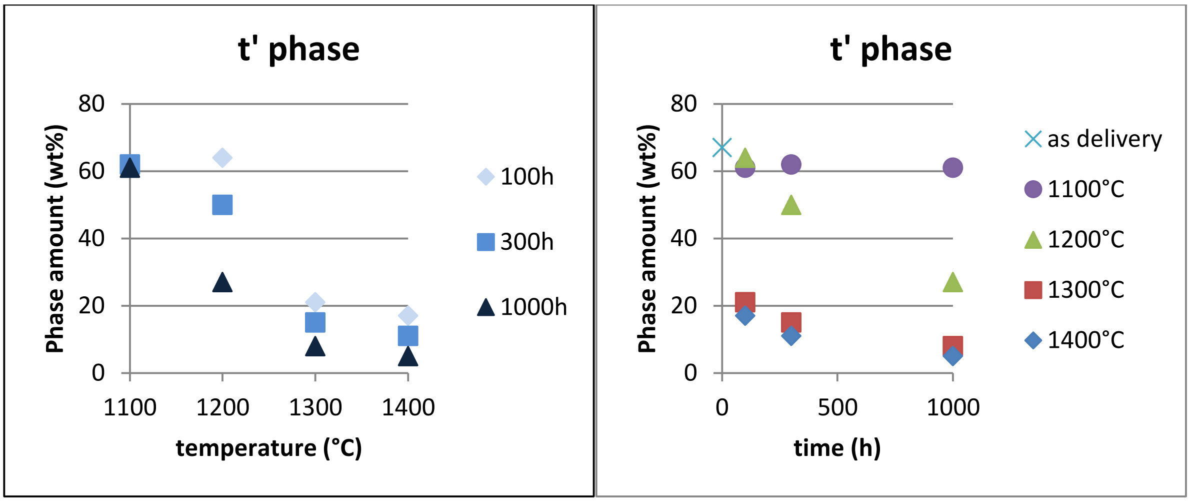

Figure 45 - Effect of time and temperature for tetragonal prime phase, measured in samples of 7YSZ powder tested at high temperature

The trend of monoclinic phase is reported in Figure 46. In this case, the effect of temperature is evident and m amount changes according to the exposure time. Indeed, while after 100 h the phase amount remains almost constant at each temperature, the quantity increases at the highest temperatures (1300 and 1400°C) for long exposure time (more evident after 1000h). The evolution with time of this phase shows that it is close to the starting condition after 100h at each temperature and at 1100 and 1200°C remains constant also after 1000h. The effect of temperature, between 1300 and 1400C, is visible already after 300h and is confirmed at 1000h.

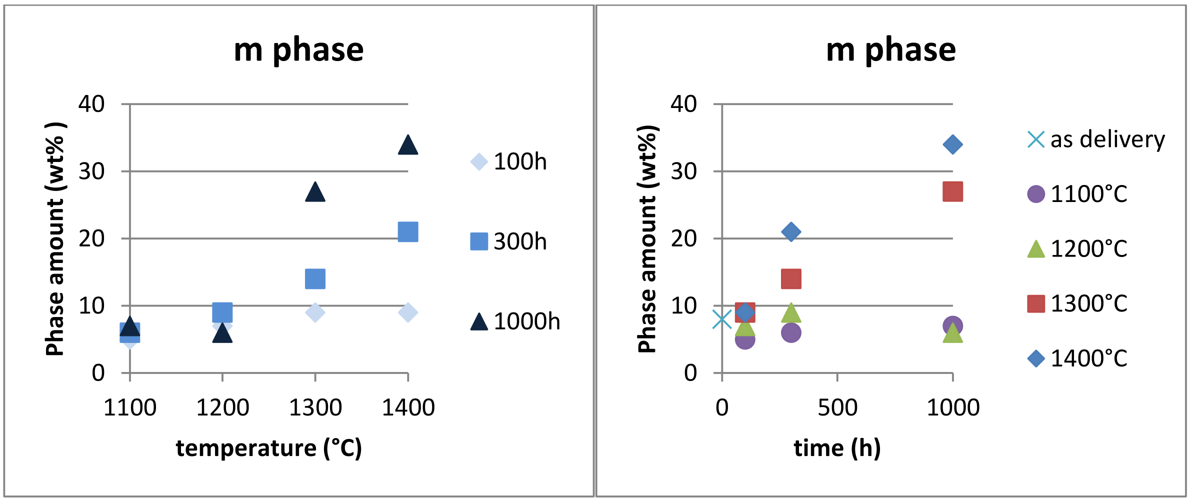

Figure 46 - Effect of time and temperature for monoclinic phase, measured in samples of 7YSZ powder tested at high temperature

The high temperature exposed powders have been analyzed with EBSD technique to evaluate monoclinic phase evolution. In Figure 47, as an example, the analysis done on a porous particle of sample exposed at 1400°C for 300h is reported.

For the porous structure a higher amount of monoclinic phase inside the tetragonal/cubic one is observed; the lamellar structure is still present and lamellae dimensions are the same, but higher amount of monoclinic grains is present. The high temperature exposure seems to promote the nucleation of monoclinic grains, not their growth.

The compact particles remain with cubic or tetragonal structure in each analyzed sample and the monoclinic phase is not present.

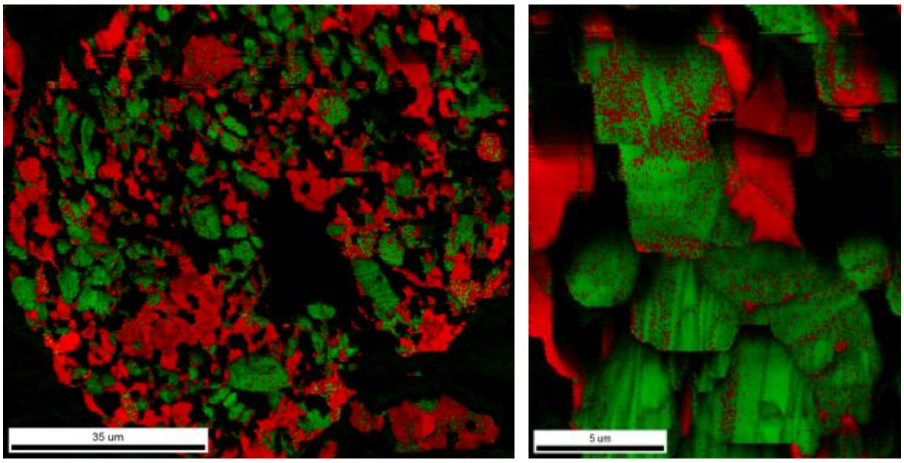

Figure 47 - EBSD analysis of porous particle of 7YSZ exposed at 1400°C for 300h. The cubic phase is identify in red, while monoclinic phase in green. On the left a particular

The trend of monoclinic phase for 14YSZ powders exposed at high temperature, is shown in Figure 48. The amount of m phase slightly decreases with temperature. The starting amount decreases already after 100h and this trend is more evident after long exposure time for low temperature, while at the highest temperature (1400°C) the amount between 100h and 1000h remain constant.

In any case, the variation of the phase always remains below 5%.

For these powders the only two stable structures are monoclinic and cubic, so, for c phase the trend is opposite to the m phase one.

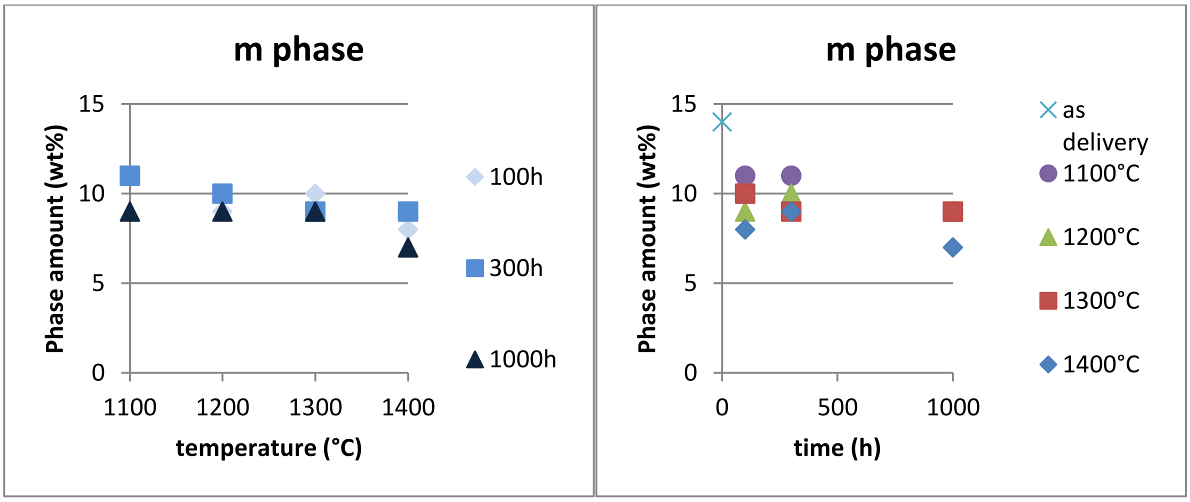

Figure 48 - Effect of time and temperature for monoclinic phase, measured in samples of 14YSZ powder tested at high temperature

The EBSD analysis show similar results for all tested samples.

In Figure 49 powder exposed at 1400°C for 300h, with a detail of a monoclinic phase grain, is reported.

The microstructure is very similar to the as delivered condition: monoclinic phase grains are inside the cubic one with a lamellar structure. The amount variation is not so evident by EBSD mapping.

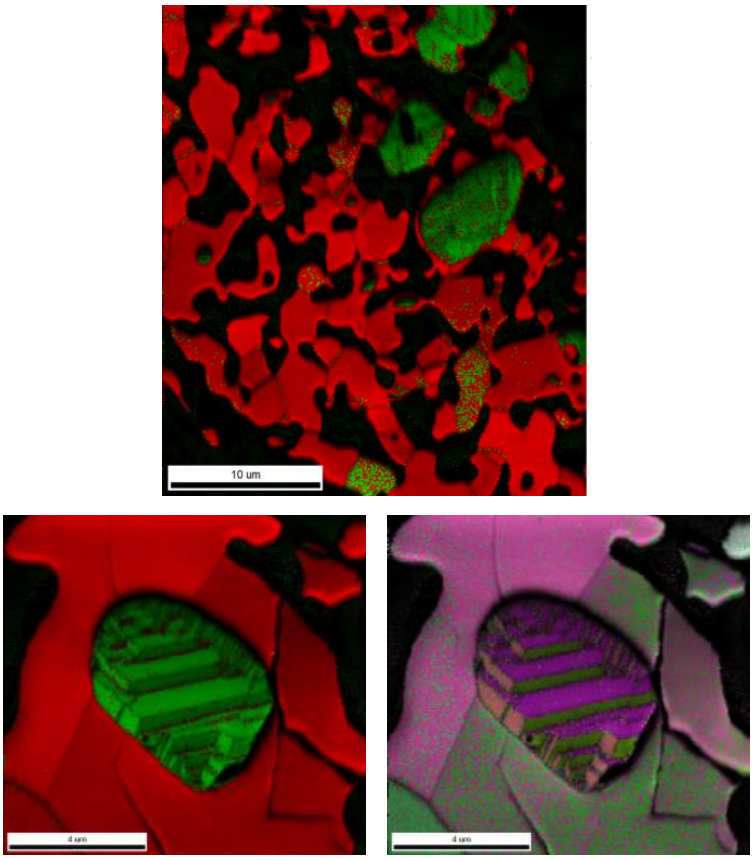

Figure 49 - EBSD analysis of porous particle of 7YSZ exposed at 1400°C for 300h. The cubic phase is identify in red, while monoclinic phase in green. Below IPF and maps phase of a particular

Finally, to check the phase distribution in as sprayed TBC using the same powders used for previous test, samples of sprayed APS TBC have been studied.

The X-Ray patterns of 7YSZ and 14YSZ are reported in Figure 50 and Figure 51, respectively.

In both samples in as sprayed condition, a decrease of monoclinic phase is observed. In particular, in 7YSZ sample, the only stable phase is tetragonal prime, probably due to the condition of plasma spray deposition (very high temperature).

The 14YSZ sample shows a decrease of monoclinic phase in favor of cubic phase, but it is still present in small amount, about 3%.

The variation between powder and sprayed samples is underlined in Figure 52.

Probably, the starting amount of monoclinic phase in 14YSZ powders is too high to allow its complete dissolution during deposition process.

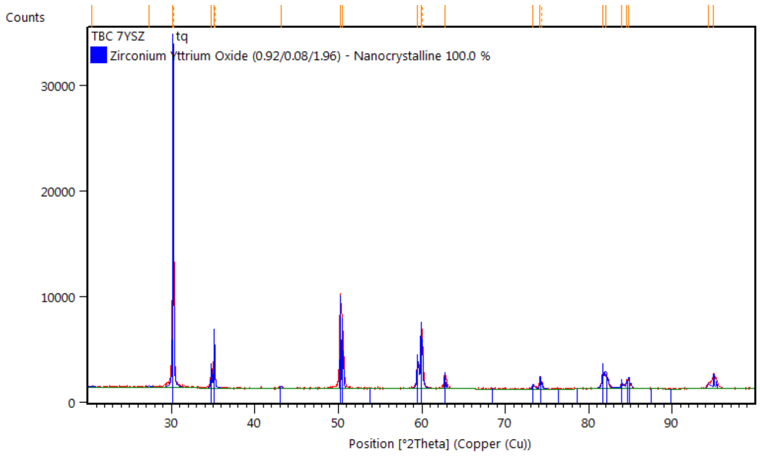

Figure 50 - X-Ray pattern and Rietveld quantification of a sprayed sample by 7YSZ powders

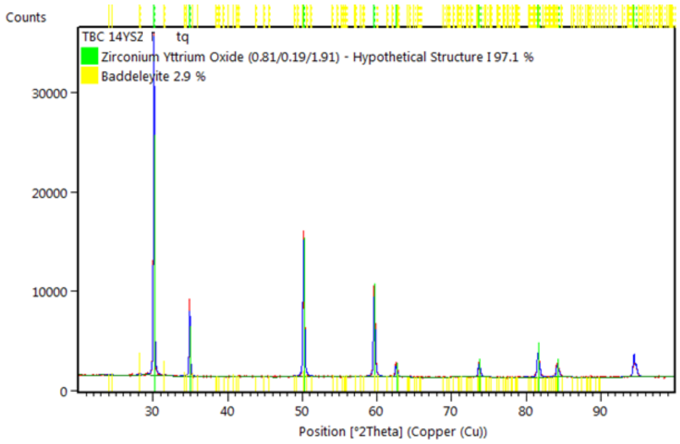

Figure 51 - X-Ray pattern and Rietveld quantification of a sprayed sample by 14YSZ powders

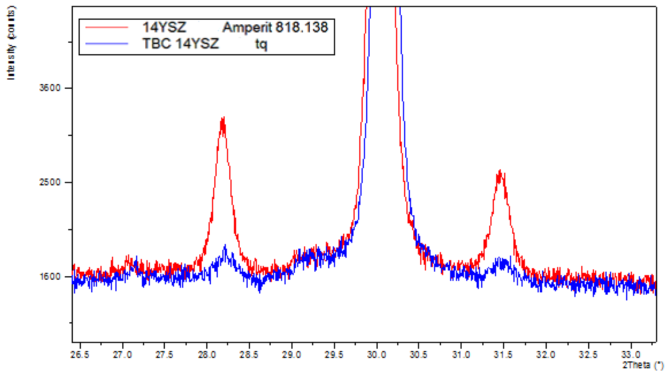

Figure 52 – Comparison by X-Ray pattern of 14YSZ powder and samples sprayed by same powders

The amount around 3% of monoclinic phase present in sprayed TBCs is the acceptable upper limit for Ansaldo specifications. New powder that have new homogenous distribution of the yttria in order to decrease the m phase quantity already in the precursors has been produced.

The comparison of the two batches of powder, the new in blue and the old in red, is reported, with details of the significant peaks of monoclinic phase, in Figure 53.

The Rietveld quantification of the new powder is reported in Table 9 together with the old lot.

The monoclinic phase amount decreases by an order of magnitude, giving only c phase in sprayed TBC using these powders.

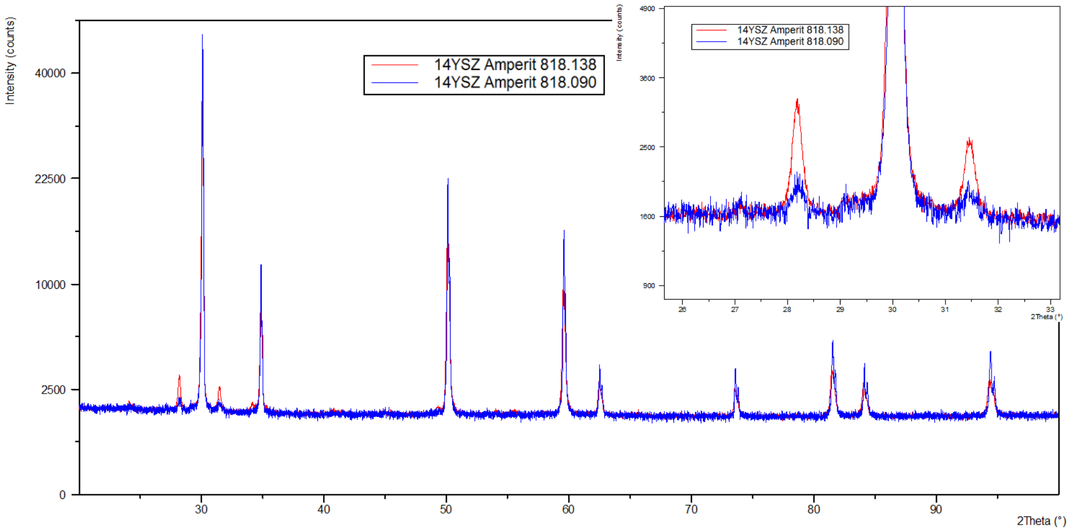

Figure 53 - Comparison by X-Ray pattern of two batch of 14YSZ powders

Table 9 - Phase quantification with Rietveld method for two batches of 14YSZ powders with agreement factors

	Phases		**Agreement factors**	
Material	c	m	R_{wp}	X^2
14YSZ_powder1	96	4	8.4	4
14YSZ_powder2	86	14	4.2	3

The work shows the importance of the study of precursor powders to define the goodness of a thermal barrier. In fact, powders with too much monoclinic phase lead to massive materials with initial phase composition out of production specifications.

The exposure at high temperature shows that, in the case of 7YSZ, the crystallographic phase evolution in the powder is the same of the sprayed coating, as described in paragraph 2.5. The temperature contribution is bigger than the effect of time and after 1000h exposure at 1400 and 1300°C the t' is almost disappeared.

The exposure at high temperature on 14YSZ powder confirm the beneficial effect of a longer sintering: sample exposed 1000h at 1400°C show a lower content of monoclinic than untreated powders.

4.2 Cooling rate effect

The transformation t → m of zirconia has long been considered an a-thermal type martensitic transformation, but recent works [80,83,84] have demonstrated the isothermal behavior of this transformation. If a rapid cooling rate is applied from high temperature exposure, the m content can be limited, but after long term exposure at room temperature or short-term exposure at low temperature the m formation can occur. Therefore, during operation of a gas turbine, in the event of rapid sequences of switching on and off, a thermal gradient can be established which could suggest the suppression of the monoclinic phase. Actually, according to these literature works, such suppression does not occur.

In this paragraph two different types of freestanding TBC (DVC and porous, see paragraph 3.1.1.3) have been exposed at high temperature and cooled with different rates. Successively, the samples have been aged 24h and 168h, at 250 and 400°C.

The effect of different cooling rates in terms of nucleation of m phase, and m growth after aging, starting from different initial conditions (different cooling rates) have been evaluated. The slow annealing has been compared with subsequent aging to study the achievement of thermodynamic equilibrium, indicated by the attainment of a constant amount of the m phase.

Moreover, the distribution of m phase inside the sample has been studied, evaluating the starting dimension of the grains and their possible growth with aging treatments.

Finally, the phase lattice parameters have been evaluated and their variation has been studied as a function of cooling rates and applied aging treatments.

The phase quantifications of DVC and porous TBC samples after different cooling rates are shown in Figure 54 and Figure 55, respectively.

From the XRD patterns, it is possible to observe that for both materials the m phase peaks are more evident for slow cooled samples and the phase quantification by Rietveld method highlights that the maximum amount of m phase is observed for the slowest cooling rate while its amount is smaller for faster cooling rates. The fast cooling inhibits, its transformation from the high temperature matrix: the obtained amount is about a half of that obtained by slow cooling from 1400°C.

The other three phases (t, t’ and c) don’t show significant differences when the cooling rate changes. The little variations of quantification are within the measurement error, estimated in about 1-3%.

The porous TBC sample cooled by air quenching has been discarded because phases quantification was not reliable, considering the very high agreement factor, as shown in Figure 55.

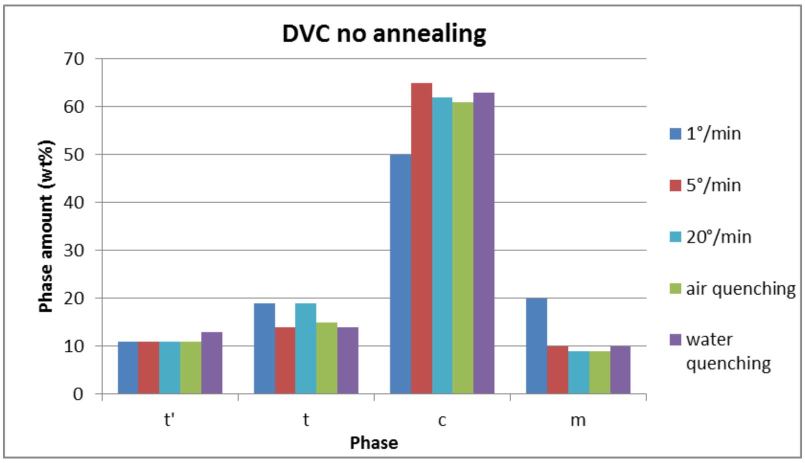

Figure 54 –Phases amount of DVC TBC with five different cooling rates

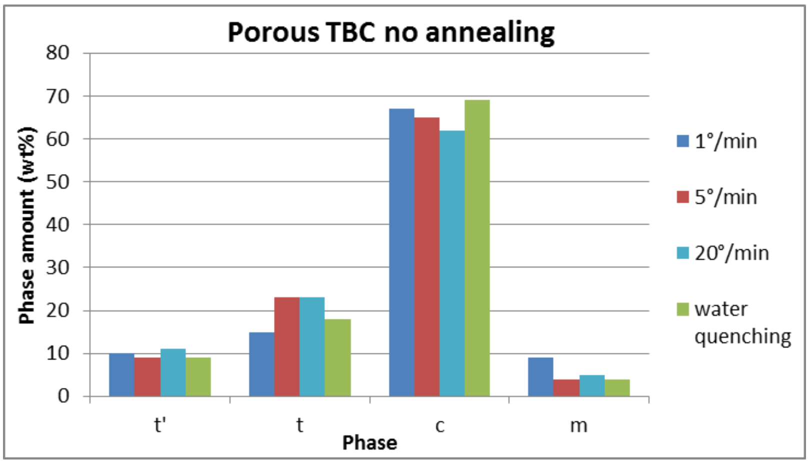

Figure 55 - Phases amount of porous TBC with five different cooling rates

In Figure 56, phase amounts observed after 1 and 5°C/min cooling rate are compared for the two tested materials. For the same cooling rate the amount of m phase obtained for porous coating is a half that obtained for DVC and after 1°C/min cooling the m phase in porous and DVC TBC are similar to the amount measured in DVC sample after fast cooling (5°C/min).

The m phase seems to be formed mainly in place of c phase for DVC TBC while, for porous coating, it seems to come from t phase, even if after fast cooling rate (from 5°C/min) the phase distribution is approximately unchanged with fluctuations related to the measurement error. The t’ phase is about 10%, constant for all the tested cooling rates and for both materials.

The phase amount and the agreement factors of Rietveld quantifications are reported in Table 10.

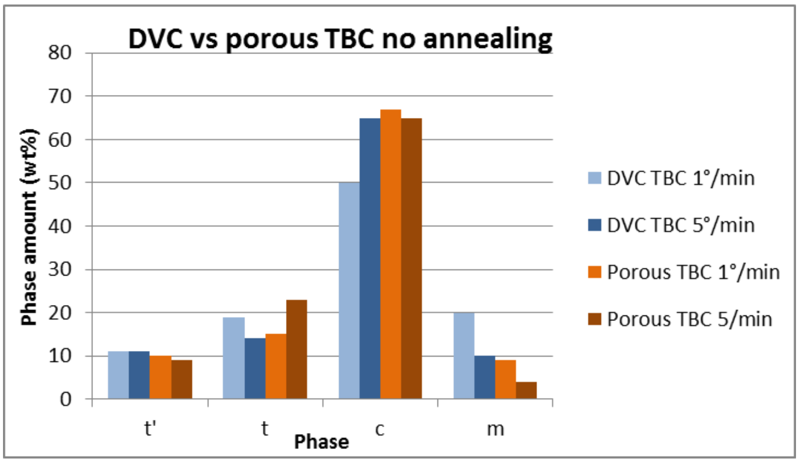

Figure 56 – Phase quantifications comparison between CVD TBC and porous after cooling treatment

Table 10 – Phase amount after Rietveld quantifications for samples after first cooling, with agreement factors

	Cooling rate	**Phases (wt%)**				**Agreement factors**	
Material		t’	t	c	m	X^2	R_{wp}
DVC TBC	1°/min	11	19	50	20	5,5	5,6
	5°/min	11	14	65	10	8,1	6,2
	20°/min	11	19	62	9	5,8	5,6
	Air quenching	11	15	61	9	8,9	7,2
	Water quenching	13	14	63	10	10	7,4
Porous TBC	1°/min	10	15	67	9	8,4	6,8
	5°/min	9	23	62	5	11,1	7,7
	20°/min	11	23	62	5	11,1	7,7
	Water quenching	9	18	69	4	4,5	5,6

The samples have been analyzed by EBSD, a technique which does not allow to distinguish the t (or t’) from c because the Kikuchi patterns are very similar, while m phase is easily identified.

The microstructure of the DVC sample cooled at 1°C/min is shown in Figure 57. The typical microstructure with small pores and vertical cracks is evident and EBSD maps highlight the crystallographic feature of the material. In particular, the different crystallographic structures are distinguished in the phase map (Figure 7-b): m (red) and t (green) phases, while the different grain orientations are shown in the IPF map.

In all the tested samples, the m phase has been found in very fine grains independently on cooling rate or material.

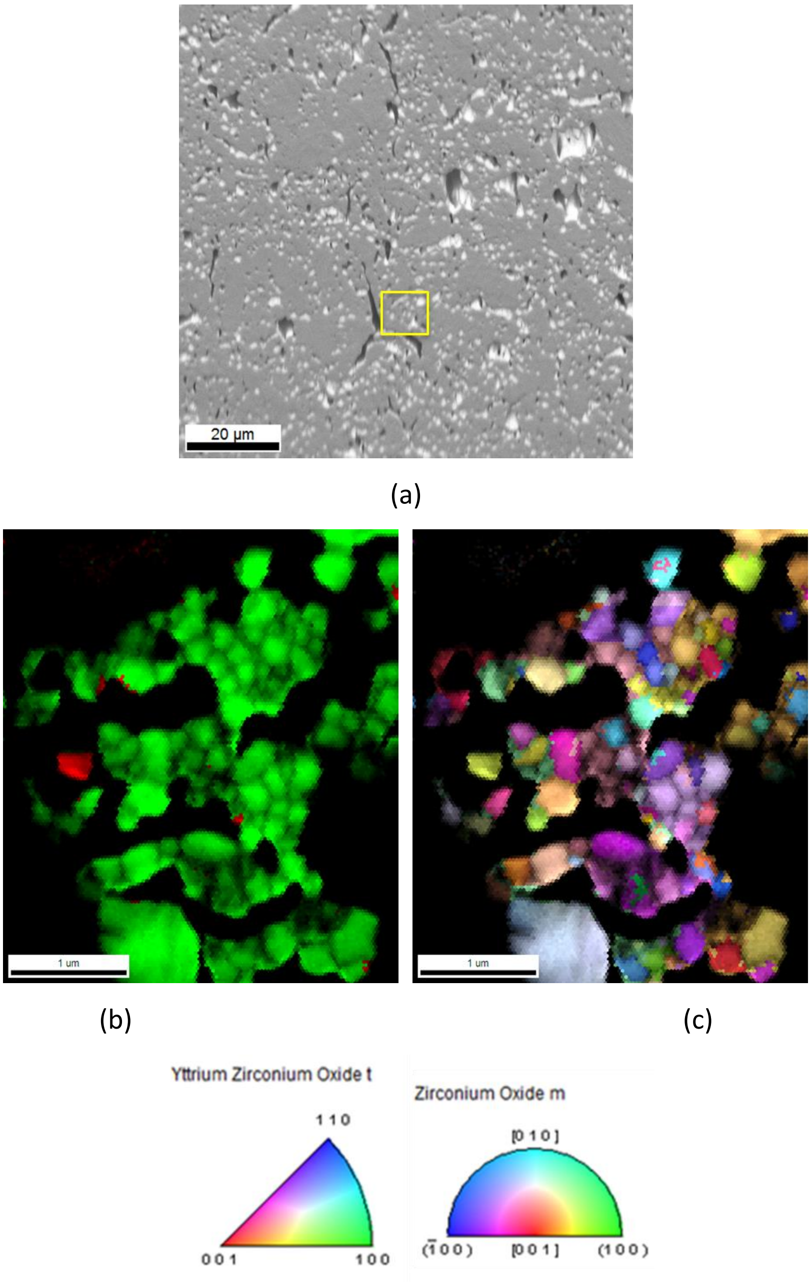

(a)

(b)

(c)

(d)

Figure 57 – SEM-FEG image of sample cooled at 1°/min (a) with "Phase" map (b) and IPF map (c). Finally is reported the legend of IPF maps (d)

4.2.1.1 Aging treatment for 24h at 250°C

All the samples cooled at different rates have been annealed at 250°C for 24 hours in order to evaluate the effect of a small increase of energy on phase distribution. In Figure 58, two XRD patters for a fast cooled DVC sample before and after aging show a clear increase of m phase after annealing. The complete results are reported in Figure 59 and Figure 60, for DVC and APS TBC respectively.

For all the tested samples, the m phase amount increases during stay at 250°C. However, the effect of the cooling rate is not suppressed by the low temperature annealing. In fact, the TBC specimens cooled at 1°C/min continue to show m phase amount higher than other samples.

In DVC samples the m phase increase is about 10%, while in APS ones the annealing effect seems even greater, especially for specimens tested after fast cooling. Moreover, the difference in m content between DVC and APS TBCs is still present after this aging. The comparison of m content vs cooling rate, before and after low temperature annealing, for both materials is shown in Figure 61. The results of phase quantifications after aging are reported in Table 11.

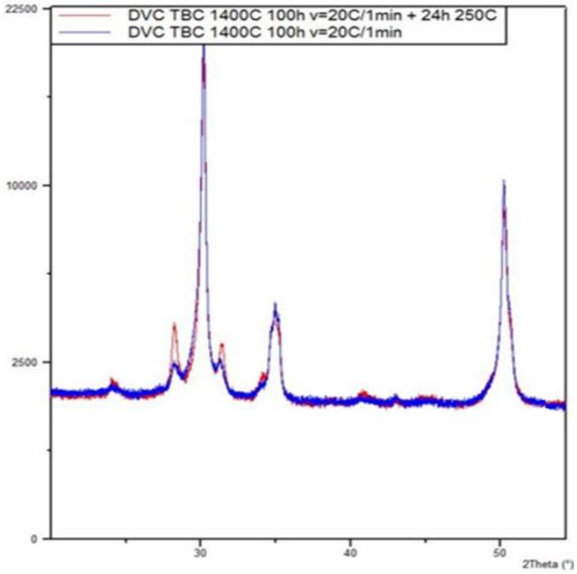

Figure 58 - X-Ray patters for a sample cooled at 20°/min of DVC TBC before and after the aging

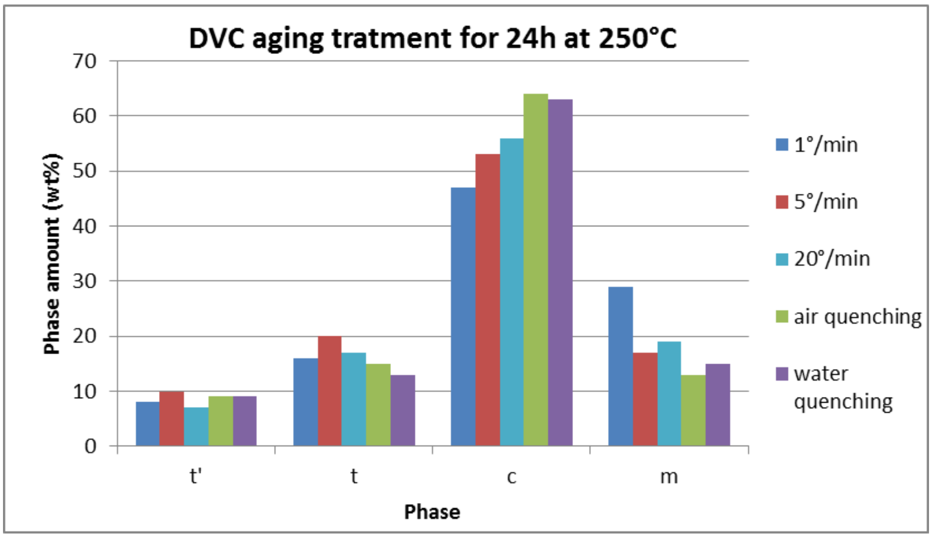

Figure 59 - Phases amount of DVC TBC after aging for 24h at 250°C, with five different cooling rates

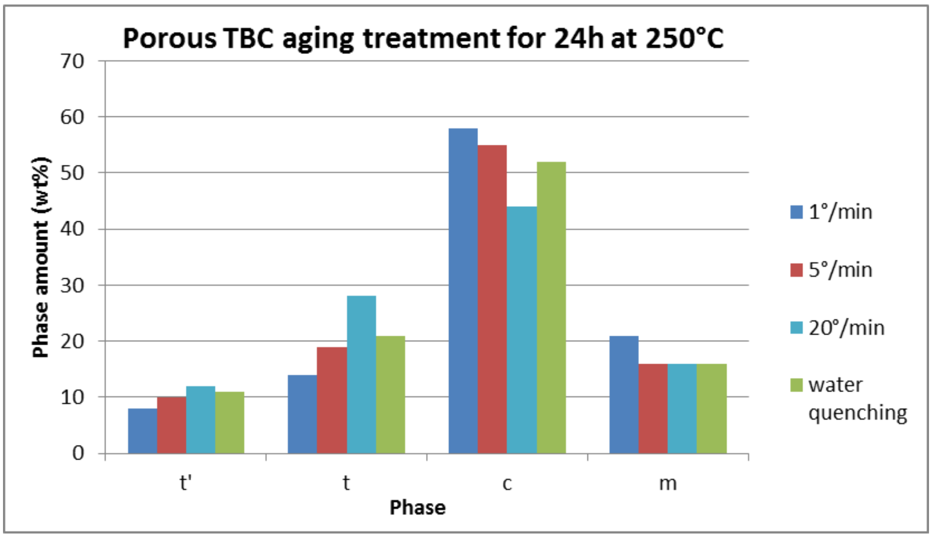

Figure 60 - Phases amount of porous TBC after aging for 24h at 250°C, with five different cooling rates

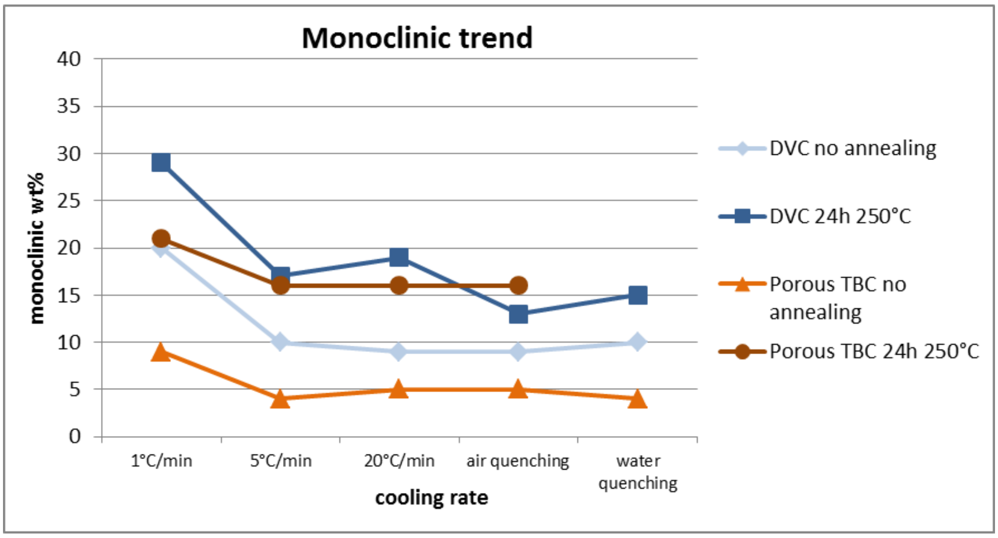

Figure 61 – Trend of monoclinic phase for DVC and porous TBC pre and post aging for 24h at 250°C

The microstructure of the DVC sample after annealing has been checked in order to understand if the m phase increase corresponds to a further m phase precipitation or to the growth of already present grains. In Figure 62, the SE micrograph and the EBSD maps are reported for the DVC sample cooled 1°/min where the higher m phase amount have been measured by XRD analysis. As observed in the samples after cooling, the m phase maintains fine grains and it is dispersed throughout the sample thickness. This means that the m phase nucleation continues during low temperature annealing, confirming the isothermal behavior of m phase formation.

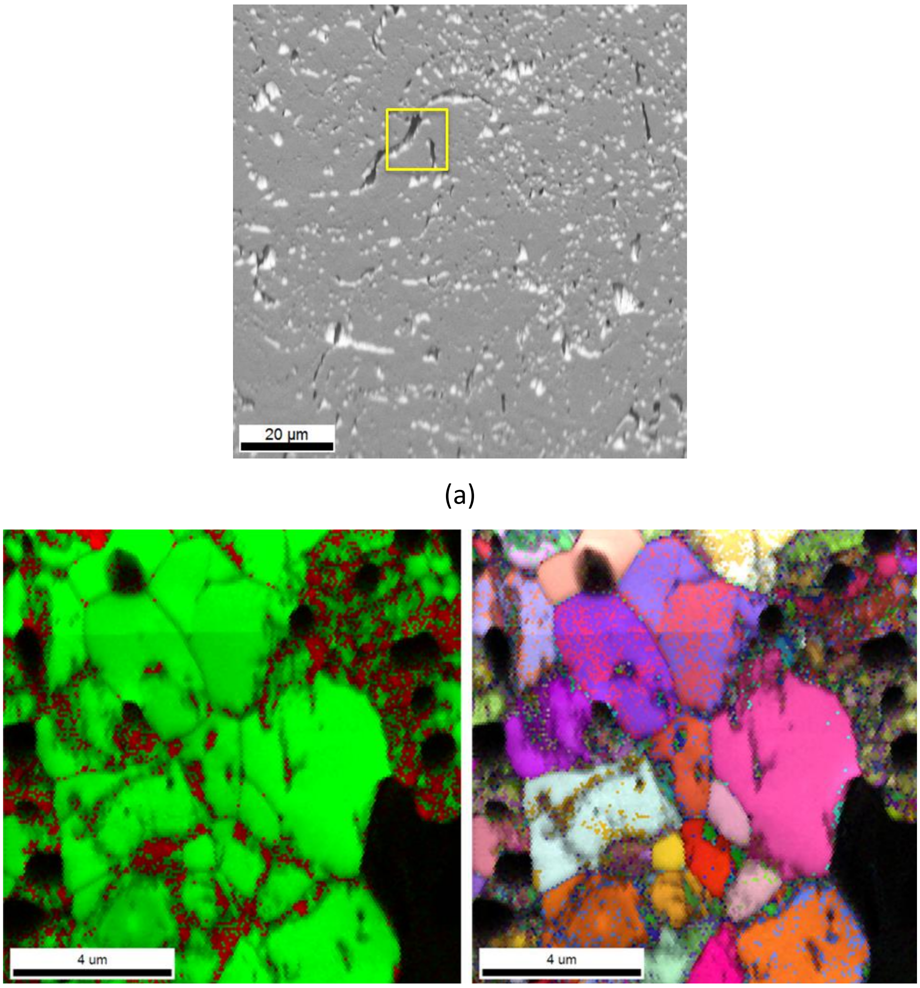

(a)

(b) (c)

Figure 62 SEM-FEG image of sample cooled at 1°/min and aged for 24h at 250°C(a), with "Phase" map (b) and IPF map (c)

Table 11 - Phase amount after Rietveld quantifications for samples after first aging for 24h at 250°C, with agreement factors

	Cooling rate	**Phases (wt%)**				**Agreement factors**	
Material		t'	t	c	m	X^2	R_{wp}
DVC TBC	1°/min	8	16	47	29	5,1	5,3
	5°/min	10	20	53	17	4,1	4,8
	20°/min	7	17	56	19	4,1	4,8
	Air quenching	9	15	64	13	5,9	5,7
	Water quenching	9	13	63	15	6,2	5,8
Porous TBC	1°/min	8	14	58	21	8,8	7,2
	5°/min	10	19	55	16	4,6	5,1
	20°/min	12	28	44	16	6,1	5,8
	Water quenching	11	21	52	16	42	5,1

4.2.1.2 *Aging treatment for 168h at 250°C*

The evolution of m phase after aging has been evaluated through a longer annealing (168 hours) at 250°C, in order to check the effect of time at this temperature. In this case, only the DVC samples have been tested, as previous results indicated that the two materials show similar behavior after annealing at 250°C.

In Figure 63, are compared the XRD patterns of samples slowly cooled and aged at 250°C with with those of samples not re-heated. The m phase peak overlap shows an increase of this phase with dwell and it confirms that m phase forms in the first hours of ageing.

In Table 12, all the quantitative results obtained for all tested samples are summarized with agreement factors.

Table 12 - Phase amount after Rietvield quantifications for samples after subsequent aging, with agreement factors

	treatment	**Phases (wt%)**				**Agreement factors**	
Cooling rate		t’	t	c	m	X^2	R_{wp}
1°/min	168h at 250°C	11	20	41	28	35,8	4,9
	24h at 400°C	8	13	51	28	16	6,7
5°/min	168h at 250°C	9	15	61	16	24	4,3
	24h at 400°C	9	17	57	17	12	4,4
Air quenched	168h at 250°C	8	15	67	11	15	5,1
	24h at 400°C	8	12	60	20	6,4	4,6

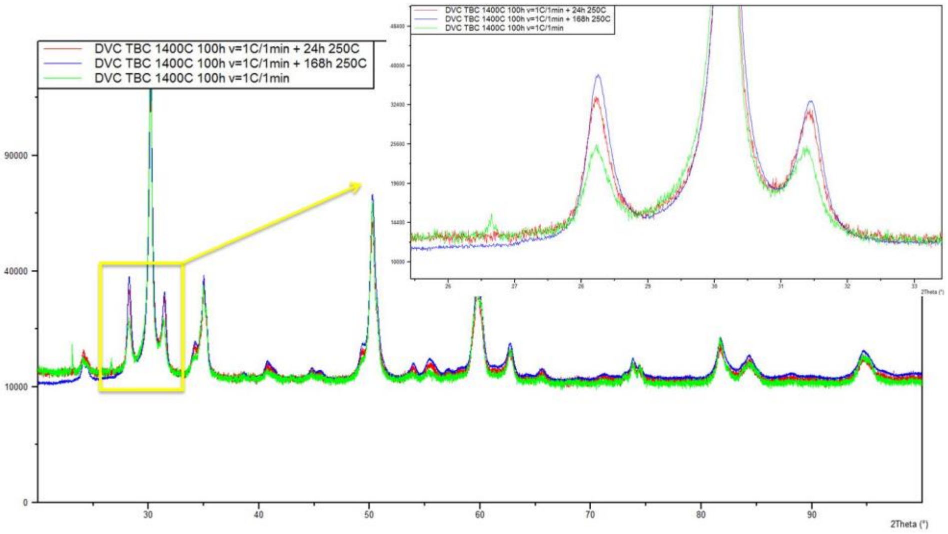

Figure 63 – Comparison of X-Ray patter of DVC TBC cooled at 1°/min without aging and aged for 24h and 168h at 250°C

The FEG-SEM analysis (Figure 64,DVC sample with cooling rate 1°/min) show that the m phase grains are still very fine after a week at 250°C and the phase is distributed throughout the TBC thickness. This observation is confirmed by the comparison of XRD patterns and their Rietveld quantification obtained from both surface and pulverized samples, as shown in Figure 65 and in Table 13.

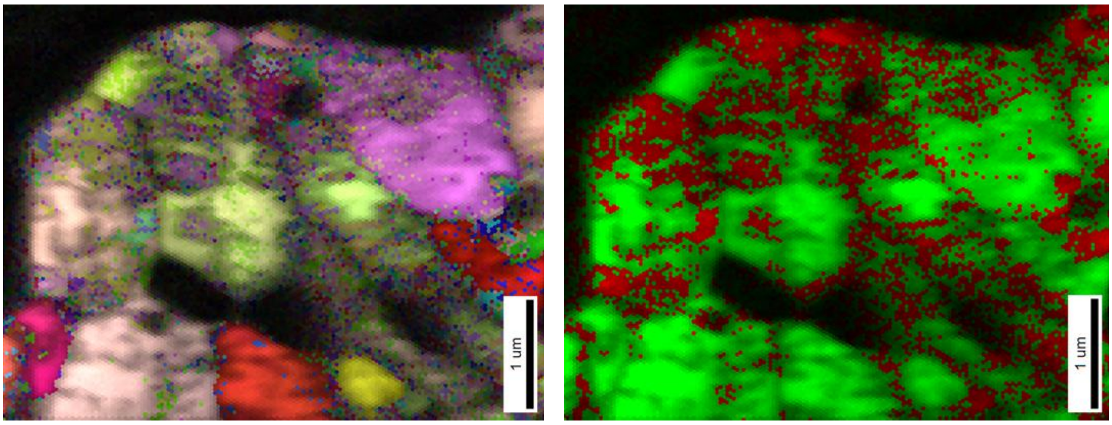

(a) (b)

Figure 64 - “Phase” map (a) and IPF map (b) of a sample cooled at 1°/min and aged for 168h at 250°C

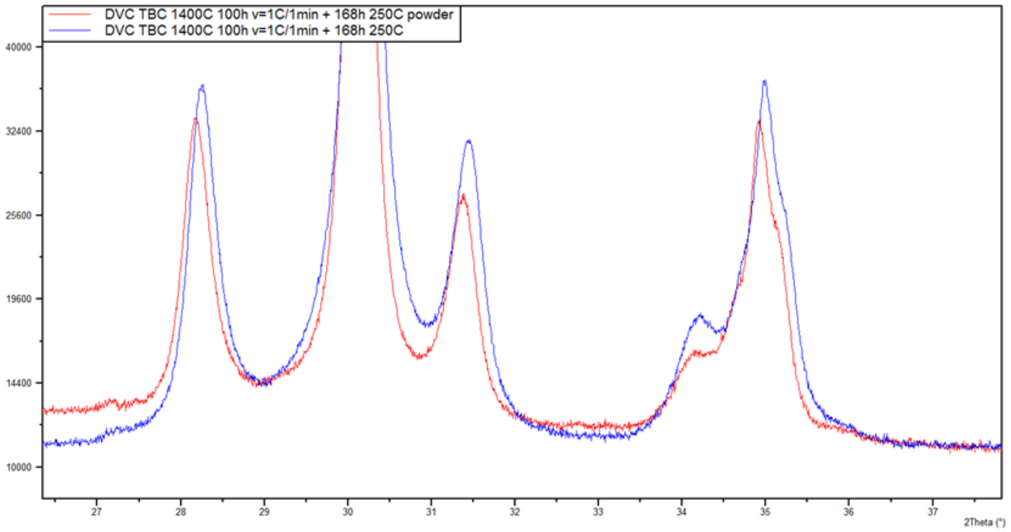

Figure 65 – Comparison between X-Ray patters of a sample aged for 168 h at 250°C, bulk and pulerized

Table 13 - Phase amount after Rietvield quantifications for sample DVC TBC cooled at 1°/min with aging for 168 h at 250°C, with agreement factors, bulk and pulverized

Type of sample	Phases (wt%)				Agreement factors	
	t’	t	c	m	X^2	R_{wp}
Surface	11	20	41	28	7.0	4.9
Pulverized	8	17	46	29	8.8	6.1

4.2.1.3 *Aging treatment at 400°C*

To check the effect of an increase in annealing temperature, aging at 400°C for 24 hours has been applied to the DVC samples. In Figure 66, are compared the XRD patterns of samples annealed at this temperature: one was cooled at 5°C/min and aged at 250°C for 168 hours, another was only cooled, the third one was annealed at 250°C for 24 hours. The m phase peaks confirm that the amount of this phase is the same even if the annealing temperature increases.

In Table 12, all the quantitative results with agreement factors are summarized for all samples tested after treatment at 250°C for 168 hours followed by 400°C for 24 hours. No difference between the two annealing heat treatments can be appreciated, except for the increase of the m phase in the air quenched sample after high temperature annealing.

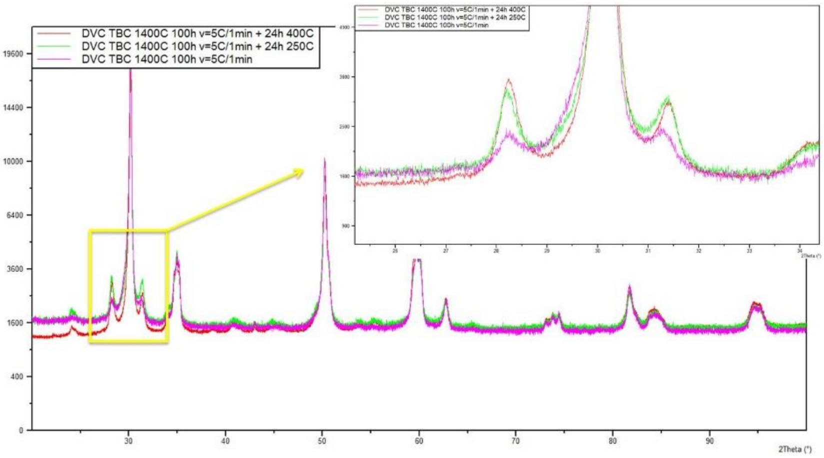

Figure 66 - Comparison of X-Ray patter of DVC TBC cooled at 5°/min without aging and aged for 24h at 250°C and 24h at 400°C

4.2.1.4 *Effect of the TBC material*

The first observation arising from the presented results is the different behavior of the two tested materials after cooling at different rates and aging at low temperature. In fact, after the same treatment, porous TBC samples show a smaller amount of m phase than DVC material. A possible explanation of this different behavior can be related to the different powder production technique used for the two sprayed materials and, most importantly, to the different spraying parameters used to obtain the two coatings. The DVC spraying parameter are strongly energetic with respect to APS TBC as higher amount of energy is necessary to obtain the desired dense microstructure, characterize by vertical cracks. The DVC spraying parameters should bring the sprayed material in a condition which, in terms of powders homogenization, is closer to the thermodynamic equilibrium and this can explain the higher amount of m phase observed in DVC for all the tested conditions.

4.2.1.5 *Effect of cooling rates and subsequent aging*

The different cooling rates tested for the two materials highlight the possibility to hinder or limit the m phase transformation if the cooling rate is sufficiently quick.

The following aging brings to an increase of m phase limited by direct cooling at room temperature for all the tested cooling rates. The m phase amount at the end of the different aging heat treatments changes as a function of the first cooling rate from 1400°C. The slowest cooling rate brings to the higher m phase amount after direct cooling at room temperature and after all the aging step explored. Moreover, for the slowest cooling rate the amount of m phase does not change with the applied aging step and it remains constant passing from 20% to 30% for DVC materials as shown in Figure 67. For a quicker cooling rate, like 5°C/min reported in Figure 68, the m phase increases at the end of the highest aging steps passing from 10% to 20%. In this case, the final m phase amount is lower than the one reached by sample cooled at 1°C/min. In Figure 70, the phase evolution for m and t' phases is reported for all the tested DVC sample. The difference between m phase for different cooling rates is clear, while t' seems not affected by cooling rates and aging, with a constant value around 10%.

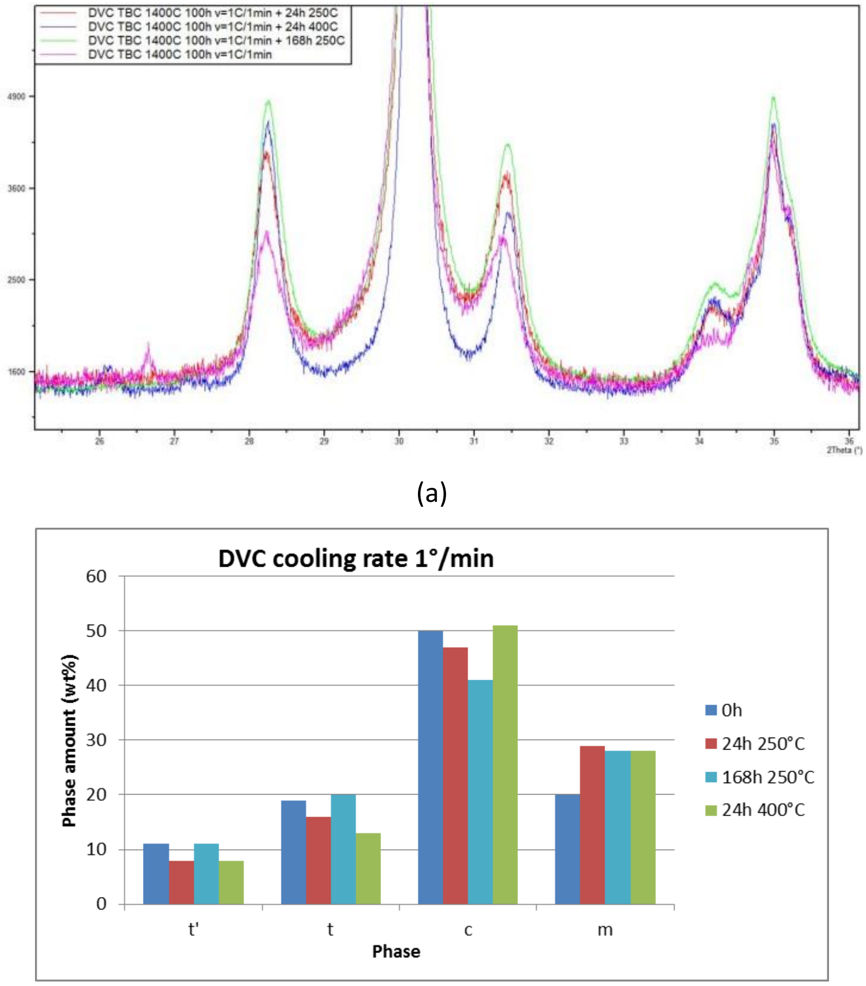

(a)

(b)

Figure 67 - X-Ray pattern (a) and phases amount (b) of DVC TBC cooled at 1°/min pre and post three after aging treatment

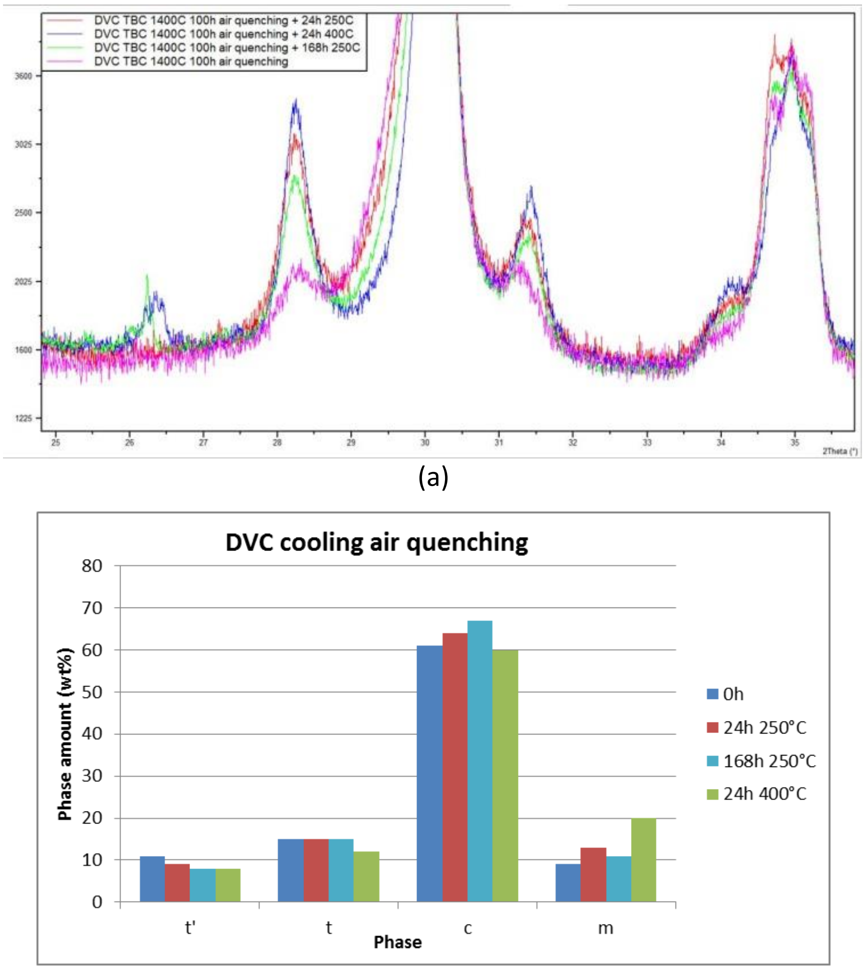

(a)

(b)

Figure 68 - X-Ray pattern (a) and phases amount (b) of DVC TBC cooled with air quenching pre and post three after aging treatment

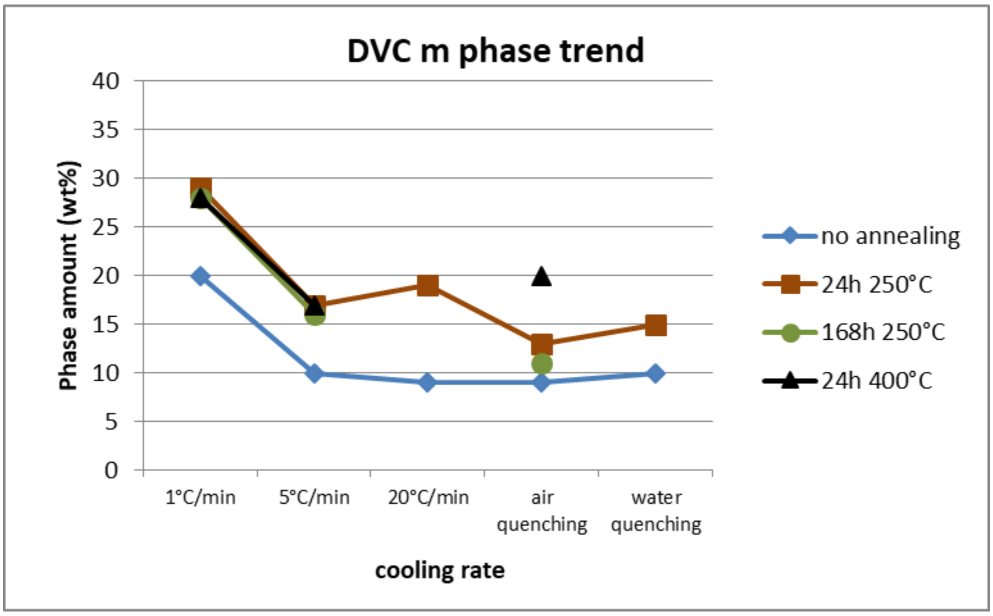

Figure 69 - Trend of m phase in DVC sample

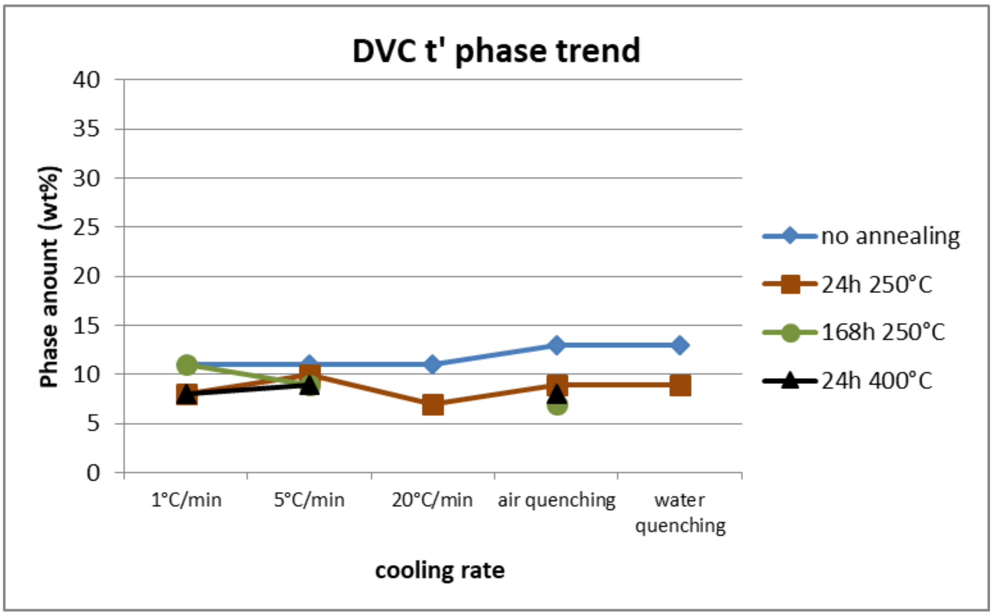

Figure 70 – Trend t’ phase in DVC sample

4.2.1.6 Evolution of phase lattice parameters

From Rietveld refinement of all the XRD patterns, lattice parameters evaluation of the TBC phases as a function of cooling rates, exposure temperature and time has been considered.

In Figure 71 the lattice parameter variation of c phase is reported. The trend shows that the parameter tends to be close to the literature value (a=5.1300 Å)[62] only after aging for the slowly cooled sample. Other aged samples and the one cooled at 1°/min without annealing show larger values of lattice parameter. This is because rapid cooling blocks a high temperature situation, where the cubic cell tends to be larger.

The Figure 72 reports the variation of lattice ratio c/a for t and t’ phase.

To simplify the discussion and clarify the inter-phase relationships, the t data are presented using a pseudo-cubic (distorted fluorite) unit cell, as used by Lefevre [85] and Scott [86]: it means that the c/a ratio of t and t’ phases decrease when the phases tend to become cubic, and approach an ideal value of √2. Then, the *a* parameters of tetragonal phases are multiplied by √2 in these graphs.

Both phases tend to keep a constant value close to the literature ratio (1.01169 for t’ and 1.01632 for t). The little variations are considered to be inside the error limit.

In this case, tetragonal phases tend to maintain their lattice parameters regardless of the cooling rate applied.

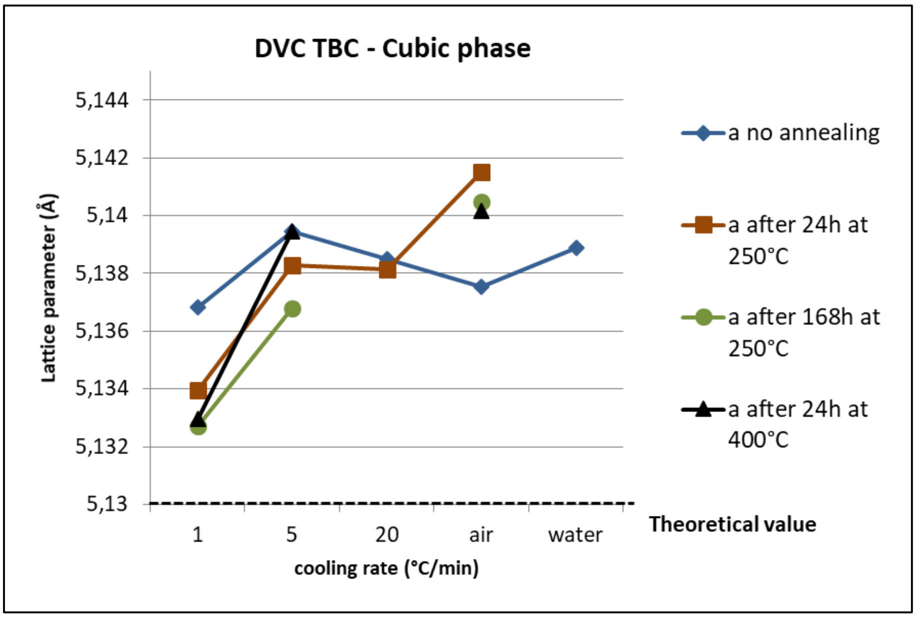

Figure 71 – Trend of lattice parameter of cubic phase

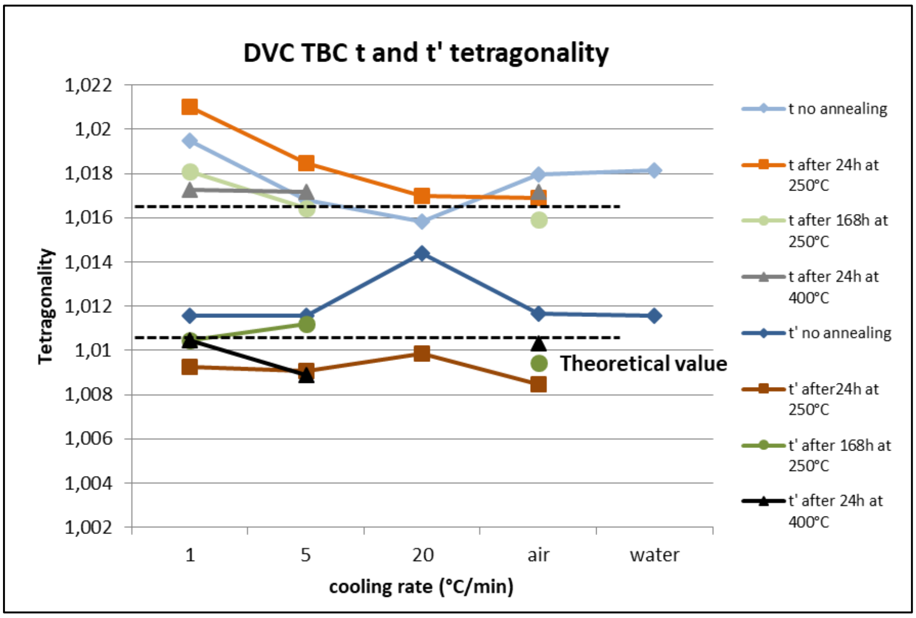

Figure 72 –Trend of ratio c/a of tetragonal and tetragonal prime phases

In the Figure 73 the cell volume of the four phases for DVC sample after the different cooling rates is reported. The t, t’ and c phases have volumes similar to each other and remains constant after all treatments. The result confirms the literature observation about an increase in cell volume of the m phase of about 5-6% compared to the other phases. Finally, a little increase of the monoclinic cell volume with cooling rate seems to be present.

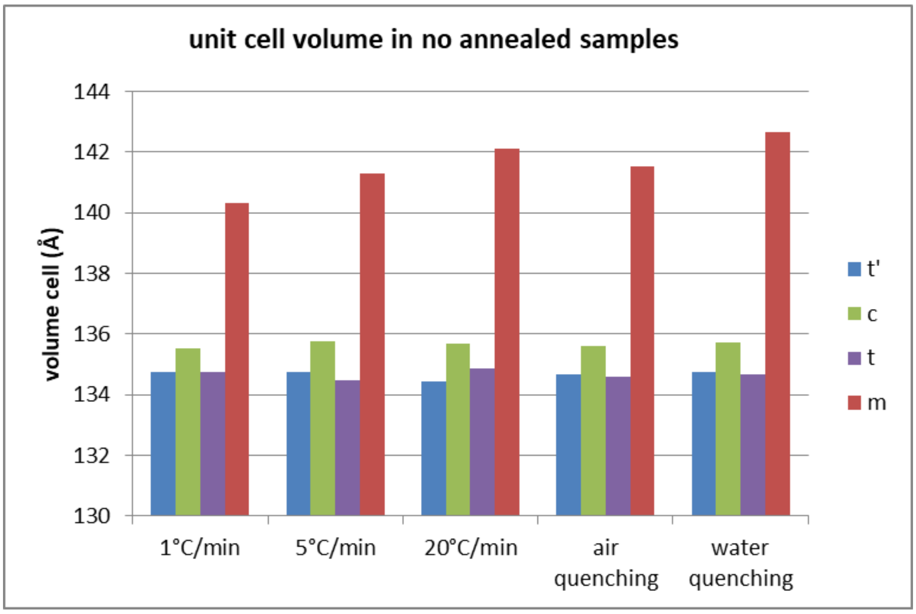

Figure 73 – Unit cell volume variation of tetragonal, tetragonal prime, cubic and monoclinic phase for no annealed samples

In Figure 74 is shown a comparison between t' and m cell volumes of samples pre and post annealing. The volume change is significant after 24h at 250°C only for m phase, as it shows always a higher volume cell with respect to only cooled samples.

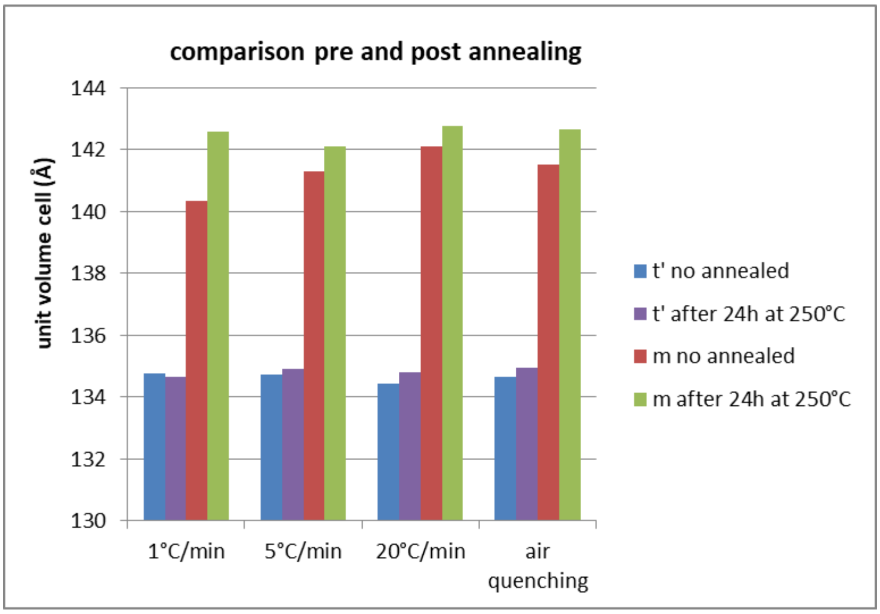

Figure 74 – Comparison between unit cell volume variation of tetragonal prime and monoclinic phases in samples no annealed and after aging for 24h at 250°C

4.2.1.7 Comparison with literature results

Present results may be discussed in comparison with the available literature data about similar materials, taking in particular consideration the suppression of the t→m phase transformation with fast cooling.

According to a work of Yashima et al. [81] subsequently used by Fabrichnaya et al. of 2004 [20] the T_0 lines for the t→c and t→m transformations have been determined. On the basis of metastable equilibrium considerations, t phase cooled below the T_0(t–m) line transforms in the m form and transforms back on heating above the T_0 line.

These papers have been used by Lughi and Clarke [80] to confirm the transition temperature in a zirconia partially stabilized by 5wt% yttria.

The T_0(t–m) line determined by Yashima et al. shows a linear trend of the type $T_0(t–m) = a X + b$ where X is the concentration of $YO_{1.5}$ in mol.%, while a and b parameters have been calculated by a least-squares fit. The resulting equation is:

$$T_0(t–m) = 1114 - 159.44X$$

Through this approximation, as reported by the same author, the T_0 line should reach zero approximately at $X(YO_{1.5}) = 7$, which implies that in a composition interval between 7 and 12 the tetragonal phase should not undergo any transformation.

In this work however, the appearance of m phase has been observed in samples at $X(YO_{1.5})=7.78$ at all tested conditions, demonstrating that, at least at low temperature, the field of existence of the monoclinic phase is extended beyond 7 mol% $YO_{1.5}$.

The m→t transition, observed at high temperature (around 400°C) by Lughi and Clarke is not detected in this work, probably due to the different exposure time. Moreover, the different results may also be due to the different measurement conditions: X Ray diffraction at room temperature after treatment at 400°C in our case, and Raman spectroscopy at high temperature in the case of Lughi and Clarke.

The two T_0 lines proposed by Yashima et al. are reported in Figure 75. In this figure A and B areas show the conditions where where t→ m and c→ t transformations occur, respectively. According to our results the t→ m transition area is extended to the field C, then to $YO_{1.5}$ compositions higher than 7mol%.

Accordingly a new T_0(t–m), not anymore linear, has been drawn (dotted line). It shows some curvature for compositions greater than 5 mol% $YO_{1.5}$[87].

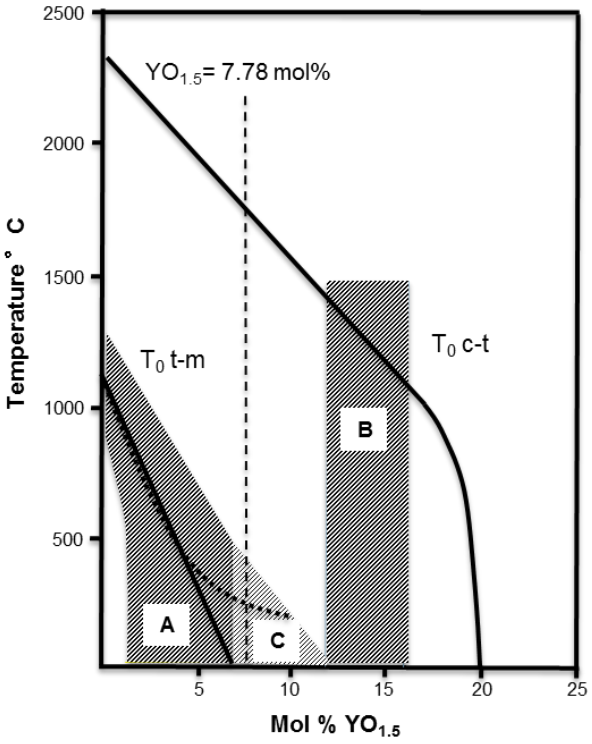

Figure 75 - T_0 lines for the t→m and c→t transformations. A and B transformation zones reported by Yashima et al.[81]**. according to the present work the A zone is extended to the area C.**

4.3 Kinetics of zirconia phases

During high temperature exposure, the tetragonal metastable (t’) structure tends to decompose into a cubic and a tetragonal structure poorer in Y_2O_3 and subsequently in a monoclinic one, which contributes to the increased brittleness of the coating, according to the reaction following sequence:

t’-YSZ → t-YSZ + c-YSZ → m-YSZ + c-YSZ

The phase transformation is therefore related to the operating conditions of the coating.

The knowledge of the kinetics of the YSZ decomposition process allows to use the quantities of the various crystallographic species as an indicator of temperature.

This information is very important for a gas turbine machine manufacturer. In fact, due to the complex geometry of the blades and the extreme difficulty of carrying out experimental measurements during actual operation, it is not possible to know exactly the real operating temperatures of the components. Temperatures have been estimated by studying the microstructural evolution of the turbine blade materials, i.e. the base metal and the metallic coating [22].

Knowing the external temperature of the TBC would allow to evaluate the component surface temperature, obtaining, in addition to another methodology for the evaluation of blade degradation, a way to evaluate the effect of the temperature drop guaranteed by the TBC.

In accordance with Witz et al.[22,88], freestanding TBC samples were aged at times and temperatures reported in Table 3.

The samples after exposure have been quantified by X-Ray diffraction and the results obtained are reported in Table 14. The critical analysis of the variation of composition in the samples allowed to reconstruct the decomposition kinetics and, subsequently, to estimate the temperature of real components.

Table 14 – Phase amount of each samples tested at high temperature for several exposure time, with agreement factors

T (°C)	t (h)	t'	c	t	m	R_{wp}	X^2
1100	1	100	0	0	0	4.8	6.1
	24	94	0	6	0	6.5	8.6
	100	91	0	9	0	6.7	10.2
	250	86	6	8	0	6	7.7
	450	78	5	17	0	9.1	18
	650	80	7	12	0	6.8	7.9
	850	76	7	17	0	8.2	14.2
	1000	68	6	26	0	8.7	16.9
	1400	50	15	35	0	5	4.7
1200	1	96	0	4	0	8.9	15.9
	10	92	5	3	0	6.1	7.2
	100	71	9	20	0	10.1	22
	200	66	8	25	0	9.3	17
	300	59	16	25	0	5.6	6.2
	1000	40	26	35	0	4.6	3.8
1300	1	77	9	14	0	7.5	12.9
	10	67	9	24	0	7	9.6
	100	35	25	40	0	5.6	6.5
	400	37	38	20	4	5.7	5.5
1400	1	66	8	26	0	7.8	13
	10	36	22	42	0	7.6	11
	100	22	46	4	28	7.6	10
	200	15	42	20	23	4.8	3.6
	300	18	31	18	33	4.8	4
	500	7	45	6	42	5.8	5.6

In Figure 76, as an example of material tested at low temperature, the X-Ray pattern obtained from the sample tested at 1100°C for 1400h (the longest exposure of this test campaign) is reported.

At this temperature, tetragonal prime phase disappears in favor of tetragonal phase at increasing times, while monoclinic phase is not stable. The cubic phase tends to form only after long time exposure (beyond 100h) at 1100°C, while it is stable at other temperatures, except for 1200°C for 1h. In Figure 77 the X-Ray pattern comparison of cubic phase existence between samples tested at 1100°C for 24h, without phase, and 1400h, where the peak of the phase is observable is reported.

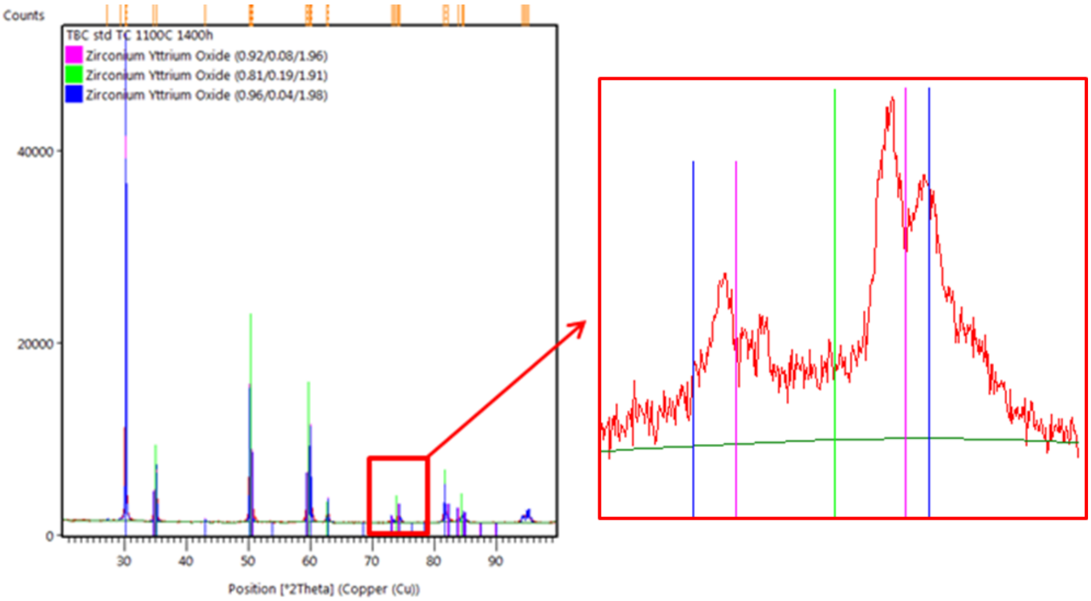

Figure 76 – X-Ray pattern of samples tested at 1100°C for 1400h. t=blue, t'=purple, c=green, m=yellow

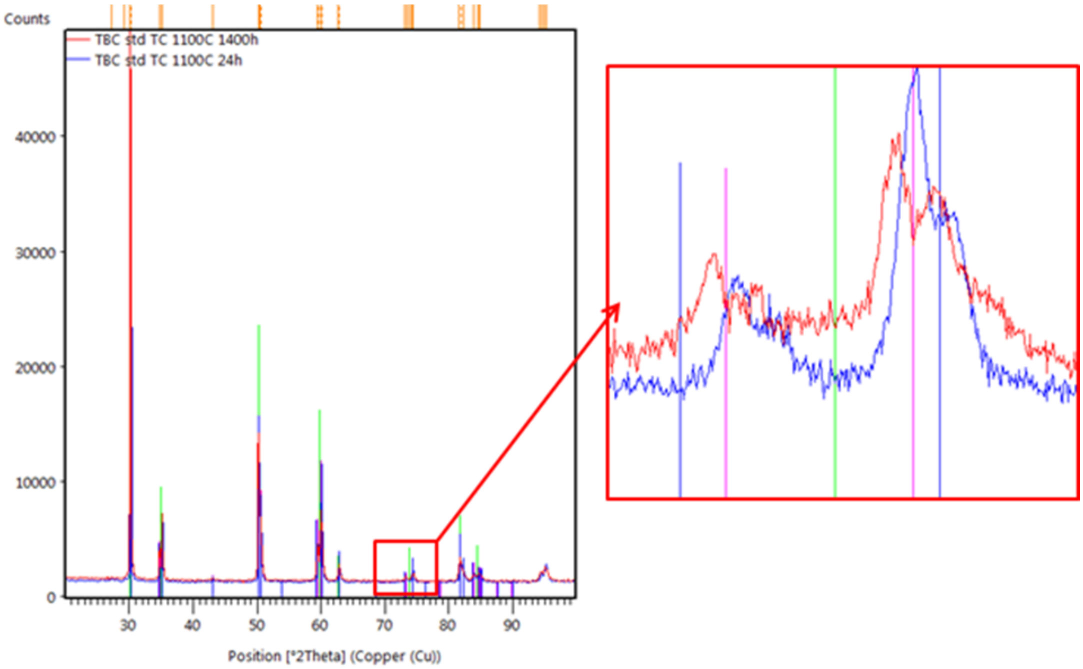

Figure 77 - X-Ray pattern comparison between samples tested at 1100°C for 24h (blue) and 1400h (yellow)

The monoclinic phase has been detected only in the samples exposed at 1300°C and 1400°C as shown in Figure 78 for the sample tested at 1400°C for 200h.

This is in accordance with the transformation process proposed by Witz et al. where the first transformation that takes place leads to the formation of the cubic and tetragonal phase; and only later it transforms giving rise to the monoclinic phase.

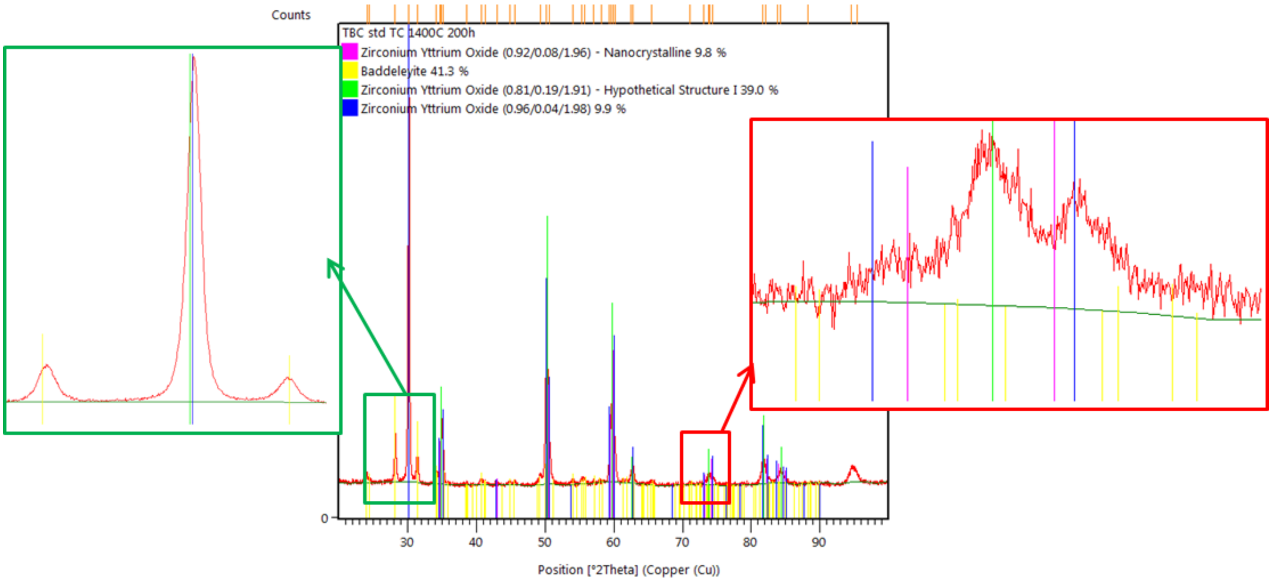

Figure 78 - X-Ray pattern of samples tested at 1400°C for 200h. t=blue, t'=purple, c=green, m=yellow

Comparison of the XRD patterns of samples exposed 100h at the four tested temperatures is shown in Figure 79. The monoclinic phase, whose peaks are around 2θ equal to 28° and 32°, is stable only at 1400°C, while the evolution of the other phases is observable through the peaks around 74°.

The cubic phase is not stable at 1100°C but it is measurable beyond 1200°C, while tetragonal prime phase decreases with exposure time.

The effect of exposure time variation at the same temperature, 1300°C, is shown in Figure 80.

The kinetics highlights an increase in the cubic and monoclinic phases, as shown by the longer-time green X-Ray pattern at the expense of the tetragonal structures.

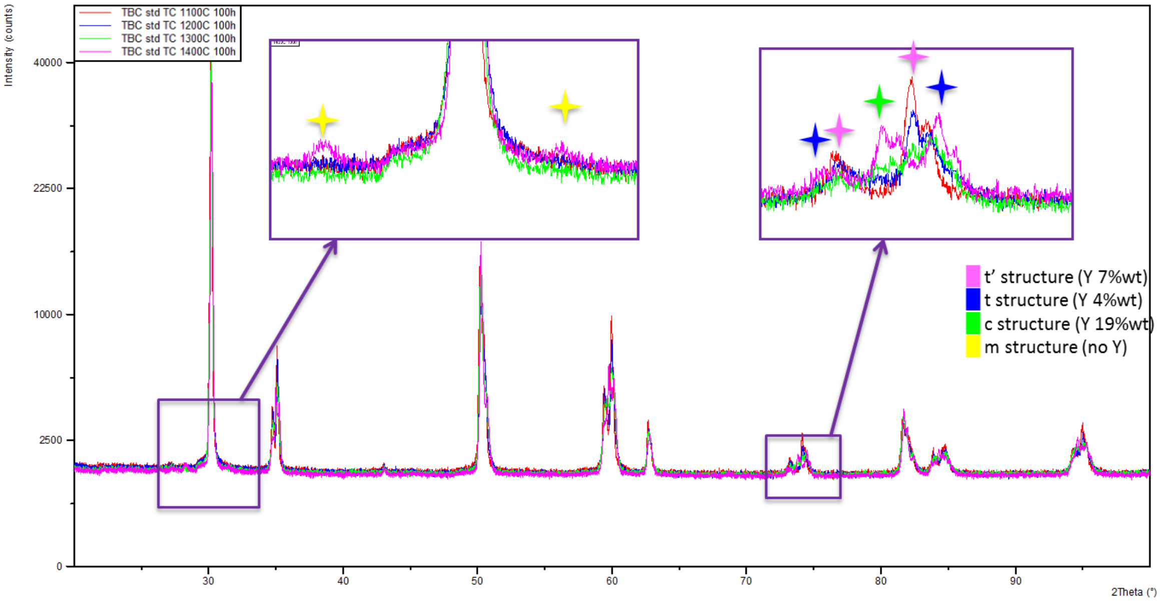

Figure 79 – X-Ray pattern comparison between samples tested at different temperatures at 100h

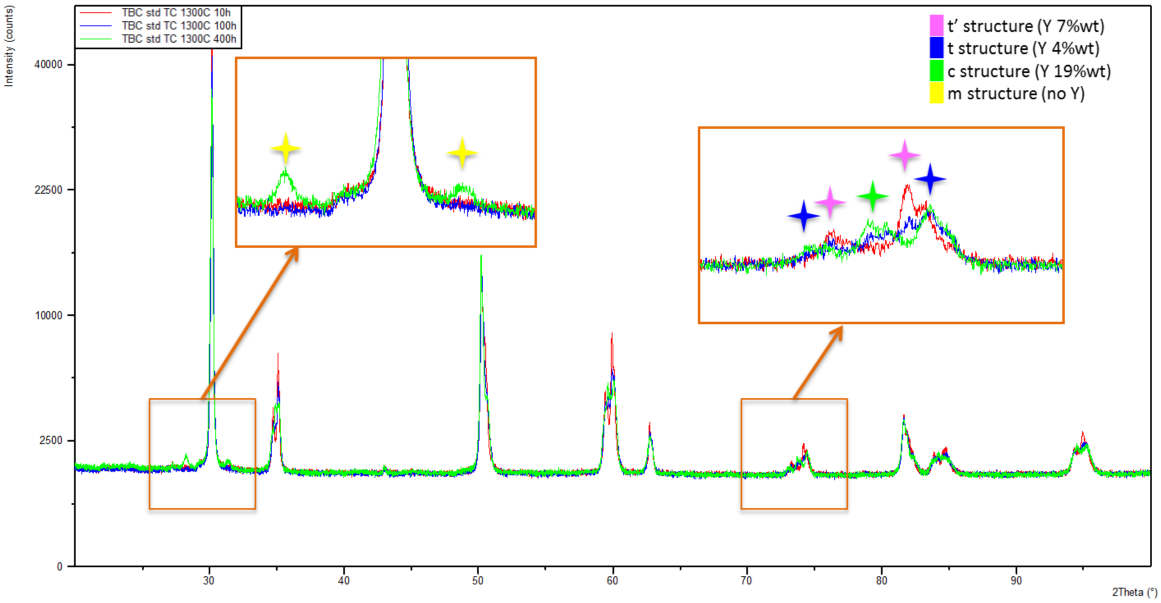

Figure 80 - X-Ray pattern comparison between samples tested at different 1300°C at different times

The trend of each phase has been reported in Figure 81. The monoclinic phase tends to increase significantly only at 1400°C and obviously a transformation kinetics cannot be defined.

Also tetragonal and cubic phases cannot be used to define a kinetic law, because t grows linearly at low temperature but at high temperature it has a trend with a maximum, while c does not have a trend definable at 1400°C.

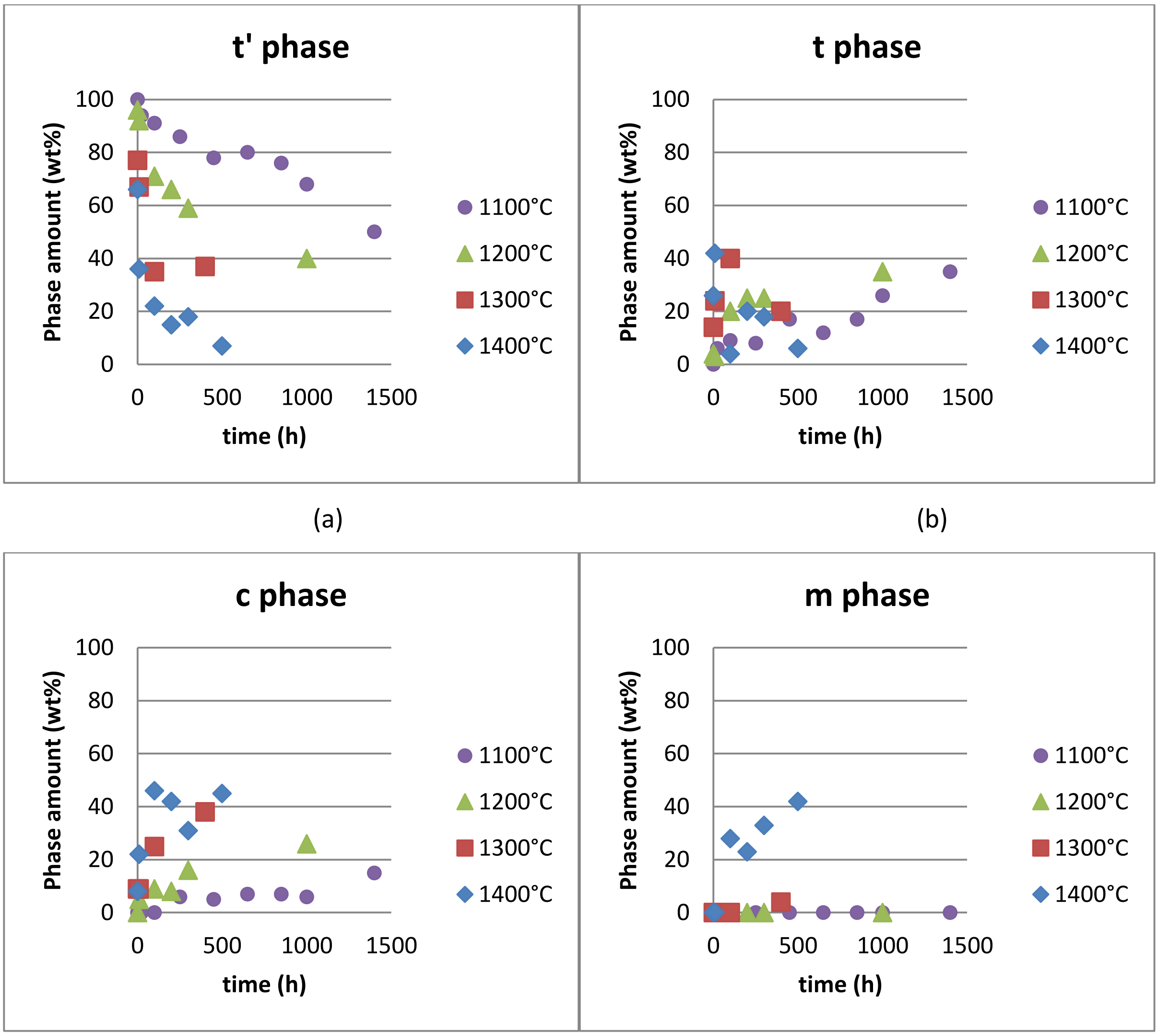

(a) (b)

(c) (b)

Figure 81 – Trend of tetragonal prime (a), tetragonal (b), cubic (c) and monoclinic (d) phases at each temperature and time exposed

The crystallographic phase t' is the most useful for evaluating the evolution of the material over time and temperature, as suggested by Witz and Bossman [88], using the empirical formula:

$$kt = g(1-\alpha_{t'}) = g'(\alpha_{t'}) = Be^{-C\alpha_{t'}}$$

with

$$k = Ae^{-\frac{E_a}{RT}}$$

where $\alpha_{t'}$ is the fraction of t' structure, *k* is the kinetic constant that depends on activation energy E_a and temperature, t is the time, R is the gas constant and A, B and C are coefficients.

By elaborating this formula, we obtain:

$$lnt = lnB - lnk - c\alpha_{t'}$$

Therefore, by graphing, for each temperature, the natural logarithm of time with respect to the quantity of t' a value for C (slope) is obtained which is approximately equal for all curves, and a value for $lnB - lnk$ (intercept) which varies with the temperature (Figure 82).

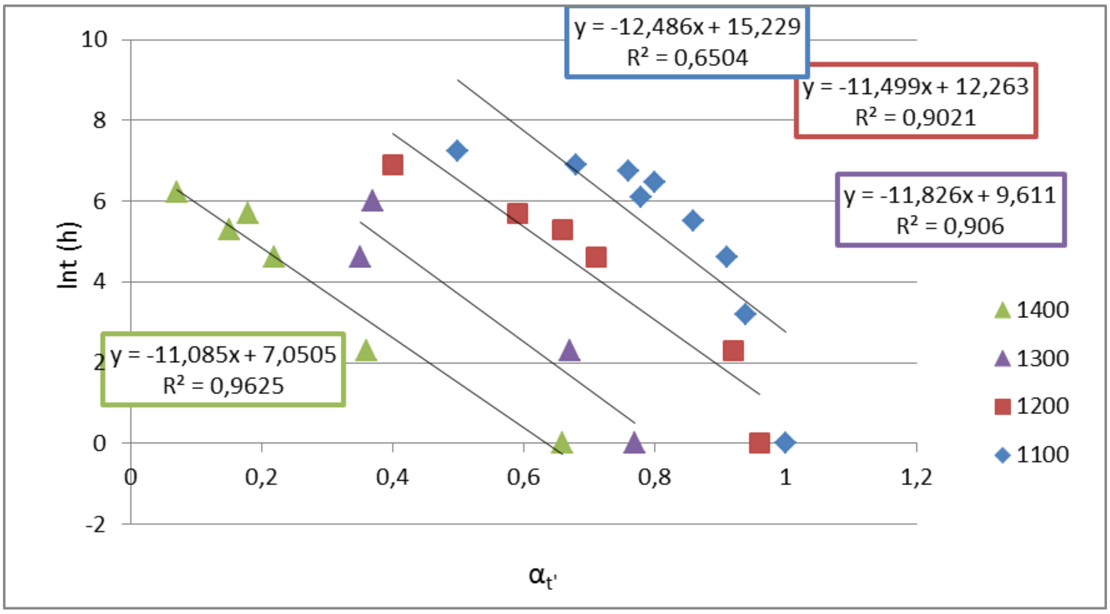

Figure 82 - Trend of the fraction of t' in relation to the natural logarithm of time for each temperature

The value of C is the average of the four values obtained from the straight lines and is: C=11.72 Instead, the intercept values depend on temperature. They can be plotted (Figure 83), as a function of temperature, according to the formula:

$$lnB - lnk = lnB - \left(lnA \cdot \left(-\frac{E_a}{RT}\right)\right) = lnB - lnA + \frac{E_a}{RT}$$

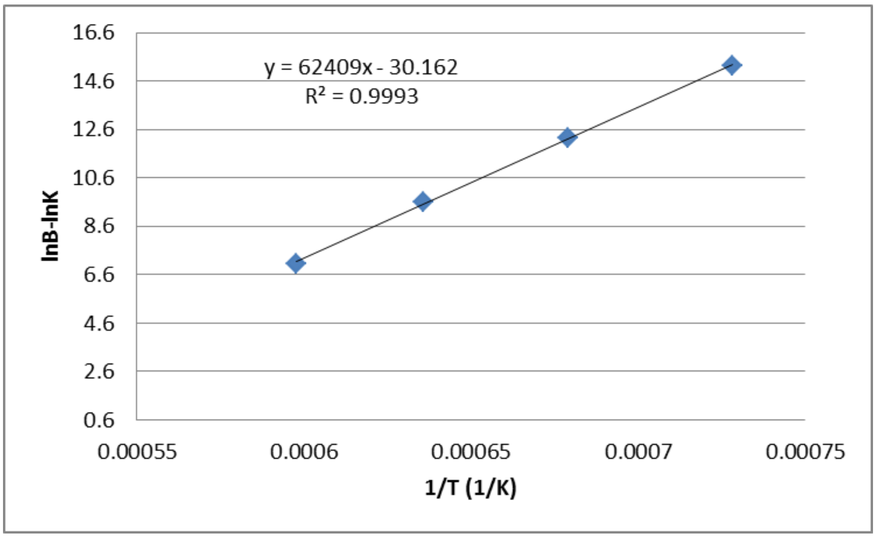

Figure 83 - Trend of the intercept obtained from the previous graph respect to the inverse of the temperature

Where:

$$lnB - lnA = 30.16$$

$$E_a = 518\text{KJ}$$

The activation energy obtained is similar to the value 580 KJ, reported in the literature by Dow Whitney [89].

The Figure 84 shows all the values obtained in this work in which the fraction of t' is related to Lnk (which contains the calculated average activation energy). The graph shows that, with the activation energy value of 518KJ, all the values can be described by a single straight line, demonstrating the agreement of the obtained experimental results.

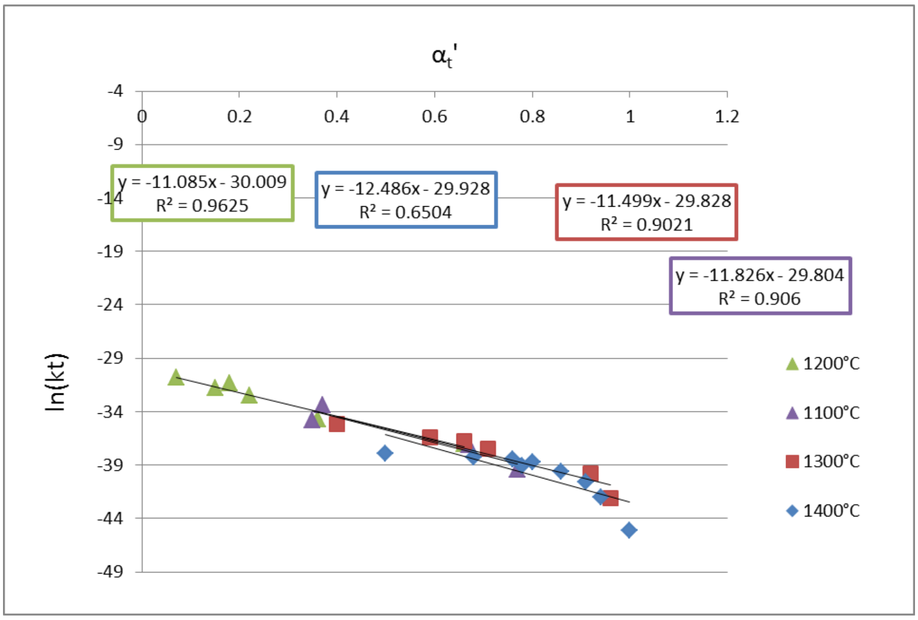

Figure 84 – Representation of all value obtain in this work

With the activation energy values and the calculated A, B and C constants, the kinetics of the transformation, useful for determining the operating temperature of real components, is represented by the following equation:

$$T = \frac{\frac{E_a}{R}}{lnt + ln\frac{A}{B} + c \cdot \alpha_{t\prime}}$$

Therefore, by evaluating the amount of phase t' present in a TBC sample coming from an area of an operated blade (XRD and Rietveld method) and knowing the operating time in the machine (firing hours), the external temperature of the component can be estimated.

4.4 Thermodynamic evolution of 7YSZ

Materials used for the study of the thermodynamic stability of the phases in the 7YSZ samples are the same used for the CMAS corrosion tests, and are described in detail in the paragraph 3.1.2.

Samples from two batches, called A and B, of zirconia were exposed to high temperatures up to 10000h. During this work, only one tetragonal phase, called t^+, has has been considered neglecting the distinction between t and t'. This is to emphasize the evolution of the monoclinic phase, which is harmful to thermal barriers coating.

The quantification results for all the tested samples at 1100°C are summarized in Figure 85-a. In both batches, the observed phases are t^+ and m, which increases with exposure time. The matrix is formed by t^+ phase, always more than 80 percent until 5000 h, while after 10000 h about 10% of c phase is observed.

The evolution of the TBC is mainly related to the formation of the m phase. It tends to increase with time up to a maximum at about 3000 h, then it decreases at 5000 h and, finally, increases again beyond the amount observed at 3000h. This behavior is common to all samples, but it is more evident in the case of samples 7B.

The thermodynamic data of Wang et al. [90] at 1100°C shown that the m phase transforms to t. Although there is large difference in DTA on heating and cooling, the authors estimated an equilibrium temperature of1100°C. Probably, at 3000 h the equilibrium is not reached as the amount of m phase is larger than equilibrium, while for longer aging times, its amount is closer to equilibrium. At the equilibrium temperature, the driving force for transformation is close to zero and it is more difficult to reach equilibrium.

The 7A samples show the same behavior even if the amount of m phases is always lower than in batch B. In the starting condition (without exposure), the m phase has been observed only in batch B: this behavior could be related to the different spraying conditions.

As for 1100°C, the samples exposed at 1200°C have been analyzed after four different aging times (Figure 85-b).

At this temperature, t^+ phase tends to decrease while the c phase increases. Indeed, the c phase is already observable in samples tested after 1000 h. The inversion of the main phase in the samples occurs between 2000 and 3000 h.

Phase analysis results of the 7YSZ samples exposed at 1300°C are reported in Figure 86-a. The matrix is made by the c phase, in agreement with the ZrO_2-Y_2O_3 phase diagram. Indeed, at this temperature a little variation of composition (as for the difference between 7YSZ and 14YSZ) is not thermodynamically significant. In both batches the m phase tends to increase with time, being already 20-30% after 300 h and 35-45% at 1000 h.

Results obtained at 1400°C are similar to those obtained at 1300°C. In Figure 86-b the detected phases in batches A and B are reported. There is no appreciable difference between analyses after 300 and 1000 h. At this temperature there are no differences between samples tested and the amount of m phase is almost equal to that of the c matrix. Presumably, at this temperature the kinetic phenomena are fast enough to reach a thermodynamically stable situation in relatively short times.

The phase analysis results of all samples with agreement factors are summarized in Table 15.

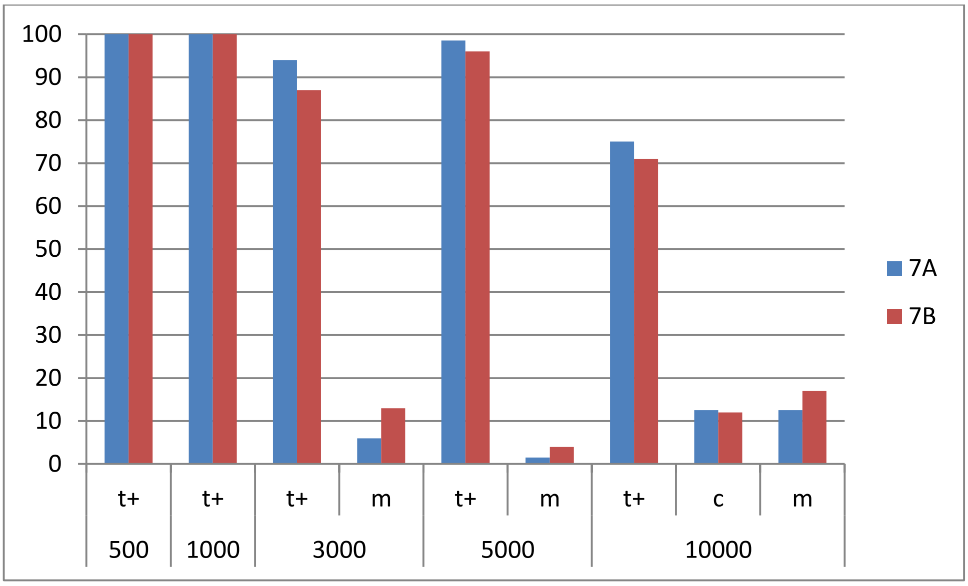

(a)

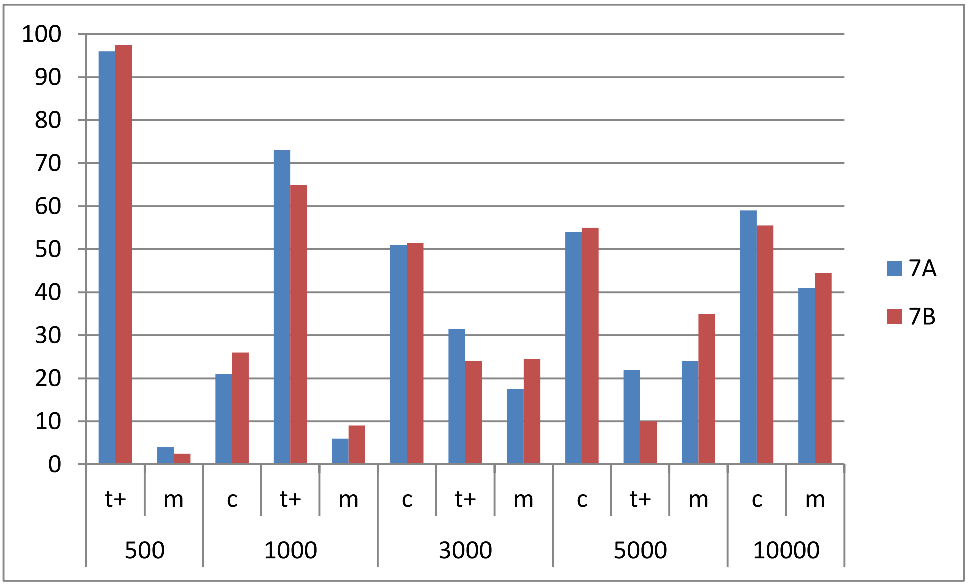

(b)

Figure 85 – Samples 7A and 7B exposed at 1100°C and 1200°C (b)

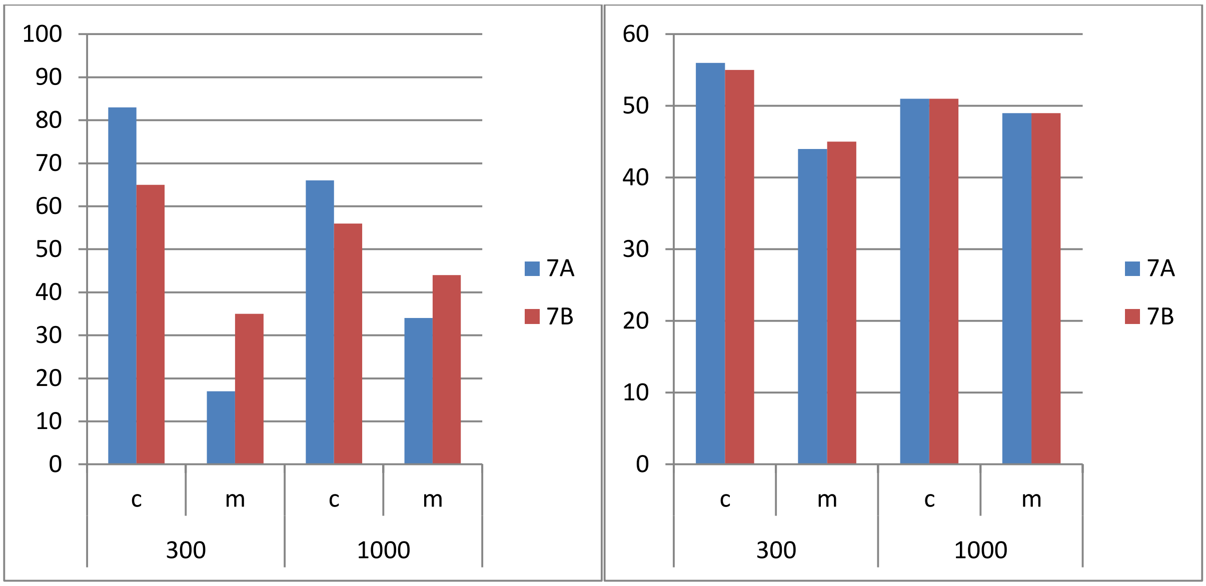

(a) (b)

Figure 86 - Samples 7A and 7B exposed at 1300°C and 1400°C (b)

Table 15 - XRD phase analysis and Rietveld agreement factors for samples 7YSZ

Temperature (°C)	Material	Time (h)	Phases (wt%)			Agreement factors	
			c	t^+	m	R_{wp}	X^2
1100	**7A**	500		100			
		1000		100			
		3000		94	6	5.9	6.6
		5000		98.5	1.5	2.2	2.8
		10000	10	71	19	5.1	1.6
	7B	500		100			
		1000		100			
		3000		87	13	5.8	2.3
		5000		96	4	5.5	2.0
		10000	12	71	17	4.8	1.5

Temperature (°C)	**Material**	**Time (h)**	**Phases (wt%)**			**Agreement factors**	
			c	t^+	m	R_{wp}	X^2
1200	**7A**	500	4		96	6.5	2.6
		1000	6	21	73	5.8	2.0
		3000	17.5	51	31.5	4.7	1.4
		5000	24	54	22	4.5	1.4
		10000	59		41	4.7	1.3
	7B	500	2.5		97.5	6.1	2.4
		1000	9	26	65	5.3	1.8
		3000	24.5	51.5	24	4.9	1.5
		5000	35	55	10	5.1	1.8
		10000	55.5		44.5	4.3	1.2
1300	**7A**	300	83		17	6.9	2.9
		1000	66		34	5.0	1.6
	7B	300	65		35	5.3	2.0
		1000	56		44	4.4	1.5
1400	**7A**	300	51		49	4.8	1.5
		1000	51		49	5.7	2.9
	7B	300	55		45	5.7	2.0
		1000	56		44	6.0	2.4

The analyzed samples show good agreement between the two batches tested. In fact the trends of the quantity of phases are similar to each other at the different temperatures chosen. In general it is noted that at 1100°C the temperature is low to facilitate the evolution of the phases and the monoclinic increases only after long exposure times. The cubic phase also begins to be stable only after 10000h. The tetragonal phase remains the predominant structure. As will be effectively explained in chapters 5 and 6 the structure is totally t', while the thermodynamically stable structure t is not observed.

At 1200°C the monoclinic increases linearly with respect to the exposure time and the inversion of the matrix from tetragonal to cubic is observed within 3000h. At high temperature only the cubic and monoclinic phases are stable and at 1400°C there is not much difference between the samples exposed to 300 and 1000h.

In fact it seems that already in a short time at 1400°C the material has reached thermodynamic equilibrium, while at 1300°C it needs some exposure time.

The results just shown have been also used for comparison with the samples of the same type used for the CMAS corrosion tests. These results allowed us to define a standard behavior due to the influence of only time and temperature. For this reason a detailed discussion of these results, also with reference to the samples exposed with corrosive will be described in the next chapter.

All information obtained in chapters 4 and 5 will be taken up in the discussion of chapter 6.

4.5 Discussion

4.5.1 Achieved results

In this chapter, various tests have been described, carried out on the standard material used as TBC, to evaluate the evolution of crystallographic structures and their degradation. To do this, various supplies of 7YSZ have been used so that the obtained values are not always perfectly superimposable, but a general trend can be described.

The different tests implied high temperature exposure of the material for exposure times up to 1000h for many tests, and up to 10000h for the investigation of the thermodynamic equilibrium.

The analysis of the powders underlined the industrial importance of this type of study, as if the powders have a high quantity of monoclinic phase (higher than 10%), it cannot be completely dissolved during the plasma spray deposition process. The study of different powder batches is also important to evaluate the role of the particle size, as a mix of different dimensions makes sintering easier.

The microstructural study of the particle sections showed different structures: pre-sintered particles, with a more compact structure without monoclinic phase, and others, more porous, showing islands with lamellar structure, typical of the t→m martensitic transformation.

A comparison with 14YSZ powders from the same manufacturer has been considered. The section of these powders showed the presence of only porous particles, and for this reason the quantity of monoclinic phase present in these particles was higher than in 7YSZ.

The powders have been exposed at high temperature up to 1000h and the evolution of the phases was observed. The analysis showed that the monoclinic phase in the 14YSZ samples is not thermodynamically stable, and, when it is present in the as delivered samples, the phase disappears at high temperature, while in the 7YSZ samples the phase is stable and increases with exposure.

The effect of different cooling rates from high temperature and subsequent low temperature annealing was studied for two 7YSZ APS TBC, DVC and porous. The two materials have been exposed at 1400°C for 1 hour and then cooled at different cooling rates, from 1 °C/min to water quenching. Subsequently, different aging treatments have been applied: 24 h at 250°C, 168 h at 250°C, and 24h at 400°C.

The results collected showed that the m phase amount is affected by the cooling rate. In particular, its formation is inhibited/hindered by fast cooling from high temperature but aging at low temperatures is sufficient to significantly increase its quantity in the material. Moreover, DVC and porous materials show similar phase evolution after first treatment and subsequent aging at 250°C for 24h, with an increase of m phase of about 10% for all measured samples. The difference is the starting amount of m phase, higher in DVC samples, probably due to different spraying parameters.

Annealing at higher temperature (400°C) or longer time (168 h) at 250°C, do not show any significant variation in the quantity of phases, except for the quenched sample (where the quantity of m phase increases with exposure at the highest temperature).

Finally, the presence of m phase in all the samples considered in this work shows that, at least at very low temperatures, the field of existence of monoclinic phase is extended beyond 7 mol%YO1.5, and this phenomenon must be taken into consideration for the materials used in gas turbines.

APS TBC from a new component has been used to determine the phase evolution in a short time and to determine an empirical law that could determine the operating temperature of the component. To obtain the information necessary to determine the kinetic evolution of the phases, the samples have been exposed up to 1400h at 1100°C, 1000h at 1200°C and up to 400-500h at high temperature (1300-1400°C). The obtained results confirmed the transformation of the phases described by Witz et al.[22] and allowed to identify t' phase as the one useful for determining the phase evolution kinetic law. In fact, this is the only phase that has a constant trend at all the tested temperatures.

Therefore, by evaluating the amount of t’ phase in a TBC sample from an operated component and knowing the operating time (firing hours), the external temperature of the part can be estimated.

The samples used to study the thermodynamic evolution, with annealing times up to 10000h, have been obtained from two different batches, deposited on superalloy plates with the standard APS method. According to our tests the two different supplies show comparable results, and the same evolution of the phases as a function of the exposure temperature. Further discussion about these results are reported in the following chapters.

4.5.2 Phase evolution after exposure at high temperature

All the data examined in this chapter give information on the variation of the t, t' c and m phases after exposure to high temperature. A common trend to all the tests can be described.

The metastable **tetragonal prime phase** decreases with increasing exposure time of the sprayed material. In the powders, the effect is evident even after 100h of exposure to the highest temperatures. In this case, however, it seems that the effect is not particularly evident at 1100°C.

The **tetragonal phase** has a more complicated course. In fact, in the case of massive samples, it tends to grow linearly at low temperatures, but its quantity has a trend with maximum at the highest temperatures. In fact, after an initial increase, the phase tends to dissolve after a few hundred hours of exposure. This phenomenon is evidently observed also in the case of powders exposed at 1400°C. The largest amount of this phase appears after 100h exposure, and then it decreases with time. On the other hand, the exposed powders also show an increase of t at 1200°C, while as in the case of the t’ phase, 1100°C seems to be a too low temperature to allow evident transformations of TBC phases to take place. The distinction of the two tetragonal phases was not carried out in the long-time exposure tests, but this question will be addressed in detail in the next chapter.

The **cubic phase** described in the massive tests and in the powders up to 1000h (paragraphs 4.1 and 4.3) has the constant tendency to increase at all exposure temperatures.

The two tests agree in showing larger growth at the highest temperatures (1300 and 1400°C) where the increase is evident already after the first 100h of exposure. The phase increase at 1200°C is limited but constant within the first thousand hours of exposure, while at 1100°C only the longest test shows a significant increase in its quantity. Tests carried out at much longer times to study the equilibrium state of the phases (paragraph 4.4), confirm the tendency of the c phase to increase at low temperature, while at high temperature it tends to decrease, despite the difference in the used material compared to the kinetic tests and therefore a different initial composition of the phases. This happens only because the tetragonal phases are not stable in these samples and therefore the growth of the monoclinic phase must occur at the expense of the cubic phase. The long-term results show that the growth of the cubic phase at 1200°C stops around 3000h, when it became the main phase of the samples. By increasing the exposure, time the quantity remains constant in both batches of examined samples. Finally, the results show that at 1100°C the formation of the cubic phase occurs only after long exposure times, it is in fact present in a small quantity (above 10%) only after 10000h of exposure.

As described in the paragraph 2.5, the **monoclinic phase** tends to form in larger quantity when the thermal barrier is exposed at high temperatures. In any case, according to our observations its formation occurs also at low temperatures, even if longer exposure times are required. In the powder samples tested, the phase clearly grows only at 1300 and 1400 °C, even if at least 300h exposure are required to observe a significant increase. This behavior distinguishes the monoclinic phase from the cubic one, which instead increased significantly even after shorter exposures at those temperatures. At lower temperatures, the effect is not clearly observed. This effect is confirmed by the results obtained on the massive samples at short times, in which a significant increase of the phase is underlined only at 1400°C, and, less markedly, at 1300°C.

In the samples exposed for long times, the phase tends to form at 1100°C after about 1000h and, after a slight initial decrease, it tends to increase linearly between 5000 and 10000h. The linear increase is also observed in samples exposed at 1200°C. The phase begins to be quantitatively considerable (less than 10%) around 1000h exposure and tends to grow steadily with the exposure time up to about 40-45% after 10000h. The increase of the phase is also observed at 1300°C, where the difference between 300 and 1000h is about 10%, while it tends to remain constant at 1400°C, having already reached the equilibrium after 300h.

From these results, we can suppose a kind of relationship between annealing temperatures and amount of monoclinic phase. In particular, after 10000h exposure at 1100°C the quantity of phase formed is comparable to the one obtained after 1000h at 1200°C. In turn, the quantity of monoclinic observed after 10000h at 1200°C is similar to that obtained after 1000h at 1300°C. This is the maximum quantity that can be reached by the system and it is comparable to that obtained after 300h at 1400°C.

All the results of the evolution of the phases will be discussed in the following chapters. An in-depth analysis of the results obtained in the long term will be developed, also in relation to the data obtained from the TBC-CMAS interaction, in chapter 5, and with respect to thermodynamic assessment, in chapter 6.

4.5.3 *Evaluation of temperature through crystallographic structures*

As described in section 4.3, the tetragonal prime phase can be used to define the service temperature of the material in the gas turbine. This was applied to real components, which had worked at a low temperature, below 1000°C [91].

However, the long-time results reported in section 4.4 show a tendency of the tetragonal phases to dissolve in favor of the cubic and monoclinic structures. The tetragonal prime phase is stable up to 10000h only at 1100°C, while it is no longer present at higher temperatures.

The fact that the t’ phase is the predominant species in low temperature samples, even after long exposure times, allows to validate the method of determining the temperature through the quantification of this phase. However, the method is no longer applicable at T≥1200°C.

At the highest temperatures (1300-1400°C), the stable phases are only cubic and monoclinic. Although the tests were carried out only up to 1000h, the results collected seem to show that, already in a short time, the material is at thermodynamic equilibrium with a comparable composition between the two structures.

However, the results show that these temperatures are too high for the use of 7YSZ, as the degradation of the material, observable with a very high increase in the monoclinic phase, occurs already after 500-1000h. For this reason, it is not necessary to have a tool to estimate the operating temperature over 1200°C.

The data collected shows, instead, that the 1200°C is the upper limit of temperature in which the material can be used. However, at this temperature, the tetragonal phases quickly evolve and are not more stable after long exposure time (beyond 5000h).

Since a gas turbine can operate up to 20000-25000h, and that this temperature can be reached, a modification of the law of determination of the operating temperature, even qualitative, must be made.

Indeed, as will be reported in the next chapters in more detail, at 1200°C the monoclinic phase increases linearly with the temperature in quantities around 20% after 3000h, 30% after 5000 and after 10000 over 40%.

Therefore, the identification of the absence of the tetragonal prime phase and the quantification of the amount of the monoclinic phase can extend the tool applicability to 1200°C, the maximum temperature for 7YSZ.

5 Experimental results: CMAS corrosion tests

In this chapter the TBC phase stability and evolution after CMAS corrosion at high temperature for long aging time has been studied. To better evaluate the effect of interaction between CMAS and TBC the same specimens have been exposed without CMAS .

The samples have been exposed at different temperatures between 1100 and 1400 °C for different exposure times (from 300 to 10000 h). The TBC material and CMAS composition used have been reported in chapter 3.1.2. After treatment, samples have been characterized by X-ray diffraction with Rietveld refinement in order to identify and quantify the phases present: matrix phases (e.g. tetragonal and cubic zirconia) as well as the harmful monoclinic zirconia and secondary phases formed by the interaction with CMAS.

In the presentation of the results the difference between the tetragonal structures has not been considered: a unique t^+ phase has been indicated, defined as the sum of t and t'. The difference between the two phases has been argued in the final discussion.

Furthermore, the samples were studied by optical and electron microscopy to evaluate the microstructural modification of the materials due to the high temperature exposure and the possible presence of CMAS. The secondary phases formed by the TBC-CMAS interaction have been studied by EDS in order to determine their chemical composition.

Moreover, the exposed samples have been analyzed by thermography to evaluate the change in physical properties due to the presence of a deposit on the surface of the thermal barrier. This technique was new for the Ansaldo Energia laboratory and it has been validated by comparing results with those obtained in another laboratory with similar instrumentation (CNR of Padova).

At the end of the chapter, obtained results are discussed in comparison with selected literature data on similar materials which underwent similar exposure conditions.

In the recent years, some work has been done about the TBC corrosion by CMAS: some of these did not use XRD analysis [47], while, in other works, X-Ray diffraction for phase identification after CMAS corrosion was used. Most of these works use a standard CMAS composition (43Si-30Ca-21Al-6Mg wt%), similar to that used in this thesis, except in some cases where the silica composition was much lower [92,93] or in [30] where the TBC used was not YSZ. In other cases, e.g. in the work of Pujol et al [94], the investigation was carried out not on sprayed samples, but on TBC powders mixed with CMAS. In other papers, the TBC-CMAS interaction has been studied by XRD analysis [48–54]. In these works, the interaction occurred at high temperature for short exposure times which only in a few cases reached 24-72 hours [48,50], while in most cases were between 2 and 8 hours.

In this thesis specimens exposed up to 10000h have been analyzed, which makes difficult the comparison with the other works found in literature.

In some papers the phase evolution of TBC without CMAS has been studied by X-Ray diffraction (XRD) [95,96]. In particular YSZ (6-8 wt%) has been investigated after long exposure times at different temperatures [22,97–101]. In this case a comparison with our results is possible.

In the work of Ballard at al [97] samples of 8YSZ were tested at three different temperatures (982-1204 and 1315°C) for different times (100-500-1000-5000-10000 hours). The specimens have been analyzed by XRD and the phases have been identified.

Di Girolamo et al [100] tested 8YSZ, by XRD analysis, after exposure at 1315°C for short times (2, 10 and 50 hours), while Witz et al [22] measured samples exposed at four temperatures (1100, 1200, 1300 and 1400°C) for different aging times. At 1100°C, samples after different aging times (1, 24, 100, 250, 450, 650, 850 and 1400 hours) have been studied, but at higher temperature the aging times were smaller: 1, 10 and 1000 hours at 1200°C, 1, 10, 100 and 1000 hours at 1300°C and, finally, 1 and 10 hours at 1400°C.

Lipkin et al [101] analyzed some samples at six different temperatures (between 982 and 1482 °C) and exposure times between 1.5 and 6980 hours. They used HJP parameter (defined as HJP=T[C+ln t], where C is a constant, T is temperature and t is time), to plot the results. Finally Cernuschi et al.[98] tested samples at 1100, 1200 and 1250°C and compared their own results to the results of other authors [22,100,101] using the HJP parameter.

The literature data about samples exposed for a long time are compared to our results in the final discussion of the chapter.

5.1 X-Ray diffraction results

5.1.1 Preliminary analysis of starting materials

The as delivered materials have been analyzed by XRD to determine which phases are present and their amount. The results are reported in

Table 16 with agreement factors obtained by Rietveld method. The single layer samples are formed by only one phase: t’ for 7YSZ and c for 14YSZ. Only for 7YSZ batch B a small amount of m phase has been detected; its presence may be due to the worse interdiffusion of yttrium during the spraying process. Both DL samples are formed by a mixture of c and t’ phases with a larger quantity of c phase because the 14YSZ layer is thicker than the 7YSZ one, as for Ansaldo specification.

Table 16 – Rietveld quantifications of samples as delivery

	Phases			Agreement factors	
Material	t’	c	m	R_{wp}	X^2
7A	100				
7B	97.5		2.5	6.9	2.5
DLA	33.5	66.5		8.3	4.3
DLB	33.5	66.5		8.0	3.9
14A		100			
14B		100			

Preliminary analysis on CMAS mixtures have been performed to evaluate their evolution at high temperature. In

Table 17 the melting points of the mixtures have been reported. These values have been obtain by DSC analysis of CMAS powders (Figure 87) [55]

Table 17 – Fusion point of CMAS mixture

CMAS	Onset melting T (°C)	Finish melting T (°C)
STD	1360.5	1303.1
ANS	1262.3	1213.9

CMAS powders after exposure at 1100°C and 1200°C inside an alumina crucible have been analyzed by XRD.

XRD patterns of STD and ANS CMAS powders exposed at 1100°C for 1000 h are compared in Figure 88. In both samples, some unreacted oxides are observable, such as corundum (Al_2O_3) and the two polymorphic forms of SiO_2 (quartz and cristobalite). In addition, mixed oxides are observed such as wollastonite ($CaSiO_3$) and a compound of the akermanite family (mixed silicate formed mainly by calcium and magnesium). The only difference between the two powders is the presence-of not reacted iron oxide in ANS CMAS

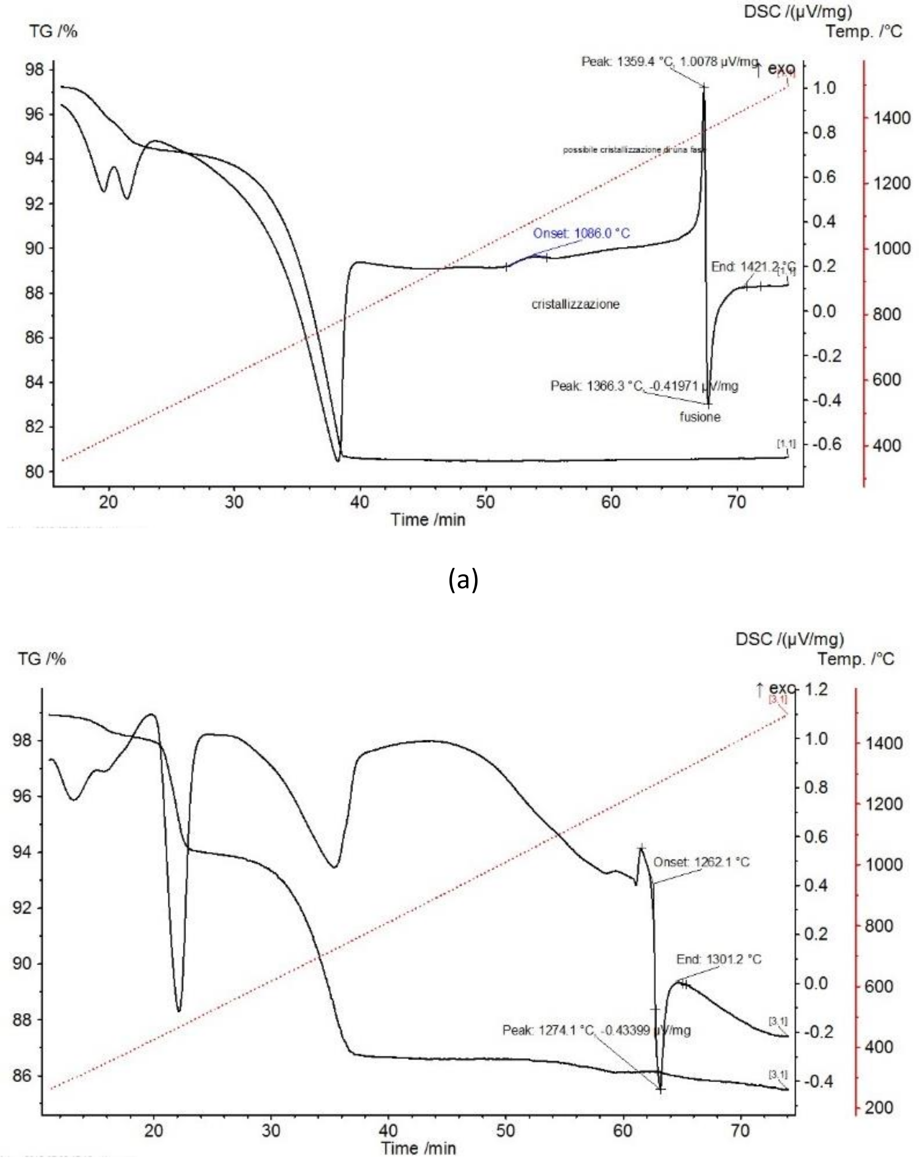

(a)

(b)

Figure 87 –DCS analysis by powders of STD (a) and ANS (b) CMAS

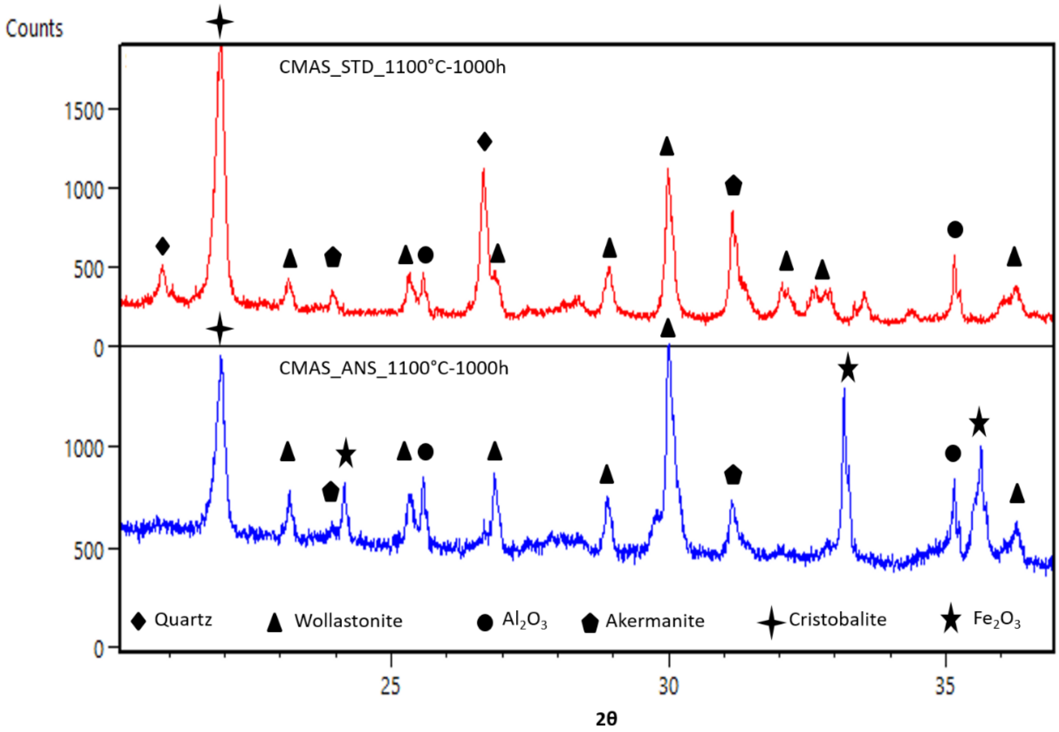

Figure 88 – Comparison between X-Ray patterns of CMAS STD and ANS at 1100°C for 1000 hours

A comparison between XRD patterns obtained at 1100°C and 1200°C are reported in Figure 89-a and Figure 89-b for STD and ANS CMAS, respectively. In Figure 89-a, referring to STD CMAS, the evolution of $CaSiO_3$ may be observed, as well as the presence of pseudowollastonite, the high temperature structure of wollastonite, at 1200°C. Indeed the transformation from wollastonite to pseudowollastonite should occur around 1130°C, as reported by Hillert et al [102].

The situation is drastically different for ANS CMAS (Figure 89-b). In this case at high temperature the original oxides are not observed, but all of them reacted to form a mixed silicate of the diopside family rich in calcium and iron. This result suggests that the ANS mixture is much more reactive than the STD one, already at lower temperature.

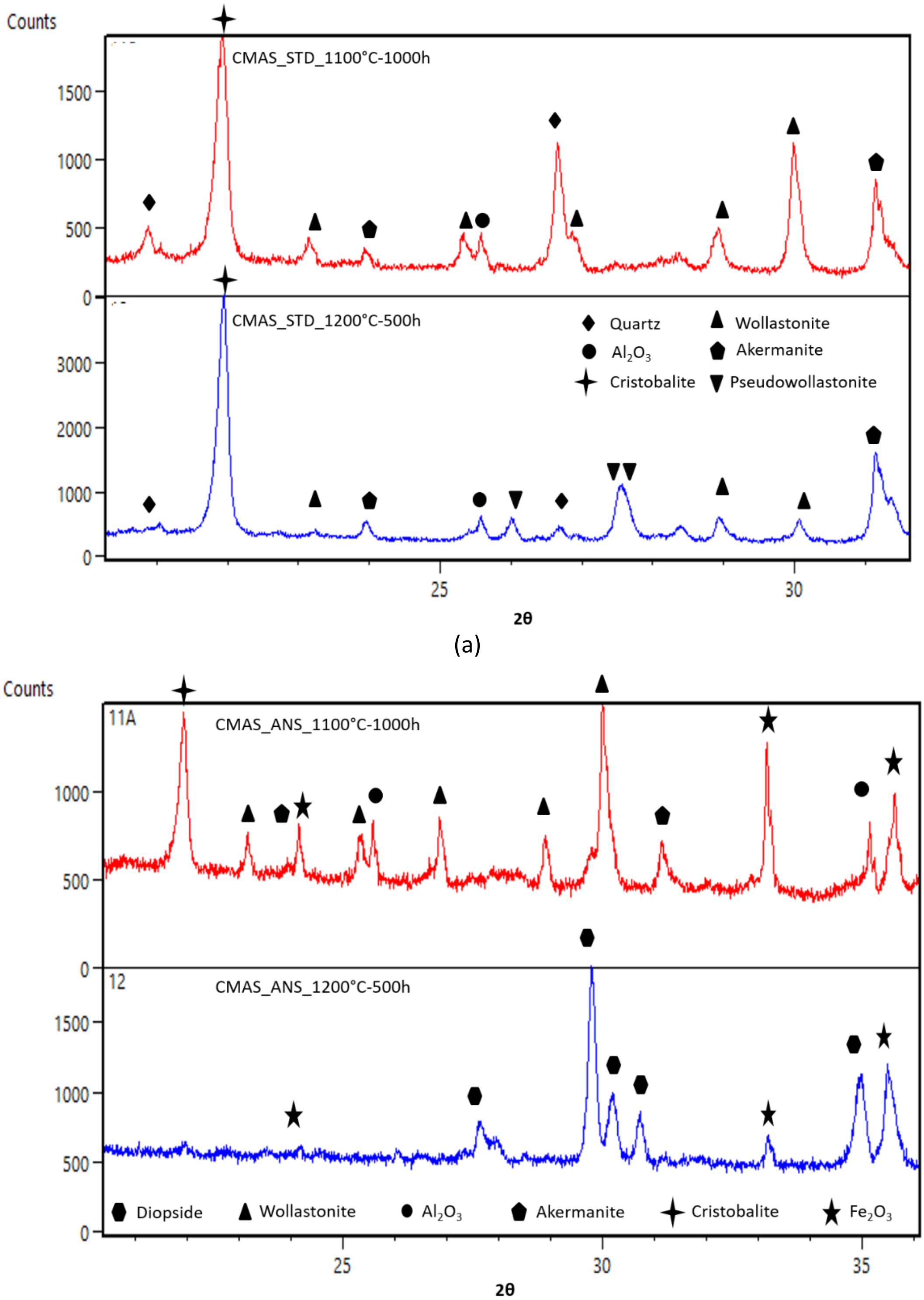

(a)

(b)

Figure 89 - Comparison between X-Ray patterns of CMAS STD (a) and ANS (b)at 1100°C for 1000 hours and 1200°C for 500 hours

The XRD diffractograms were obtained from milled TBC powders because the aim of the work is to evaluate the microstructural evolution of thermal barrier coating under the effect of time, temperature and CMAS. In fact, the XRD patterns obtained from sample surfaces are affected by larger errors and phase analysis by Rietveld method is more difficult, as shown in Figure 90 where diffractograms of external surface and powders are compared for a 7YSZ sample.

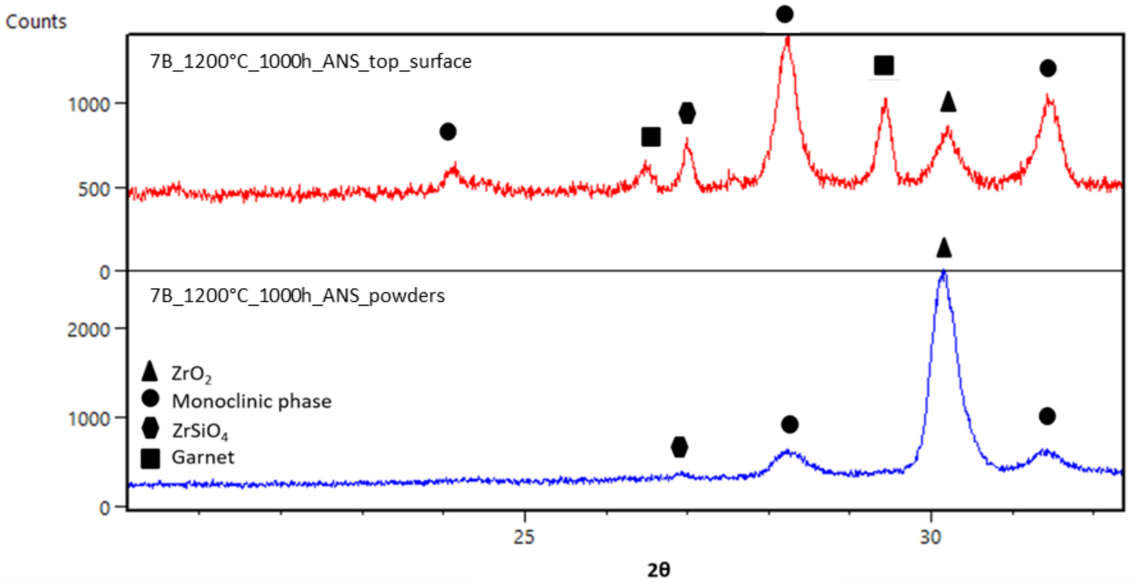

Figure 90 – XRD patters of a sample on external surface and on powders for a 7YSZ sample

5.1.2 Analysis of heat treated materials: 7YSZ

5.1.2.1 Results after treatment at 1100°C

At 1100°C, two different batches, 7A and 7B, have been exposed and the phase quantifications are reported in Figure 91. In all conditions, the phases observed are tetragonal, t^+, (always more than 80 percent) and monoclinic, m, which increases with exposition time. After 5000 h some secondary phases have been detected, $Ca_3Y_2Si_6O_{18}$ (CYSO in this work) and SiO_2, but only the first one is formed by interaction between TBC and CMAS, while SiO_2 is probably a contaminant of the alumina sample holder transferred by contact to the specimen. After 10000 h no secondary phase are present, but the cubic phase begins to form from tetragonal phase. For batches A and B the amounts of detected phases do not differ by more than 5% after interaction with both the CMAS mixtures for all the considered aging times.

The evolution of the TBC constitution is mainly related to the formation of the monoclinic phase. This behavior seems to be accelerated by the presence of CMAS for both compositions, as shows in Figure 92.

The monoclinic phase tends to increase with time up to a maximum at about 3000 h, then it decreases at 5000 h and, finally goes up again after 10000 h. This behavior is common to all samples, but it is more evident in the case of samples 7B_STD and 7B_NC.

The 7A_NC samples show the same behavior even if the amount of m phases is always lower respect to batch B. In the starting condition (without exposure), the m phase was observed only in batch B: this behavior could be related to different spraying conditions.

A summary of all phase amounts determined by XRD analysis and completed by agreement factors resulting from the Rietveld refinements are reported in

Table 18.

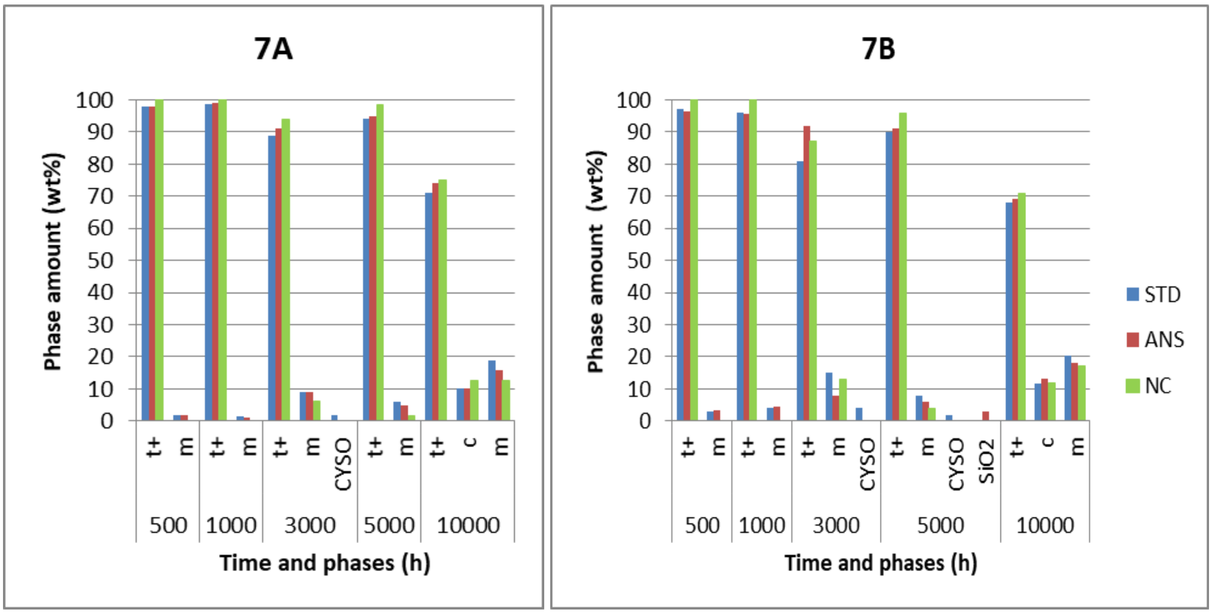

(a) (b)

Figure 91 - Constitution of 7YSZ samples exposed at 1100°C with STD CMAS, ANS CMAS and without CMAS (NC). Batch A (a) and B (b)

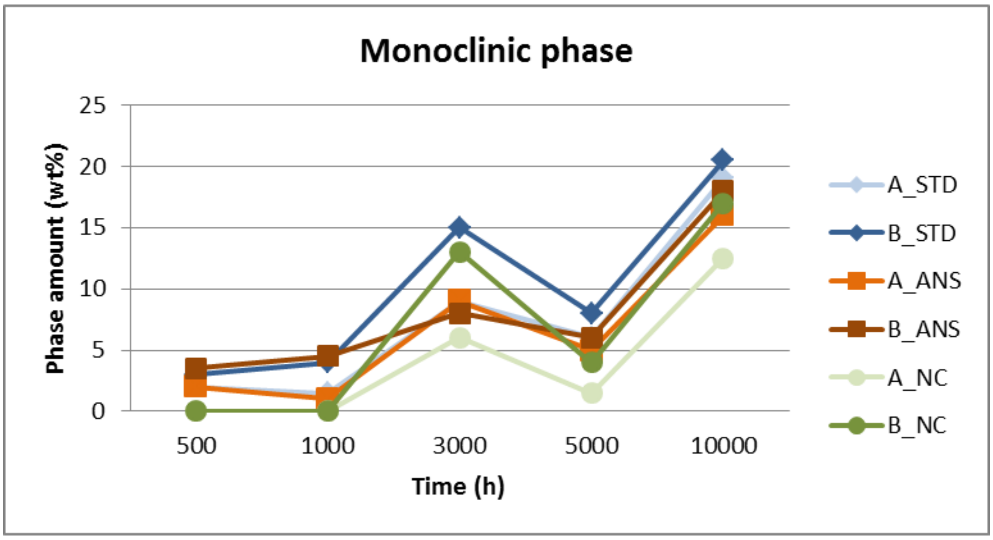

Figure 92 – Amount of monoclinic phase as a function of the exposure time at 1100°C for all the investigated samples

Table 18 – XRD phase analysis and Rietveld agreement factors for samples 7 tested at 1100°C

	Time (h)	**Phases (wt%)**					**Agreement factors**	
Material		t+	c	m	CYSO	SiO_2	R_{wp}	X^2
7A_STD	500	98		2			11.9	3
	1000	98.5		1.5			8.5	2.5
	3000	89		9	2		14.4	2.9
	5000	94		6			5.9	2.1
	10000	71	10	19			5.1	1.6
7A_ANS	500	98		2			11.9	3.0
	1000	99		1			8.5	2.5
	3000	91		9			14.4	2.9
	5000	95		5			5.9	2.1
	10000	74	10	16			5.2	1.6
7A_NC	500	100						
	1000	100						
	3000	94		6			5.9	6.6
	5000	98.5		1.5			2.2	2.8
	10000	75	12.5	12.5			5.0	1.7
7B_STD	500	97		3			8.1	2.3
	1000	96		4			10.2	3.7
	3000	81		15	4		8.6	2.0
	5000	90		8	2		5.7	2.0
	10000	68	11.5	20.5			5.3	1.6
7B_ANS	500	96.5		3.5			12.0	4.0
	1000	95.5		4.5			12.8	5.3
	3000	92		8			11.1	3.5
	5000	91		6		3	5.8	2.2
	10000	69	13	18			4.8	1.6
7B_NC	500	100						

	1000	100						
	3000	87		13			5.8	2.3
	5000	96		4			5.5	2.0
	10000	71	12	17			4.8	1.5

5.1.2.2 Results after treatment at 1200°C

As for 1100°C, the samples exposed at 1200°C have been analyzed after four different aging times (Figure 93). The results are shown in Figure 94 and Figure 95, where the comparison between the two batches after corrosion by STD and ANS CMAS is reported. In the case of samples subject to STD CMAS (Figure 94), the difference between phase amounts in the two batches is less than 10% and it increases after long exposure times (3000 and 5000 h). The batch B seems to be more susceptible than batch A to the formation of monoclinic phase at the expenses of the cubic phase. The corrosion by ANS CMAS seems to create more differences between batches, as shown in Figure 95. The largest difference in phase constitution occurs at short exposure times (500 and 1000 h). The corrosion seems to favor the formation of cubic phase in batch B already after 500 h, while at 1000 h it is more than double of batch A. Instead, at 3000 and 5000 h, phase amounts become similar with differences lower than 5%.

The samples after 10000 h have the same phase composition independently to the type of tested CMAS.

In addition to the main phases, m, t+ and c, a few secondary phases resulting from the interaction with CMAS have been identified. They are $Ca_3Y_2Si_6O_{18}$ (CYSO), Garnet and Zircon ($ZrSiO_4$), silicates formed by elements from TBC (Yttrium and Zirconium) and from CMAS (especially Iron and Calcium). In all samples, the amount of secondary phases is less than 10%, except for sample with STD CMAS after 5000h, where zircon is close to 15%. For both CMAS compositions, the interaction between CMAS and TBC at 1200°C is stronger than at 1100°C.

An example of phase identification on samples exposed with and without CMAS is reported in Figure 96. The peaks of CYSO are observed in the sample tested with STD-CMAS, while peaks of Garnet are found in the sample with ANS-CMAS. No secondary phases have been detected in sample exposed without CMAS.

For both batches, a greater amount of monoclinic phase has been observed in the samples with ANS-CMAS at all the analyzed aging times. On the other hand, the samples exposed without CMAS already show the presence of monoclinic phase after 500 h, while the cubic phase appears only after 1000 h of exposure.

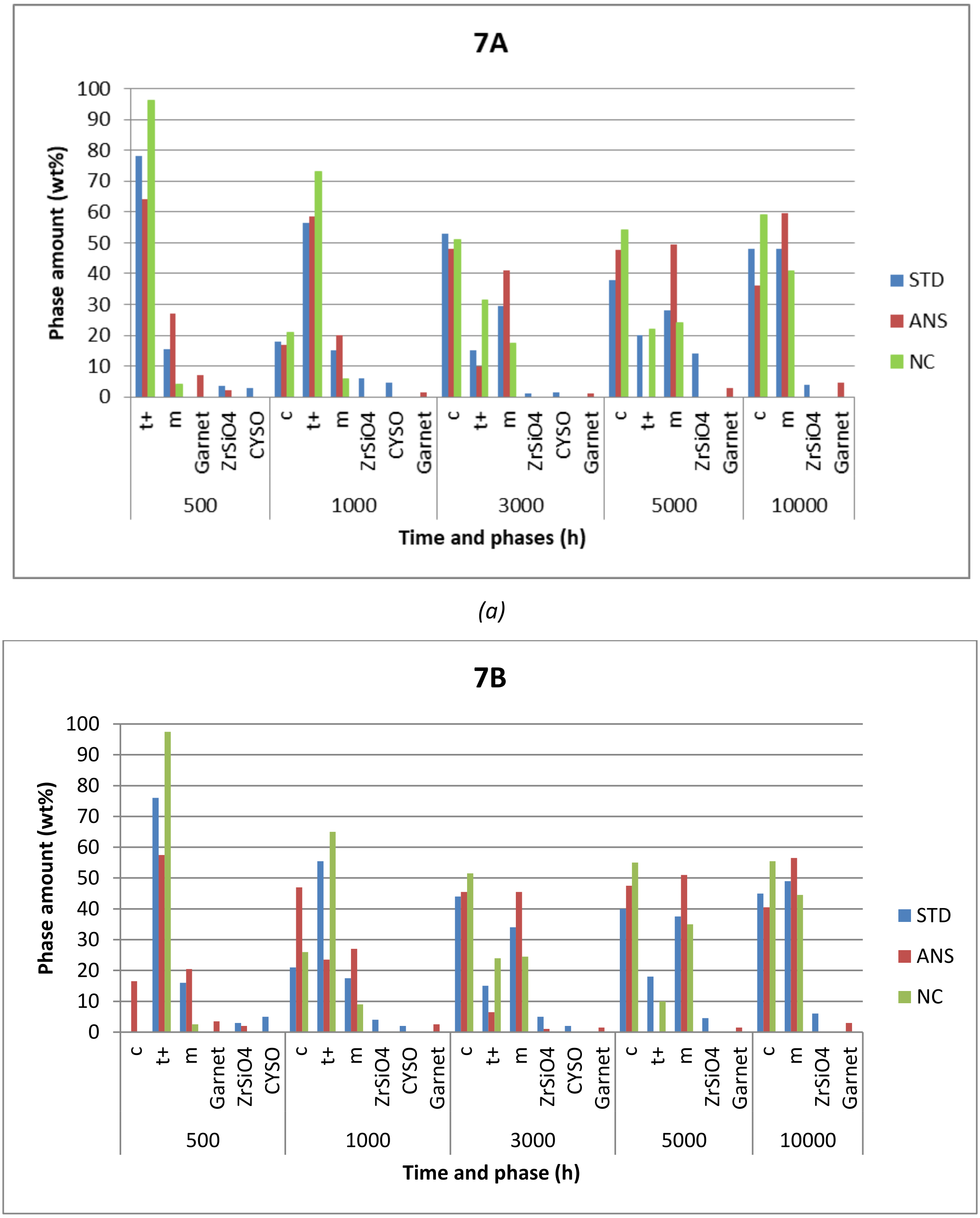

(a)

(b)

Figure 93 – Results at 1200 for 7A (a) and 7B (b)

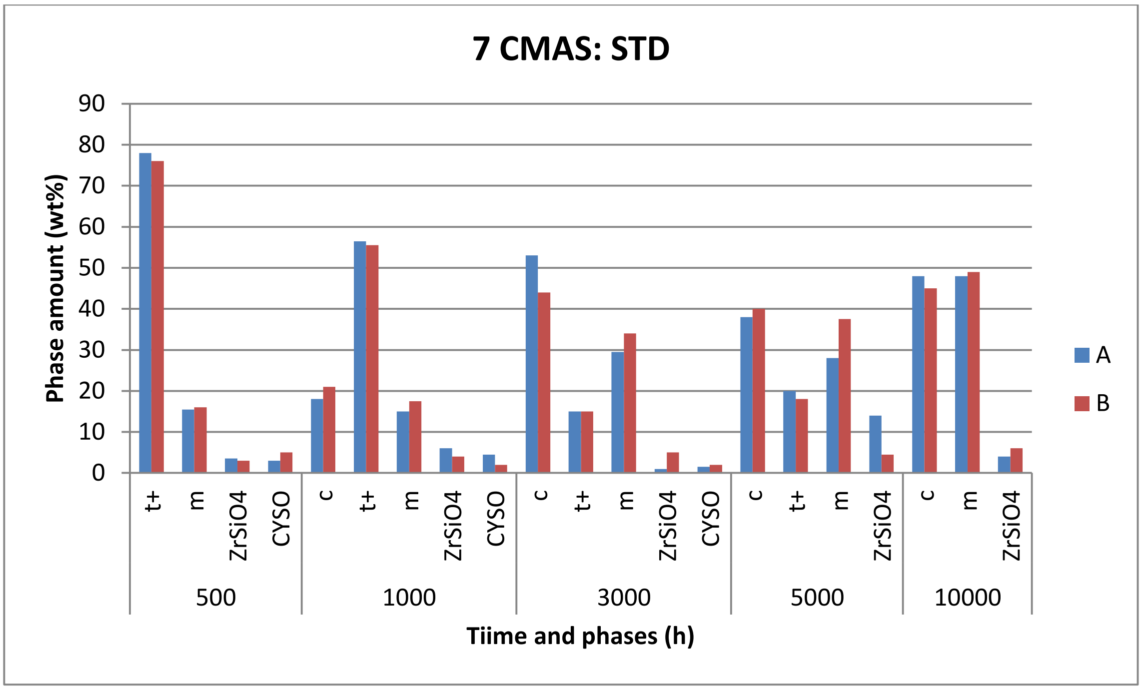

Figure 94 – Phase analysis of samples 7A and 7B with STD CMAS after 500, 1000, 3000 and 5000 h exposure at 1200°C

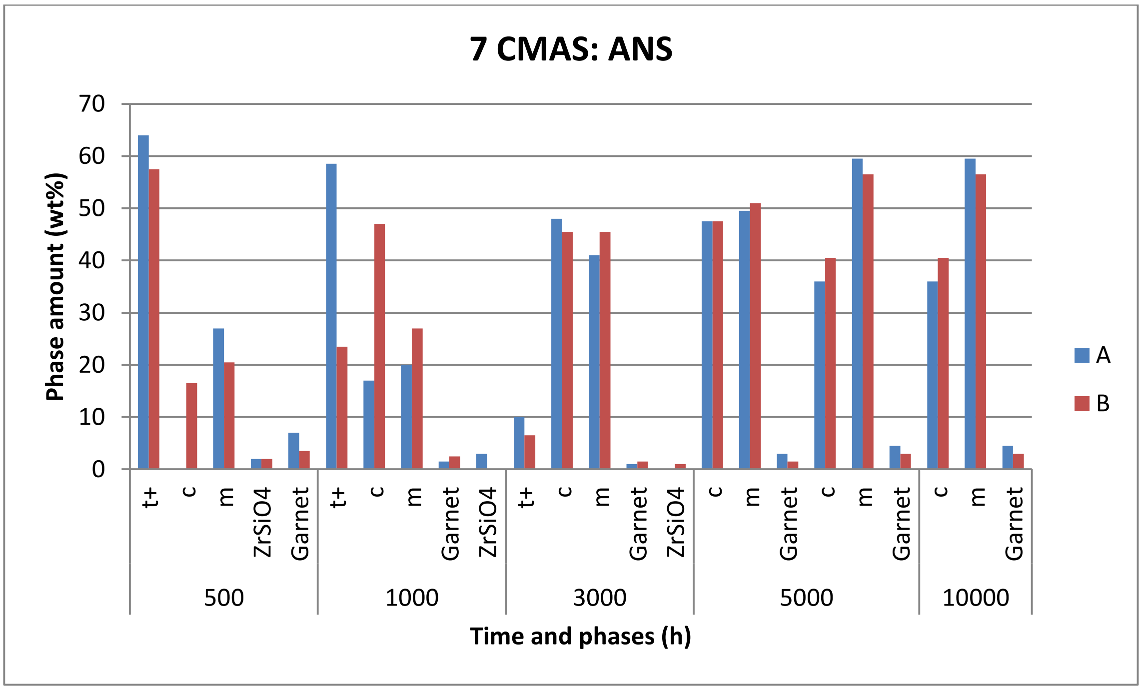

Figure 95 - Phase analysis of samples 7A and 7B with ANS CMAS after 500, 1000, 3000 and 5000 h exposure at 1200°C

The amount of monoclinic phase in 7YSZ samples exposed at 1200°C is reported in Figure 97 as a function of the exposure time. Unlike samples exposed at 1100°C, the trend is linear for all samples and the effect of CMAS corrosion is evident: all samples with CMAS show more monoclinic phase than samples without CMAS.

In particular, the ANS CMAS forms a greater amount of monoclinic phase in any condition (both batches). The STD CMAS, compared with samples without CMAS, seems to have a greater effect for short times (500 and 1000h) with about 15% of monoclinic phase against the 3-4% in samples without CMAS. The difference decreases with time and at 5000 hours there are no significant differences.

At 10000 h, the amount of monoclinic phase present in the samples tested without CMAS is the same to sampled tested with STD CMAS, while sample tested with ANS CMAS show again a greater quantity of this phase.

In Figure 98 are reported the amount of tetragonal and cubic phases as a function of the exposure time at 1200°C. Tetragonal phase tends to decrease while the cubic phase increases. The inversion of the main phase in the samples occurs between 2000 and 3000 h. Samples exposed without CMAS tend to invert the matrix later, but always before 3000 h. The only exception is the sample of the 7A_ANS where the cubic phase already present at 5000 h: in this case, the phase inversion is observed before 1000 h. After 10000 h, the matrix is always cubic and the tetragonal phase is not stable. The cubic phase remains almost constant between 3000 and 10000 h. So, at long time of exposure, the monoclinic phase seems formed from tetragonal phase, while the cubic phase increases only for short aging time (before 3000 h).

The phase analysis results of all samples with agreement factors are summarized in Table 19.

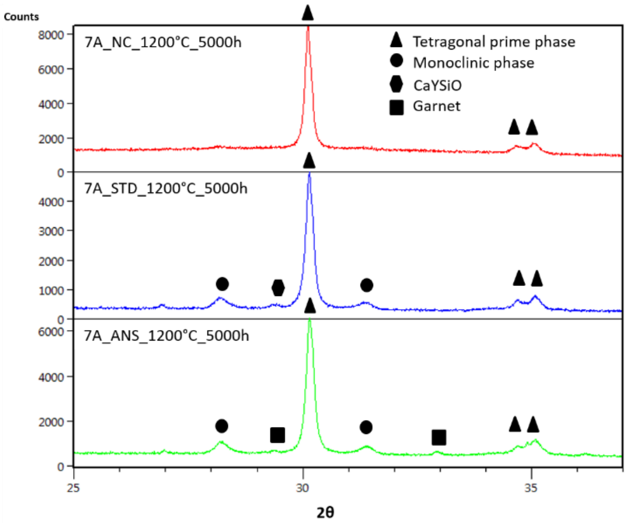

Figure 96 – X-Ray patterns of sample 7YSZ exposed for 500 h at 1200°C; with STD and ANS CMAS, and without CMAS

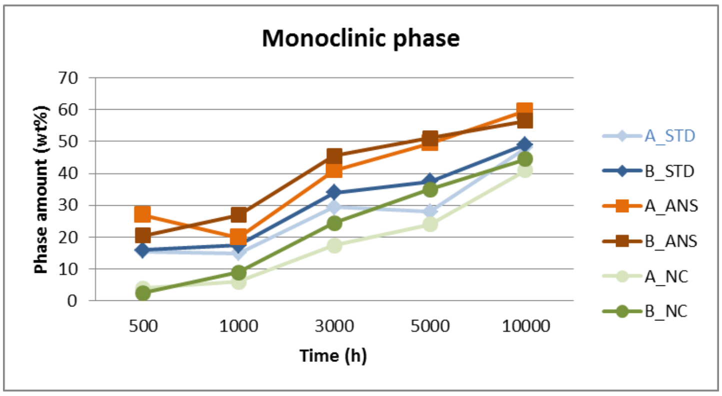

Figure 97 – Amount of monoclinic phase in all samples exposed at 1200°C as a function of the exposure time

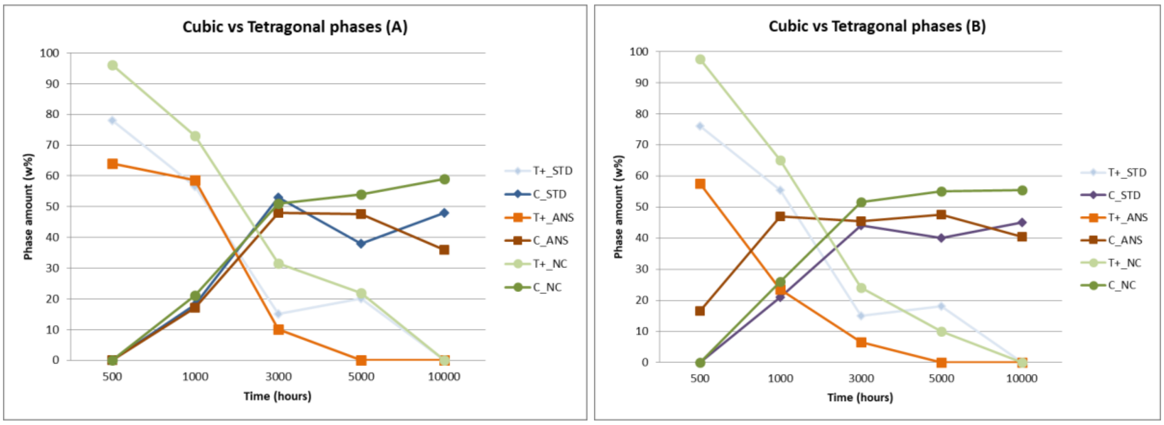

Figure 98 - Amount of cubic and tetragonal phases in all samples exposed at 1200°C as a function of the exposure time

Table 19 – Phase quantification and agreement factors on samples 7, tested at 1200°C

Material	Time (h)	Phases (wt%)						Agreement factors	
		c	t+	m	CYSO	Garnet	$ZrSiO_4$	R_{wp}	X^2
7A_STD	500		78	15.5	3			7.7	2.3
	1000	18	56.5	15	4.5			7.7	2.0
	3000	53	15	29.5	1.5			7.7	1.5
	5000	38	20	28				4.6	1.4
	10000	48		48			4	4.9	1.6
7A_ANS	500		64	27		7	2	9.2	2.7
	1000	17	58.5	20		1.5	3	8.3	3.0
	3000	48	10	41		1		4.8	1.6
	5000	47.5		49.5		3		5.6	2.0
	10000	36		59.5		4.5		5.0	1.7
7A_NC	500		96	4				6.5	2.6
	1000	21	73	6				5.8	2.0
	3000	51	31.5	17.5				4.7	1.4
	5000	54	22	24				4.5	1.4
	10000	59		41				4.7	1.3
7B_STD	500		76	16	5			10.4	2.5
	1000	21	55.5	17.5	2			6.9	1.6
	3000	44	15	34	2			8.1	1.3
	5000	40	18	37.5				5.6	2.0
	10000	45		49			6	4.8	1.7

Material	Time (h)	Phases (wt%)						Agreement factors	
		c	t+	m	CYSO	Garnet	$ZrSiO_4$	R_{wp}	X^2
7B_ANS	500	16.5	57.5	20.5		2	3.5	7.5	2.1
	1000	47	23.5	27		2.5		7.8	2.5
	3000	45.5	6.5	45.5		1.5	1	7.2	2.0
	5000	47.5		51		1.5		5.5	1.8
	10000	40.5		56.5		3		5.8	2.0
7B_NC	500		97.5	2.5				6.1	2.4
	1000	26	65	9				5.3	1.8
	3000	51.5	24	24.5				4.9	1.5
	5000	55	10	35				5.1	1.8
	10000	55.5		44.5				4.3	1.2

5.1.2.3 Results after treatment at 1300°C

The phase analysis results of the 7YSZ samples exposed at 1300°C are reported in Figure 99. At this temperatures only 300 and 1000h have been considered, as at 1400°C. Secondary phases identified at lower temperatures are not stable in this condition, with the exception of Zircon, that has melting point just below 1700°C [103]. The matrix is made by the cubic phase, in agreement with the ZrO_2-Y_2O_3 phase diagram. Indeed, at this temperature a little variation of composition of yttria in zirconia (as a difference between 7YSZ and 14YSZ) is not thermodynamically significant. This will be highlighted in the paragraph 5.1.3.At this temperature no relevant difference is observed in phase analysis of samples with and without CMAS. In both batches the monoclinic phase tends to increase with time, being already 20-30% after 300 h up to 35-45% at 1000 h.. This suggests that the TBC-CMAS interaction is not so relevant at this temperature and phase evolution is mainly due to kinetic and thermodynamic factors.

The phase analysis results of all samples with agreement factors are summarized in Table 20.

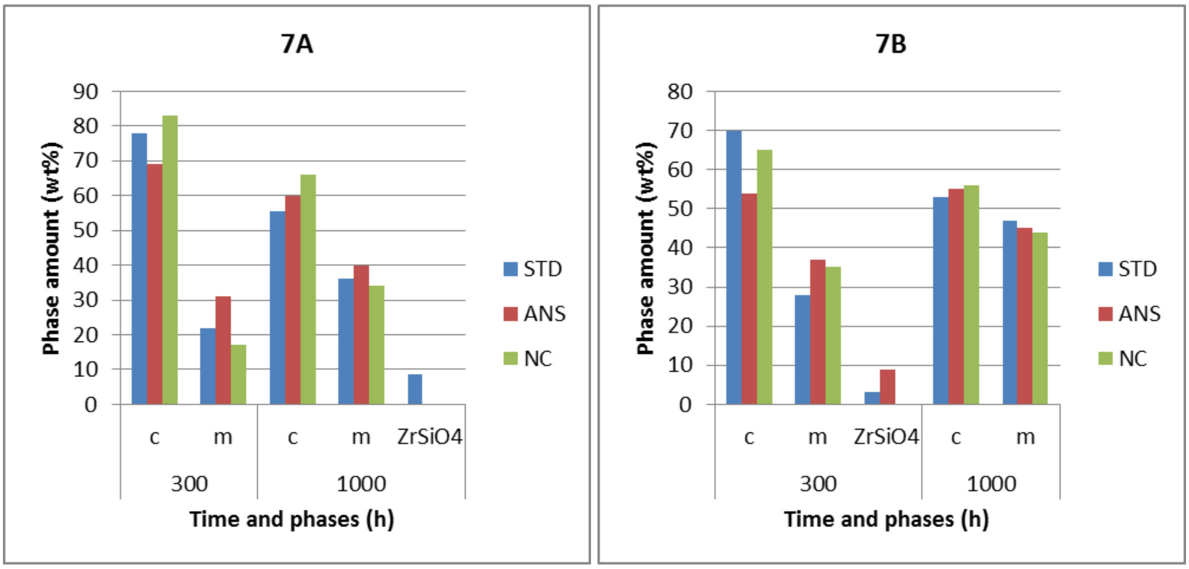

Figure 99 - Phase analysis of samples 7A and 7B after 300 and 1000 h exposure at 1300°C.

Table 20 – Phase quantification and agreement factors on samples 7, tested at 1300°C

Material	Time (h)	Phases (wt%)			Agreement factors	
		c	m	$ZrSiO_4$	R_{wp}	X^2
7A_STD	300	78	22		8.2	2.9
	1000	55.5	36	8.5	5.7	2.0
7A_ANS	300	69	31		6.1	1.9
	1000	60	40		4.5	1.4
7A_NC	300	83	17		6.9	2.9
	1000	66	34		5.0	1.6
7B_STD	300	70	28	3	7.2	2.5
	1000	53	47		9.1	3.0
7B_ANS	300	54	37	9	7.6	3.3
	1000	55	45		8.0	1.4
7B_NC	300	65	35		5.3	2.0
	1000	56	44		4.4	1.5

5.1.2.4 Results after treatment at 1400°C

Results obtained at 1400°C are similar to those obtained at 1300°C. In Figure 100 are reported phase amounts detected in batches A and B. At this temperature, there is no appreciable difference between analyses after 300 and 1000 h and there are no differences between samples tested with or without CMAS. The amount of monoclinic phase is almost equal to that of the cubic matrix. Presumably, at this high temperature the kinetic is fast enough to reach a thermodynamically stable situation in relatively short times. As an example, XRD patters of 7A sample (with and without CMAS) after 1000h are shown in Figure 101

The phase analysis results of all samples with agreement factors are summarized in Table 21.

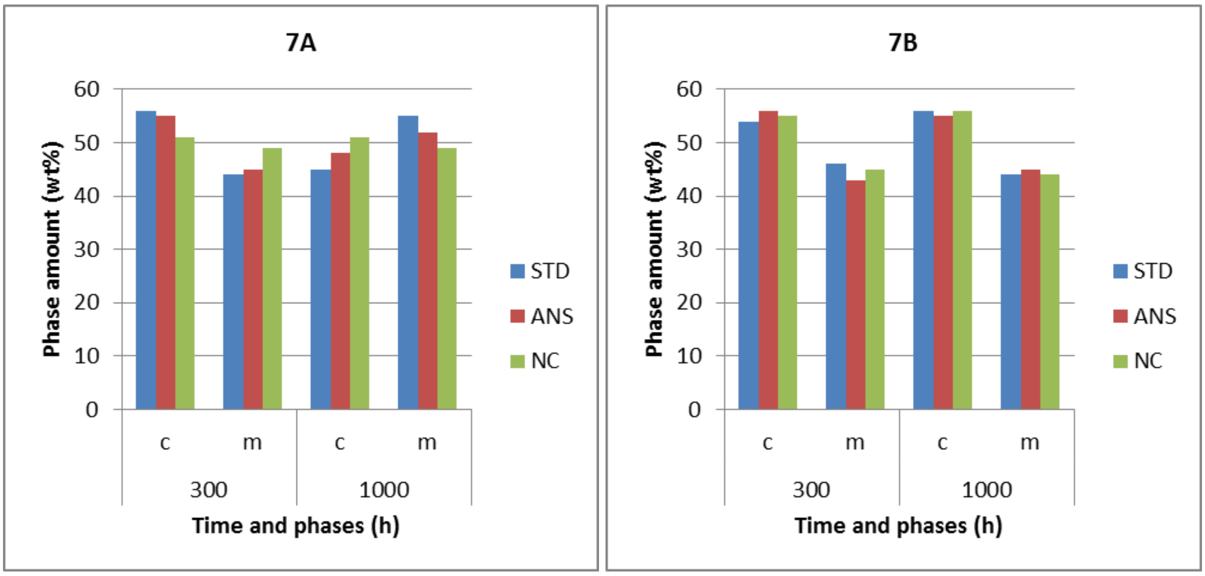

Figure 100 - Phase analysis of samples 7A and 7B after 300 and 1000 h exposure at 1400°C.

Table 21 – Phase quantification and agreement factors on samples 7, tested at 1400°C

	Time (h)	Phases (wt%)		Agreement factors	
Material		c	m	R_{wp}	X^2
7A_STD	300	55	45	7.7	2.7
	1000	45	55	7.7	3.4
7A_ANS	300	56	44	6.7	2.0
	1000	48	52	5.9	2.9
7A_NC	300	51	49	4.8	1.5
	1000	51	49	5.7	2.9
7B_STD	300	54	46	10.0	5.8
	1000	56	44	14.7	5.4
7B_ANS	300	56	43	6.1	1.7
	1000	55	45	9.1	2.7
7B_NC	300	55	45	5.7	2.0
	1000	56	44	6.0	2.4

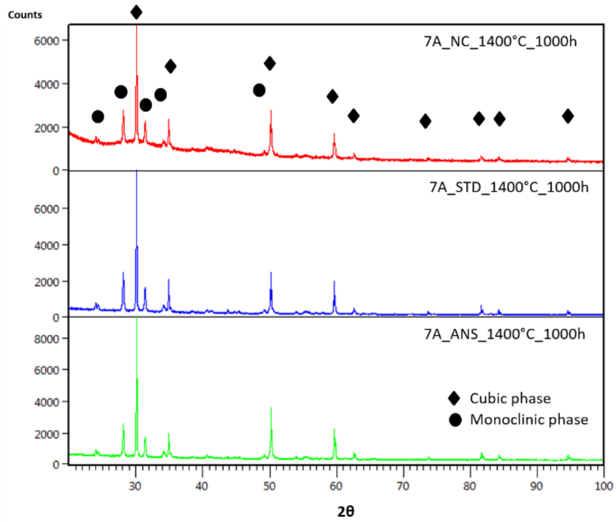

Figure 101 – XRD patterns of 7YSZ samples after 1000 at 1400°C without CMAS, with STD CMAS and with ANS CMAS

5.1.3 Analysis of heat treated materials: 14YSZ

5.1.3.1 Results after treatment at 1100°C

The 14YSZ samples have been studied at 1100°C in the same way as 7YSZ. However, due to limited quantity of material available, it was not possible to reach the longest aging times for both batches. In these samples the cubic phase is already stable in as delivered condition and it is observed also for all exposure times tested. No phase changes are observed after interaction with CMAS. A comparison between XRD patters of 7YSZ and 14YSZ exposed 5000 h at 1100°C is reported in Figure 102. In the 14YSZ samples, peaks of the monoclinic phase are not observed. Same situation is observed after 10000 h.

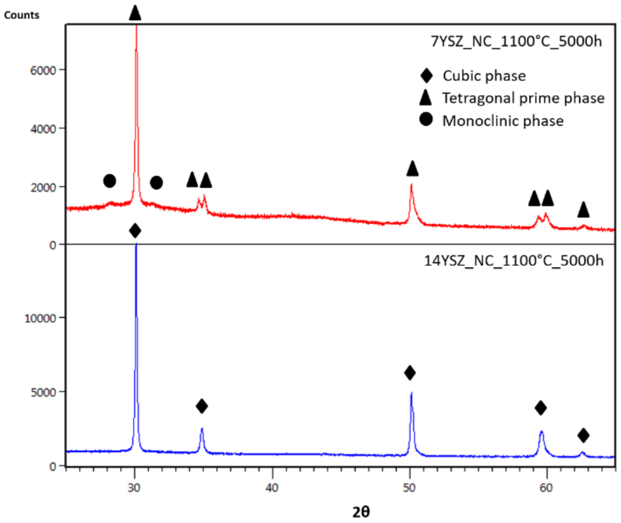

Figure 102 - Comparison between X-Ray patterns of samples 7YSZ and 14YSZ tested 5000 h at 1100°C

5.1.3.2 Results after treatment at 1200°C

At 1200°C, some interaction between 14YSZ and CMAS has been observed, as shown in Figure 103. In fact, garnet, zircon and $Ca_3Y_2Si_6O_{18}$ are identified even if their amounts are less than 10% in all analyzed samples. The matrix is formed by cubic phase, tetragonal phase is not stable and monoclinic phase appears already after 1000 h in samples with ANS CMAS and after 3000 h in sample with STD CMAS. Then in remains constant for longer exposure times. In sample exposed without CMAS, small quantity of monoclinic phase appears after 5000 h.

Therefore, ANS-CMAS seems to be more reactive than STD-CMAS. It seems to affec kinetic more than thermodynamic factors.

The phase analysis results of all samples with agreement factors are summarized in Table 22. Also at this temperature, due to limited quantity of material available, it was not possible to reach the longest aging times for all samples.

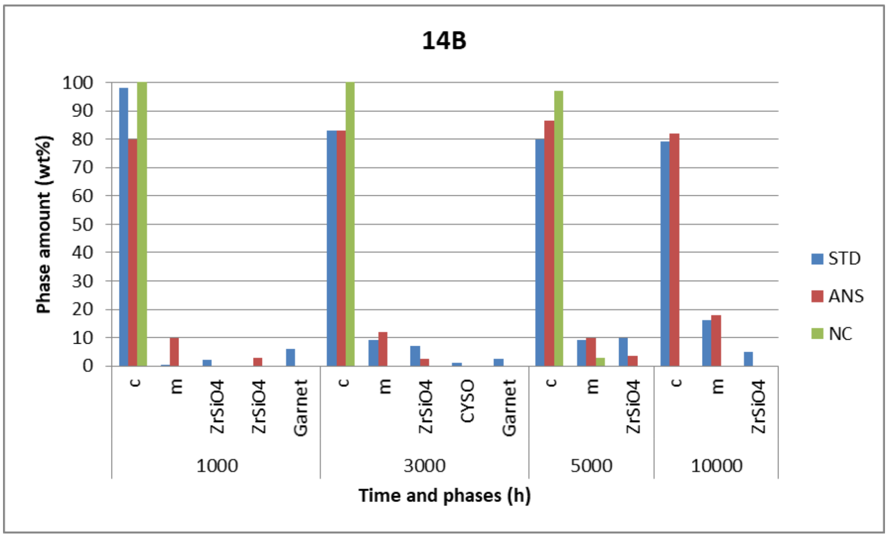

(a)

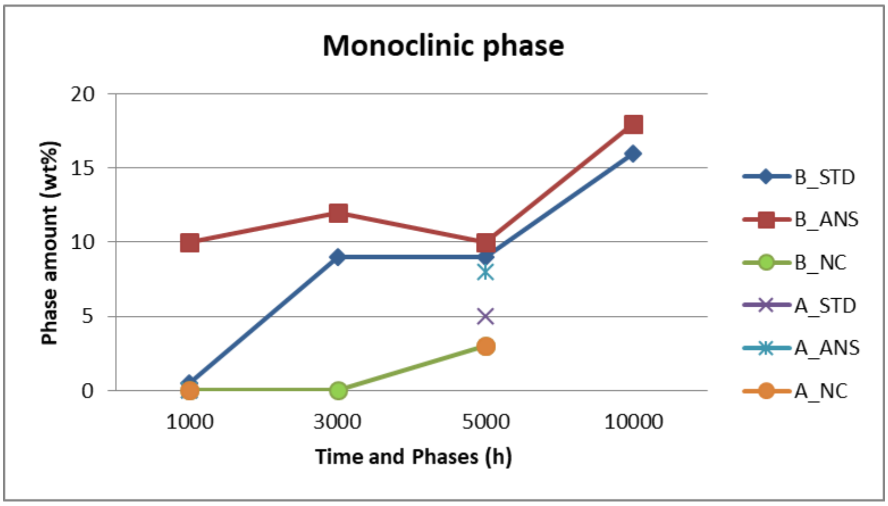

(b)

Figure 103 - Phase analysis of sample 14YSZB after exposure at 1400°C for several times (a), amount of monoclinic phase as a function of the exposure time for both batches (b)

Table 22 - Phase quantification and agreement factors on samples 14, tested at 1200°C

	Time (h)	Phases (wt%)					Agreement factors	
Material		c	m	CYSO	Garnet	$ZrSiO_4$	R_{wp}	X^2
14A_STD	1000	100						
	3000	///	///	///	///	///	///	///
	5000	87	6			5	6.1	2.0
14A_ANS	1000	100						
	3000	///	///	///	///	///	///	///
	5000	86	8			6	5.0	1.9
14A_NC	1000	100						
	3000	///	///	///	///	///	///	///
	5000	97	3				9.6	5.5
14B_STD	1000	98	0.5			2	16.7	11.2
	3000	83	9	1		7	12.4	5.9
	5000	80	9			10	8.4	4.3
	10000	79	16			5	7.7	3.8
14B_ANS	1000	80	10		6	3	13.8	5.6
	3000	83	12		2.5	2.5	11.9	6.2
	5000	86.5	10			3.5	5.4	1.9
	10000	82	18				6.1	2.5
14B_NC	1000	100						
	3000	100						
	5000	97	3				9.7	6.2
	10000	93.5	6.5				6.4	4.0

5.1.3.3 Results after treatment at 1300°C

The exposition at 1300°C of 14YSZ samples with and without CMAS does not bring to any phase transformation as they are 100% c phase. Some samples exposed with STD CMAS show a small amount of monoclinic phase at 300 h, which however is no observable at 1000 hours. This fact suggests that the presence of monoclinic phase after 300 h could be a quantification error, because the amount is inside of measurement error (1-3%).

The X-ray patterns of 7YSZ and 14YSZ sample (similar patterns for both batches) after 300 and 1000 h are reported in Figure 104 as an example.

The phase analysis results of all samples with agreement factors are summarized in Table 23. The missing samples are due to the limited quantity of material available.

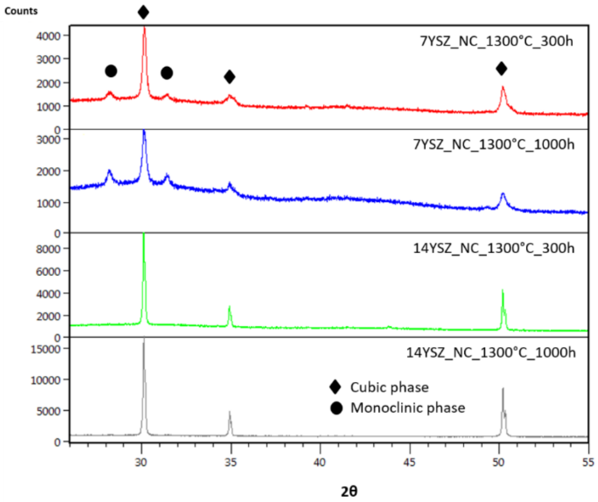

Figure 104 - XRD patterns of 7YSZ and 14YSZ after 300 and 1000 h exposure at 1300°C

Table 23 - Phase quantification and agreement factors on samples 14, tested at 1300°C

	Time (h)	Phases (wt%)			Agreement factors	
Material		c	m	$ZrSiO_4$	R_{wp}	X^2
14A_STD	300	97	1	2	19.1	18.2
	1000	92		8	9.4	2.6
14A_ANS	300	100				
	1000	95		5	10.3	3.0
14A_NC	300	100				
	1000	100				
14B_STD	300	95	3	2	9.7	3.8
	1000	///	///	///	///	///
14B_ANS	300	100				
	1000	///	///	///	///	///
14B_NC	300	100				
	1000	100				

5.1.3.4 Results after treatment at 1400°C

After exposure at 1400°C, the 14YSZ samples remain cubic in all condition tested. In particular no monoclinic phase is observed in samples, as can be seen in Figure 105.

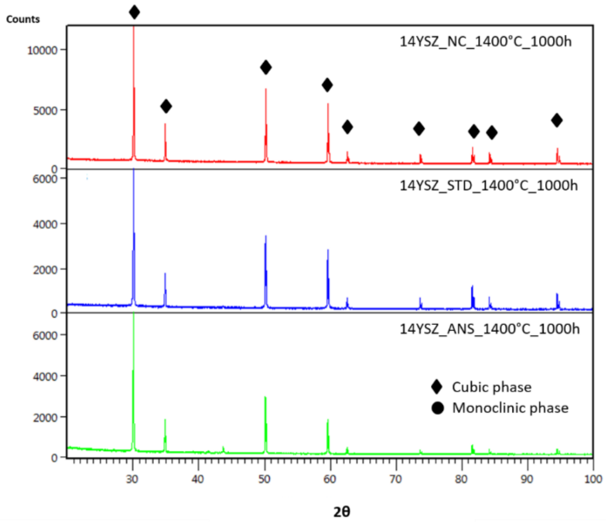

Figure 105 – XRD patters of 14YSZ sample after 1000 h at 1400°C

5.1.4 Analysis of heat treated materials: Double layer

5.1.4.1 Results after treatment at 1100°C

Phase analysis results of double layer (DL) samples exposed at 1100°C are reported in Figure 106 and Figure 107. Sample of both batches have been exposed with and without CMAS. In general the matrix of these samples is made by a mixture of c and t^+ phases, coming essentially from 14YSZ and 7YSZ layers respectively.

Small amounts of secondary phases have been identified only in batch A. The amount of these phases does not exceeds 5 w%, probably because the kinetics is inhibited by the low temperature. The presence of silica may be due to sample holder contamination, as already seen in the case of 7YSZ, but the amount of SiO_2 after 5000h (about 20 w% in DLA_STD and 10% in DLA_ANS) is very high.

The m phase is already present after 500 h, coming from the 7YSZ layer, and increases linearly with exposure time. The amount of this phase never reaches 10%.

In batch B secondary phases are not present and monoclinic phase appears only after 5000 h. The behavior of the monoclinic phase is evident observing the samples after 5000 h exposure: (without CMAS) trend of the samples of two batches to form at this temperature in batch A the amount of monoclinic phase is is about 5% either with or without CMAS, while in batch B it is observed (about 4%) only with presence of CMAS.

as for the m phase formation the different batches brings to slightly different results at this exposure temperature. In general, at 1100°C the presence of CMAS seems to accelerate the m phase formation but the final amount is probably the equilibrium one for the considered composition.

In Figure 108 the cubic and tetragonal phases as a function of time, for both batches are reported: the t^+ phase decreases while cubic phase increases, as already observed in samples 7YSZ. The inversion of main phase in the samples occurs between 2000 and 3000 h for all tested samples. This is due to the fact that the c phase is already present in as delivered conditions from the 14YSZ layer and its amount increases from the t$^+$ phase transformation in 7YSZ layer. The difference between DLA and DLB can be ascribed to the different 7YSZ layer in terms of batch powders, spraying parameters and possible thickness variations

The phase analysis results of all samples with agreement factors are summarized in Table 24.

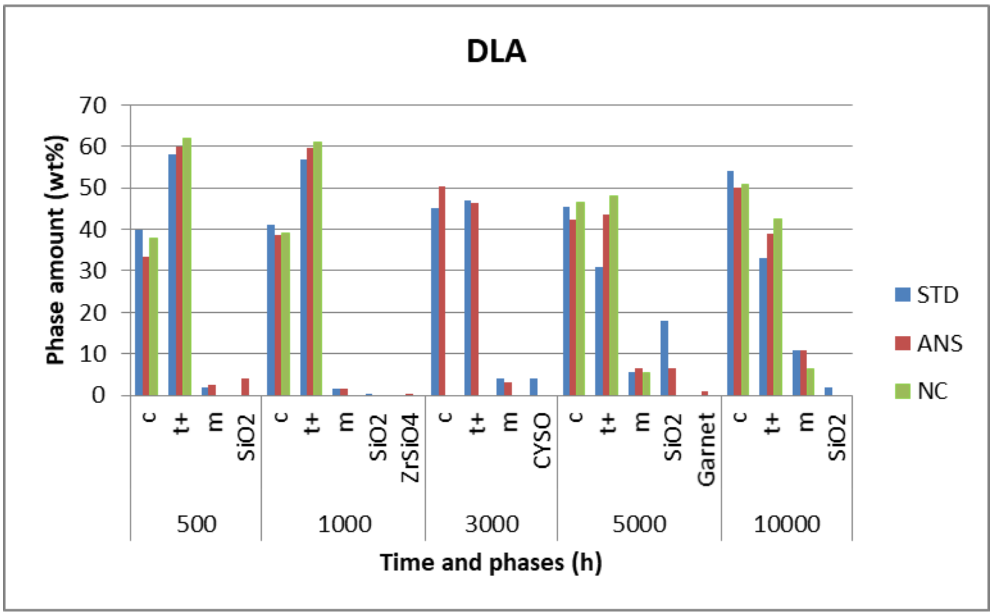

Figure 106 - Phase analysis of double layer (DL) samples with (STD and ANS) and without (NC) CMAS exposed at 1100°C for 500, 1000, 3000 ,5000 and 10000 h in batch A

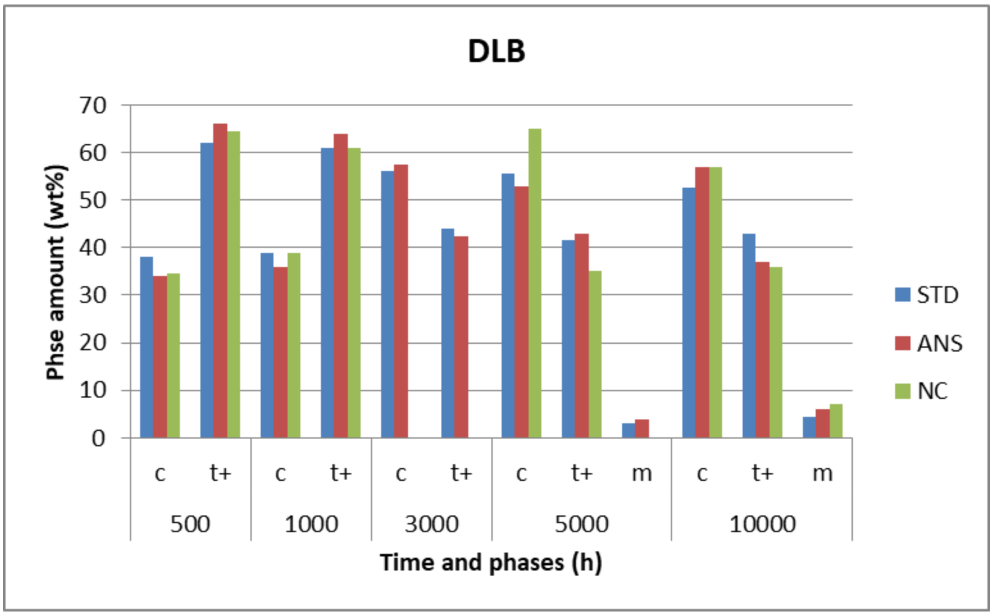

Figure 107 - Phase analysis of double layer (DL) samples with (STD and ANS) and without (NC) CMAS exposed at 1100°C for 500, 1000, 3000,5000 and 10000 h in batch B

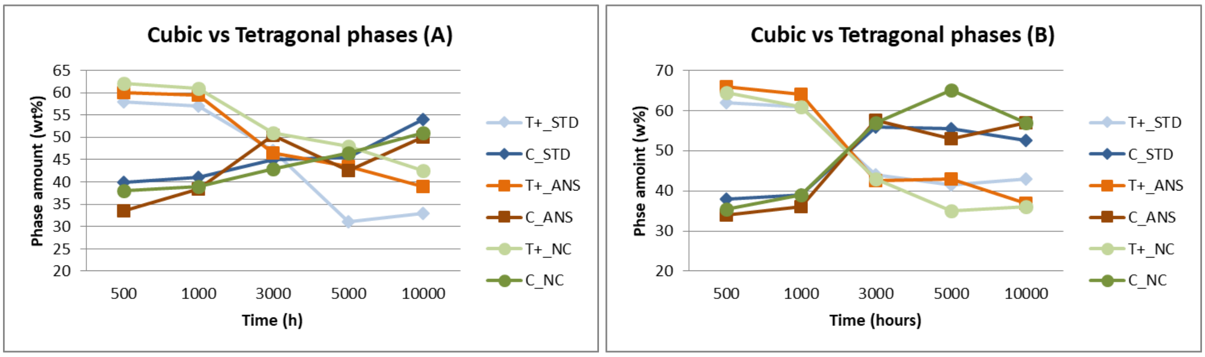

(a) (b)

Figure 108 – Amounts of cubic and tetragonal phases after 500, 1000, 3000 and 5000 h exposure at 1100°C.in batch A (a) and batch B (b)

Table 24 - Phase quantification and agreement factors on samples DL, tested at 1100°C

Material	Time (h)	Phases (wt%)							Agreement factors	
		c	t+	m	CYSO	Garnet	$ZrSiO_4$	SiO_2	R_{wp}	X^2
DLA_STD	500	40	58	2					10.0	4.8
	1000	41	57	1.5				0.5	8.9	3.9
	3000	45	47	4	4				8.1	2.9
	5000	45.5	31	4.5				18	4.9	1.5
	10000	51	42.5	6.5					6.3	2.5
DLA_ANS	500	33.5	60	2.5				4	9.8	4.6
	1000	38.5	59.5	1.5			0.5		10.6	5.4
	3000	50.5	46.5	3					7.4	2.6
	5000	42.5	43.5	6.5		1		6.5	5.2	1.7
	10000	50	39	11					5.2	1.8
DLA_NC	500	38	62						6.6	4.2
	1000	39	61						6.5	5.3
	3000	43	51	6					5.5	2.4
	5000	46.5	48	5.5					6.4	2.7
	10000	54	33	11					4.3	1.2
DLB_STD	500	38	62						8.2	4.2
	1000	39	61						9.7	5.3
	3000	56	44						6.8	2.4
	5000	55.5	41.5	3					6.5	2.7
	10000	52.5	43	4.5					6.5	2.6

Material	Time (h)	Phases (wt%)							Agreement factors	
		c	t+	m	CYSO	Garnet	$ZrSiO_4$	SiO_2	R_{wp}	X^2
DLB_ANS	500	34	66						15.0	7.1
	1000	39	61						11.3	4.7
	3000	57.5	42.5						9.9	5.2
	5000	53	43	4					6.2	2.3
	10000	57	37	6					5.8	2.1
DL7B_NC	500	35.5	64.5						7.9	2.5
	1000	39	61						6.7	2.9
	3000	57	43						6.3	2.7
	5000	65	35						5.5	1.8
	10000	57	36	7					5.7	2.0

5.1.4.2 Results after treatment at 1200°C

Phase analysis of double layer (DL) samples tested at 1200°C are reported in Figure 109 for batch A, and Figure 110 for batch B. The observed secondary phases (below 5%) are the same found for the other tested materials. Zircon detected in the DLA sample exposed 5000 h without CMAS, is probably due to a contamination by other specimens or the sample holder.

The amount of monoclinic phase as a function of exposure time is shown in Figure 111: its trend is similar to that shown by 7YSZ samples exposed at the same temperature (Figure 97). Indeed, the trend is linear and the phase increases with time. In particular, it seems to be constant for the first 1000 h, then increases linearly. Only sample DLA_STD shows a maximum at 3000 h. A possible explanation for this behavior can be related to a fluctuation of thickness of the two layers and a relative major contribution of 7YSZ to the measured m phase. However, this trend has been already observed for 7YSZ at 1100°C

The main important difference with the 7YSZ is that the effect of CMAS corrosion is less evident. In particular, ANS CMAS does not seem to produce a greater quantity of monoclinic phase. The DLA_NC after 5000 h has an amount of monoclinic phase superior to all the other specimens. This is the only case where this phenomenon has been observed. Again, a possible explanation can be related to relative thickness fluctuation between 7YSZ and 14YSZ. Moreover, comparing the two batches, it appears that all the DLA samples, with and without CMAS, form more m phase than DLB points, except for DLA_STD after 5000h. So, the 7YSZ layer of the DLB system seems to be less reactive than the one used for DLA, which is the same tested as 7A. Unfortunately, no tests are available for 7YSZ single layer samples produced with the same powders used for DLB.

Amounts of cubic and tetragonal phases in the two batches are compared in Figure 112. Also in this case, the decrease of the tetragonal phase and the increase of the cubic one, more evident in DLA samples, are observed, confirming the stability and the lower reactivity of 7YSZ layer of DLB. An inversion of the matrix is not visible in these samples because the cubic phase is always present in greater quantity, coming from 14YSZ layer.

The phase analysis results of all samples with agreement factors are summarized in Table 25.

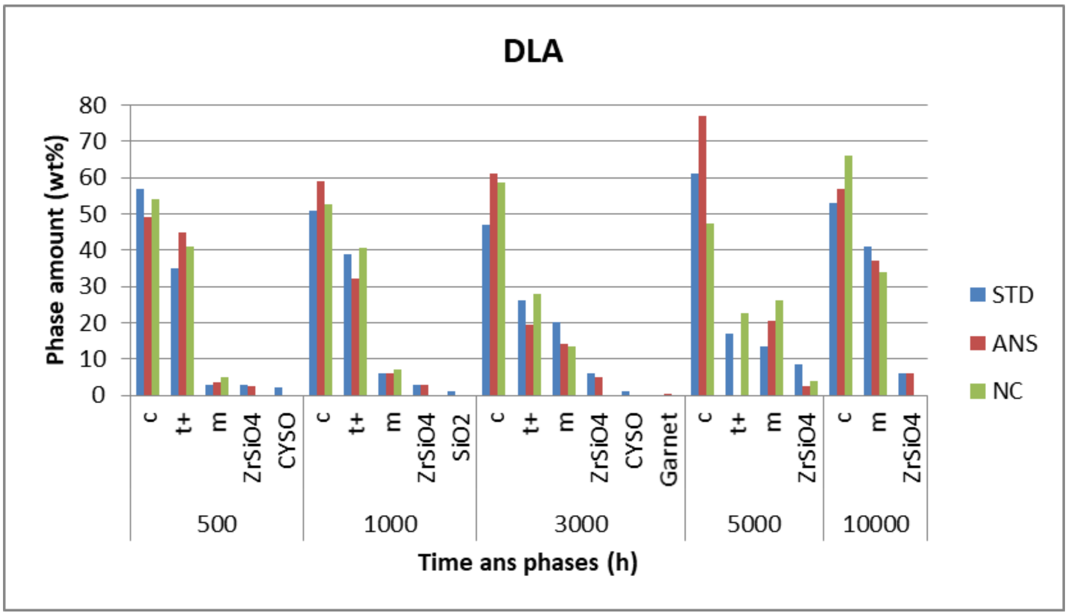

Figure 109 - Results of Double layer samples exposed at 1200°C for 500, 1000, 3000 and 5000 hours for the first batch. At each temperature the samples are tested with CMAS STD, CMAS ANS and without mixture of oxide.

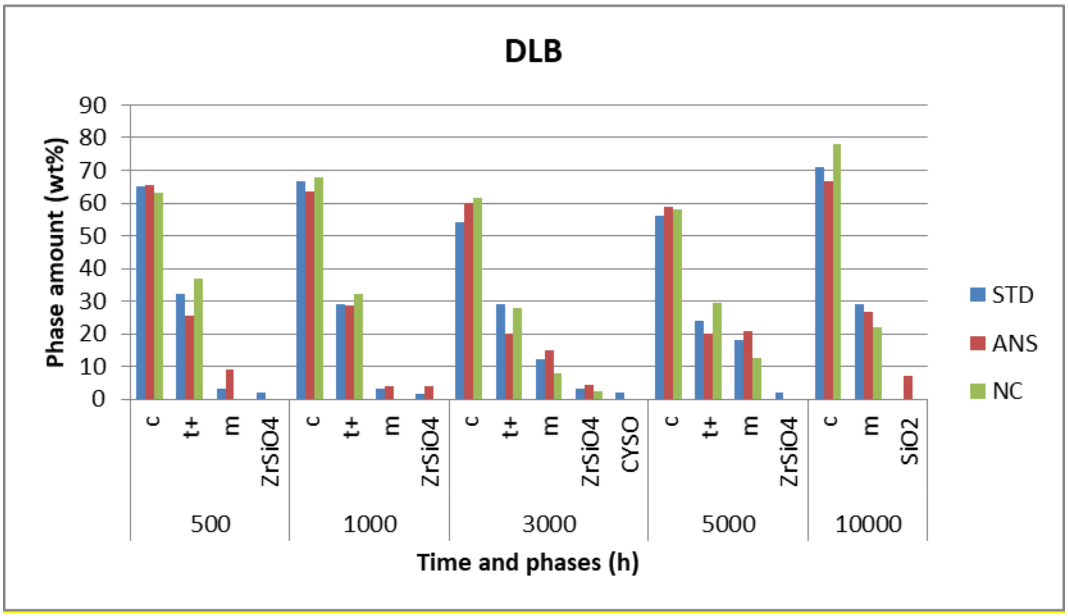

Figure 110 - Results of Double layer samples exposed at 1200°C for 500, 1000, 3000 and 5000 hours for the second batch. At each temperature, the samples are tested with CMAS STD, CMAS ANS and without mixture of oxide.

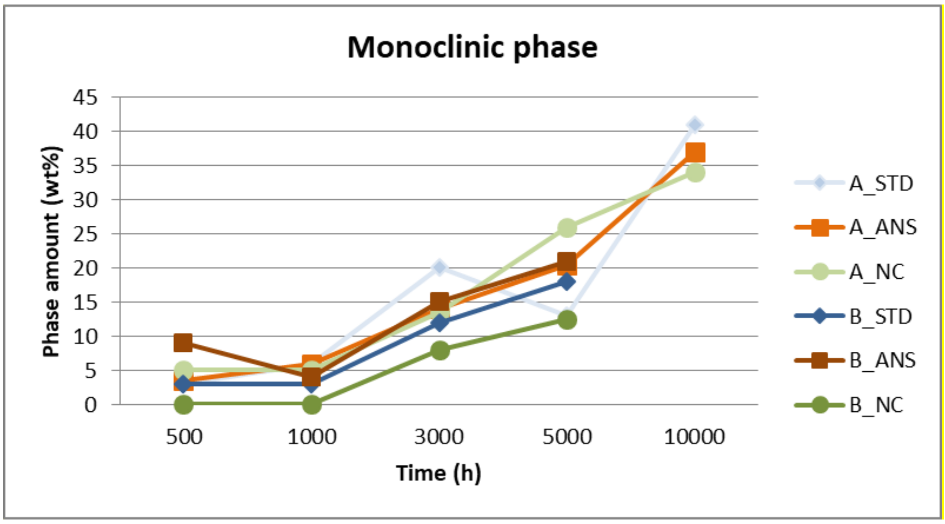

Figure 111 - Amount of monoclinic phase in double layer (DL) samples after 500, 1000, 3000 and 5000 h exposure at 1200°C.

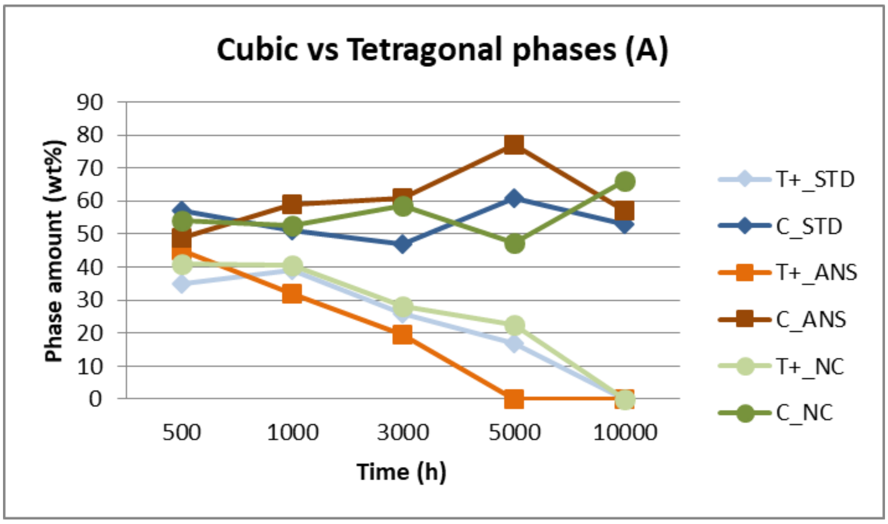

(a)

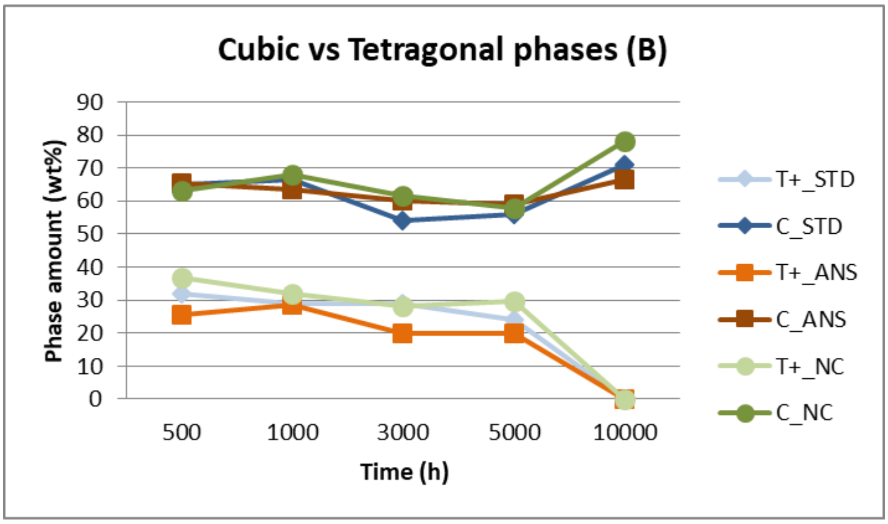

(b)

Figure 112 - Amounts of cubic and tetragonal phases after 500, 1000, 3000 and 5000 h exposure at 1200°C.in batch A (a) and batch B (b)

Table 25 – Phase quantification and agreement factors on samples DL, tested at 1200°C

Material	Time (h)	Phases (wt%)							Agreement factors	
		c	t+	m	CYSO	Garnet	$ZrSiO_4$	SiO_2	R_{wp}	X^2
DLA_STD	500	57	35	3	2		3		9.4	3.6
	1000	51	39	6			3	1	8.7	3.6
	3000	47	26	20	1		6		8.4	2.7
	5000	61	17	13.5			8.5		5.5	1.8
	10000	53		41			6		5.8	2.0
DLA_ANS	500	49	45	3.5				2.5	11.1	3.8
	1000	59	32	6				3	12.4	6.2
	3000	61	19.5	14		0.5		5	5.5	1.9
	5000	77		20.5				2.5	7.2	3.1
	10000	57		37			6		5.1	1.6
DLA_NC	500	54	41	5					7.0	3.0
	1000	52.5	40.5	7					6.5	2.6
	3000	58.5	28	13.5					5.7	2.0
	5000	47.5	22.5	26				4	4.9	1.5
	10000	66		34					6.4	2.5
DLB_STD	500	65	32	3			2		10.0	3.9
	1000	66.5	29	3			1.5		10.3	5.0
	3000	54	29	12	2		3		5.7	2.2
	5000	56	24	18			2		6.2	2.4
	10000	71		29					5.4	3.0
DLB_ANS	500	65.5	25.5	9					9.2	1.9
	1000	63.5	28.5	4			4		11.5	4.3
	3000	60	20	15			4.5		6.1	2.4
	5000	59	20	21					6.1	2.1
	10000	66.5		26.5				7	5.4	1.7
DL7B_NC	500	63	37						10.2	6.6
	1000	68	32						8.3	4.8
	3000	61.5	28	8				2.5	5.6	2.0
	5000	58	29.5	12.5					6.1	2.1
	10000	78		22					6.0	2.2

5.1.4.3 *Results after treatment at 1300°C*

Phase analysis results of double layer specimens exposed at 1300°C are reported in Figure 113. As in the case of 7YSZ, there is no difference between samples exposed with and without CMAS and between the measurements obtained at 300 and 1000 h in both batches.

The phase analysis results of all samples with agreement factors are summarized in Table 26.

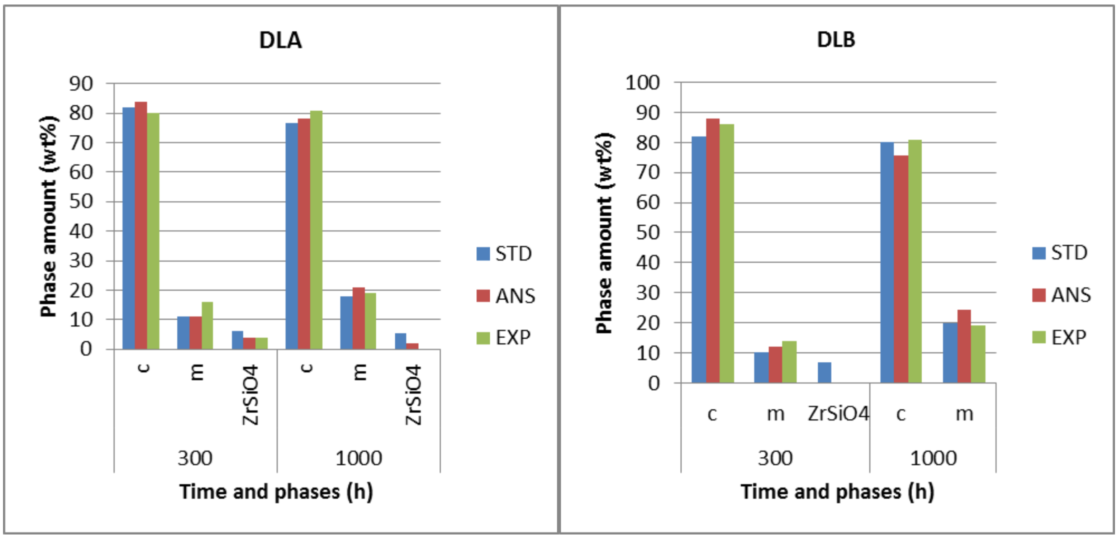

Figure 113 - Phase analysis of double layer (DL) samples with (STD and ANS) and without (NC) CMAS exposed at 1300°C for 300 and 1000 h, batch A (left) batch B (right)

Table 26 – Phase quantification and agreement factors on samples DL, tested at 1300°C

Material	Time (h)	Phases (wt%)			Agreement factors	
		c	m	$ZrSiO_4$	R_{wp}	X^2
DLA_STD	300	82	11	6	9.9	6.1
	1000	76.5	18	5.5	12.6	6.8
DLA_ANS	300	84	11	4	11.3	7.1
	1000	78	21	21	13.1	6.9
DLA_NC	300	80	16	4	9.0	5.0
	1000	81	19		10.6	6.4
DLB_STD	300	83	10	7	12.8	7.6
	1000	80	20		7.6	1.9
DLB_ANS	300	88	12		10.3	5.5
	1000	75.5	24.5		7.0	2.3
DLB_NC	300	86	14		6.9	2.8
	1000	81	19		9.8	5.8

5.1.4.4 Results after treatment at 1400°C

Phase analysis results after treatment at 1400°C are shown in Figure 114 and confirm the trends observed in 7YSZ samples.

The only secondary phase observed in small quantity is zircon, present only in some samples.

The phase analysis results of all samples with agreement factors are summarized in Table 27.

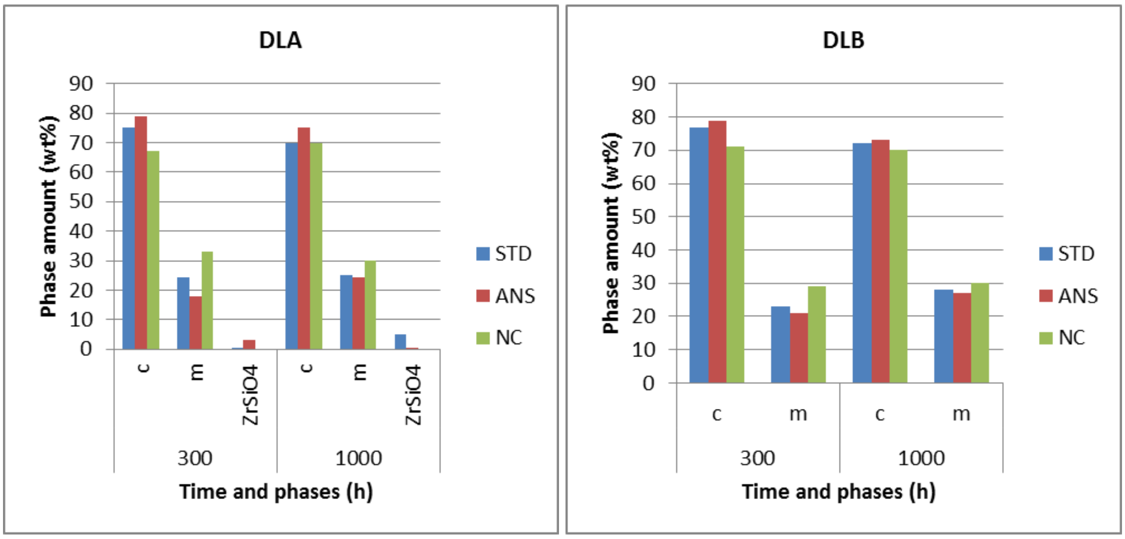

Figure 114 - Phase analysis of double layer (DL) samples with (STD and ANS) and without (NC) CMAS exposed at 1400°C for 300 and 1000 h, batch A (left) batch B (right)

Table 27 – Phase quantification and agreement factors on samples DL, tested at 1400°C

	Time (h)	Phases (wt%)			Agreement factors	
Material		c	m	$ZrSiO_4$	R_{wp}	X^2
DLA_STD	300	75	24.5	0.5	6.6	2.7
	1000	70	25	5	14.1	8.8
DLA_ANS	300	79	18	3	9.5	5.8
	1000	75	24.5	0.5	11.8	5.6
DLA_NC	300	67	33		8.1	3.9
	1000	70	30		10.9	6.9
DLB_STD	300	77	23		14.9	9.1
	1000	72	28		10.7	7.0
DLB_ANS	300	79	21		9.6	4.5
	1000	73	27		11.1	7.5
DLB_NC	300	71	29		11.1	7.9
	1000	70	30		6.5	2.3

5.2 Microscopy results

In this chapter, only some of the samples examined with the X-ray diffraction technique will be treated. No evident differences have been observed in the batches of the same type of sample, therefore this difference will no longer be highlighted.

5.2.1 Microstructural modifications

The 7YSZ samples exposed to 1100°C without the presence of CMAS are shown in the Figure 115 at different exposure times.

The observed microstructure is similar to the original one, with the presence of irregularly shaped pores and micro-cracks due to the APS deposition method.

The effect of temperature is marginal as no particular microstructural changes are observed between the samples exposed for a short time and those exposed for 10000h.

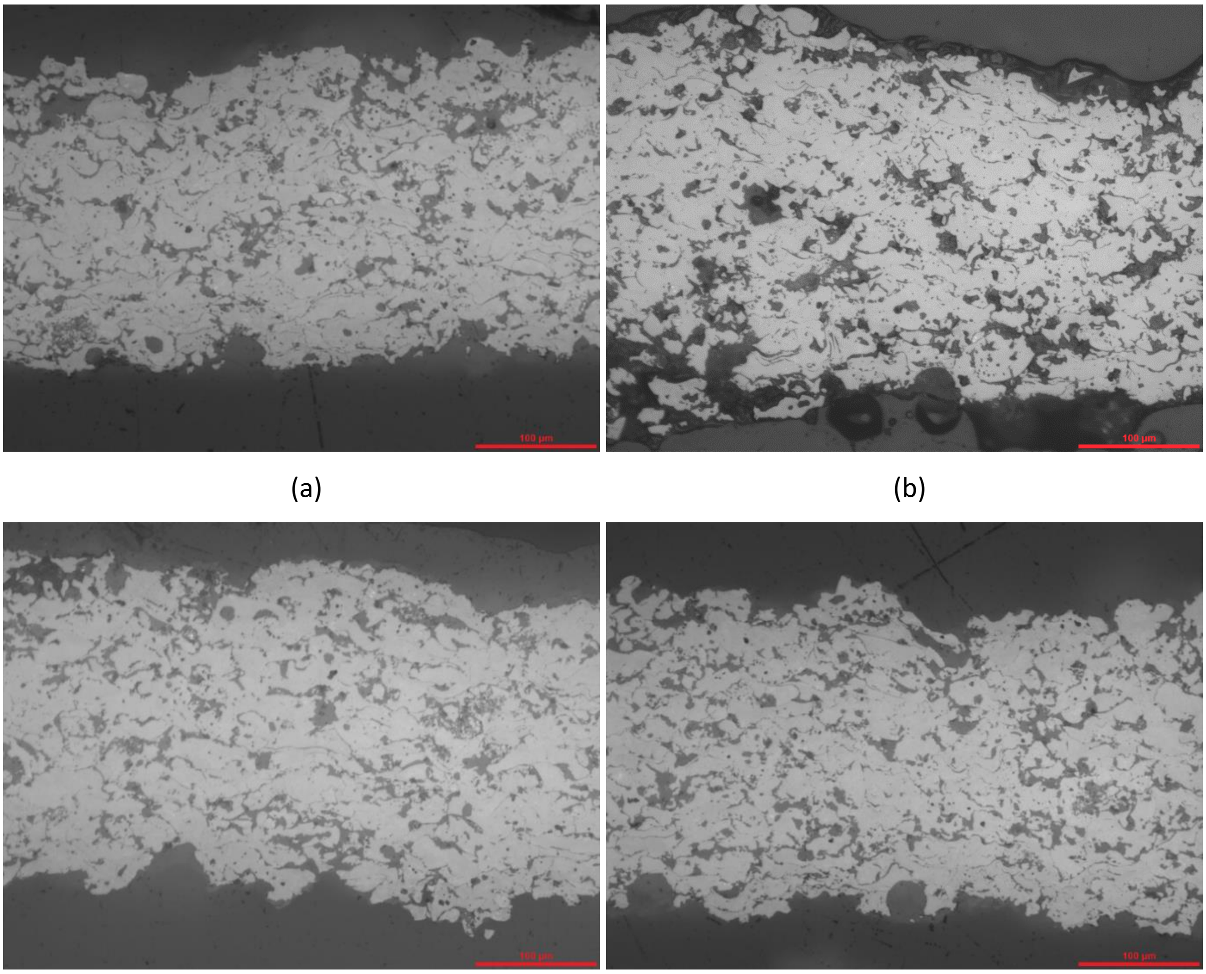

(a) (b)

(c) (d)

Figure 115 – Optical microscope images x200: 7YSZ exposed at 1100°C for 1000h (a) 3000h (b), 5000h (c) and 10000h (d)

The samples tested at 1200°C for times between 1000 and 10000 hours are reported in Figure 116. The microstructure is similar to that observed at lower temperatures, its morphology still resembles the original one.

Only at long times, around 10,000 h, the micro-cracks tend to stick each other and the sample is more compact. The shape and distribution of larger pores do not seem to undergo significant changes as the exposure time varies.

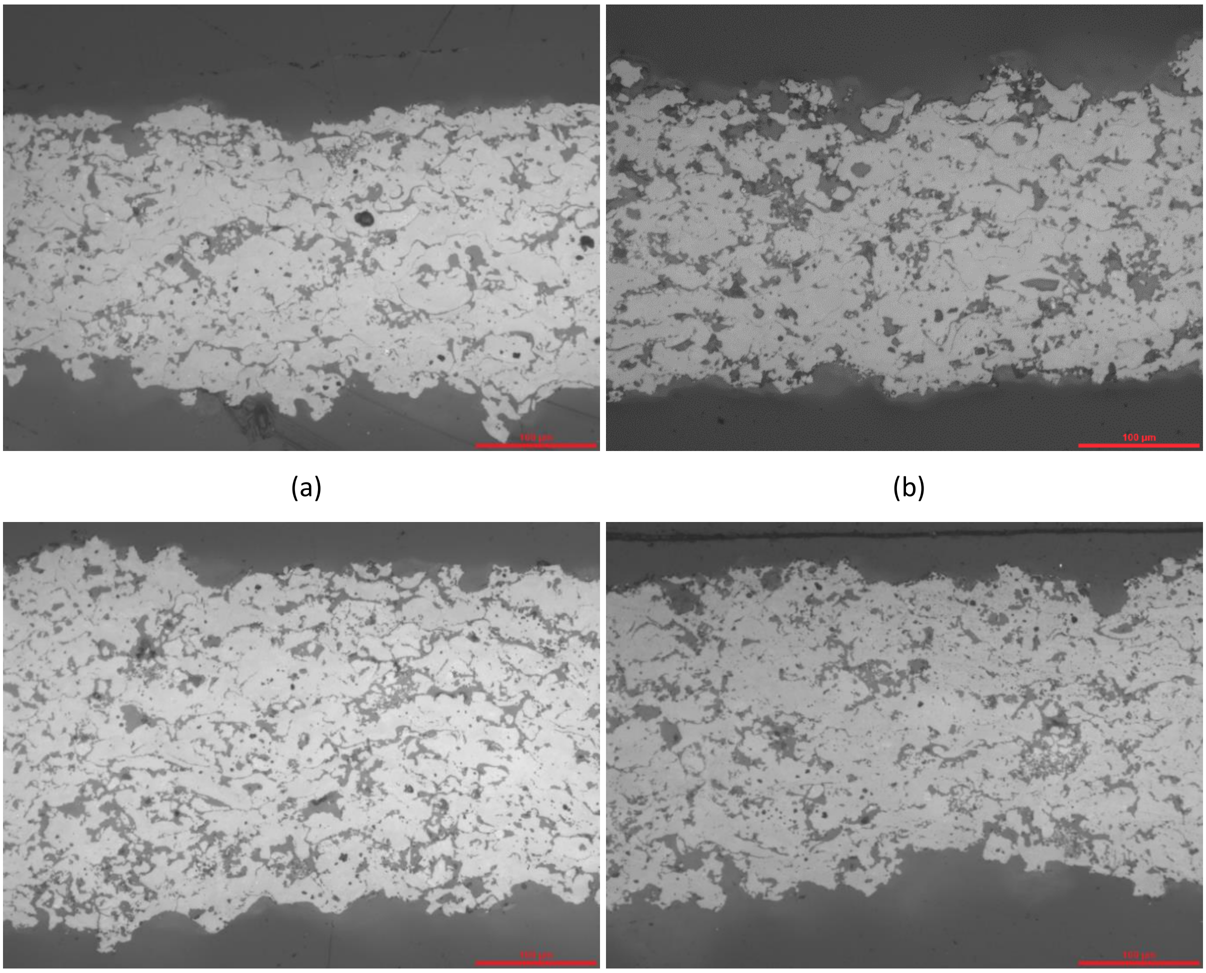

(a) (b)

(c) (d)

Figure 116 - Optical microscope images x200: 7YSZ exposed at 1200°C for 1000h (a) 3000h (b), 5000h (c) and 10000h (d)

The samples exposed for 1000h to higher temperatures are reported in the Figure 117 .

In this case the temperature effect is very evident. The sample exposed at 1300°C for 1000 h has a structure similar to that observed at 1200°C at a longer time (10000 h), but the changes seem even more evident. The micro-cracks are mainly “welded”, the pores tend to round off and the original structure is more difficult to observe.

The sample exposed to 1400°C shows a completely sintered sample in which the micro-cracks formed during the deposition of the material are no longer visible and the porosities tend to have a regular shape due to the growth of the zirconia grains.

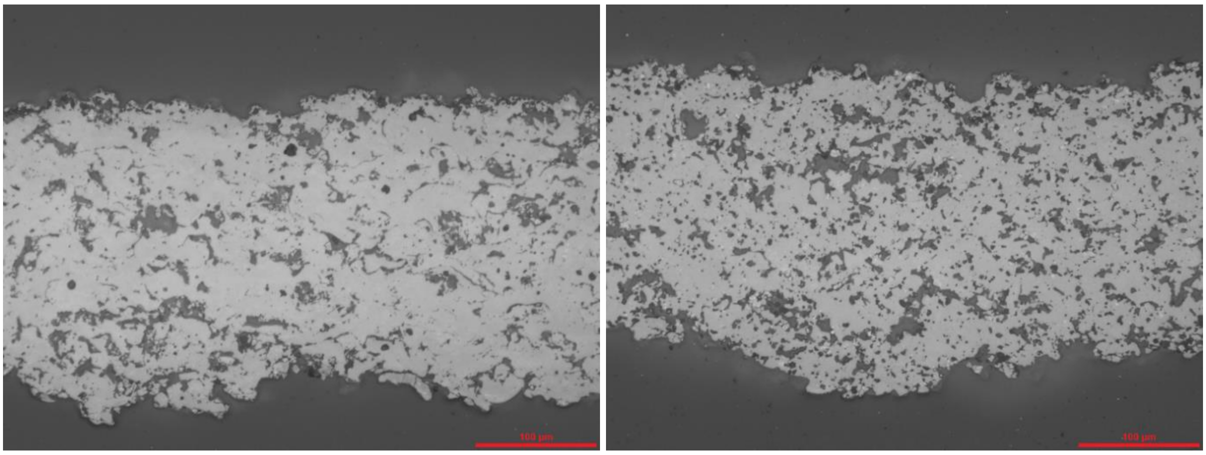

(a) (b)

Figure 117 - Optical microscope images x200: 7YSZ exposed at 1300°C for 1000h (a) and at 1400°C for 1000h (b)

The 14YSZ samples exposed to low temperatures (1100 and 1200°C) are shown in the Figure 118.

In this case only the short time (1000 h) and long time (10000 h) micrographs are shown, without reporting the intermediate times.

This type of material does not seem to be subject to microstructural changes under any of the conditions treated, and the sample exposed to 1200°C for 1000 h has a structure similar to that observed in the sample exposed to 1100°C for 1000 h and to the original one.

As in the case of 7YSZ, only the sample exposed to longer times at 1200°C seems to have undergo small changes due to sintering. These phenomena are more evident in the sample exposed to 1300°C for 1000 h (Figure 119), in which the micro-cracks are more difficult to observe and the porosities tend to become rounded.

The analysis on samples exposed without CMAS show microstructural changes such as sintering and rounding of the pores, related to the exposure temperature, regardless of the type of material. The sintering effects are not observable at 1100°C even after long exposure times while they are evident above 1300°C already at 1000 h. The samples exposed to 1200°C are the only ones that show a structural change as a function of the exposure time, even if these phenomena are observable only after long aging times.

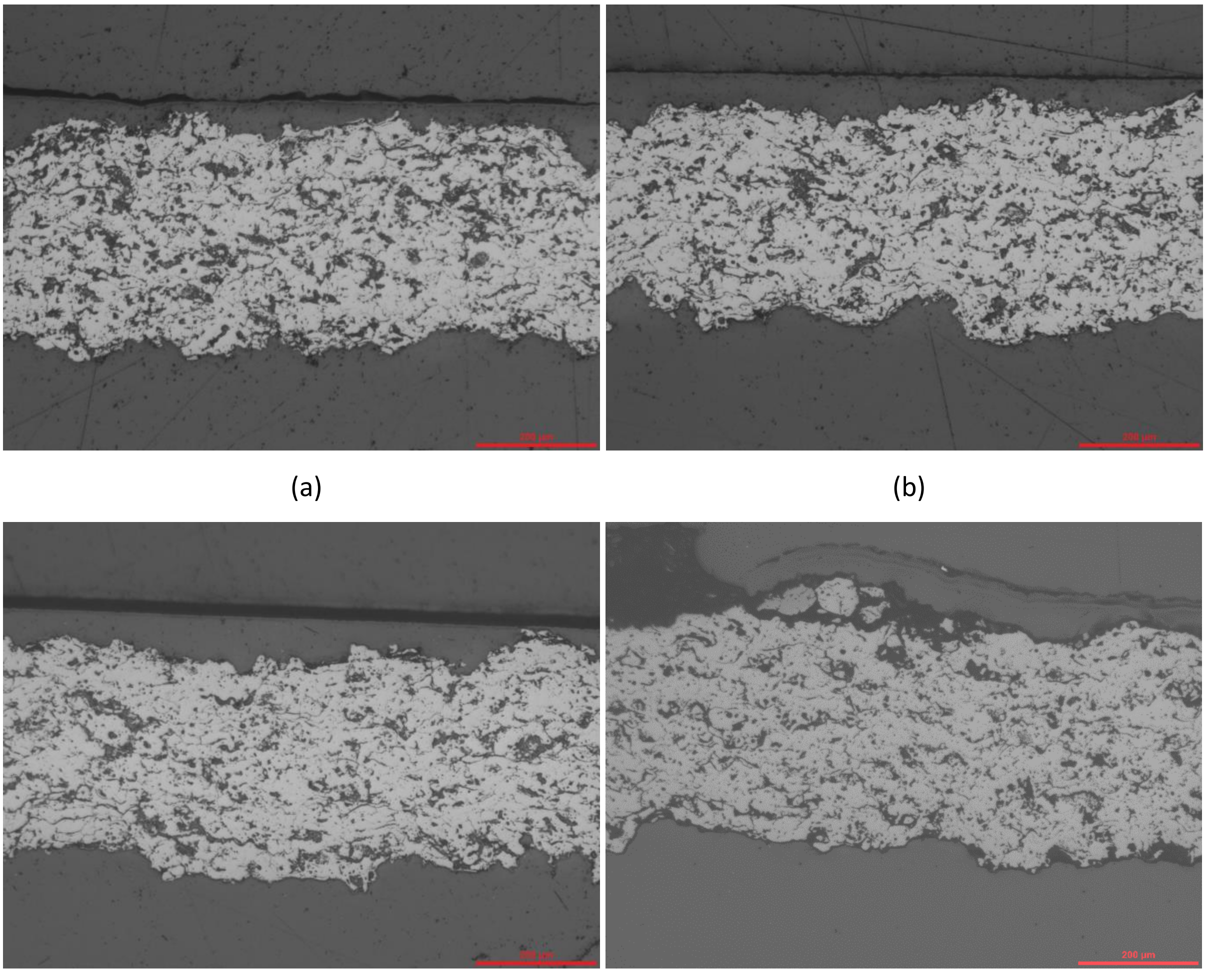

(a) (b)

(c) (d)

Figure 118 – Optical microscope images x100: 14YSZ exposed at 1100°C for 1000h (a) and 10000h (b), 14YSZ exposed at 1200°C for 1000h (c) and 10000h (d)

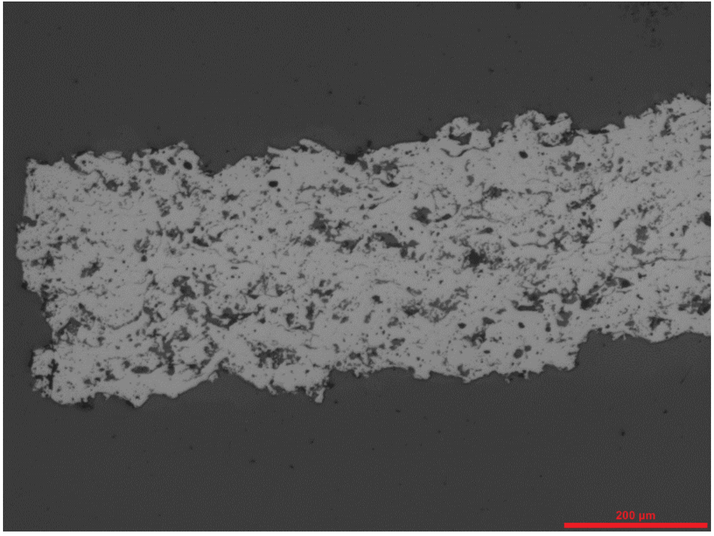

Figure 119 - Optical microscope images x100: 14YSZ exposed at 1300°C for 1000h

The micrographs of the 7YSZ samples exposed to 1100°C for different times with the STD and ANS CMAS mixtures are shown in the Figure 120.

The images are shown in order of increasing exposure time. On each line the samples exposed with CMAS STD are shown on the left and those with CMAS ANS on the right.

As in the case of samples exposed without CMAS, at 1100 °C the temperature is too low to observe evident structural changes, regardless of time and presence and type of corrosive.

No difference appears in cracks and pores, compared to those observed in samples without CMAS. Furthermore, no interaction layer was observed between the deposit and the base material.

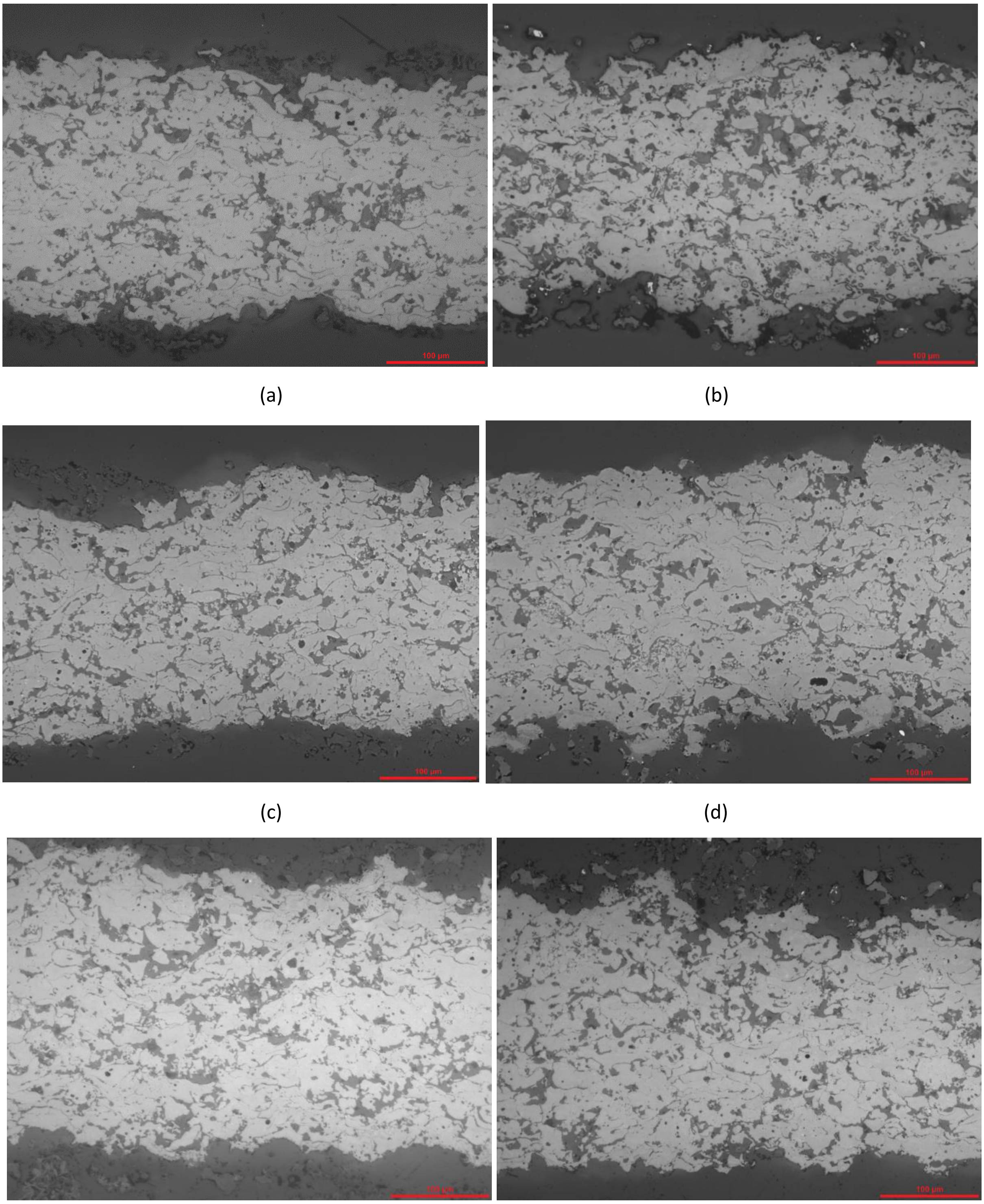

(a) (b)

(c) (d)

(e) (f)

Figure 120 - Optical microscope images x200: 7YSZ exposed at 1100°C for 1000h STD(a) and ANS (b), 5000h STD(c) and ANS (d), 10000h STD(e) and ANS (f)

Similarly, the results obtained on samples exposed to 1200 °C are shown in the Figure 121, where the four analyzed times are reported: 1000, 3000, 5000 and 10000 h.

In this case, however, the effect of the presence of CMAS is evident. Unlike what has been observed in the case of samples exposed without corrosive, the microstructure of the studied samples is very different already after 1000 hours of exposure.

The micro-cracks are not observable in any studied sample, while the pores tend to become rounded with the increase of the exposure time. In particular, the samples exposed with ANS CMAS seem to produce a greater change in the shape of the pores already after a short time of exposure, while the sample exposed with STD mixture still shows pores that recall the original structure after 1000 h.

The effect of pore rounding appears to be similar in the two types of CMAS when the exposure time increases (over 5000h).

The interaction layer is already observable at a short time in both types of CMAS and it is approximately one sixth/one fifth of the overall thickness of the specimen. This layer tends to remain constant as the exposure time varies. The structural modifications of the sample, on the other hand, affect the entire thickness of the sample and not only the reaction layer with the CMAS.

A quantitative assessment of porosity would have been necessary to consolidate the visual assessments reported in this thesis. Unfortunately, a quantitative method that would allow to accurately evaluate the small differences in porosity between the various samples has not been optimized. In fact, the images magnification is too low to quantitatively appreciate variations. Electron microscope images at higher magnification (x1000) have been obtained, but, also in this case, the measurement error is in the order of the measured porosity variation. This is probably related also to the processing software used. For this reason only a macroscopic variation of the samples microstructure has been discussed in this thesis.

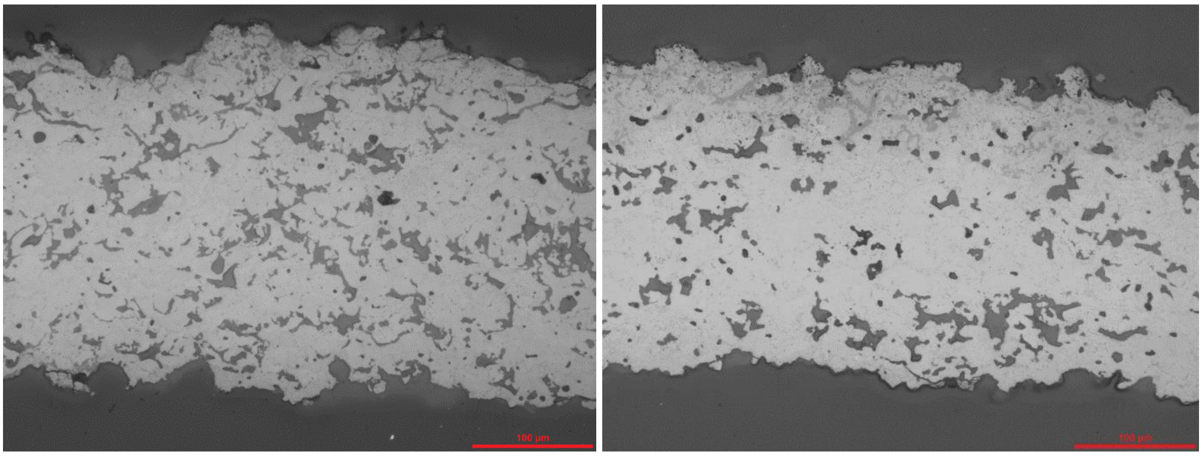

(a) (b)

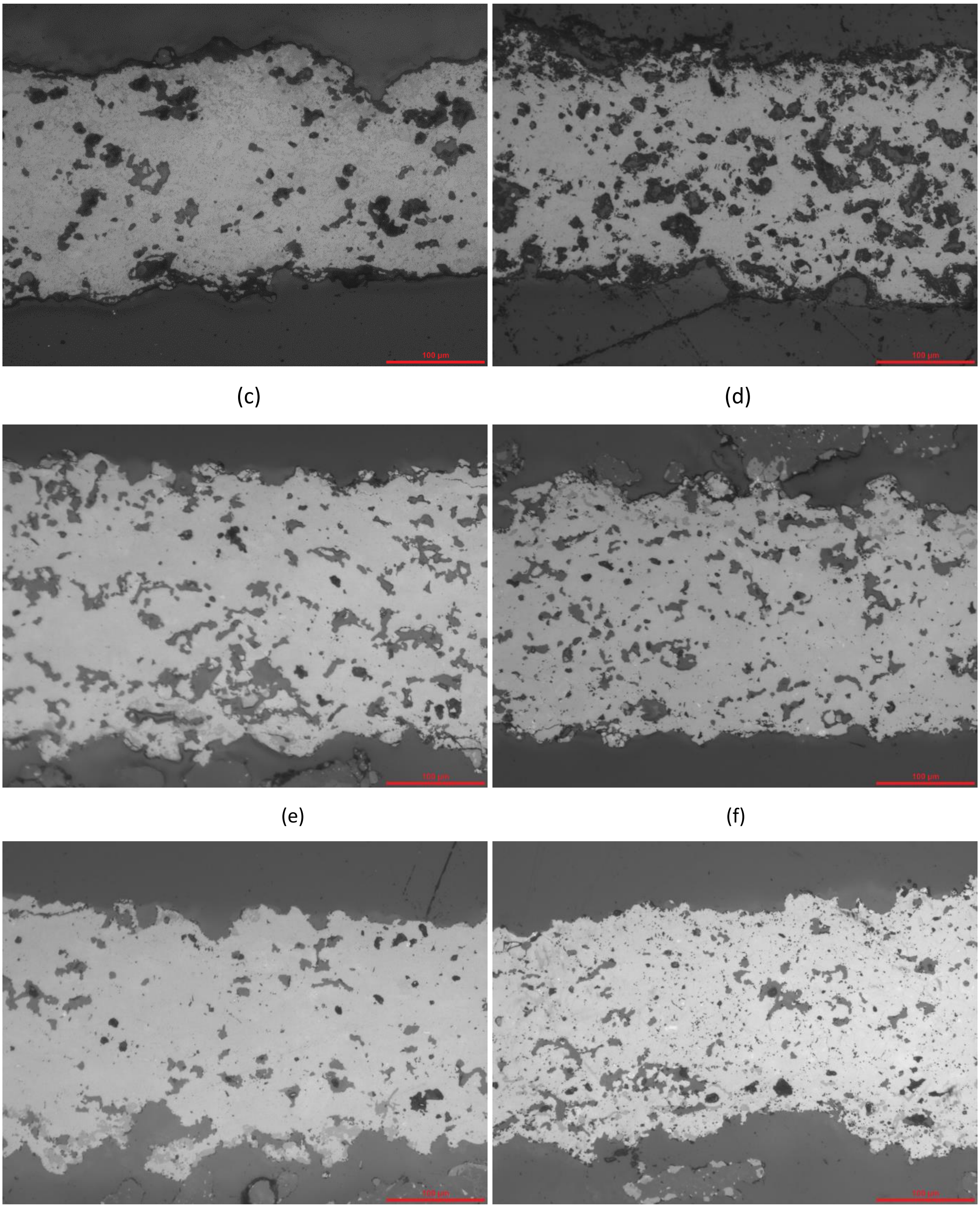

(c) (d)

(e) (f)

(g) (h)

Figure 121 - Optical microscope images x200: 7YSZ exposed at 1200°C for 1000h STD (a) and ANS (b), 5000h STD (c) and ANS (d), 5000h STD (e) and ANS (f), 10000h STD (g) and ANS (h)

The interaction layer (red rectangle) is underlined in the Figure 122, where SEM (x600) images of two samples exposed at 1100°C (Figure 122-a) and 1200°C (Figure 122-b) for 3000 h with ANS CMAS are reported as an examples.

At 1100°C a not yet reacted CMAS deposition layer can be observed, while the interaction layer is not evident. The deposit is no longer visible at 1200°C, where however an interaction layer between the TBC and CMAS is evident with the formation of secondary phases. The thickness of this layer is approximately one fifth / one sixth of the total sample thickness.

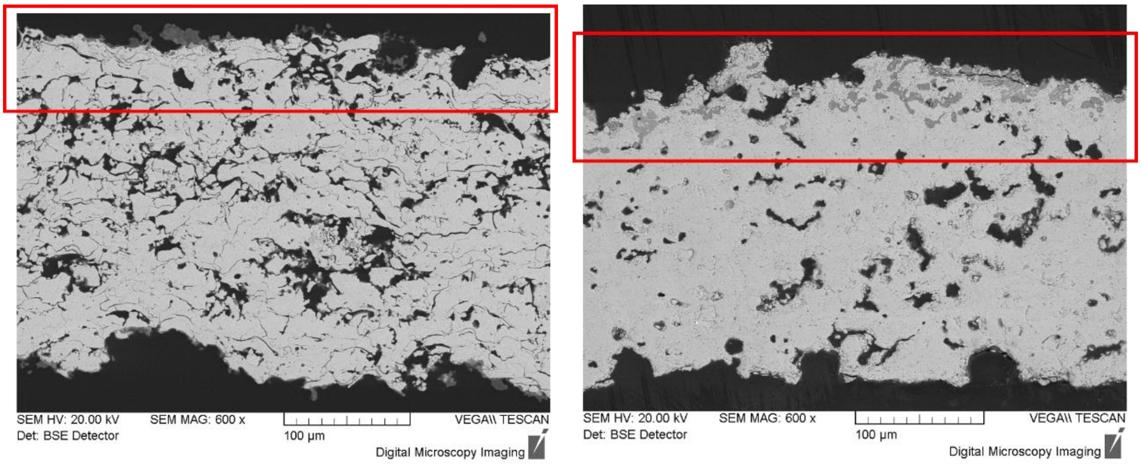

(a) (b)

Figure 122 – Images by SEM (x600) of samples treated at 1100°C (a) and 1200°C (b) exposed for 3000h with ANS CMAS

The effects on the microstructure of the material exposed to high temperature (1300 and 1400°C) with the CMAS mixtures are highlighted in the Figure 123.

The differences between 1300 and 1400°C are extremely small, as between the two types of CMAS. In this case, the effect of material sintering is made evident by completely closed micro-cracks and very rounded porosities. Furthermore, the growth of cubic zirconia grains is evident with the formation of the monoclinic phase at the grain boundary.

The interaction layer with the CMAS is no longer evident, and this phenomenon will be discussed in the next paragraph.

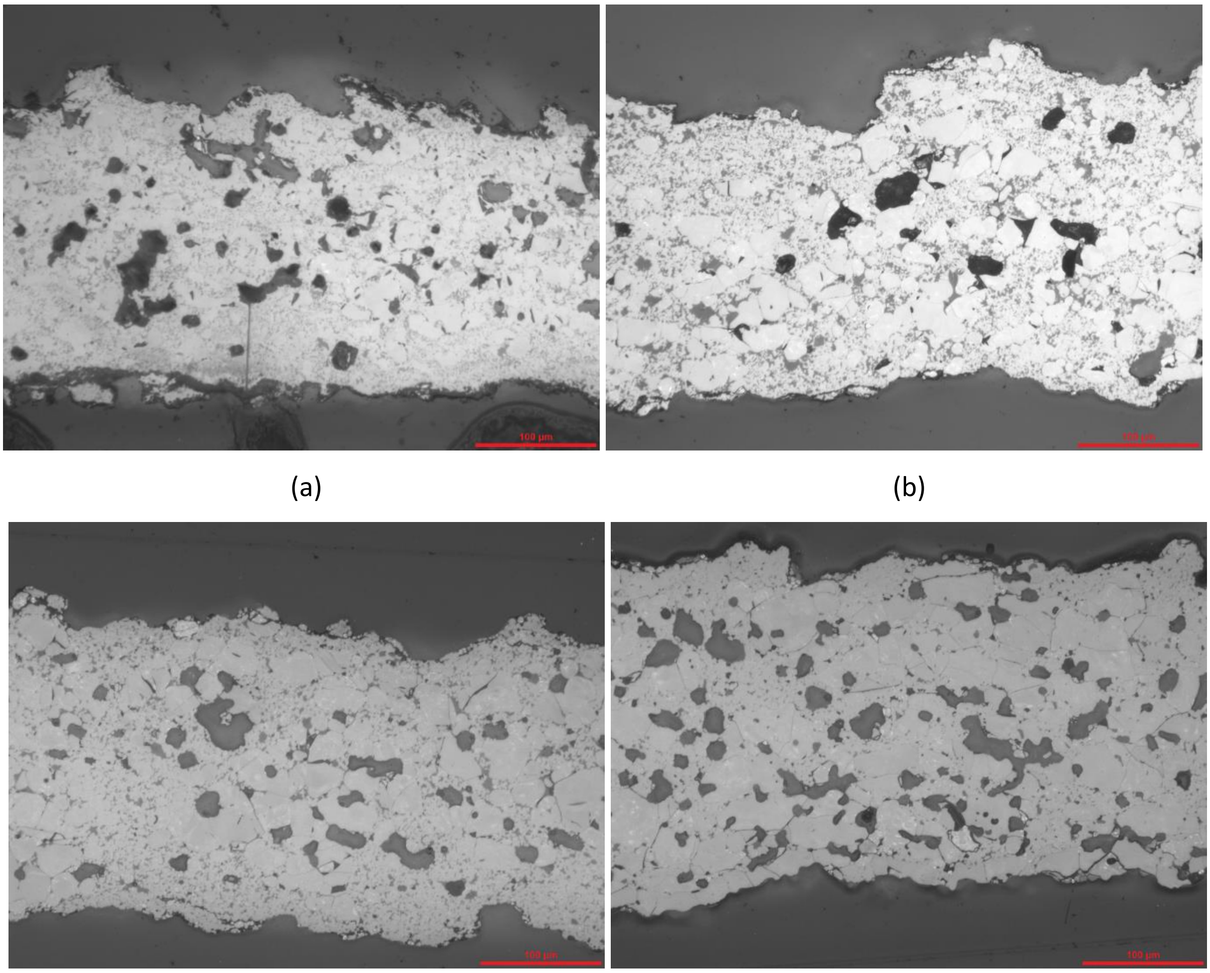

(a) (b)

(c) (d)

Figure 123 - Optical microscope images x200: 7YSZ exposed at 1300°C for 1000h STD (a) and ANS (b), and at 1400°C for 1000h STD (c) and ANS (d),

Similarly to the 7YSZ samples, the images of the 14YSZ samples exposed to 1100 ° C with CMAS are shown in the Figure 124.

As for the other samples exposed to this temperature, the presence of CMAS is not sufficient to determine a structural change regardless of the exposure time.

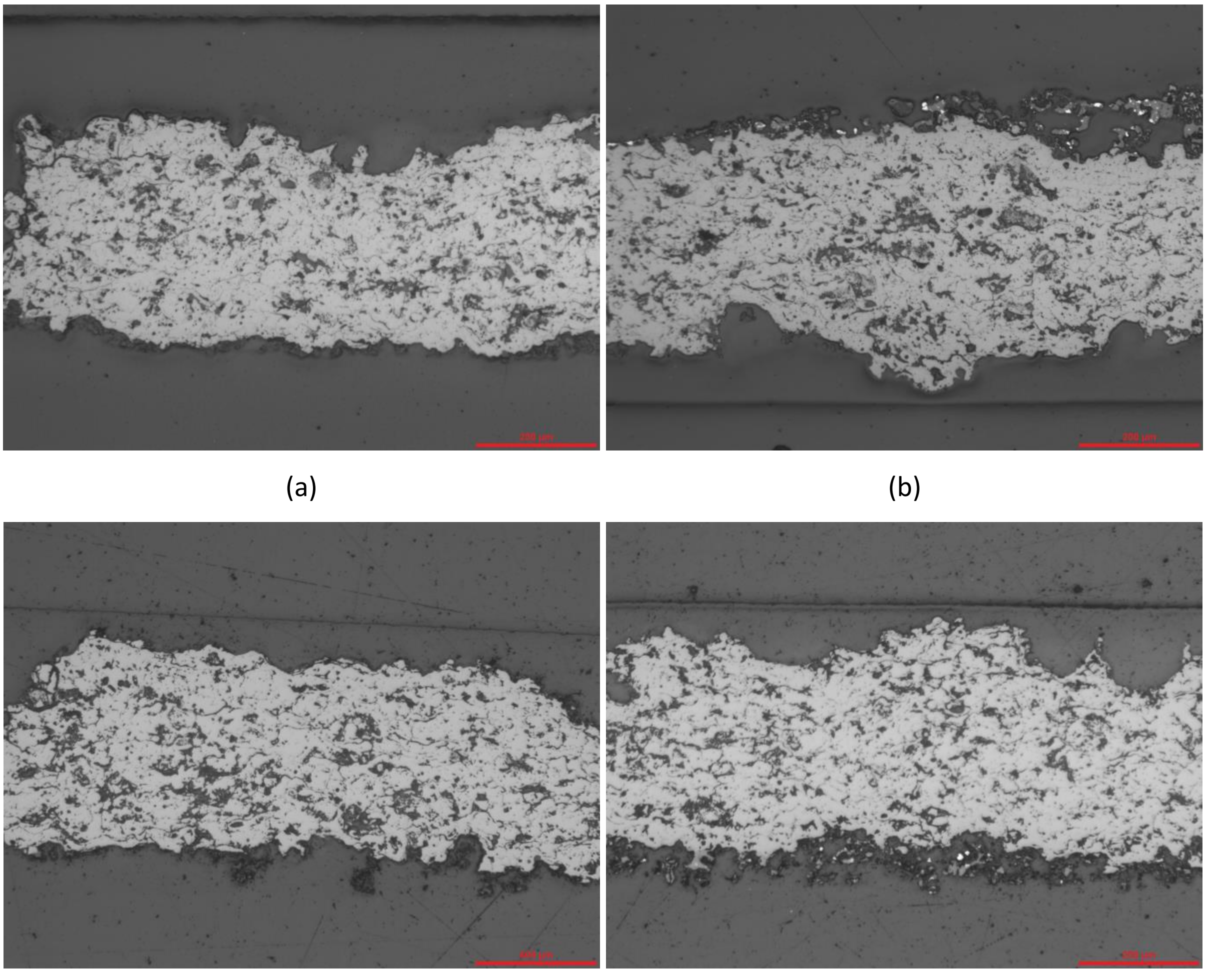

(a) (b)

(c) (d)

Figure 124 - Optical microscope images x100: 14YSZ exposed at 1100°C for 1000h STD(a) and ANS (b), 10000h STD(c) and ANS (d)

Samples exposed to 1200°C are shown in the Figure 125. As in the case of the 7YSZ samples, the microstructure seems to be strongly modified by the presence of CMAS already after 1000 h, with a greater sintering effect than in the samples exposed without corrosive. Also in this case, the CMAS with iron seems kinetically more active as it modifies the structure of the material in shorter exposure times.

The structures after 10000 h seem very similar to each other and the reaction layer between the substrate and the corrosive is no longer evident. The structural modification involves, as in the case of 7YSZ samples, the entire thickness of the specimen regardless of the reaction layer.

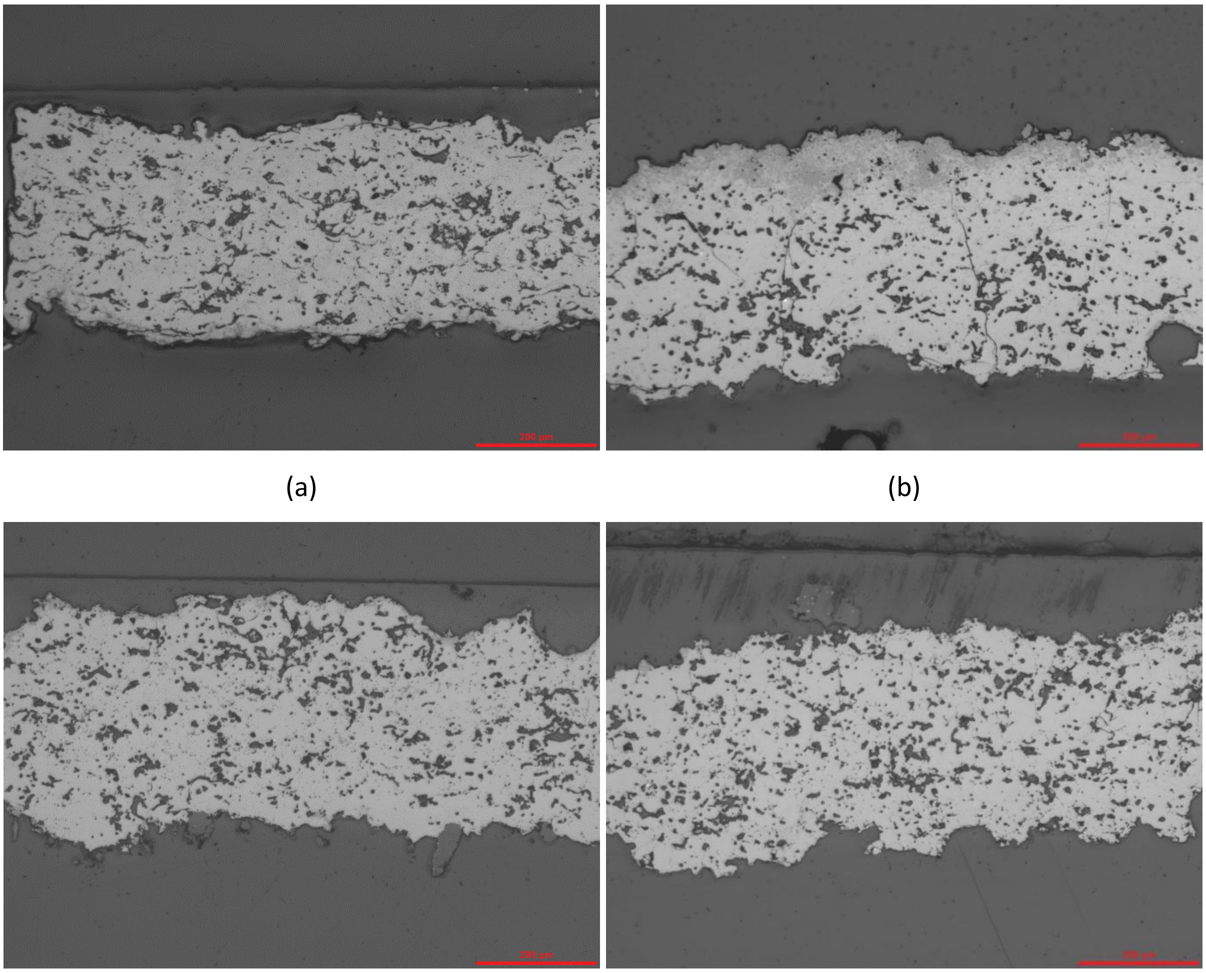

(a) (b)

(c) (d)

Figure 125 - Optical microscope images x100: 14YSZ exposed at 1200°C for 1000h STD(a) and ANS (b), 10000h STD(c) and ANS (d)

The 14YSZ samples exposed with CMAS at 1400 are shown in the Figure 126 .

The microstructure is completely modified and the reaction layer between the sample and the CMAS is no longer observable, exactly as observed in the 7YSZ samples exposed under the same conditions.

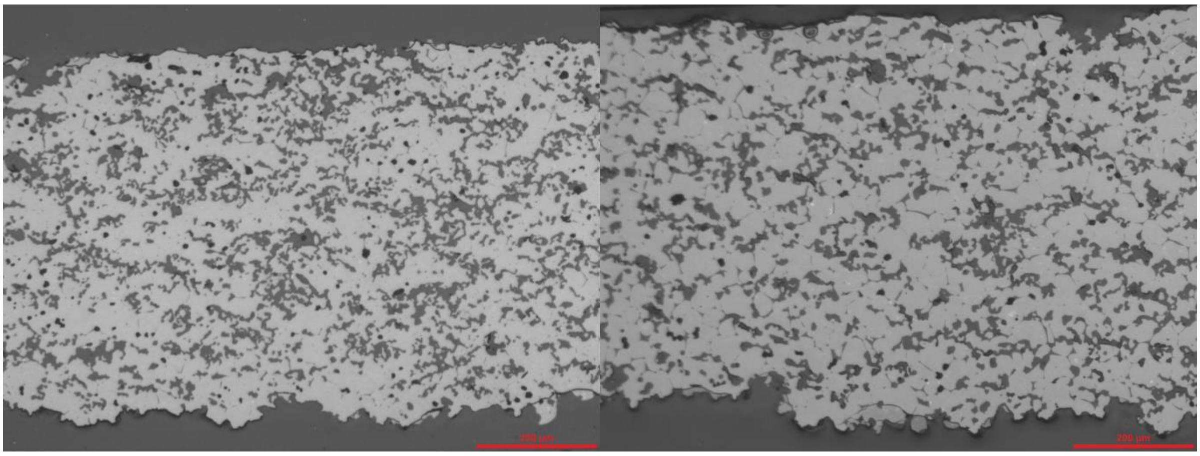

(a) (b)

Figure 126 - Optical microscope images x100: 14YSZ exposed at 1400°C for 1000h STD(a) and ANS (b)

In conclusion, the microstructural analysis shows that the two materials have similar behavior when exposed under the same conditions. The 1100°C temperature is too low to produce structural changes, regardless of the exposure time and the presence of CMAS. At temperatures above 1300°C a sintering effect appears. It is already evident in samples exposed without corrosive, but the presence of CMAS increases “welding” of the micro-cracks and rounding of the pores. An interaction layer is no longer observable at this temperature in the samples exposed with CMAS.

At 1200°C samples without CMAS begin to show a sintering effect only at long times. It consists in the modification of the cracks without change in the pores shape. The presence of CMAS at this temperature considerably modifies the microstructure already in a short time, by accelerating the sintering phenomenon throughout the thickness of the specimen. The difference between the two CMAS is not particularly evident as far as the microstructural changes are considered, but ANS CMAS seems to modify the material more quickly than STD CMAS, even if this phenomenon is mitigated at longer exposure time. This observation is in good agreement with the XRD analysis which generally highlighted a greater reactivity of ANS CMAS.

5.2.2 Secondary phases formed by CMAS interaction and effect of high temperature

The samples analyzed by SEM confirmed the presence of the phases detected by X-ray diffraction.

The study has been carried out through maps and punctual analysis to determine the interaction layer of the CMAS and the composition of the secondary phases.

All the characterized samples, regardless of the type of materials tested, showed the same microstructural evolution.

The only significant difference, highlighted in this paragraph, is that different CMAS form different secondary phases, confirming XRD observation.

Figure 127 shows, as an example, the EDS analysis on a 7YSZ specimen exposed for 1000h at 1200 ° C with a STD CMAS mixture. From the EDS maps, shown in the right part of the figure, it is possible to observe how calcium and silicon have penetrated into the material creating a reaction layer.

The maps of the other elements (aluminum and magnesium) are not reported, as they do not significantly interact with TBC, in agreement with the literature.

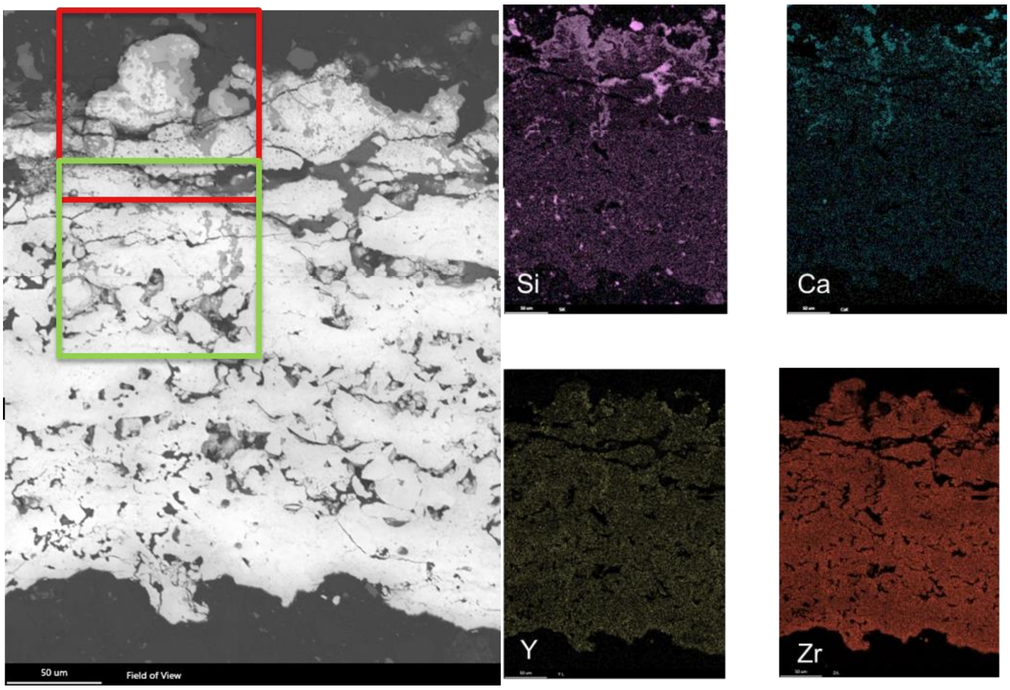

Figure 127 – EDS maps on samples 7YSZ exposed at 1200°C for 1000 h with STD CMAS

With red and green squares, the areas in which specific EDS analyzes have been carried out to identify the composition of the secondary phases, evaluating the external layer, in contact with the CMAS, and a deeper layer were highlighted.

The results of the surface area and the tables with the compositions of the phases (expressed both in weight and mol percent), represented by the red square are shown in Figure 128, while those of the underlying area (in green) are shown in Figure 129.

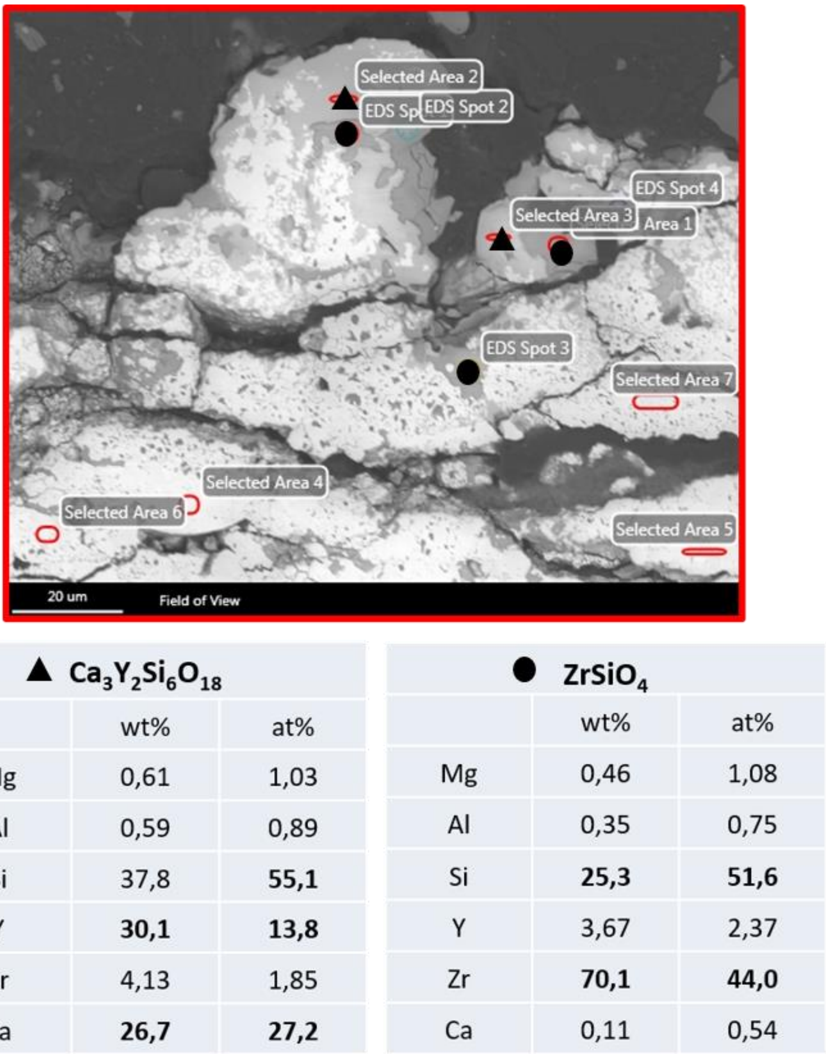

▲ $Ca_3Y_2Si_6O_{18}$		
	wt%	at%
Mg	0,61	1,03
Al	0,59	0,89
Si	37,8	**55,1**
Y	**30,1**	**13,8**
Zr	4,13	1,85
Ca	**26,7**	**27,2**

● $ZrSiO_4$		
	wt%	at%
Mg	0,46	1,08
Al	0,35	0,75
Si	**25,3**	**51,6**
Y	3,67	2,37
Zr	**70,1**	**44,0**
Ca	0,11	0,54

Figure 128 – EDS punctual analysis of secondary phases on external part of the sample

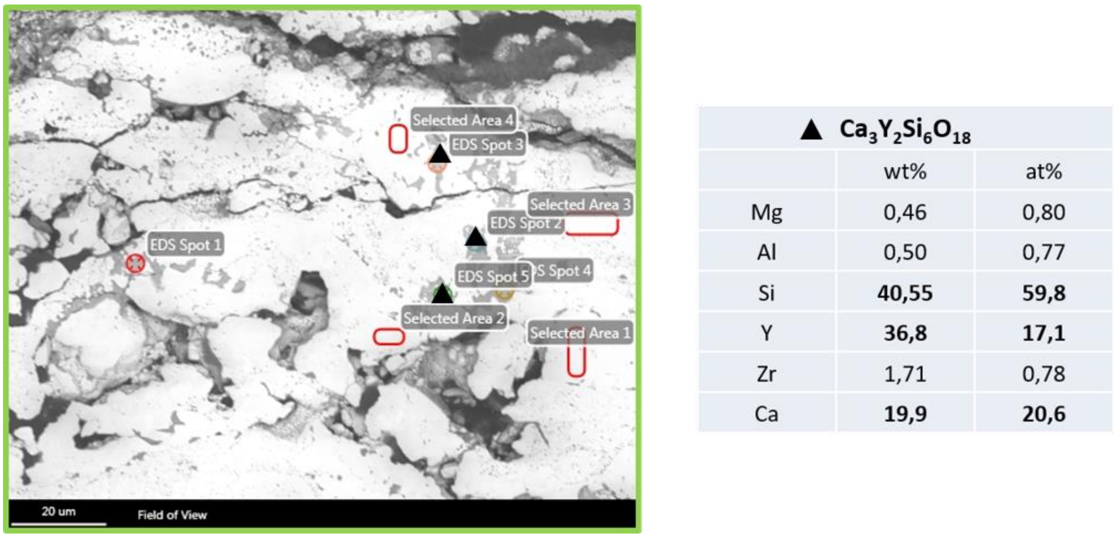

▲ $Ca_3Y_2Si_6O_{18}$		
	wt%	at%
Mg	0,46	0,80
Al	0,50	0,77
Si	**40,55**	**59,8**
Y	**36,8**	**17,1**
Zr	1,71	0,78
Ca	**19,9**	**20,6**

Figure 129 – EDS punctual analysis of secondary phases in the middle of the sample

In the area near the surface, two secondary phases are distinguished, zircon ($ZrSiO_4$) and a silicate of calcium and yttrium ($Ca_3Y_2Si_6O_{18}$). Both phases are stoichiometric compounds that practically do not solubilize other elements in their lattice except for silicon and zirconium in the case of zircon, and calcium yttrium and silicon in the case of silicate.

The analysis performed in the center of the sample shows the presence of the silicate only with a composition that, within the limits of experimental uncertainty, is quite similar to that observed in the area close to the surface.

The composition of the secondary phases does not vary with the exposure time or with the type of TBC used. The long-time interaction layer is almost comparable to that shown in Figure 1 concerning a sample exposed for 1000 hours.

A similar study carried out on samples exposed to 1200C with ANS CMAS mixture is shown in Figure 130, after 1000 h (Figure 130-a) and 10000 h (Figure 130-b).

As in the case of the samples treated with STD mixture, the composition of the secondary phases remains constant regardless of the exposure time, and the interaction layer is approximately one third of the total thickness.

The secondary phases are formed both on the surface layer of contact with the mixture of oxides and in a layer immediately below, as described for the other mixture analyzed in Figure 128 and Figure 129.

The difference with the STD mixture is the presence of iron which enters the secondary phases stabilizing another compound than that observed in the mixtures without iron oxide. Aluminum and magnesium are always difficult to evaluate using EDS maps.

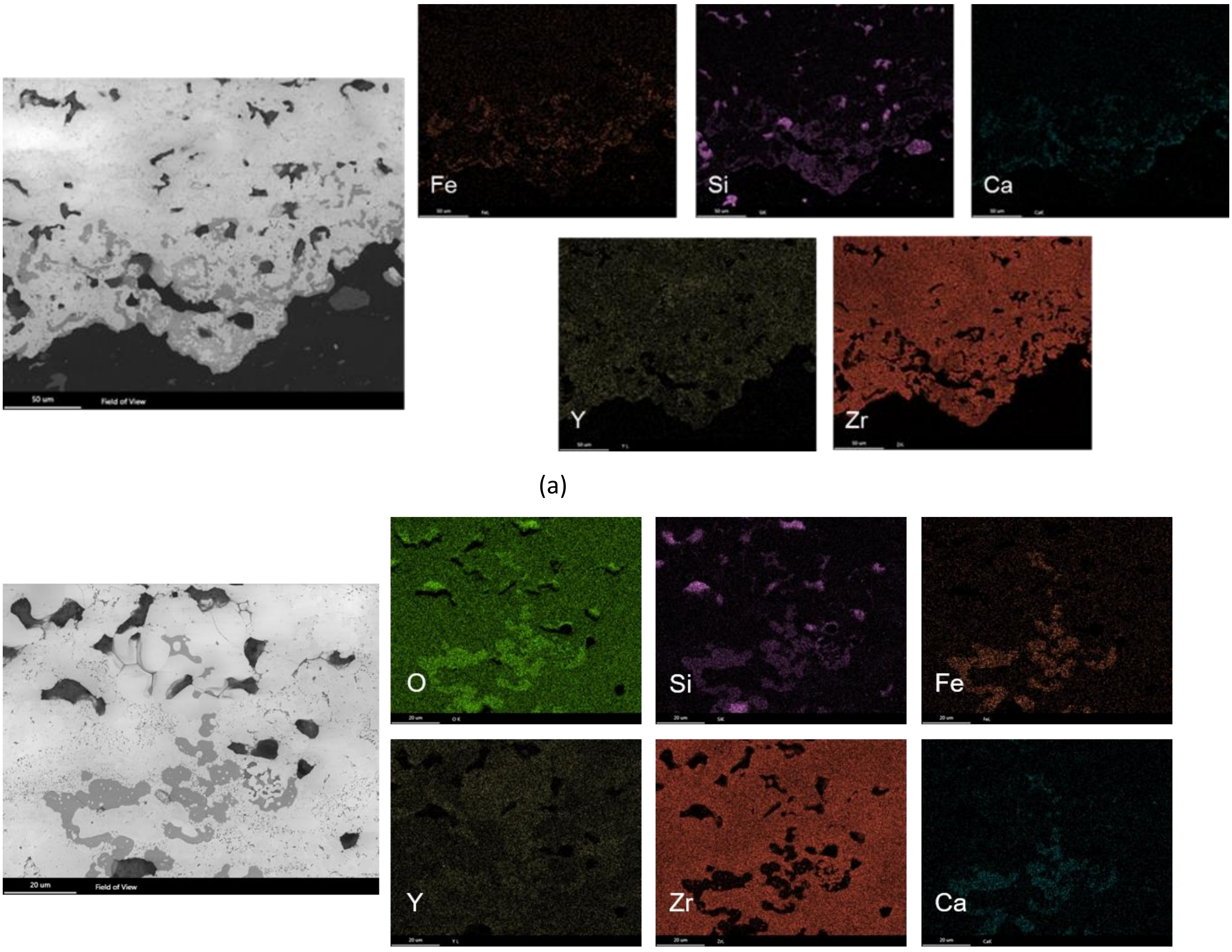

(a)

(b)

Figure 130 – EDS maps on samples 7YSZ exposed at 1200°C for 1000 h with ANS CMAS (a) and particular of EDS maps on samples 7YSZ exposed at 1200°C for 10000 h with STD CMAS (b)

The Figure 131 shows the punctual analysis obtained on the sample exposed to 1200C for 1000h. As in the previous case, zircon is stable with a stoichiometric composition formed solely of silicon and zirconium, without solubilization of other elements. Garnet has a specific secondary phase of this type of interaction and, as in the case of CYSO, it solubilizes a lot of yttrium. This allows the monoclinic phase to form more easily.

The punctual analysis measured in the matrix in distinct areas allows observing a substantial decrease of the yttrium in certain areas of the sample, defining the monoclinic phase zones. The difference of the monoclinic phase with respect to the matrix (cubic and / or tetragonal) is also observable through the shape of the grains of the sample: the phases rich in yttrium tend to increase, while the monoclinic phase forms small grains close to each other due to the type of formation of this phase (martensitic type)

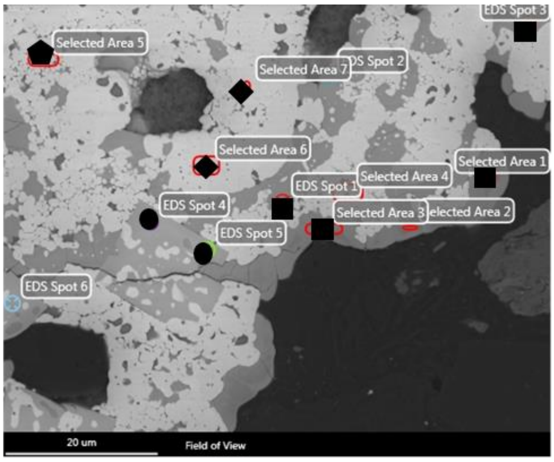

◆ **Matrix (c)**		
	wt%	at%
Fe	3,69	5,42
Mg	1,3	4,40
Al	0,76	2,31
Si	0,93	2,72
Y	**7,74**	**7,18**
Zr	**84,9**	**76,7**
Ca	0,63	1,30

⬟ **Matrix (m)**		
	wt%	at%
Fe	2,57	3,67
Mg	0,61	1,96
Al	0,9	2,65
Si	3,16	6,16
Y	**4,38**	**3,92**
Zr	**86,9**	**75,8**
Ca	1,52	3,02

● **ZrSiO4**		
	wt%	At%
Fe	1,21	1,41
Mg	0,566	1,31
Al	0,426	0,88
Si	**26,17**	**52,6**
Y	2,9	1,852
Zr	**69,83**	**43,2**
Ca	0,11	0,15

■ **Garnet**		
	wt%	at%
Fe	**24,13**	**18,75**
Mg	3,34	5,99
Al	1,89	3,06
Si	**21,27**	**32,76**
Y	**18,98**	**9,31**
Zr	4,19	1,98
Ca	**26,19**	**28,17**

Figure 131 - EDS punctual analysis of secondary phases in the sample interacted with ANS CMAS

The analysis on a 14YSZ sample is reported, as an example, in Figure 132.

The EDS maps do not seem to show secondary phases in the analysis of all thickness of the sample (Figure 132-a) and only the presence of silica in the holes of the specimen is found, derived from the cleaning powder used.

However, the higher magnification analysis of the contact surface with the CMAS (Figure 132-b) shows a microstructure comparable to that described for the other samples. This confirms that the type of secondary phases formed is unchanged, according to the type of substrate used, and the differences can only be on the total quantity of the present phase. In fact, in 14YSZ samples the amount of secondary phases is often below the detection limit of X-ray diffraction.

As in the case of 7YSZ samples, the exposure time does not change the composition of the secondary phases and does not particularly affect the interaction layer increase.

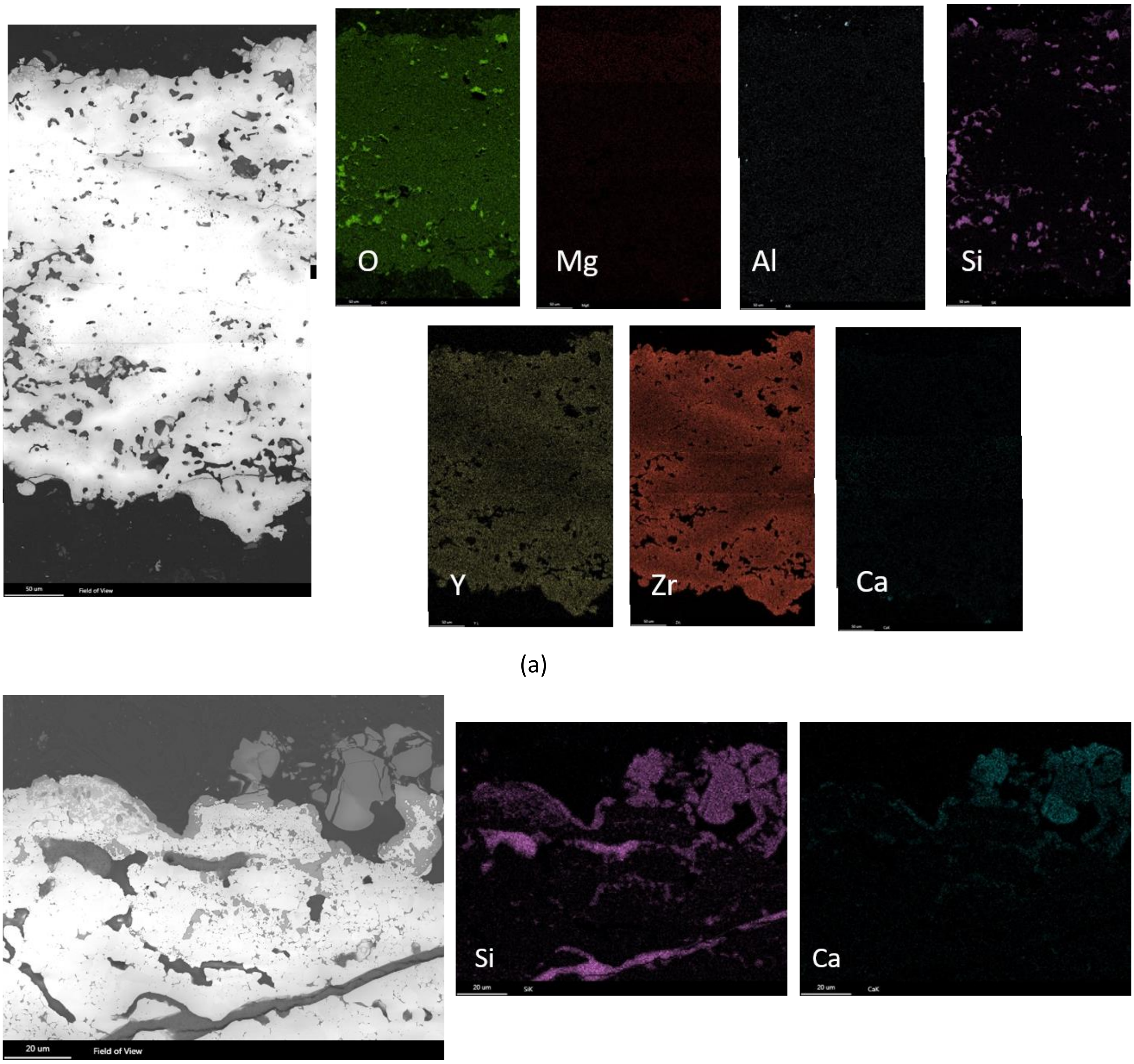

(a)

(b)

Figure 132 – EDS maps of all thickness (a) and particular of external layer (b) of 14B samples exposed at 1200°C for 5000h with STD CMAS

Analyzes carried out on samples exposed to high temperatures (1300 and 1400°C) never show secondary phases, with the exception of zircon. The microstructural analysis of a DL sample exposed for 1000 h at 1400°C is shown in the Figure 133 with the tables relating to the quantifications of the phases.

The analysis has been carried out on the opposite surface with respect to that on which the CMAS mixture was deposited. In fact, at this temperature the mixtures, regardless of the type used, are completely liquid, as confirmed by the DCS analyzes reported in Figure 87.

For this reason, the mixture crosses the entire thickness of the sample through the porosities and interacts only on the lower surface, forming zircon. The low or missing interaction of CMAS with TBC is confirmed by the composition of the CMAS mixture inside porosities which resulted to be the original one. Evidently, the temperature is too high to stabilize other secondary phases on the lower surface. Another reason may be due to the reduced quantity of CMAS available to interact with the material, due to trapping in the holes.

⬢ **Holes**		
	wt%	at%
Mg	**4,62**	**6,44**
Al	**10,6**	**13,4**
Si	**45,2**	**54,5**
Y	12,7	4,86
Zr	3,95	1,46
Ca	**22,7**	**19,2**

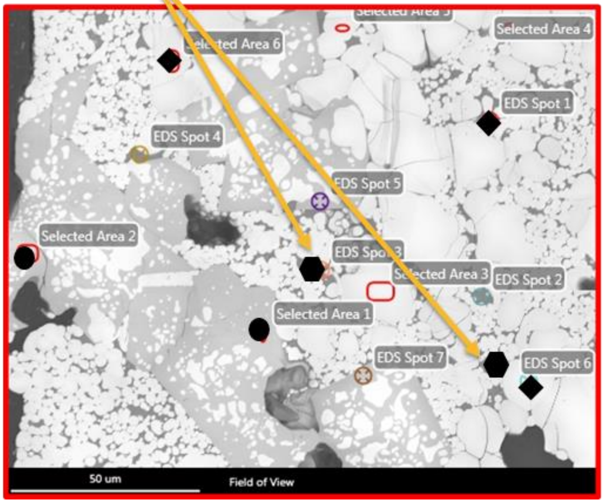

◆ **Matrix**		
	wt%	at%
Mg	0,31	1,14
Al	0,16	0,53
Si	0,91	2,85
Y	**13,7**	**13,53**
Zr	**84,3**	**80,8**
Ca	0,5	1,08

● **$ZrSiO_4$**		
	wt%	at%
Mg	0,56	1,30
Al	0,49	1,02
Si	**26,3**	**52,7**
Y	1,65	1,05
Zr	**70,9**	**43,8**
Ca	0,025	0,037

Figure 133 – EDS analysis of a DL sample exposed for 1000h at 1400C

An evaluation on the shape and size of the grains in the studied samples can be evaluated by EBSD analysis.

Figure 134 shows an analysis carried out by FEG-SEM with EBSD probe on a double layer sample (14YSZ overlying a 7YSZ layer) exposed for 300 h at 1400°C. In the image two different types of maps are reported: on the left the IPF map (inverse pole figures), useful to observe size and morphology of the grains, and on the right the "phase" map which highlights the different phases present with different colors.

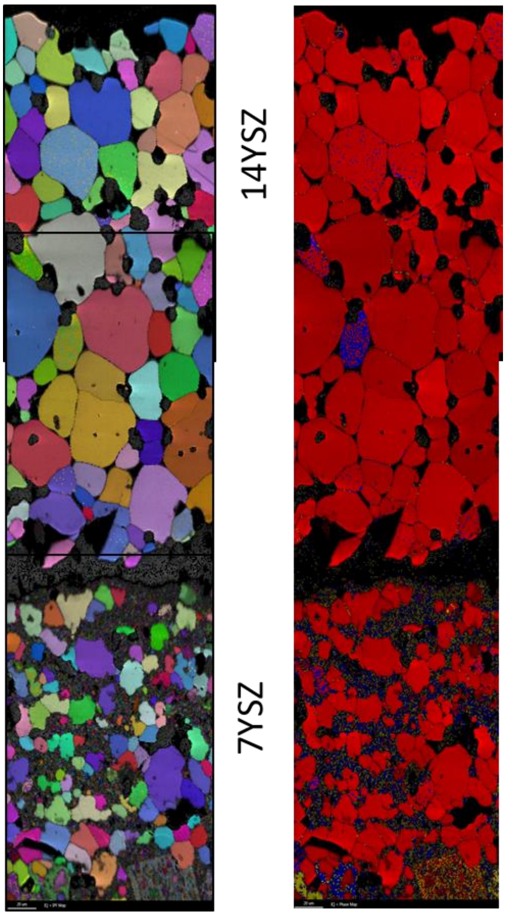

Figure 134 – EBDS IPF (a) and PHASE (b) maps of 14DLA exposed for 1400°C for 300h with STD CMAS

From the high-temperature analyzes it is observed that the grains of the material, especially those of the 14YSZ layer, grow a lot, more than in the material without CMAS. Furthermore, in the 7YSZ layer the monoclinic phase (in blue in the phase map) and the zircon near the lower surface (yellow phase in the phase map) are found. This result confirms that the monoclinic phase detected by X-ray diffraction in the double layer samples comes exclusively from the 7YSZ layer, while the 14YSZ one remains unaltered.

A detail of the transformation of the monoclinic phase in the layer with 7% of Y_2O_3 is shown in Figure 135, where, through the IPF map, it is possible to observe the m phase lamellar structure typical of the martensitic transformation of this phase.

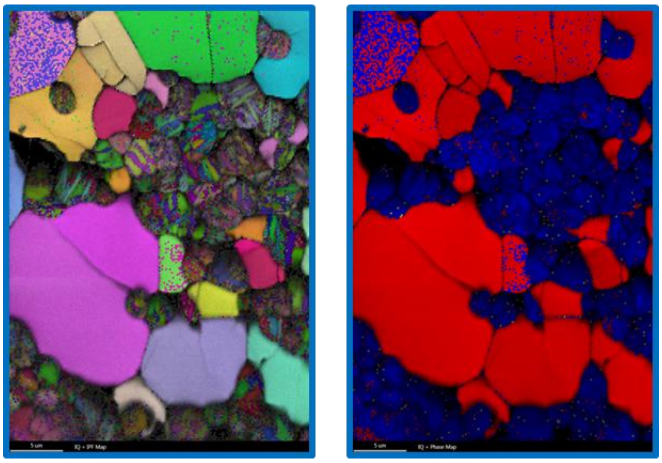

Figure 135 – Particular of 7YSZ part in sample

5.3 Physical proprieties results

The diffusivity measurements of the materials described in the previous paragraphs were measured by thermography.

The purpose of this study is to evaluate how the exposure to high temperature, and therefore the microstructural and phase distribution modification, affects the physical properties of the material. In fact, as described in chapter 2.5, thermal conductivity is a very important characteristic of thermal barriers, and the massive presence of the monoclinic phase worsens it considerably.

The diffusivity tests have been obtained on free standing samples covered with a layer of conductive graphite. Five measurements per sample have been carried out to have a correct value of the diffusivity.

The measurements obtained at the Ansaldo Energia materials laboratory, using a flash source, are shown in Table 28.

The CNR of Padova, with a laser source and using samples with standard geometry (13 mm), has replicated some obtained values. For each sample 16 measurements per sample have been done, to validate the measurements made at Ansaldo Energia. The results are shown in the Table 29.

The difference between the values obtained from the two analyzes is shown graphically in the Figure 136 (regarding only 7YSZ and DL without CMAS) and shows a small discrepancy, which allows us to consider the values shown in the Table 28 as reliable. In general, the measurements obtained through the analyzes carried out in the Ansaldo Energia materials laboratory tend to be slightly higher than those obtained at the CNR in Padua. This may be due to the diversity of instrumentation used, even with the same type of calculation software.

In any case, the comparison was made only to validate the technique used in Ansaldo (new instrumentation) considering as the true value the value obtained by the CNR (more experts in this type of measurement). The comparison allows to validate the technique as the difference between the two measures is always less than 5%, which is the defined acceptability limit in this type of analysis.

Table 28 - Measurements obtained at the Ansaldo Energia materials laboratory

		NC		**STD**		**ANS**	
	Time	Diffusivity (10^{-7})	St.dev. (10^{-7})	diffusivity(10^{-7})	St.dev. (10^{-7})	diffusivity(10^{-7})	St.dev. (10^{-7})
7YSZ	0						
	0	3,46	0,03				
	1100						
	3000	4,23	0,07	3,13	0,04	3,15	0,02
	5000	4,44	0,07	3,35	0,09	4,25	0,12
	10000	5,53	0,06	4,54	0,07	4,09	0,07
	1200						
	3000	5,43	0,18	6,45	0,15	8,58	0,13
	5000	7,86	0,57	8,83	0,37	10,00	0,92
	10000	8,48	0,19	6,95	0,14	9,67	0,20
	1300						
	1000	8,73	0	12,45	0,36	11,07	0,07
14YSZ	0						
	0	2,98	0,03				
	1100						
	5000	4,49	0,11	5,47	0,17	4,07	0,08
	10000	4,76	0,06	4,47	0,09	4,32	0,05
	1200						
	3000	5,79	0,27	8,49	0,25	7,87	0,11
	5000	5,23	0,18	6,83	0,14	6,95	0,18
	10000	4,93	0,16	6,09	0,21	6,46	0,26
	1300						
	1000	7,38	0,44	7,08	0,80	9,20	0
DL	0						
	0	2,29	0,015				
	1100						
	3000	3,54	0,04	3,68	0,02	3,40	0,12
	5000	3,64	0,04	3,50	0,02	3,25	0,02
	10000	5,06	0,07	4,02	0,06	4,28	0,07
	1200						
	3000	5,62	0,030	6,35	0,07	5,92	0,04
	5000	4,86	0,042	5,11	0,03	4,97	0,06
	10000			5,71	0,04	5,37	0,05
		1300					
	1000	6,24	0,08	7,4	0,01	7,70	0,09

Table 29 - Measurements obtained at the CNR-ITC laboratory

		NC		STD		ANS	
	Time	diffusivity(10^{-7})	St.dev. (10^{-7})	diffusivity(10^{-7})	St.dev. (10^{-7})	diffusivity(10^{-7})	St.dev. (10^{-7})
7YSZ	0						
	0	3,07	0,12				
	1100						
	5000	4,24	0,16	2,81	0,10	3,43	0,13
	1200						
	5000	6,40	0,26	7,60	0,30	8,64	0,34
	1300						
	1000	8,17	0,33	16,10	0,78	13,70	0,66
DL	0						
	0	1,81	0,41				
	1100						
	5000	3,27	0,82	3,10	0,08	2,92	0,08
	1200						
	5000	4,31	0,11	4,75	0,14	4,60	0,11
	1300						
	1000	4,92	0,11	5,59	0,18	5,90	0,15

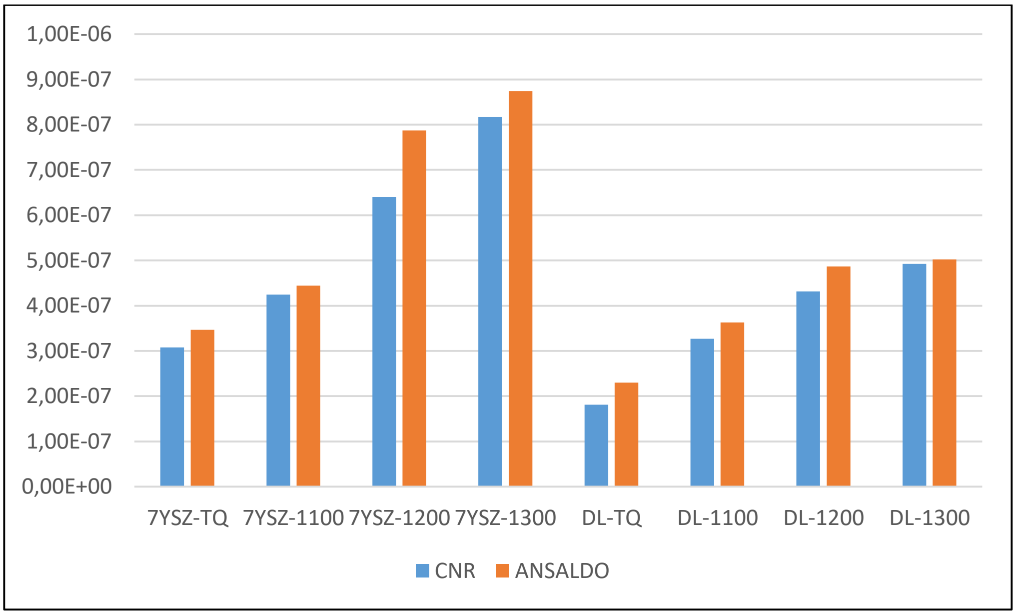

Figure 136 - Difference between the values obtained from CNR of Padova and Ansaldo laboratory

The diffusivity values, obtain for one batch of each material, are reported in Figure 137. The samples without CMAS are reported with continuous line, the STD samples with dashed line, while samples with CMAS ANS with dotted line.

The results seem to show that the most important effect about variation of diffusivity is the temperature, while the effect of presence of CMAS is less evident.

The diffusivity has the same trend independently to the type of material tested, but the greatest growth is observed in the 7YSZ samples.

The diffusivity in samples as prayed is similar for 7YSZ and 14YSZ, while seems to be smaller in DL materials. This could be related to small differences in porosity, which are difficult to measure.

At 1100°C, the materials show the constant values, with a slight increase in diffusivity only after 10000 h of exposure.

At 1300°C the only sample measured (after 1000h) does not allow to evaluate the evolution over time, but an increase in diffusivity seems evident due to the presence of CMAS.

At 1200°C, the samples of 7YSZ show an increase up to 5000 h with a subsequent decrease in diffusivity (or constant values), while for 14YSZ and DL the descent is already observable after 3000 h.

The trend does not traces the variation of monoclinic phase shown in chapter 5.1.In fact, the diffusivity depends to various factors such as present phases, porosity, cracks and other local defects.

Finally, the instrumentation present in the CNR lab permits to obtain value of diffusivity measured in air and in vacuum. The difference of the two measurements allows in percentage a qualitative evaluation of the effect of sintering in samples exposed to high temperatures. The values are shown in the Figure 138.

In both type of material, a decrease in values between those obtained in air and in vacuum is observed. This effect seems more evident with the presence of CMAS.

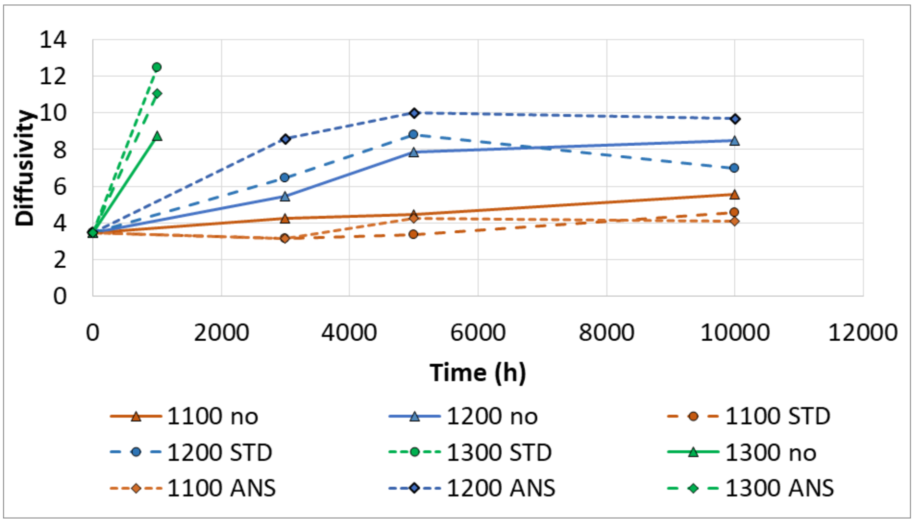

(a)

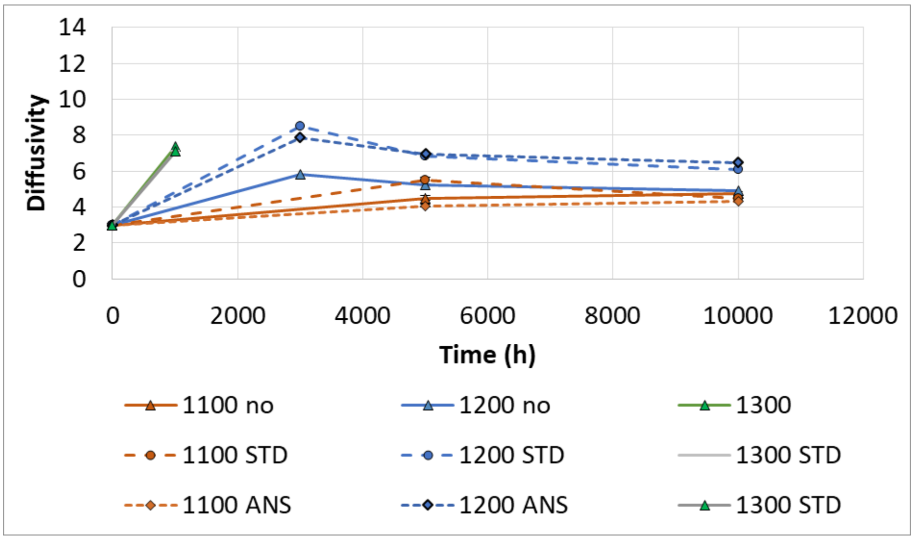

(b)

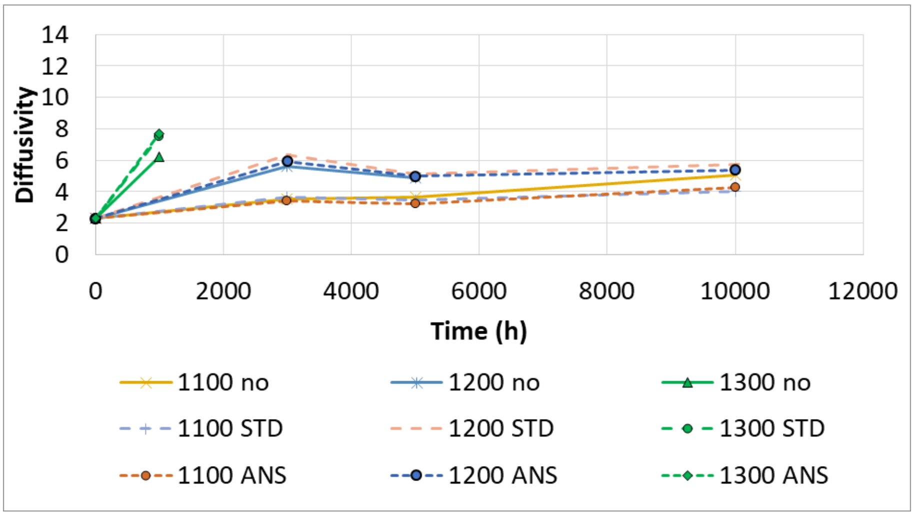

(c)

Figure 137 - Variation of the diffusivity of the samples 7YSZ (a), 14YSZ (b) and DL (c) exposed to 1100, 1200 and 1300°C for different times.

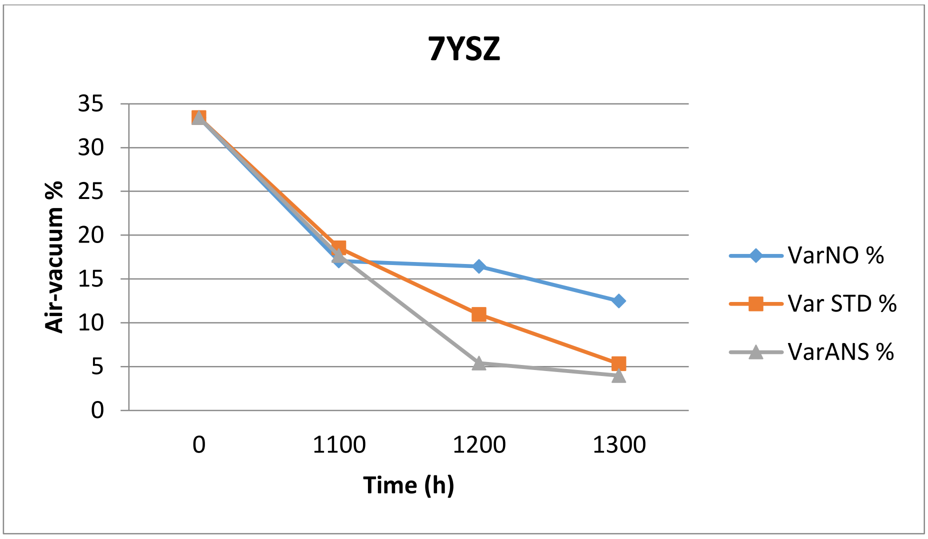

(a)

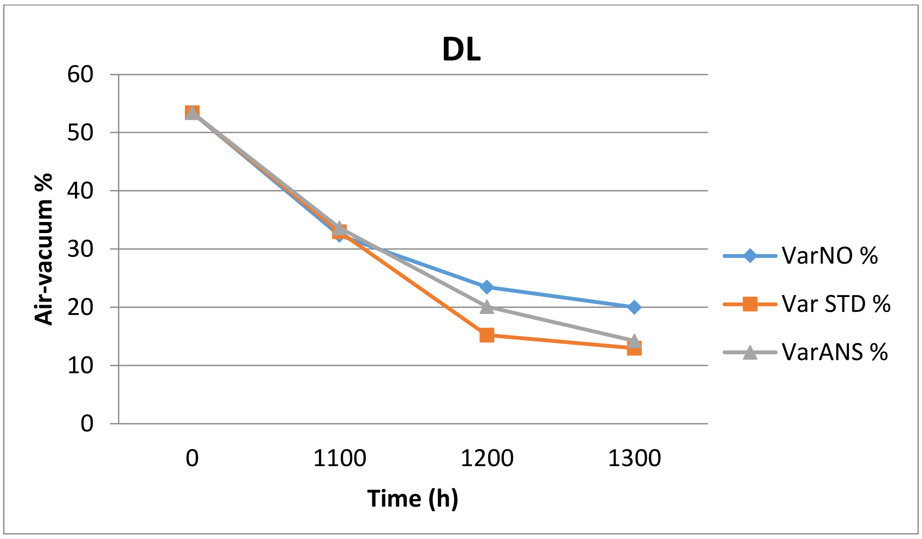

(b)

Figure 138 - Percentage difference in diffusivity variation between measurements in air and in vacuum for 7YSZ (a) and DL (b) samples

The diffusivity measurements performed during this thesis work allowed to validate a new technique for the Ansaldo Energia laboratory, determining the instrumental setup, the acquisition methods and the data processing. This was possible thanks to the collaboration with the CNR of Padua, which made it possible to compare measurements made on the same specimens and to optimize the post-data acquisition processing file.

Although only in the initial phase of knowledge of the technique, the results obtained on the samples exposed in a high temperature oven show a trend similar to that measured by the usual analysis techniques of a materials laboratory.

In fact, an effect of the increase in diffusivity limited to 1100°C and much higher at 1300°C is confirmed. At 1200°C the diffusivity increases with time, as happens for the monoclinic phase, up to 5000h and then remains constant. This happens because other factors (such as porosity) intervene in the diffusivity measurement that will have to be evaluated in the future to evaluate other physical properties such as thermal conductivity.

Finally, the difference in the measurements carried out in air and in vacuum, even if only on a qualitative level, confirm the tendency to sinter the material with increasing temperature and with the presence of CMAS, as described in the paragraph 5.2.

5.4 Discussion

The experimental results presented in the previous section are discussed in the following for all tested materials: 7YSZ, 14YSZ and DL.

5.4.1 Comparison between samples with and without CMAS

5.4.1.1 7YSZ evolution

According to the literature data, 7YSZ is the material where greater phase modifications occurs after exposure at high temperature.

Regardless of the presence of CMAS, at 1100 °C the matrix always remains t^+ for all exposure times, while the c phase tends to form after short times at 1200 °C, becoming the main phase always before 3000 h. At higher temperatures (1300 and 1400°C) the c phase is the only one detected.

The presence of CMAS mainly affects the evolution of the m phase.

Figure 139 shows the m phase evolution in the two 7YSZ batches for all the tested temperatures. Samples with STD CMAS, ANS CMAS and without CMAS are reported in separate plots. The thermodynamic equilibrium is reached after 300h at 1400 °C and after 1000 h at 1300 °C (in particular, for samples with CMAS). The effect of CMAS corrosion is mostly evident at 1200°C, where the m phase grows faster than in the case of the samples without CMAS. Especially samples with ANS CMAS show an amount of m phase after 3000-5000 h, comparable to that measured at the highest temperatures. Finally, a temperature of 1100°C seems too low to detect important variations of phase amounts as a consequence of the CMAS interaction.

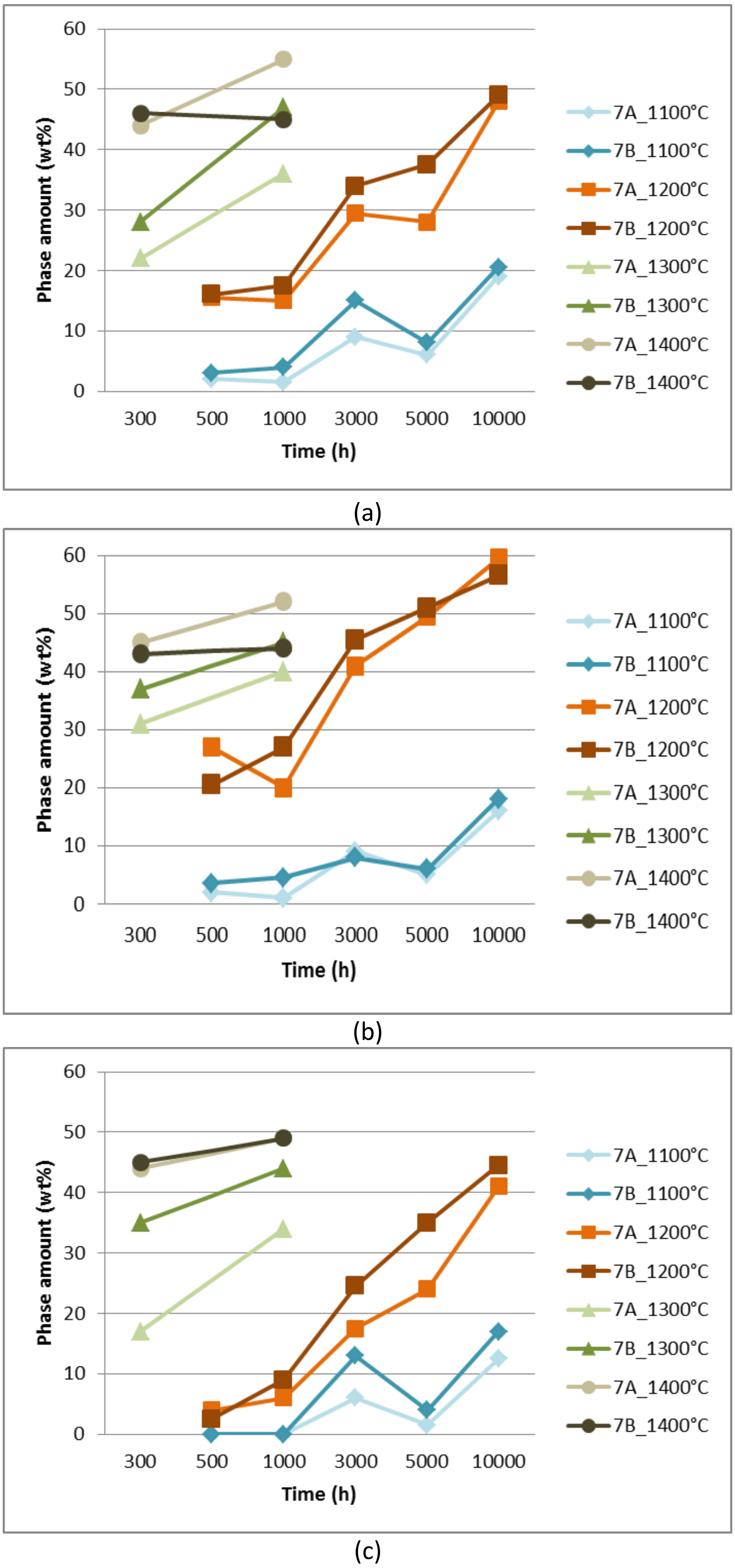

Figure 139 – Trend with time of m phase amounts at all tested temperatures in a 7YSZ sample tested with STD CMAS (a), ANS CMAS (b) and without CMAS (c).

5.4.1.2 14YSZ stability

The 14YSZ samples maintain the c structure at all the temperatures, regardless of the presence of the CMAS. Only at 1200°C, about 10% of m phase has been identified, which could be the thermodynamic equilibrium amount. As previously observed in 7YSZ, the ANS mixture seems to favor the phase transformation kinetics. Samples exposed without CMAS show the presence of small quantity of m phase only after 5000 h. This quantity is within the limits of the measurement uncertainty. Samples exposed for longer aging times could confirm the presence of this phase also in samples without CMAS. The effect of CMAS at 1200°C seems to accelerate phase transformations, acting on kinetic phenomena rather than modifying the thermodynamic equilibrium of the starting material.

5.4.1.3 DL behavior

The HJP parameter, proposed by Lipkin et al.[101] and used by Cernuschi et al.[98], allows to plot in the same graph phase quantification results of different samples exposed for different times and at different temperatures. It is defined as:

$$HJP=T[C+\ln t]$$

where T is the temperature in K, t is the exposure time in h and C is a constant (C=27).

The HJP parameter has been used to plot trends of the m (Figure 140-a), c (Figure 140-b), and t^+ phases (Figure 140-c) for all the results obtained in the present work.

Trend lines have been added to better appreciate the evolution of these phases for all the materials tested. The continuous line refers to 7YSZ, the dashed one refers to DL and the dotted line refers to 14YSZ.

As for the m phase (Figure 140-a) the three trends are not very different at low HJP, while they are clearly dissimilar for HJP > 50000. Indeed, at high HJP values, the amount of m phase is around 50% in 7YSZ, less than 10% in 14YSZ and shows an intermediate value in DL.

Similar behavior is shown by the c phase reported in Figure 140-b where, at high HJP values, it is possible to observe clearly different phase amounts: higher quantity in 14YSZ, lower quantity in 7YSZ, and an intermediate situation in DL.

T^+ is never stable in 14YSZ samples, so in Figure 140-c only 7YSZ and DL are shown. In this case different trends can be observed at low HJP values, while for HJP > 50000 this phase disappears in all the samples.

In this type of graph, it is difficult to appreciate the effect of CMASs on samples, but it is clear that DL samples have an intermediate situation with respect to the single layer ones.

Although the CMAS has been sprayed on the 14YSZ layer, the oxide mixture mainly interacts with the 7YSZ, because the mixture exposed to high temperature percolates by gravity towards the lower layer, causing an accelerate formation of m phase with respect to samples without CMAS.

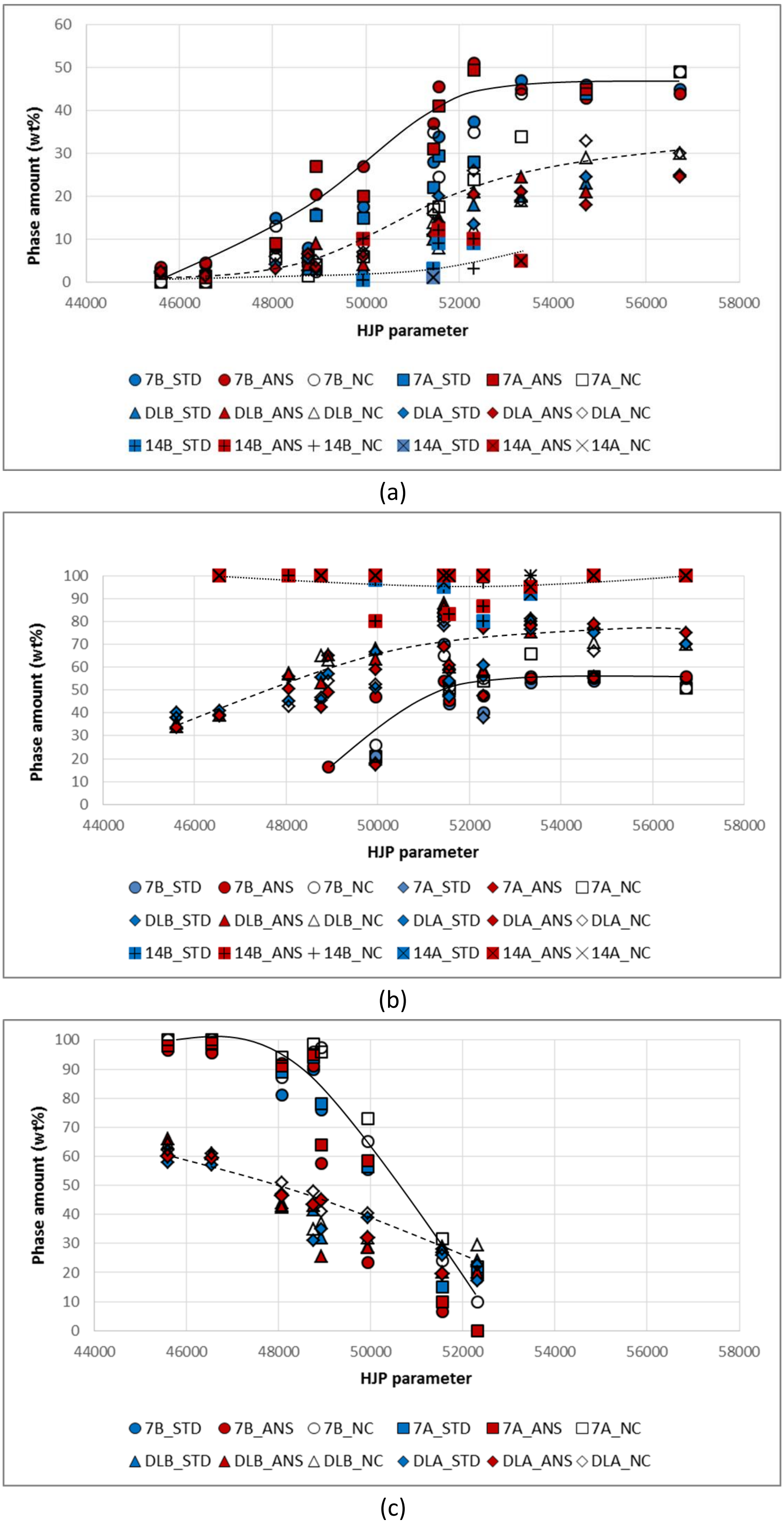

Figure 140 – m (a), c (b) and t (c) phase evolution in all samples tested

5.4.1.4 Secondary phases formation

Secondary phases formed by interaction between TBC and CMAS do not exceed 5-10%, mainly because the quantity of CMAS deposited is limited and because the secondary phases tend to form on surfaces before it percolates in the bulk. Therefore, they are less recognizable in the XRD analysis of the pulverized samples.

The main phases resulting from the interaction between TBC and CMAS are silicates formed by yttrium present in YSZ and calcium (forming CYSO) or iron (forming Garnet) present in CMAS. These phases are found especially after treatment at 1200°C. Indeed, at 1100°C their formation is inhibited by kinetics, while at higher temperature (1300 and 1400°C), interaction is probably reduced due to the CMAS melting points lower than these testing temperatures. In fact, above 1300°C the liquid CMAS tend to penetrate in the porosity of materials, arriving at the bottom of the sample holder. In this way, the CMAS does not remain enough time in contact with the TBC to adequately interact. Furthermore, there is the risk of polluting other samples placed on the same sample holder. So, there is not much difference between the samples tested with and without CMAS at the highest temperatures.

The only phase formed by CMAS corrosion at the higher temperatures is zircon ($ZrSiO_4$), thanks to its high melting point. This secondary phase does not depletes the yttrium matrix, so it should not cause an increase of m phase.

5.4.2 Comparison with literature results

Comparison with previous works is not easy because, usually, short exposure times have been used in the investigation of interactions between TBC and CMAS.

Only in a few cases, long exposure times have been applied to materials similar to those investigated in this theasis. In such cases a comparison is possible, and it is shown in Figure 141. To merge all results about one phase in the same graph, HJP parameter has been used. From the present theasis only 7YSZ has been considered (open symbols), because most of the literature works use materials with 7-8 wt% yttria.

In Figure 141-a, the evolution of t phase with HJP is shown without distinction between t and t’. So, the sum t+t’ has been reported in the graph when the two values were available.

In Figure 141-b, the trend of c phase is reported. In some papers, the quantity of t’’ was reported separately, but here it is plotted in the same graph of c phase, as already done by Cernuschi [98].

Finally, in Figure 141-c, the amount of m phase is shown.

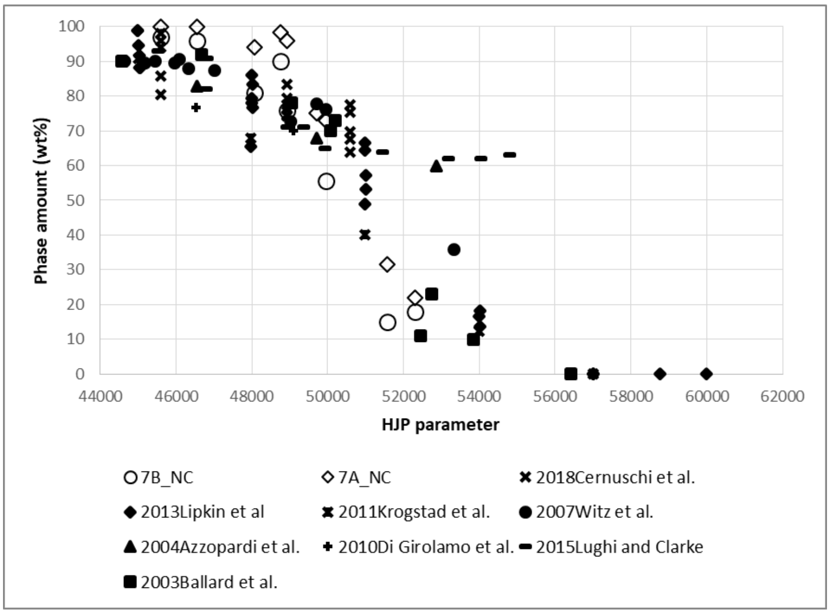
Phase amount (wt%)
0
10
20
30
40
50
60
70
80
90
100
44000
46000
48000
50000
52000
54000
56000
58000
60000
62000
HJP parameter
7B_NC
7A_NC
2018Cernuschi et al.
2013Lipkin et al
2011Krogstad et al.
2007Witz et al.
2004Azzopardi et al.
2010Di Girolamo et al.
2015Lughi and Clarke
2003Ballard et al.

(a)

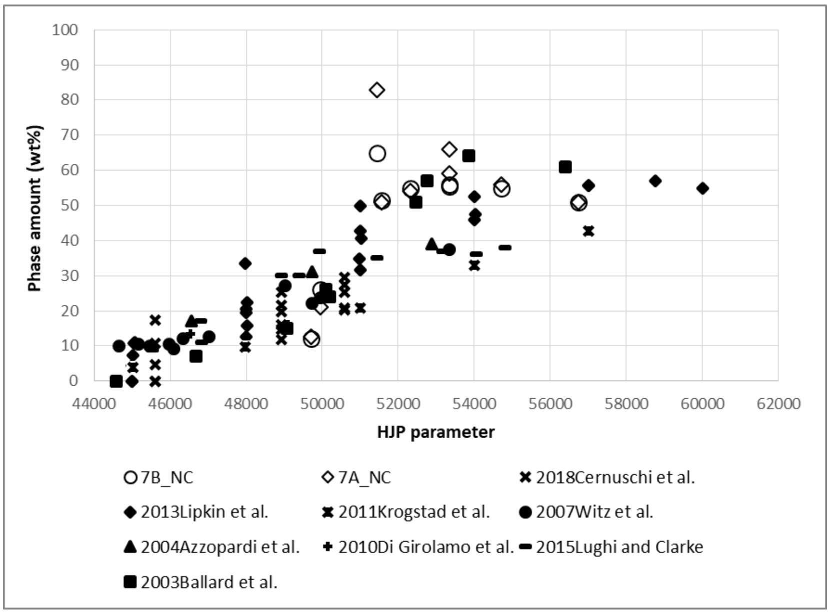
Phase amount (wt%)
0
10
20
30
40
50
60
70
80
90
100
44000
46000
48000
50000
52000
54000
56000
58000
60000
62000
HJP parameter
7B_NC
7A_NC
2018Cernuschi et al.
2013Lipkin et al.
2011Krogstad et al.
2007Witz et al.
2004Azzopardi et al.
2010Di Girolamo et al.
2015Lughi and Clarke
2003Ballard et al.

(b)

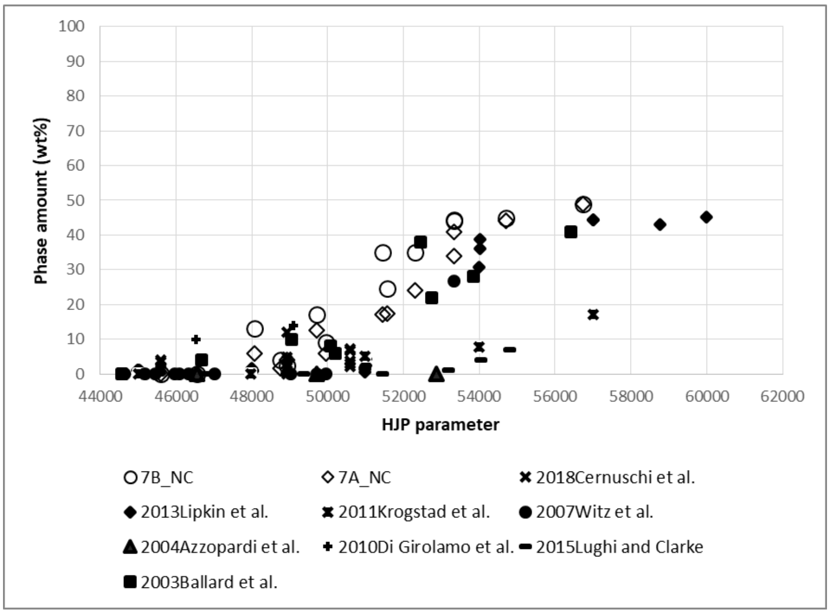

(c)

Figure 141 – Comparison with literature results of t (a) c (b) and m (c) phase evolution

The comparison shows a general good agreement in all tested ranges. Indeed, t phase tends to decrease around HJP 49000-50000 and to reach zero around HJP 55000. The c phase increases up to a maximum around HJP 51000-53000, remaining almost constant at higher HJP values. The amount of m phase is small (less of 10%) until HJP 51000, subsequently it has a rapid increase at HJP 51000-53000 and then it remains constant at about 50% for high HJP values.

Only values obtain by Azzopardi et al.[104], Lughi and Clarke[105] and Krogstad et al.[106] show a different behaviour: in these works the t phase, at high HJP, remains more stable at the expenses of c and, especially, m phases. In particular, m phase remains below 10% for all the studied HJP values. These differences are probably due to the different spraying methods used by these authors to produce the samples: Lughi and Clarke[105] and Azzopardi at al.[104] used samples obtained by EB-PVD, while Krogstad et al.[106] synthesized materials from powders.

5.4.3 Lattice parameter at 1100 and 1200°C

The large number of XRD analyses carried out in this work makes possible a discussion about lattice parameter variations with temperature and exposure time for the t’ and c phases. Trends of the *a* and *c* lattice parameters of t’ phase in 7YSZ samples are reported as a function of the exposure time in Figure 142 for samples treated at 1100 °C, and in Figure 143 for samples at 1200 °C.

The graphs show a general tendency of c parameter to increase and a parameter to decrease with increasing exposure time, regardless of the presence or type of CMAS. This is more evident at 1200°C, because at 1100°C the transformation is too slow.

These phenomena are explained by thermodynamic factors. Indeed, the t’ phase is not stable and is formed during plasma spay deposition (in out of equilibrium conditions). During exposure time, this phase tends to transform into t phase. The lattice parameters reported in literature for the two phases are listed in Table 30.

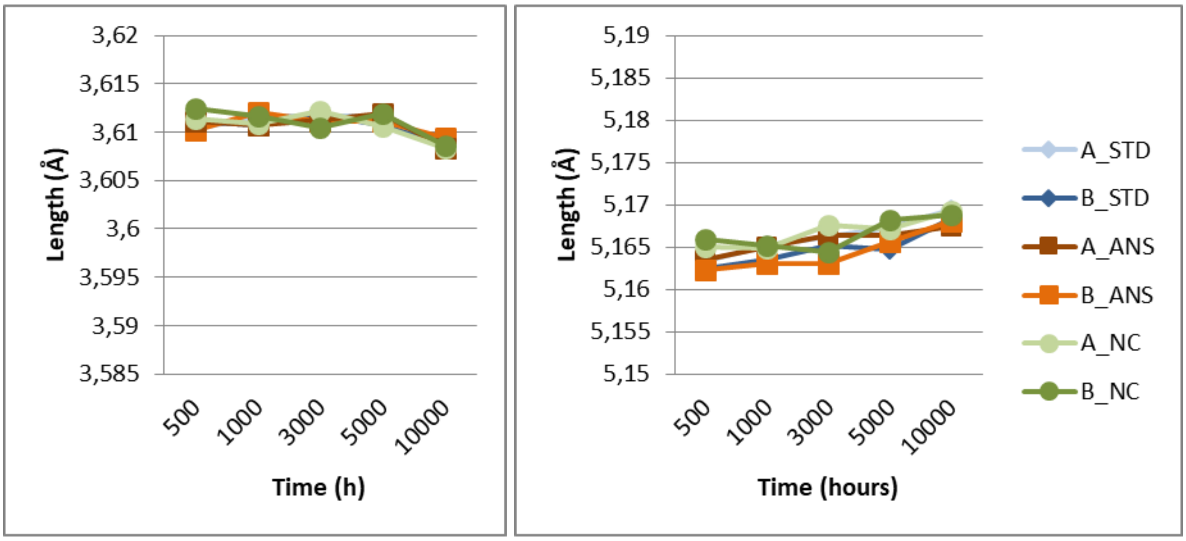

(a) (b)

Figure 142 – Lattice parameter of t’ phase a (a) and c (b), calculated by Rietveld method on 7YSZ samples exposed at 1100°C after 500, 1000, 3000 and 5000 h

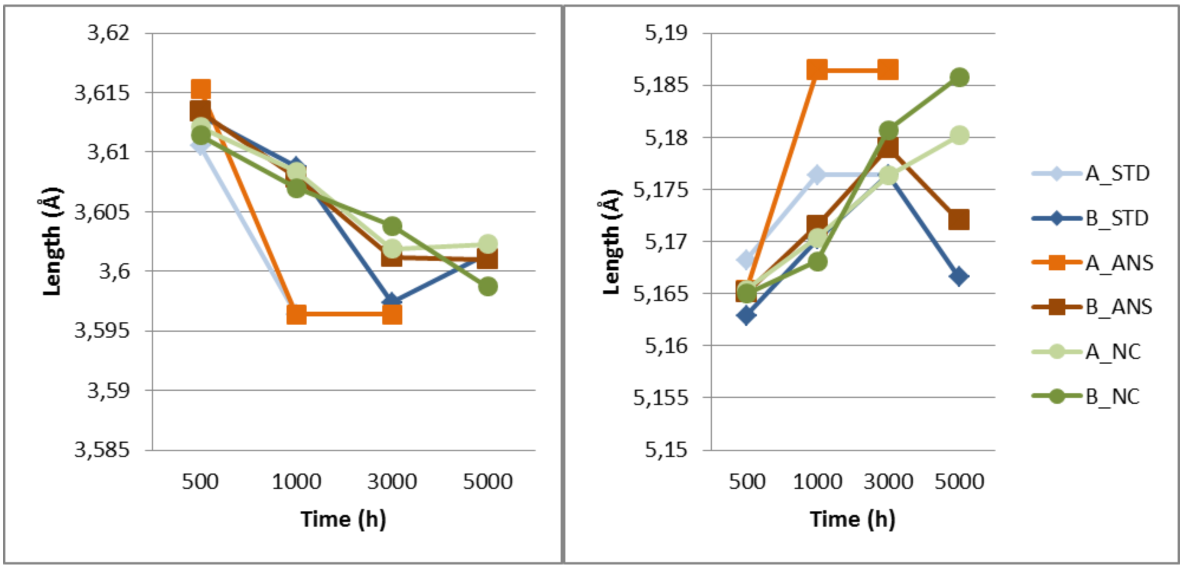

(a) (b)

Figure 143 - Lattice parameter of t’ phase a (a) and c (b), calculated by Rietveld method on 7YSZ samples exposed at 1200°C after 500, 1000, 3000 and 5000 h

Table 30 – Lattice parameter of t [60] and t’[61] phases

Phase	Lattice parameter (Å)	
	a	*c*
t’	3.6100	5.1650
t	3.6040	5.1800

The evolution of lattice parameter *a* of the c phase is reported in Figure 144 for 7YSZ and 14YSZ exposed at 1200°C. For 14YSZ samples the a parameter tends to remain constant around the literature value (*a*=5.1300 Å) [62], while for 7YSZ there is more scatter. For this material, c phase tends to form at about 1000 h in out of balance conditions. Indeed, the starting value is always higher than the reference one and tends to decrease, according with thermodynamic, with the aging time. As observed at this temperature for m phase, the ANS CMAS seems to accelerate this phenomenon.

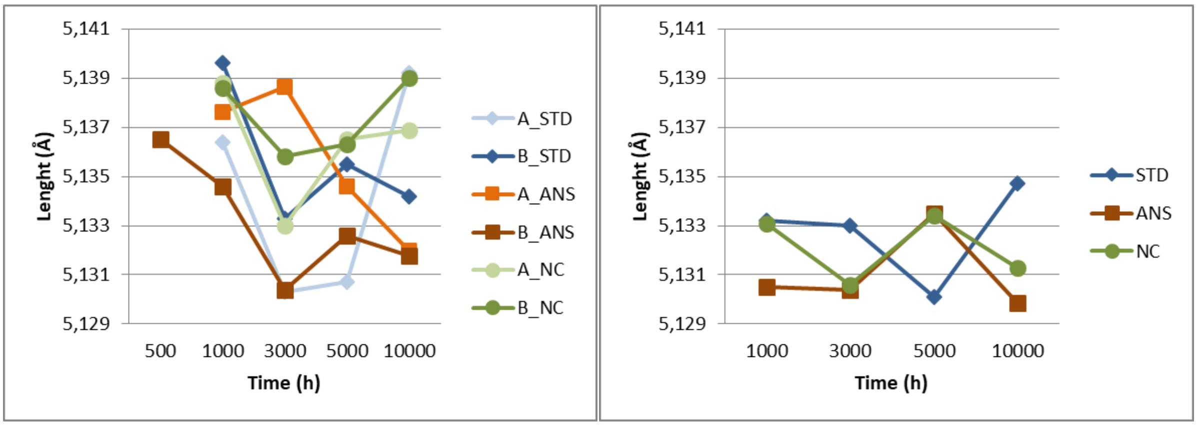

(a) (b)

Figure 144 - Lattice parameter of c phase, calculated by Rietveld method on 7YSZ (a) samples and 14YSZ (b) exposed at 1200°C after 500, 1000, 3000,5000 and 10000 h

In some literature papers [85,86,107,108] the variation of lattice parameter with respect to the composition of yttria is studied.

The most significant works were summarized by Krogstad[106], showing a good correlation between them. To simplify the discussion and clarify the interphase relationships, the tetragonal data are presented using a pseudo-cubic (distorted fluorite) unit cell, as used by Lefevre [85] and Scott[86]. The c/a ratio decreases with $YO_{1.5}$ concentration and it approaches an ideal value of$\sqrt{2}$.

In Figure 145 the comparison of t and c lattice parameters calculated by Krogstad[106] and obtained in this work is reported. The parameters obtained after 1200°C at 5000 h, that can be considered the ones closer to the equilibrium, are shown with open symbols.

The c phase lattice parameter agrees with other values reported in literature, while bigger differences are observed for t phase. Probably because the t phase studied in this work is not yet in complete thermodynamic equilibrium. This is confirmed by comparing the *c/a* ratio of the t parameters with those of the literature, reported in Figure 146, where the value obtained in this work is out of the trend shown by samples in equilibrium conditions.

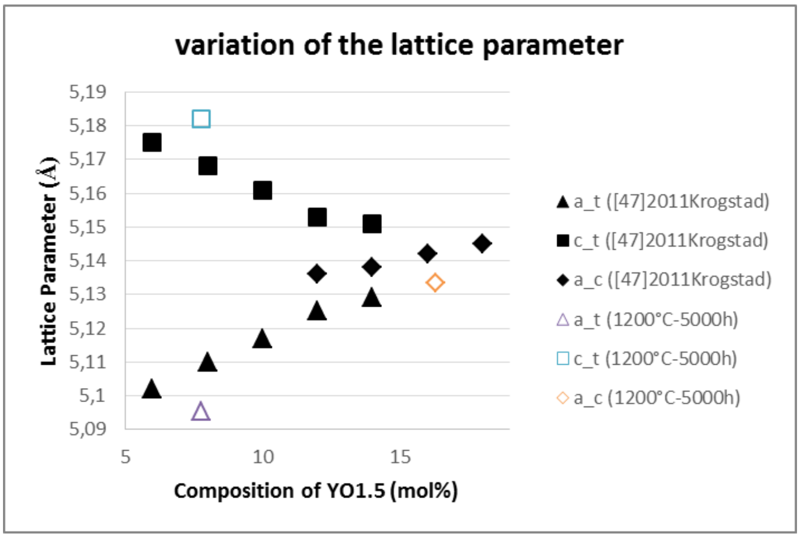

Figure 145 – Comparison of variation of the lattice parameters (c and t phases) between literature and this work

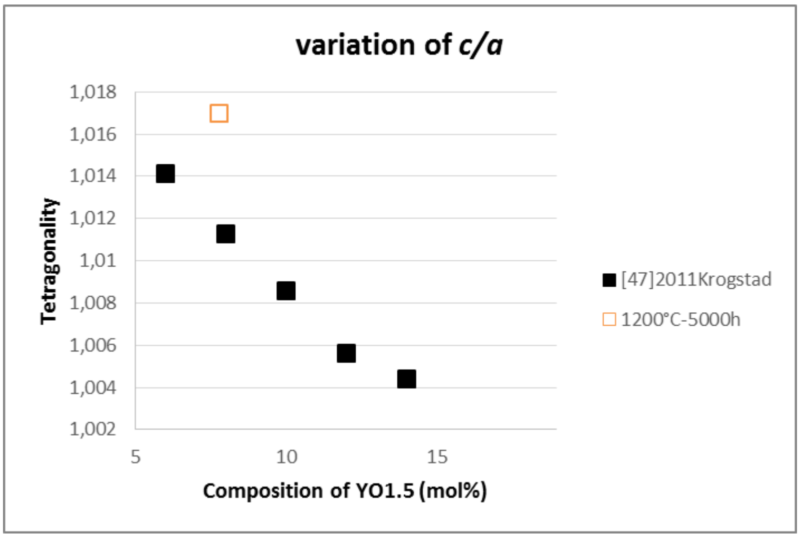

Figure 146 - Comparison of variation of c/a (t phases) between literature and this work

6 Phase modelling and thermodynamic assessment of oxide systems

6.1 Phase modelling

In Table 31 is reported the main solid solution phases studied in this work, where is underlined the crystal structure and the thermodynamic model used. In this case with the symbol C^+ is indicated the mixture of cations in that sublatice.

Table 31 - MgO-Y_2O_3-ZrO_2 phases: crystal structure and thermodynamic phase models

Phase	Pearson symbol / Prototype / Space Group	Sublattices	Thermodynamic Model
F-ZrO_2 Fluorite	cF12 CaF_2 Fm-3m	O in 8*c* Zr in 4*a*	$(4a)_2\ (8c)_4$ $(C^+)_2\ (O^{2-},Va)_4$
T-ZrO_2	--- --- $P4_2/nmc$	O in 4*d* Zr in 2*b*	$(2b)_2\ (4d)_4$ $(C^+)_2\ (O^{2-},Va)_4$
M-ZrO_2	--- --- $P2_1/c$	O in 4*e’* + 4*e”* Zr in 4*e*	$(4e)_2\ (4e + 4e)_4$ $(C^+)_2\ (O^{2-},Va)_4$
C-Y_2O_3	cI80 (Mn0.5Fe0.5)2O3 Ia-3	O in 48*e* Y in 24*d* + 8*a* Va in ¼ of 16*c*	$(24d + 8a)_2\ (48e)_3\ (1/4 \text{ of } 16c)_1$ $(C^+)_2\ (O^{2-},Va)_3\ (O^{2-},Va)_1$
H-Y_2O_3	hP5 La_2O_3(HT) $P6_3/mmc$	O in 4*f* + 2*a* Y in 4f Va in 2b	$(4f)_2\ (4f + 2a)_3\ (2b)_1$ $(C^+)_2\ (O^{2-},Va)_3\ (O^{2-},Va)_1$
MgO, Halite	cF8 NaCl Fm-3m	Mg in 4*a* O in 4*b*	$(4a)_1\ (4b)_1$ $(C^+,Va)_1\ (O^{2-})_1$

6.1.1 *M-ZrO_2, T-ZrO_2 and Fluorite models*

A model $(C^+)_2\ (O^{2-},Va)_4$ has been adopted in according with crystallographic information to study these phases. The interaction parameters for the different end members created by the model can be evaluated, in particular when we consider systems formed by cations with charge +4 and +3 (like ZrO_2-Y_2O_3 system). Indeed, the neutral planes that are formed in the space of the site fractions must be considered in these systems. In a model formed by 4 species (Y^{3+}, Zr^{4+}, Va, O^{2-}) and 2 sublattices, the combination of the end members forms a square reported in Figure 147 [109].

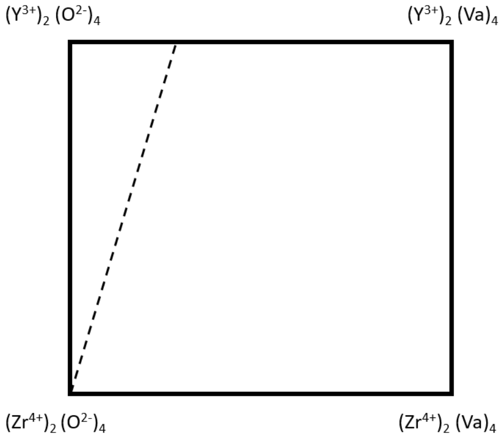

Figure 147 - Composition square for the ZrO_2 phase in the Y_2O_3-ZrO_2 system related to the occupation of the interstitial sublattice. Possible compositions are indicated by the dashed neutral line

In this square the stable corner is (Zr^{4+}:O^{2-}), the zirconia, and it is connected by an electroneutrality line (dashed) to a point placed in between two charged end-members: the positive (Y^{4+}:O^{2-}) and the negative (Y^{4+}:Va). When they are taken with the ratio 1:4 electroneutrality is obtained. The Gibbs energy of the neutral compound $(Y^{3+})_2(\ O^{2-}{}_{3/4},Va_{1/4})_4$ can be defined as GZRO2 + Z1 (where Z1 is a parameter to be optimized).

From this it is possible to write:

$$GZRO2 + Z1= 3/4\ G(Zr^{4+}:O^{2-})+1/4\ G(Zr^{4+}:Va)+4RT\ (3/4 \ln 3/4 + 1/4 \ln 1/4)$$

The last term is an entropic factor (a number on the basis of T).

The ZR^{4+}:Va parameter is defined as GZRO2 minus 4 oxygen ions, so, with reciprocal reactions, it is possible obtain the two end members remainder: (Y^{4+}:O^{2-}) and (Y^{4+}:Va).

6.1.2 C-Y_2O_3 and H-Y_2O_3 models

According to crystal structure data of C-Y_2O_3 there are two different positions occupied by Y^{3+} (24d and 8b) and one by O^{2-}(48e). The two Y^{3+} positions were merged into one thermodynamic sublattice since there is no data showing different occupancy of these positions in case of substitution of Y^{3+} by other cations. In case of substitution of Y^{3+} by ion with 4+ charge (for exemple Zr^{4+}) additional oxygen should be introduced to keep electroneutrality: therefore the interstitial position 16c was considered[110], which can be partially occupied by O^{2-}. In case of substitution of Y^{3+} by ion with 2+ charge (for exemple Mg^{2+}) vacancies are necessary to keep electroneutrality: therefore vacancies in the 48e site were considered.

The resulting thermodynamic model used to describe C-Y_2O_3 in the ternary system MgO-Y_2O_3-ZrO_2 system is then $(Mg^{2+},Y^{3+},Zr^{4+})_2\ (O^{2-},Va)_3\ (O^{2-},Va)_1$.

The presence of vacancies in the second sublattice occupied by O^{2-} is necessary to respect the electroneutrality in the MgO-Y_2O_3 system, while the presence of O^{2-} in the third interstitial site is necessary to maintain electroneutrality in Y_2O_3-ZrO_2 system.

Previous discussion of the C-Y_2O_3 model can be applied to H-Y_2O_3.

In the literature, Chen et al. [111] already introduced both O^{2-} and vacancies in both anionic and interstitial sublattices.

The interaction parameters for the different end members created by the model can be evaluated by considering the neutral planes that are formed in the space of the site fractions.

In the Y_2O_3-ZrO_2 system the most important square domain is that related to the occupation of the interstitial sublattice (Figure 148). It includes, at opposite corners, the two neutral configurations Y_2O_3 (Y^{3+}:O^{2-}:Va) and ZrO_2 (Zr^{4+}:O^{2-}:O^{2-}). They are connected by the neutral line, dashed in the figure.

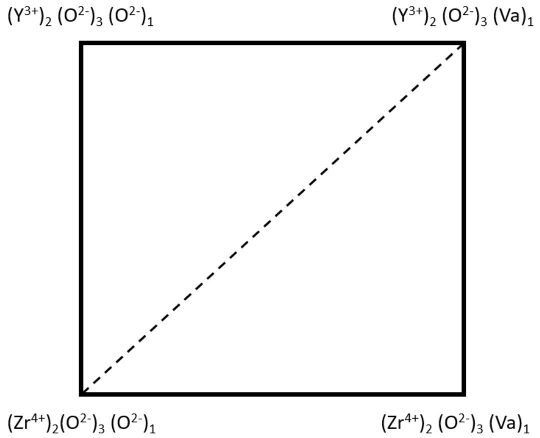

Figure 148 - Composition square for the Y_2O_3 phase in the Y_2O_3-ZrO_2 system related to the occupation of the interstitial sublattice. Possible compositions are indicated by the dashed neutral line

The end member Y^{3+}:O^{2-}:Va is the stable yttria, while Zr^{4+}:O^{2-}:O^{2-} is ZrO_2 with the byxbyite crystal structure (slightly destabilized fluorite). There were suggestions that Y_2O_3 with fluorite structure is sub-solidus phase [112–114], but according to the latest data of Ushakov and Navrotsky [115] it is metastable.

The other two end members can be defined in terms of addition or subtraction of oxygen to the two stable configurations.

In Figure 149 the second square is presented, which corresponds to the simultaneous variation of the occupation of the second and third sublattices. In this square the only stable corner is (Y^{3+}:O^{2-}: Va), connected by an electroneutrality line (dashed) to a point placed in between two charged end-members:

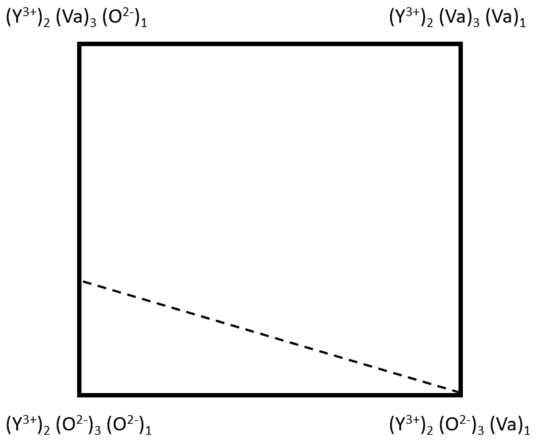

Figure 149 - Composition square for the Y_2O_3 phase in the Y_2O_3-ZrO_2 system related to the occupation of the second and third sublattices. Possible compositions are indicated by the dashed neutral line.

the positive (Y^{3+}:O^{2-}: O^{2-}) and the negative (Y^{3+}:Va: O^{2-}). When they are taken with the ratio 1:3 electroneutrality is obtained. The Gibbs energy of the neutral compound $(Y^{3+})_2(O^{2-}{}_{2/3},Va_{1/3})_3O^{2-}$ can be defined as GY2O3 + V1 (where V1 is a parameter to be optimized).

From this it is possible to write:

GY2O3 + V1= 2/3 G(Y^{3+}:O^{2-}: O^{2-})+1/3 G(Y^{3+}:Va: O^{2-})+3RT (2/3 ln 2/3 + 1/3 ln 1/3)

The last term is an entropic factor (a number on the basis of T).

Therefore, having defined Y^{3+}:O^{2-}: O^{2-}, it is possible to obtain the description of Y^{3+}:Va: O^{2-}, the last end members of this square Y^{3+}:Va:Va, which participates in the reciprocal reaction:

Y^{3+}:O^{2-}: O^{2-} + Y^{3+}:Va: Va = Y^{3+}:Va: O^{2} + Y^{3+}:O^{2-}: Va

can be determined assuming that the Gibbs energy of the reaction is equal to zero.

The last two end members Zr^{4+}:Va:Va and Zr^{4+}:Va:O^{2-}in the whole cube reported in Fig. 11 are calculated by applying the appropriate reciprocal reactions.

The cube with the electronutrality plane of the Y_2O_3 phase is the upper horizontal square shown in Figure 150.

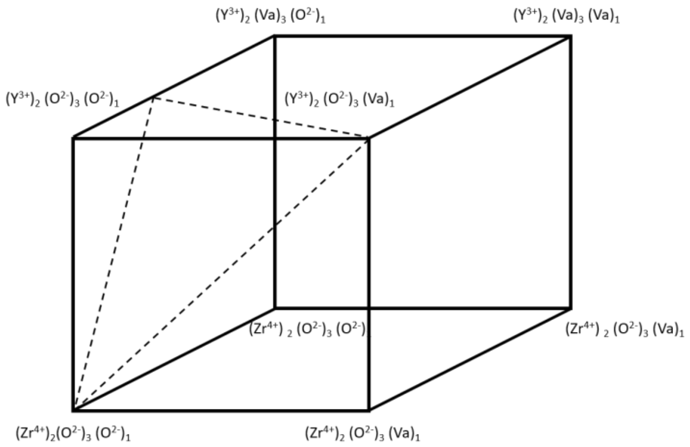

Figure 150 - Composition space for the Y_2O_3 phase in the Y_2O_3-ZrO_2 system related to the occupation of the three sublattices. Possible compositions are indicated by the dashed neutral plane.

The MgO- Y_2O_3 system is described starting from the square created by the replacement of oxygen by vacancy in the second sublattice according to the reaction:

$2\ (Mg^{2+})_2(O^{2-})_3(Va)+(Mg^{2+})_2(Va)_3(Va)=6MgO$

Neutral compound MgO with structure of byxbyite described as $(Mg^{2+})_2(O^{2-}{}_{2/3},Va_{1/3})_2(Va)_1$ is shown as a point in Figure 151.

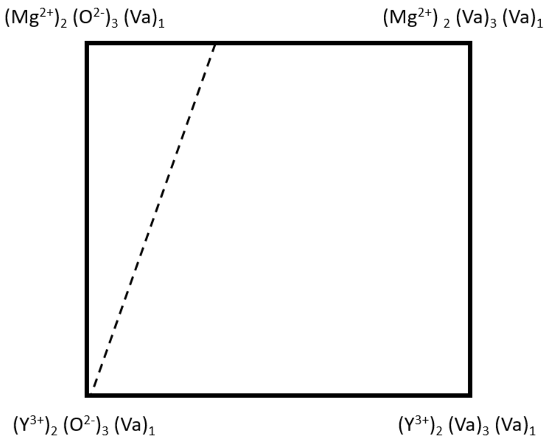

Figure 151 – Composition square for the Y_2O_3 phase in the MgO-Y_2O_3 system related to the occupation of the first and second sublattices. Possible compositions are indicated by the dashed neutral line.

Here we can describe the electronutral point as 2GMgO + V2, therefore:

$$2GMgO + V2= 2/3\ G(Mg^{2+}: O^{2-}:Va) +1/3\ G(Mg^{2+}:Va:Va) +3RT(2/3 \ln 2/3 + 1/3 \ln 1/3)$$

Using the reciprocal reaction:

$$Y^{3+}:O^{2-}: Va + Mg^{2+}:Va: Va = Y^{3+}:Va: Va + Mg^{2+}:O^{2-}: Va$$

and assuming that its Gibbs energy is equal to zero together with electroneutrality reaction is possible to define the two unknown end members Mg:O^{2-}:Va and Mg:Va:Va.

In the same way in the last square, the remaining end members are defined (Figure 152).

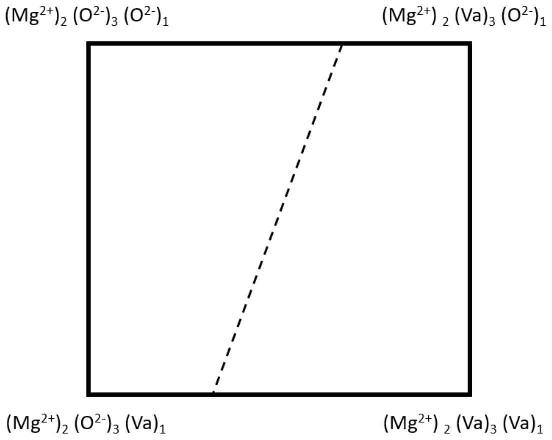

Figure 152 – Composition square for the Y_2O_3 phase in the MgO-Y_2O_3 system related to the occupation of the second and third sublattices. Possible compositions are indicated by the dashed neutral line.

The last electro-neutrality reaction is:

$$(Mg^{2+})_2(O^{2-})_3(O^{2-})+2(Mg^{2+})_2(Va)_3(O^{2-})=6MgO$$

The Gibbs energy of the neutral compound $(Mg^{2+})_2(O^{2-}{}_{1/3},Va_{2/3})_3(O^{2-})$ is defined as:

$$2\ GMgO + V3= 2/3\ G(Mg^{2+}: O^{2-}: O^{2-}) +1/3\ G(Mg^{2+}:Va:O^{2-}) +3RT(2/3 \ln 2/3 + 1/3 \ln 1/3)$$

Using the reciprocal reaction:

$$Mg^{2+}:O^{2-}: Va + Mg^{2+}:Va: O^{2} = Mg^{2+}:Va: Va + Mg^{2+}:O^{2}:O^{2}$$

and assuming its Gibbs energy is equal to zero, the Gibbs energies of unknown end-members Mg^{2+}:O^{2-}:O^{2-} and Mg^{2+}:Va:O^{2-} can be determined.

Finally, the electro-neutrality planes of the ternary system are shown in Figure 153.

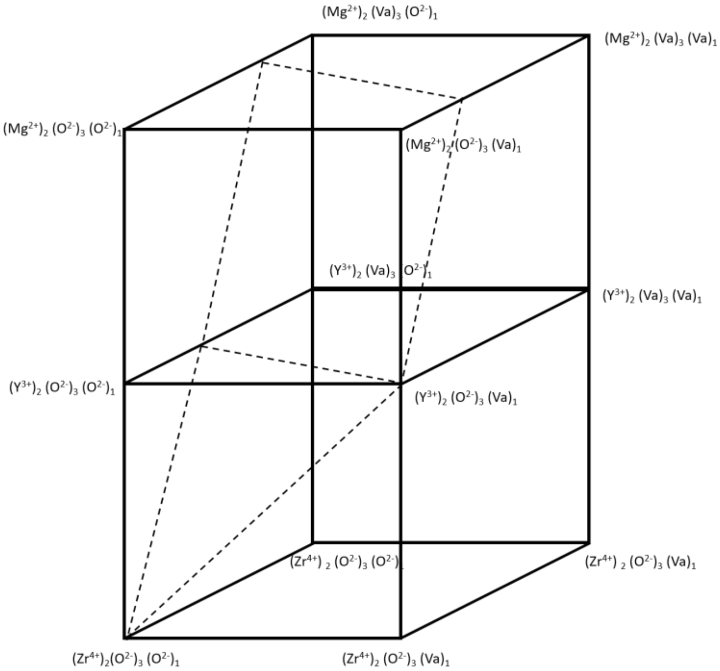

Figure 153 – Composition space for the Y_2O_3 phase in the MgO-Y_2O_3-ZrO_2 system related to the occupation of all sublattices. Possible compositions are indicated by the dashed neutral plane.

6.1.3 Halite model

In this work the model used to describe the halite is $(C^+,Va)_1\ (O^{2-})_1$. The presence of vacancies in the first sublatices has been necessary to study the interaction between ions with charge 2+ with ions with charge 3+ (as yttrium). The system used as example to describe the model is CaO-Y_2O_3 (because in MgO-Y_2O_3 there is no solubility in halite phase).

The combination of 3 species in only one sublattice come to create a triangle formed by end members and reported in Figure 154.

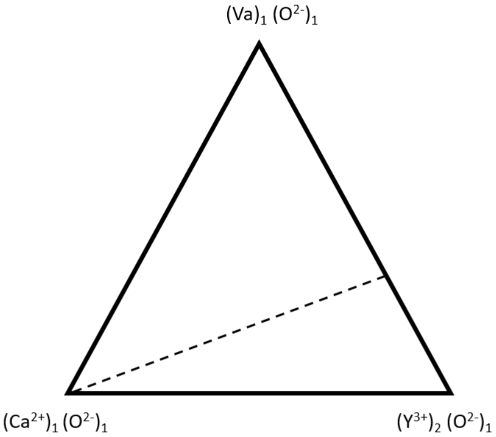

Figure 154 - Composition triangle for the CaO phase in the CaO-Y_2O_3 system related to the occupation of the interstitial sublattice. Possible compositions are indicated by the dashed neutral line

In this square the stable corner is $(Ca^{2+}:O^{2-})$, the calcia, and it is connected by an electroneutrality line to a point placed in between two charged end-members: the positive $(Y^{3+}:O^{2-})$ and the negative (Va:

O^{2-}). When they are taken with the ratio 1:3 electroneutrality is obtained. The Gibbs energy of the neutral compound $(Y^{3+}_{3/4}, Va_{1/4})_1(O^{2-})_1$ can be defined as GY2O3 - GHSEROO + H1 (where H1 is a parameter to be optimized).

From this it is possible to write:

$$GY2O3 - GHSEROO + H1 = 3(1/3\ G(Va^{+}:O^{2-}) + 2/3\ G(Y^{3+}:Va) + 3RT\ (1/3 \ln 1/3 + 2/3 \ln 2/3)$$

The Va: O^{2-} parameter is defined by [116] and so, it is possible obtain the values of $Y^{3+}:O^{2-}$.

6.2 Thermodynamic assessment for oxide database Al_2O_3-CaO-MgO-SiO_2-Y_2O_3-ZrO_2

During the thesis work, a first step for the creation of a multicomponent database between oxides has been created. The current database does not yet allow calculations on complex systems such as CMAS-TBC interaction, but can be a basis for the implementation of the missing systems.

In this work, all binary systems between oxides of the species Al2O3, CaO, MgO, SiO_2, Y_2O_3 and ZrO_2 have been entered in the database so that they are consistent with each other.

As for the ternary systems, work has focused on the MgO-SiO_2-Y_2O_3-ZrO_2 systems. Of these, the MgO-Y_2O_3-ZrO_2 system has been studied in depth as an excellent example of modeling of complex terminal phases (cubic and hexagonal Y2O3, see chapter 6.1.2). The system has been evaluated also with experimental results thanks to the support of Professor Olga Fabrichnaya and her group, which led to the publication of a paper[117].

The modeling of the CaO ternary systems is just mentioned, while that of the Al_2O_3 ternary systems has not been possible to critically evaluate it.

6.2.1 MgO-SiO_2-Y_2O_3-ZrO_2 quaternary system

6.2.1.1 MgO-SiO_2

The phase diagram does not show any phase solubility and two intermediate stoichiometric compounds are present: forsterite (Mg_2SiO_4) and pyroxene ($MgSiO_3$).

The MgSiO3 presents three different polymorphic structures: ortho, proto e clino pyroxene.

Thermodynamic data for the liquid phase in the MgO-SiO_2 system had been assessed by Swamy et al.[118]. However, because data for forsterite (Mg_2SiO_4) were modified by Saxena [119], a reassessment of the liquid parameters was carried out by Fabrichnaya in 2000 [120], also considering experimental work by Hageman and Oonk [121]. The phase diagram published by Fabrichnaya in 2004 [122], is reported in Figure 155. The calculated Fabrichnaya's parameters are used also in this work.

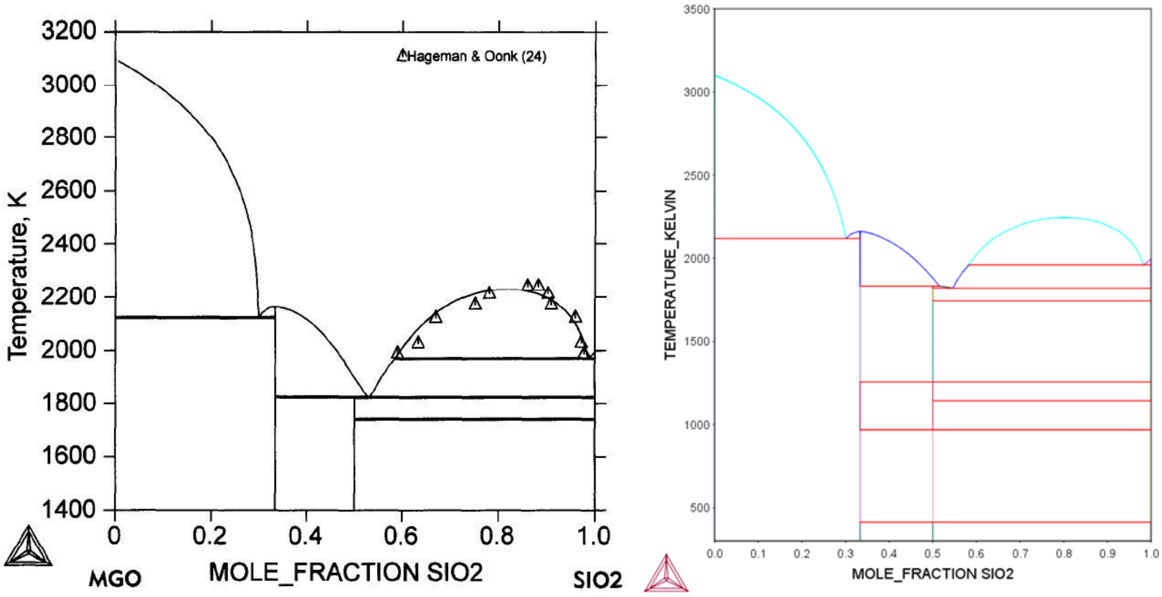

Figure 155 – Phase diagram published by Fabrichnaya[122] **(left) and assessed in this work (right)**

6.2.1.2 MgO-Y_2O_3

Phase relations in the MgO-Y_2O_3 system are relatively simple and were studied in several works [123,124]. Two invariant equilibria have been reported by [124]: the solubility of MgO in C-Y_2O_3 and H-Y_2O_3 gives rise to the H-Y_2O_3 ⇄ C-Y_2O_3 + Liquid metatectic reaction at about 2590 K, while at about 2380 K the eutectic reaction Liquid ⇄ MgO + C-Y_2O_3 occurs. The system has been critically reviewed and modeled by Du and Jin [125]. Unfortunately phase models used by Du are not consistent with those adopted in the present work and a reassessment of the system was necessary, supported to new experimental results[117].

Since very little data were available for the eutectic reaction in the MgO-Y_2O_3 system it was also decided to verify the temperature of this eutectic reaction using DTA and eutectic composition by microstructure investigation after DTA.

The XRD investigation of sample prepared at equimolar composition in the MgO-Y_2O_3 system at 1923K indicated two phases: MgO and C-Y_2O_3 solid solution, as reported in Table 32. The results are consistent with SEM/EDX study of sample after heat treatment shown in Figure 156.

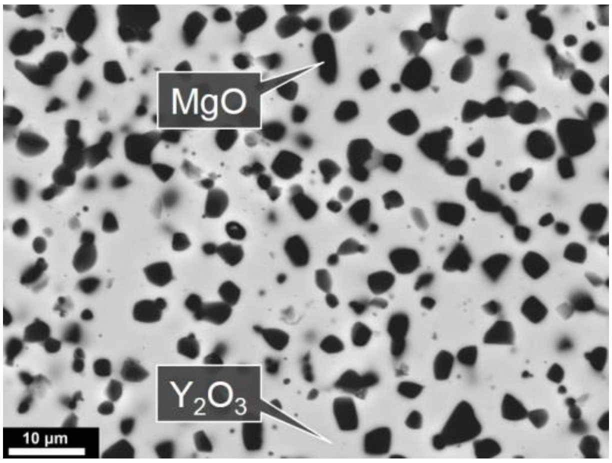

Figure 156 - Microstructure of Y_2O_3-MgO sample ZMY-B1 (ratio 1:1) at 1923 K. Dark phase is MgO and light grey is C-Y_2O_3.

The results of DTA investigation are presented in Figure 157. Two transformations occurring at temperatures close to each other were revealed in DTA on heating: the first one is the eutectic at 2328 K and the second one is the liquidus at 2331 K. Cooling curve indicated the same reverse transformations (small effect for solidification start and large effect for eutectic reaction) both occurring with undercooling. The temperature of the eutectic reaction was accepted as 2328 K, the onset point of heat effect on heating curve. The obtained temperature is 25 K lower than that determined by Lopato and Tresvyatsky [123] and therefore is within uncertainty limits indicated by them. It should be noted that a eutectic temperature of 2383 K was given in a later work of Tresvyatskii et al. [124] and 2353 K in the work of Shevchenko et al. [126].

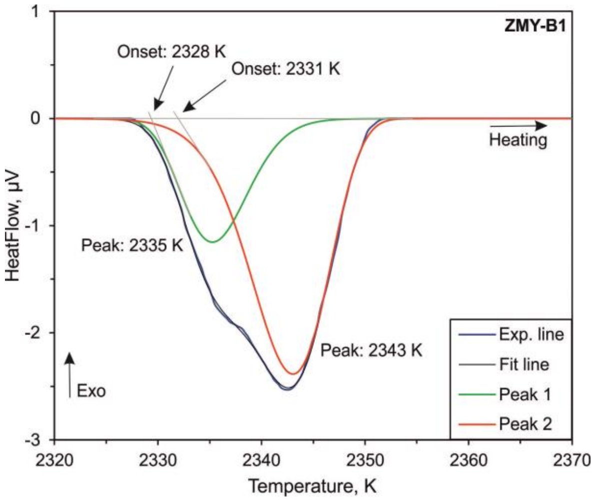

Figure 157 - DTA heating curve for Y_2O_3-MgO sample heat treated at 1923 K.

Results of SEM/EDX investigation indicated eutectic microstructure and primary grains of Y_2O_3 (Figure 158). The composition measurements by EDX indicated that sample was contaminated due to reaction of molten sample with crucible material (8 mol% W). That is why measured eutectic compositions were not accepted for thermodynamic assessment. The eutectic composition was then accepted to be equal to 52 mol% MgO from [12].

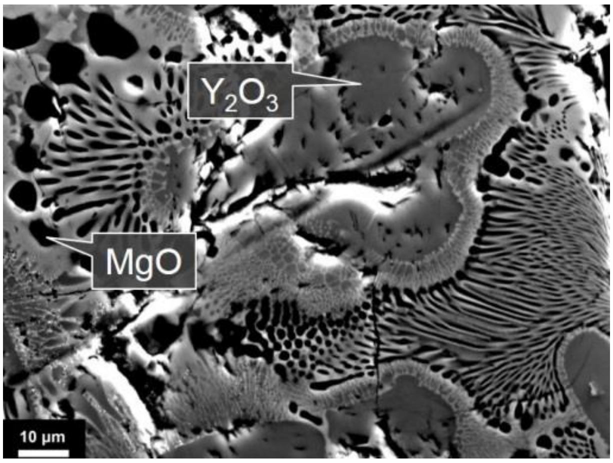

Figure 158 - Microstructure of Y_2O_3-MgO sample ZMY-B1 after DTA

Table 32 - The sample compositions of the MgO-Y_2O_3 system along with the ICP-OES and XRD results

Sample	Nominal sample composition and sample composition by ICP-OES*, mole fraction		Annealing temperature, K / annealing time, days	Phases by XRD	Vol%	Lattice parameter, Å
	MgO	Y_2O_3				*a*
ZMY-B1	0.5	0.5	1923/5	MgO	22	4.2106
	0.501	0.499		C-Y_2O_3	78	10.5900

The end members of cubic and hexagonal Y_2O_3 (C-Y_2O_3 and H-Y_2O_3) have been evaluated to describe the stability of the phases, while the mixing parameters L(Mg^{2+},Y^{3+} : O^{-2} : Va) and L(Mg^{2+},$Y3^{+}$: Va : Va) of C-Y_2O_3 and L(Mg^{+2},Y^{+3}:O^{-2}) of liquid have been determined by means of the Parrot module to fit the experimental data.

The assessed MgO-Y_2O_3 phase diagram is shown in Figure 159 [117].

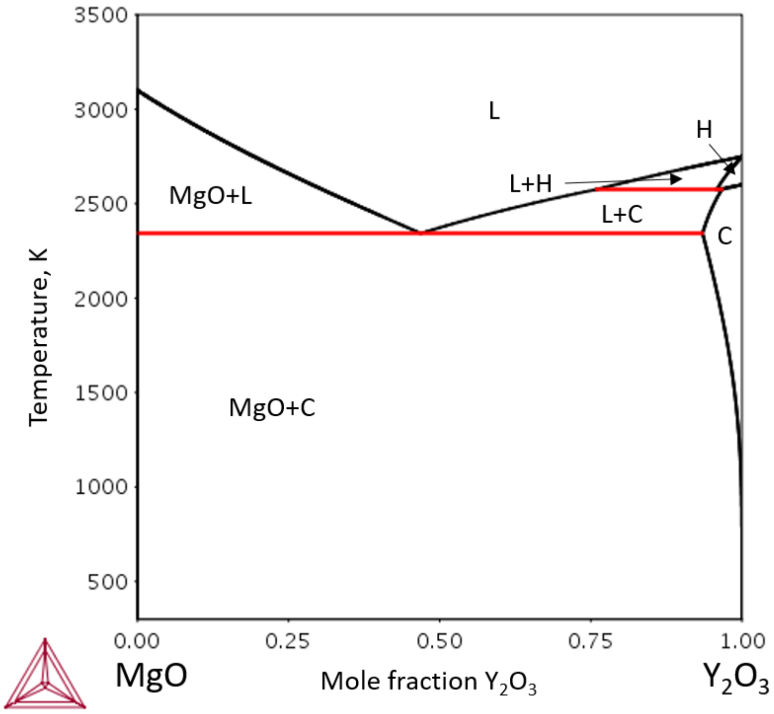

Figure 159 – Calculated phase diagram of the MgO-Y_2O_3 system based on the description of the present work (L=Liquid, H=H-Y_2O_3, C=C-Y_2O_3)

6.2.1.3 MgO-ZrO_2

The MgO-ZrO_2 system does not form any intermediate compound. Only the terminal phases halite on the MgO side and M-ZrO_2, T-ZrO_2 and F-ZrO_2 (monoclinic, tetragonal and fluorite structures, respectively) on the ZrO_2 side are present. F-ZrO_2 shows an appreciable solubility range: it dissolves about 20 mol% of MgO at the eutectic temperature. One eutectic equilibrium Liquid $\rightleftarrows$ MgO + F-ZrO_2 at 2375 K and one eutectoid F-ZrO_2 $\rightleftarrows$ MgO + T-ZrO_2 at 1683 K are quite well defined experimentally. A second eutectoid equilibrium M-ZrO_2 $\rightleftarrows$ MgO + M-ZrO_2 was determined at about 1360 K.

Several authors have conducted experimental investigations of phase equilibria in the MgO-ZrO2 system. A review of experimental works was presented by Bochvar and Rokhlin [127], while the first thermodynamic modeling of this system was performed by Du and Jin[128]. Further works about modeling of the system were done in the following years [129–131] and, more recently, all this works have been confirmed and reviewed by Pavlyuchkov et al.[132].

Thermodynamic assessment of the system used in the present work was performed by Pavlyuchkov et al.[132] and the calculated phase diagram is presented in Figure 160.

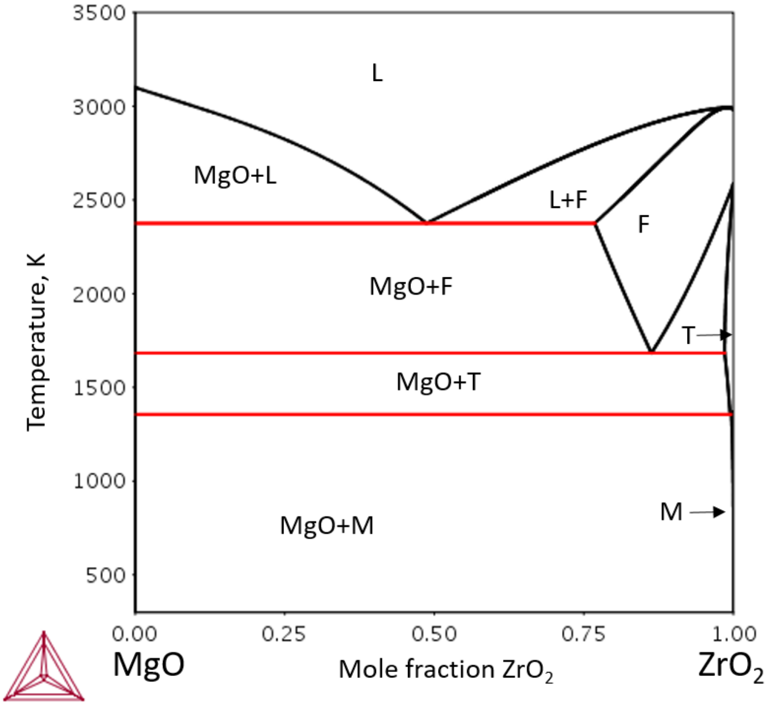

Figure 160 - MgO-ZrO$_2$ phase diagram according to thermodynamic description by Pavlyuchkov et al.[132] **(L=Liquid, F=F-ZrO$_2$, T=T-ZrO$_2$, M=M-ZrO$_2$).**

6.2.1.4 SiO$_2$-Y$_2$O$_3$

In the Y_2O_3–SiO_2 system there are two compounds, Y_2SiO_5 and $Y_2Si_2O_7$, with two and four allotropic transformations, respectively. The phase diagram of this system was experimentally studied in many works [121,133–136]. Toropov and Bondar[133] and Hageman and Oonk [121] studied the liquid miscibility gap around 2000-2450 K in the SiO_2-rich region, while Bondar [134] and Warsaw and Roy [136] confirmed the congruent melting character of Y2SiO5 and incongruent melting of $Y_2Si_2O_7$. The system has been assessed independently by Cupid and Seifert [137] and Mao at al. [138]. Subsequently, Pan et al. [139] considered previous assessment works and improved the liquid parameters. In this work the assessment published by Pan has been used, and the resulting phase diagram is reported in Figure 161

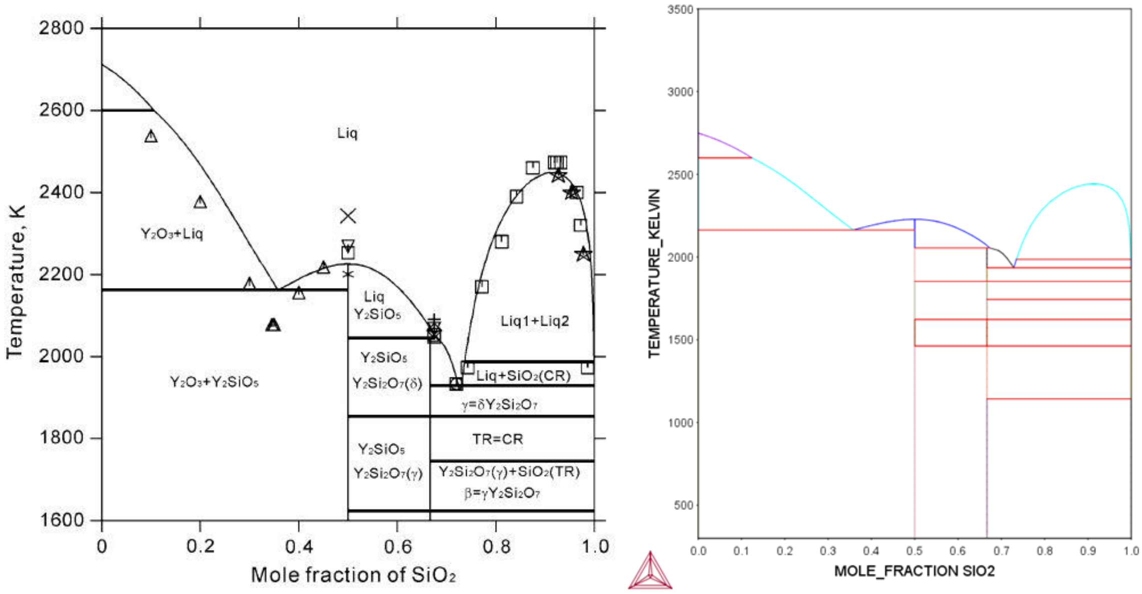

Figure 161 – SiO_2-Y_2O_3 diagram phase published by Pan [139] **(left)and used in this work (right)**

6.2.1.5 SiO_2-ZrO_2

The SiO_2-ZrO_2 system form only one intermediate compound at 50 mol% of SiO_2, $ZrSiO_4$, called Zircon. The terminal phases, M-ZrO_2, T-ZrO_2 and F-ZrO_2 on the ZrO_2 side and the three allotropic forms of SiO_2 (Silica, Tridymite and Cristobalite) have no solubility in the system. Zircon is stable up to about 1950 K, immediately below the eutectic equilibrium Liquid ⇄ Cristobalite + T-ZrO2, as observed in several experimental works[140–144]. In the system a liquid immiscibility gap is present between 2500 and 2700 K in the range 20-40 mol% SiO2, studied by Barlett[145], Toropov and Galakhov[146] and Telle et al[147]. The liquidus in the SiO2-ZrO2 system was investigated by Zhirnova [148], Toropov and Galakhov [146], and Kamaev[140].

The only thermodynamic assessment of the system was published by Kwon and Jung [103] which considers all the experimental works mentioned. The phase models used by Kwon are not consistent with those adopted in the present work and a reassessment of the system was necessary. The liquid and zircon parameters have been modified by means of the Parrot module, considering all experimental data. The phase diagram calculated by Kwon is reported in Figure 162-a, while phase diagram assessed in this work is shown in Figure 162-b.

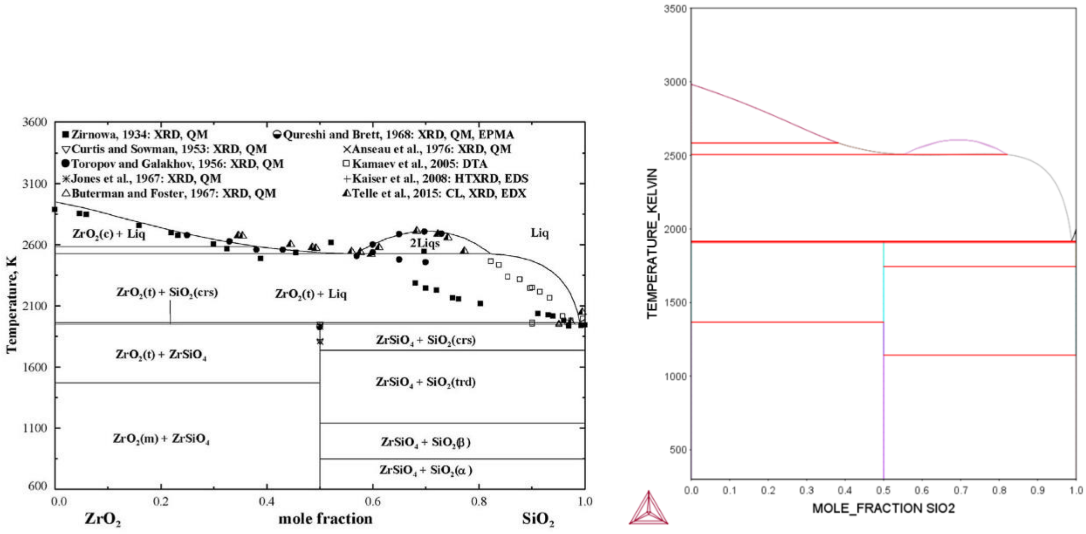

Figure 162 – ZrO_2-SiO_2 phase diagram reported by Kwon and Jung[103] **(a) calculated in this work (b)**

6.2.1.6 Y_2O_3-ZrO_2

One intermediate phase, $Y_4Zr_3O_{12}$, is present in the Y_2O_3-ZrO_2 system. The Y_2O_3-ZrO_2 phase relations were carefully investigated, mainly in the ZrO_2-rich region, due to the interest for YSZ, a material used as Thermal Barrier Coating for protection of superalloys exposed at high temperatures. Actually Y_2O_3 is highly soluble in F-ZrO_2 (up to about 70 mol% at 2800 K) and stabilizes the cubic ZrO_2 down to room temperature.

Nevertheless phase equilibria in this system are affected by some uncertainty, mainly related to the uncertainty affecting the transition temperatures from F-ZrO_2 to T-ZrO_2 to M-ZrO_2 in pure ZrO_2.

Experimental investigations of the Y_2O_3-ZrO_2 system have been critically reviewed by Fabrichnaya et al. [20]. Thermodynamic parameters of the Y_2O_3-ZrO_2 system were re-assessed using a two-sublattice model for ZrO_2 based solid solutions [149]. Thermodynamic parameters for ZrO_2 were re-assessed by Wang et al. [90] based on DTA investigations of the ZrO_2-HfO_2 system. Zinkevich [150] re-assessed parameters for the rare earth oxides. The last re-assessment of the Y_2O_3- ZrO_2 system was performed by Fabrichnaya [151] using data of Wang [90] and Zinkevich [150]for pure oxides. The phase diagram calculated using the thermodynamic description by Fabrichnaya [151] is shown in Figure 163. This assessment is used in the present work.

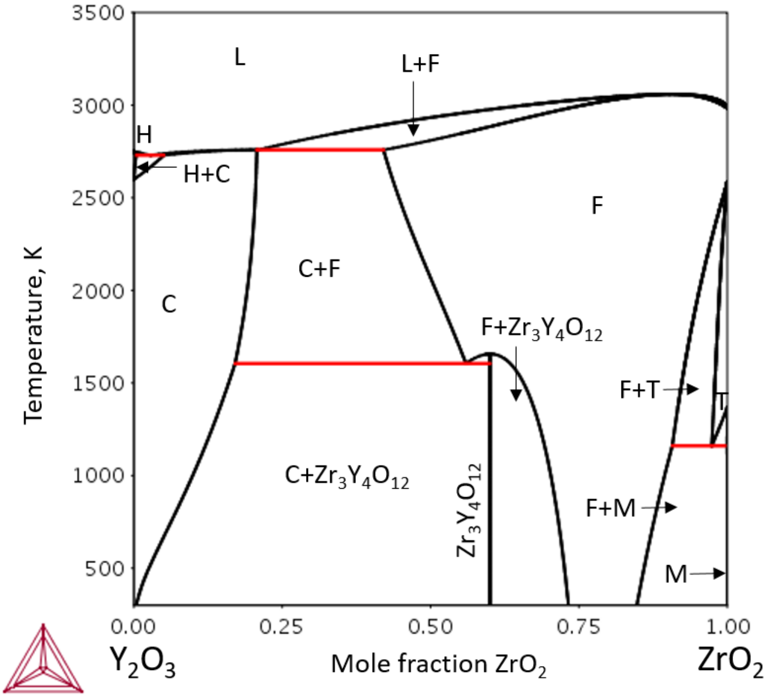

Figure 163: Y_2O_3-ZrO_2 phase diagram according to thermodynamic description by Fabrichnaya et al. [151] **(L=Liquid, C=C-Y_2O_3, H=H-Y_2O_3, F=F-ZrO_2, T=T-ZrO_2, M=M-ZrO_2).**

6.2.1.7 MgO-SiO_2-Y_2O_3

The only paper about this system was published by Kuang at al.[152]. The calculated isothermal section at 1273K of the ternary system is reported in Figure 164-a. The only intermediate phase is apatite, which has been reassessed in this work. The model used refers to the work of Poerschke et al. [153], a paper regarding crystallographic studies of phases in the CaO-SiO_2-Y_2O_3 system.

To describe apatite a five sublattice model has been used: $(Mg^{+2},Y^{+3},VA)_4(Y^{+3})_6(SI^{+4})_6(O^{-2})_{24}(O^{-2},VA)_2$.

Although the modeling of the phase is complex and similar to that described for phase Y_2O_3, it has not been highlighted in the chapter of thermodynamic models (chapter 5.1) since apatite appears only in a couple of systems studied in this work.

The isothermal section at 1273 K obtained by a new assessment of the system is shown in Figure 164-b.

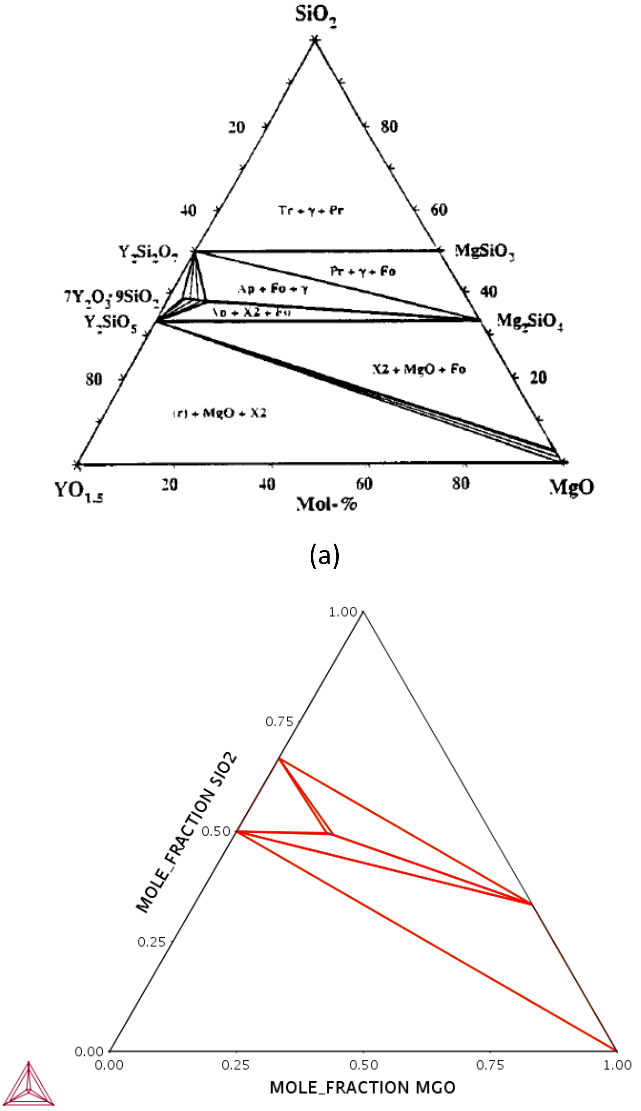

(a)

Figure 164 – Section of MgO-SiO$_2$-Y$_2$O$_3$ system reported by Kuang [152] **and calculated in this work at 1273 K**

6.2.1.8 *MgO-Y$_2$O$_3$-ZrO$_2$*

Experimental data for the MgO-Y$_2$O$_3$-ZrO$_2$ system are quite limited and contradictory. Scott [154] investigated the phase relations in the ternary system at high temperatures; they determined boundaries of the fluorite stability field in the range of 1623 to 1873 K and constructed the isothermal section at 1873 K.

Hallmann and Stubican [155] investigated phase relations and constructed isothermal sections at 1493 and 1693 K.

Lopato et al. constructed isothermal sections at 1573, 1693, 1723 and 2173 K based on experimental results. The two lower temperature sections from refs [155] and [156] are displayed in Figure 165. The most important difference between the two papers concerns the three-phase fields including Y$_4$Zr$_3$O$_{12}$. According to Lopato three-phase equilibria F-ZrO$_2$+C-Y$_2$O$_3$+MgO and Y$_4$Zr$_3$O$_{12}$+F-ZrO$_2$+C-Y$_2$O$_3$ are stable, equilibria including Y$_4$Zr$_3$O$_{12}$ phase are close to the ZrO$_2$-Y$_2$O$_3$ boundary system and Y$_4$Zr$_3$O$_{12}$ is not in equilibrium with MgO. However, according to Hallemann and Stubican there is a two-phase equilibrium $Y_4Zr_3O_{12}$ + MgO and two three-phase equilibria $Y_4Zr_3O_{12}$ + MgO + C-Y_2O_3 and $Y_4Zr_3O_{12}$ + MgO + F-ZrO_2. It is not clear if the difference is due to temperature difference or the equilibrium was not reached in one of the studies. In the work of Scott an extrapolated isothermal section at 1523 K was presented being in agreement with [155] but it is not supported by experimental data.

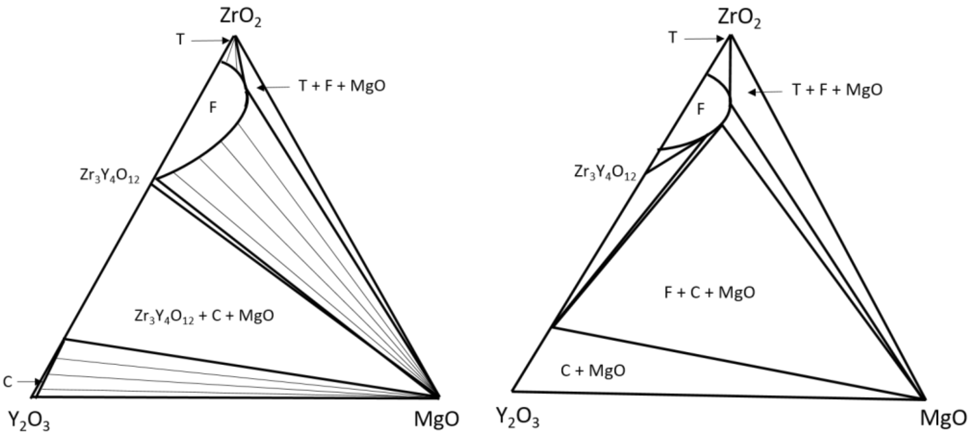

Figure 165 - MgO-Y_2O_3-ZrO_2 isothermal section at 1493 K by Hallemann et al. (C=C-Y_2O_3, F=F-ZrO_2, T=T-ZrO_2) (a) and MgO-Y_2O_3-ZrO_2 isothermal section at 1573 K by Lopato (C=C-Y_2O_3, F=F-ZrO_2, T=T-ZrO_2) (b).

Comparing phase diagrams at 1693 K presented by Hallmann and Lopato it can be seen that only one three-phase equilibrium F-ZrO_2+C-Y_2O_3+MgO was indicated in both studies but there were some quantitative differences in the determined phase compositions. According to Lopato et al. the tie-triangle F-ZrO_2+C-Y_2O_3+MgO is wider and more extended towards the MgO-ZrO_2 binary than indicated by Hallemann and Stubican. Scott indicated only one tie-triangle F-ZrO_2+C-Y_2O_3+MgO at 1873 K similar to Lopato et al. at 1693 and 1923 K. However it was substantially narrower than the ones at 1693 and 1923 K indicated by Lopato. It should be noted that Scott prepared samples from oxide powders, while co-precipitation method was used by Lopato et al. and Hallemann and Stubican. In case of slow reaction rate the co-precipitation method allows a faster achievement of equilibrium.

Liquidus surface and four vertical sections were constructed based on DTA, microscopic and XRD investigations and refractive index measurements by Shevchenko et al. [126]. A ternary eutectic was found at 2313 K with a liquid composition of 29 mol.% ZrO2 and 51 mol.% MgO.

The system has been thermodynamically assessed by Jin and Du [157]. In their paper all the experimental works [126,154–156] were considered. The high temperature results by Hallmann and Lopato were in reasonable agreement with each other and were used by Jin to describe the ternary system.

The differences in experimental data at low temperature (1493-1573 K) between Hallmann and Lopato were not discussed by Jin and Du, because their description qualitatively reproduced both of them due to the difference in temperature. It should be noted that according to Scott the tie-triangle F-ZrO_2+C-Y_2O_3+MgO was narrower than in both Hallmann and Lopato. Therefore it was not possible to reproduce the compositions of F-ZrO_2 and C-Y_2O_3 in equilibrium with MgO according to Scott with the thermodynamic description based on Hallmann and Lopato. This contradiction was discussed and another set of parameters was suggested to reproduce data of Scott. It should be noted that in the assessment of Jin and Du low temperature data (1493-1693 K) got lower weight than high temperature data.

An analysis of the experimental results of Lopato et al. and Hallemann and Stubican revealed several inconsistencies between data of these authors. As mentioned above, at 1493 K Hallmann and Stubican indicated the three-phase fields: $Y_4Zr_3O_{12}$+F-ZrO_2+MgO and $Y_4Zr_3O_{12}$+C-Y_2O_3+MgO, while Lopato et al. indicated other ones at 1573 K: F-ZrO_2+C-Y_2O_3+MgO and $Y_4Zr_3O_{12}$+C-Y_2O_3+F-ZrO_2. Therefore new experimental investigation of phase equilibria at 1493 and 1573 K was necessary to understand the reason for such differences in the phase relations, which can be due to the temperature difference or the fact that equilibrium was not reached in one of the works or some mistake in data interpretation. Besides this, there were large inconsistencies in the compositions of phases participating in three-phase equilibrium F-ZrO_2+C-Y_2O_3+MgO at 1693 K determined in above mentioned works. The three-phase field F-ZrO_2+C-Y_2O_3+MgO determined by Scott at 1873 K was substantially narrower than the one determined by Lopato et al. at 1693 and 1923 K. Therefore, to resolve these inconsistencies in literature five ternary compositions were selected for investigation. The sample compositions and results of X-ray analysis of samples after heat treatment at 1493, 1573, 1693 and 1923 K are presented in Table 33.

It can be seen that equilibrium $Y_4Zr_3O_{12}$+C-Y_2O_3+MgO was indicated at 1493 K. Therefore our results are consistent with Hallemann and Stubican. Our results at 1573 K show phase equilibrium F-ZrO_2+MgO+C-Y_2O_3 similar to Lopato et al., but at the same time the equilibrium between $Y_4Zr_3O_{12}$ and MgO was also found which was not found by Lopato. Both in the present work and in the work of Lopato et al., the samples were obtained by co-precipitation and the temperature was 1573 K. The reason of the inconsistency between the present work and Lopato could be that $Y_4Zr_3O_{12}$ and C-Y_2O_3, both being superstructure of fluorite, were not distinguished by Lopato, or the temperature in their study was higher than 1573 K. It should be noted that at temperatures of 1573 K three-phase assemblage F-ZrO_2+C-Y_2O_3+MgO was indicated for the sample ZMY-4 and four phase assemblage F-ZrO_2+C-Y_2O_3+$Y_4Zr_3O_{12}$+MgO with substantial amount of $Y_4Zr_3O_{12}$ for sample ZMY-5. These results can only be explained by the presence of two different areas of fluorite stability separated by a $Y_4Zr_3O_{12}$+MgO two-phase field. In the narrow composition range close to ZMY-5 there are three three-phase fields: two narrow F-ZrO_2+MgO+$Y_4Zr_3O_{12}$ fields with different compositions of fluorite phase and F-ZrO_2+C-Y_2O_3+MgO field. Probably due to local concentration inhomogeneity four phases formed.

DTA of sample ZMY-5, shown in Figure 166, indicated onset at 1643 K that is lower than stability limit of $Y_4Zr_3O_{12}$ in the ZrO_2-Y_2O_3 system. Probably the observed effect is related to F-ZrO_2+C-Y_2O_3 ⇄ $Y_4Zr_3O_{12}$+MgO which can be at slightly lower temperature due to overheating.

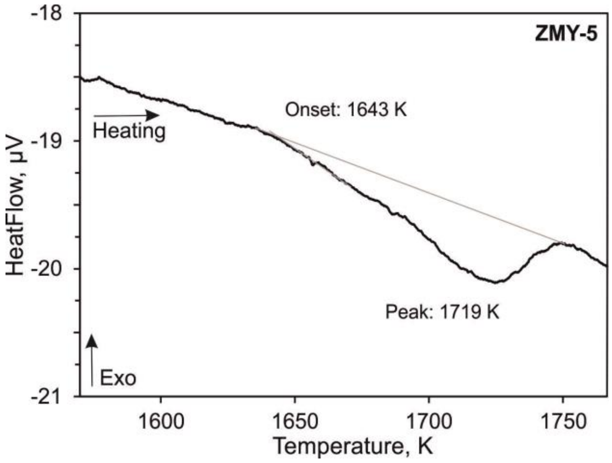

Figure 166 - DTA heating curve for sample ZMY-5

At 1693 and 1923 K for sample composition ZMY-1 and ZMY-4 three-phase equilibrium F-ZrO_2+C-Y_2O_3+MgO was indicated. Two-phase assemblage F-ZrO_2+MgO was found for ZMY-2 and ZMY-5 samples. According to Lopato compositions of sample ZMY1, 2, 4 and 5 at the mentioned temperatures should be in the three-phase field F-ZrO_2+C-Y_2O_3+MgO. Also according to Lopato et al. our sample ZMY-3 should be in two-phase field F-ZrO_2+T-ZrO_2 at 1493 and 1693 K and in single fluorite phase field at 1923 K, while according to our data this sample contained only fluorite phase at all studied temperatures. Thus our results appeared to be in better agreement with phase diagram of Hallemann and Stubican at 1693 K indicating F-ZrO_2+C-Y_2O_3+MgO for ZMY-1, 4 compositions, F-ZrO_2+MgO for ZMY-2, 5 compositions and single phase fluorite for ZMY-3 composition. It should be noted that determination of compositions of fluorite and C-Y_2O_3 using SEM/EDX was difficult due to slow reaction rate of phase separation even at 1923 K. SEM/EDX results (element mapping) for sample ZMY-4 heat treated for 10 days is presented in Figure 167. Formation of Y_2O_3 and ZrO_2-rich grains can be observed but their size was too small for quantitative quantification.

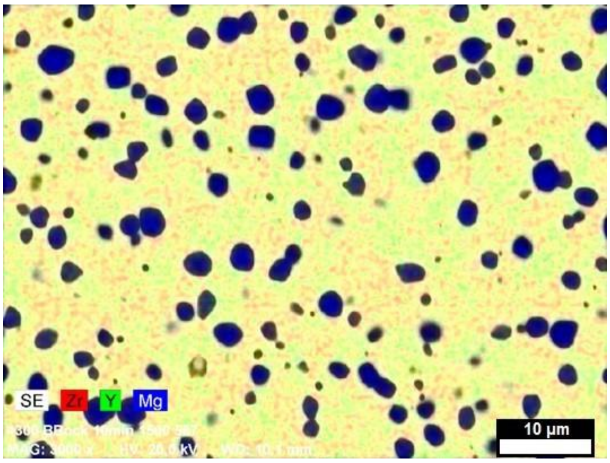

Figure 167 - Element mapping for ZMY-4 sample heat treated at 1923 K for 10 days.

DTA investigation of sample ZMY-4 up to 2493 K indicated smeared heat effect with on-set at 2315 K (see Figure 168-a). It does not look as eutectic reaction compared with eutectic reaction in the binary system Y_2O_3-MgO: effect is not sharp enough. The temperature difference for reaction in binary and ternary system is small being within uncertainty of measurement. However the microstructure investigation confirmed the eutectic character of this reaction L ⇄ MgO+F-ZrO_2+C-Y_2O_3 (see Figure 168-b). The measured eutectic composition 70 mol.% MgO, 12 mol.% ZrO_2 and 18 mol.% Y_2O_3 is substantially different from that determined by Shevchenko (51 MgO, 29 ZrO_2 and 20 Y_2O_3, in mol.%), while the temperature of the transformation (2313 K) is in reasonable agreement with the present work. The second peak at 2347 K probably corresponds to liquidus temperature.

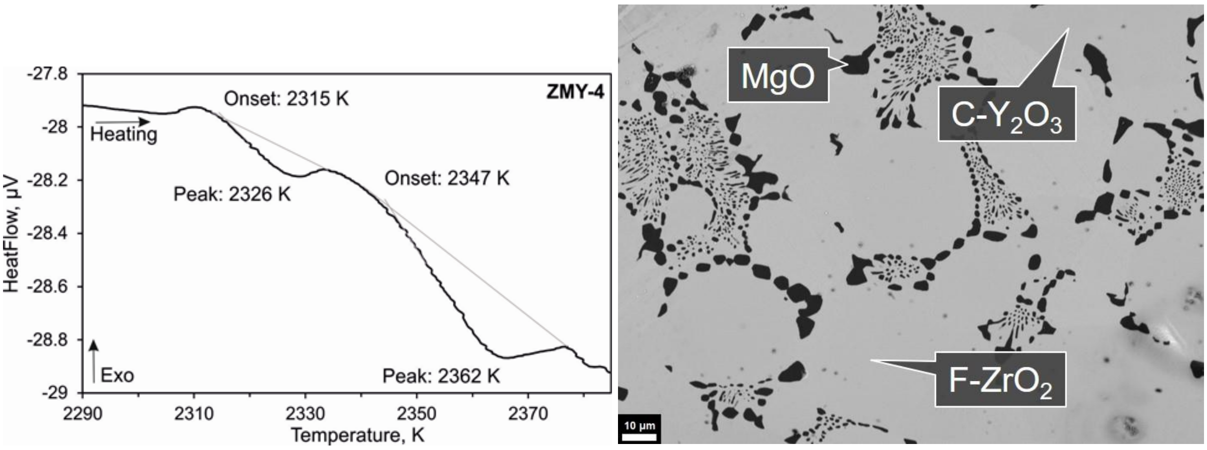

(a) (b)

Figure 168 - DTA heating curve for sample ZMY-4. (a) and Microstructure of sample ZMY-4 after DTA (b)

Table 33 - The sample compositions of the MgO-Y2O3-ZrO2 system along with the ICP-OES and XRD results

Sample	Nominal sample composition and sample composition by ICP-OES*, mole fraction			Annealing temperature, K / annealing time, days	Phases by XRD	Vol%	Lattice parameter, Å
	ZrO_2	MgO	Y_2O_3				*a*
ZMY-1	0.2	0.3	0.5	1493/8	MgO	11	4.2123
	0.204*	0.311	0.485		C-Y_2O_3	89	10.5258
				1573/6	MgO	13	4.2186
					F-ZrO_2	13	5.2682
					C-Y_2O_3	74	10.5392
				1693/5	MgO	9	4.2135
					F-ZrO_2	39	5.2505
					C-Y_2O_3	52	10.5274
				1923/5	MgO	12	4.2163
					F-ZrO_2	8	5.2687
					C-Y_2O_3	80	10.5357
ZMY-2	0.5	0.3	0.2	1493/2	MgO	18	4.2108
	0.500*	0.301	0.199		F-ZrO_2	82	5.1855
				1573/6	MgO	19	4.2105
					F-ZrO_2	81	5.1839
				1693/5	MgO	20	4.2117
					F-ZrO_2	80	5.1846
				1923/3	MgO	21	4.2146
					F-ZrO_2	79	5.1878
ZMY-3	0.865	0.045	0.090	1493/10	F-ZrO_2	100	5.1313
	0.874*	0.043	0.083	1573/6	F-ZrO_2	100	5.1353
				1693/7	F-ZrO_2	100	5.1321
				1923/5	F-ZrO_2	100	5.1301

Sample	Nominal sample composition and sample composition by ICP-OES*, mole fraction K / annealing time, days			Annealing temperature,	Phases by XRD	Vol%	Lattice parameter, Å
	ZrO_2	MgO	Y_2O_3				*a*
ZMY-4	0.3	0.3	0.4	1493/7	MgO	15	4.2175
	0.291*	0.311	0.398		C-Y_2O_3	68	10.5038
					$Y_4Zr_3O_{12}$	17	*a* = 9.7654 *c* = 9.1429
				1573/6	MgO	15	4.2188
					F-ZrO_2	22	5.2432
					C-Y_2O_3	63	10.5042
				1693/6.5	MgO	15	4.2172
					F-ZrO_2	26	5.2384
					C-Y_2O_3	59	10.5099
				1923/4.5	MgO	12	4.2156
					F-ZrO_2	43	5.2403
					C-Y_2O_3	45	10.5187
ZMY-5				1493/7	MgO	13	4.2118
					C-Y_2O_3	2	10.5077
					$Y_4Zr_3O_{12}$	84	*a* = 9.7254 *c* = 9.0992
				1573/6	MgO	6	4.2200
					F-ZrO_2	16	5.2370
					C-Y_2O_3	2	10.5077
					$Y_4Zr_3O_{12}$	76	*a* = 9.7374 *c* = 9.1161
				1693/6.5	MgO	19	4.2184
					F-ZrO_2	81	5.2299
				1923/5	MgO	21	4.2159
					F-ZrO_2	79	5.2295

In order to fit the experimental results in the ternary system it was necessary to evaluate a ternary interaction parameter for the fluorite phase and C-Y_2O_3 to stabilize the three-phase field $Y_4Zr_3O_{12}$+MgO+C-Y_2O_3 at low temperature (1493 K) and to get both phase asseblages F-ZrO_2 + C-Y_2O_3 + MgO and $Y_4Zr_3O_{12}$ + MgO at 1573 K.

Calculations show that at 1600 K tie-line MgO+$Y_4Zr_3O_{12}$ changed to F-ZrO_2 + C-Y_2O_3 due to invariant reaction F-ZrO_2 + C-Y_2O_3 ⇄ MgO + $Y_4Zr_3O_{12}$. The phase $Y_4Zr_3O_{12}$ is not stable at 1693 K because according to phase diagram of Y_2O_3-ZrO_2 system it decomposed at 1657 K.

Calculated isothermal sections at 1493, 1573, 1693 and 1923 K together with experimental data obtained in this study are presented in Figure 169 a-d, respectively. Liquidus surface calculated without introducing ternary parameters appeared to be in a good agreement with experimental data of Shevchenko et al.[126] and temperature measured in the present study using DTA. The calculated liquidus surface is presented in Figure 170. According to calculations there is one ternary eutectic reaction at 2354 K and two eutectic maxima e1 at 2415 K and e2 at 2363 K.

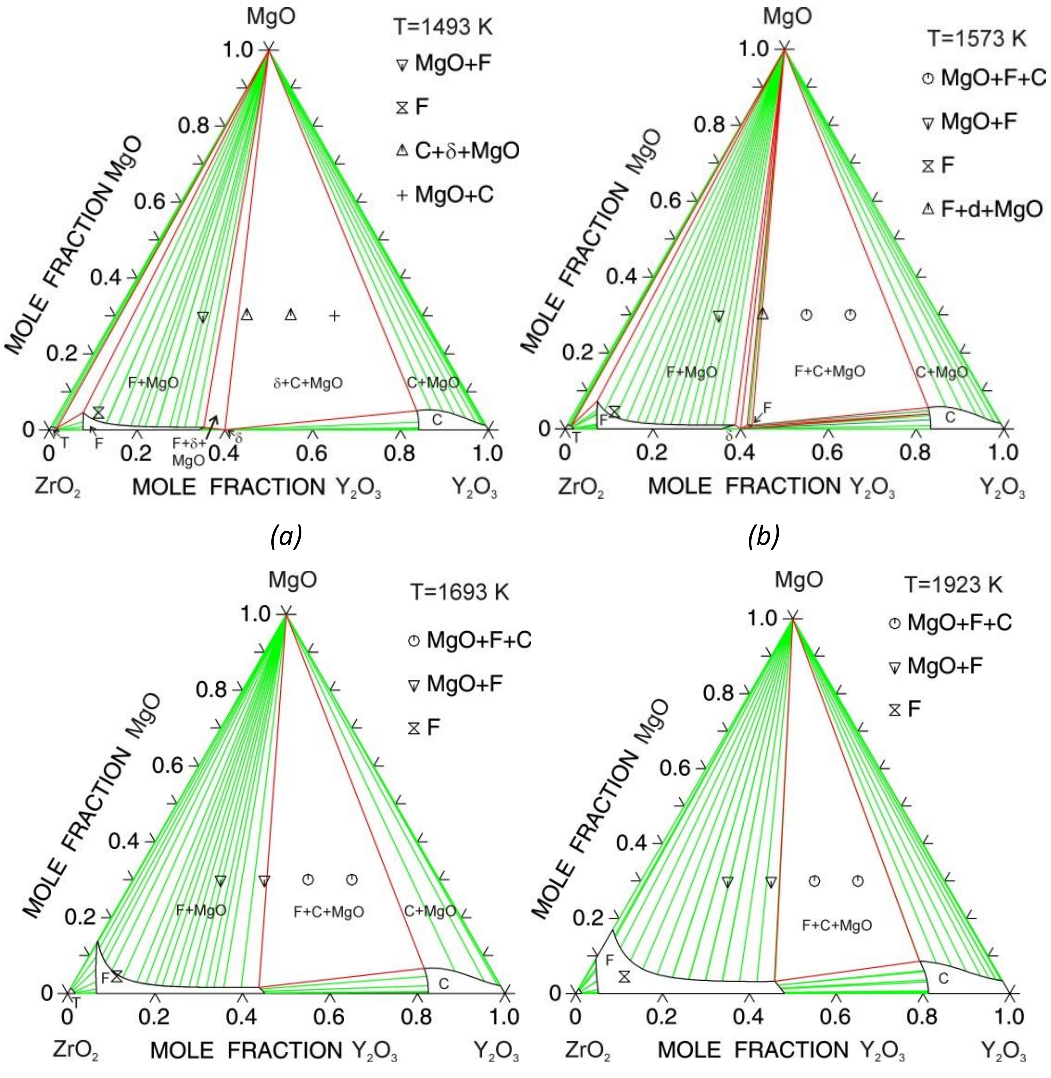

(a) *(b)*

(c) *(d)*

Figure 169 - MgO-Y_2O_3-ZrO_2 system: calculated isothermal sections with experimental results obtained in this work. Phase Y4Zr3O12 is denoted as: a) at 1493 K, b) at 1573 K, c) at 1693 K, d) at 1923 K.

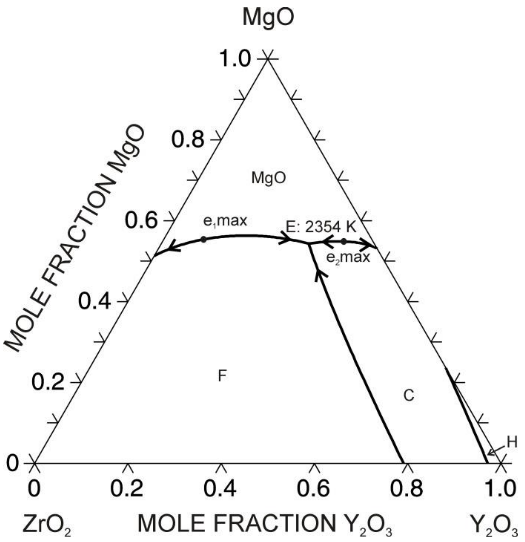

Figure 170 - Calculated liquidus surface of the $MgO-Y_2O_3-ZrO_2$ system

6.2.1.9 *$MgO-SiO_2-ZrO_2$*

In the $MgO-SiO_2-ZrO_2$ ternary system, no intermediate compounds are stable. The system is only the combination of the three binary subsystems. In Figure 171 is reported the isothermal section at 1700 K studied by Pandit and Jacob [158] where the experimentally investigated compositions are indicated.

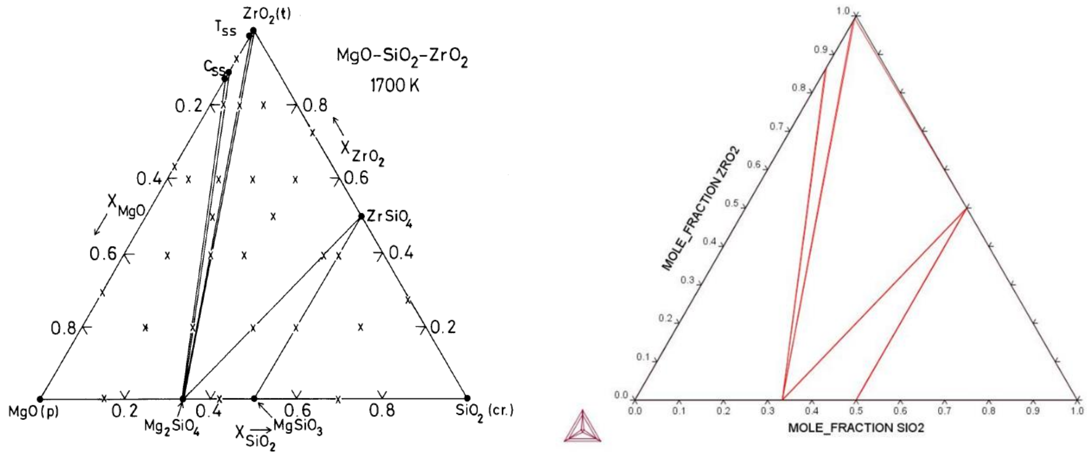

(a) (b)

Figure 171 – Isothermal section at 1700 K for the MgO-SiO2-ZrO2 system calculated by Pandit and Jacob[158](a) and obtained in this work (b)

6.2.1.10 *$SiO_2-Y_2O_3-ZrO_2$*

No experimental work or thermodynamic assessment is present in literature. This is strange because $SiO_2-Y_2O_3-ZrO_2$ is the principal ternary system for the study of the interaction between CMAS (formed by about 50 wt% SiO_2) and TBC (normaly Zirconia with 7-8 wt% Y_2O_3).

An isothermal section at 1773K calculated by means of the thermodynamic database created during this work is reported in Figure 172 of the system. It has been obtained by extrapolation of the binary subsystems.

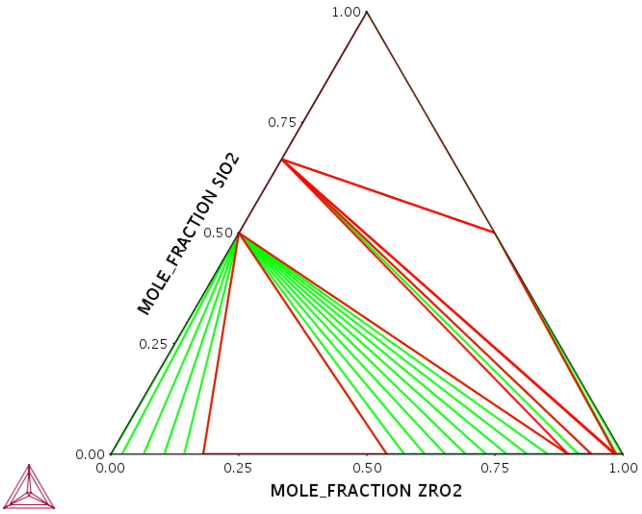

Figure 172 - Isothermal section at 1773K for the SiO2-Y2O3-ZrO2 system calculated with database obtained in this work

6.2.2 Other systems evaluated

6.2.2.1 Al_2O_3-CaO

In the Al_2O_3-CaOsystem, there are four intermediate stoichiometric phases, namely $3CaO \cdot Al_2O_3$ (abbreviated as C3A), $CaO \cdot Al_2O_3$ (CA), $CaO \cdot 2Al_2O_3$ (CA2) and $CaO \cdot 6Al_2O_3$ (CA6) . C3A and CA6 phases form through peritectic equilibria: CaO+ Liquid ⇄ C3A at 1817K and Al_2O_3+ Liquid ⇄ CA6 at about 2150K. The other two stoichiometric phases form by congruent melting: at 1877 and 2040 K for CAand CA2 respectively. The last equilibrium in the system is an eutectic reaction: Liquid ⇄ C3A + CA at 1640 K.

Experimental investigations of phase equilibria in the Al_2O_3-CaO system have been conducted by several authors and they have been confirmed and reviewed by Hallstedt[159]. The thermodynamic assessment by Hallstedt has been used in subsequent works [160–162], which confirm the goodness of the modelling. The thermodynamic parameters obtained by Hallstedt [159] for all compounds adopted in the present work and the resulting phase diagram is reported in Figure 173.

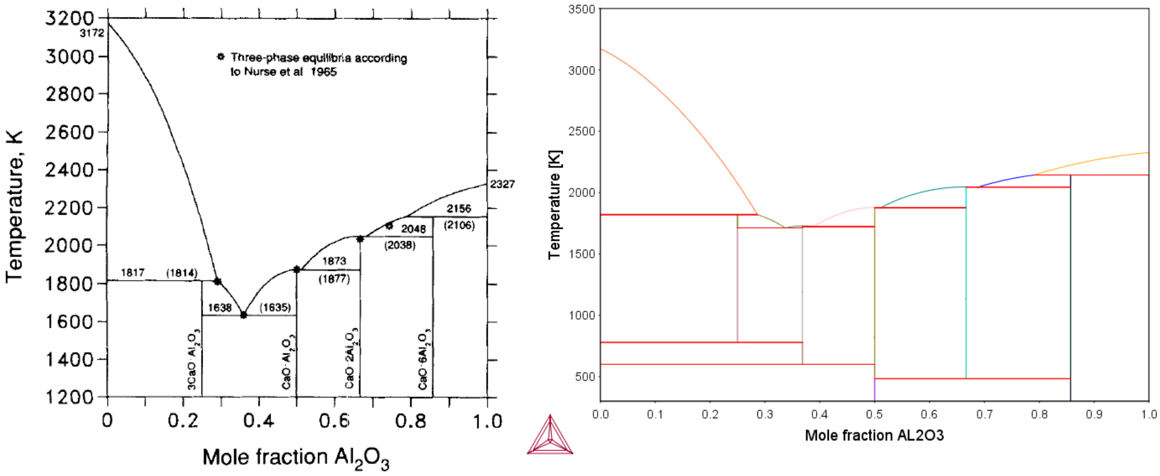

Figure 173 - Al_2O_3-CaO diagram phase published by Hallstedt [159] (left) and used in this work (right)

6.2.2.2 Al_2O_3-MgO

The system Al_2O_3-MgO presents an intermediate compound $MgAl_2O_4$, (spinel), which has been studied in depth for its interesting properties, especially in Earth sciences. Spinel has an high melting point, at about 2373 K. Experimental results [163,164] indicated that it is almost stoichiometric at lower temperatures while its homogeneity range increases at temperatures above 1473 K extending in the direction of Al2O3.

Previous experimental results and thermodynamic assessments of this system ([161,165,166]), have been summarized by Zienert [116], which improved the information about this systems with new experimental results. The model of the spinel phase has been implemented by Hallstedt [165] and its approach has been used in this work to describe the model of the phases. Actually spinel is not very important in the systems studied in this work and for this reason the model proposed by Hallstedt and used by Zienert has been adopted without further refinement.

The Al_2O_3-MgO parameters calculated by Zienert have used in this work and the resulting phase diagram is reported in Figure 174.

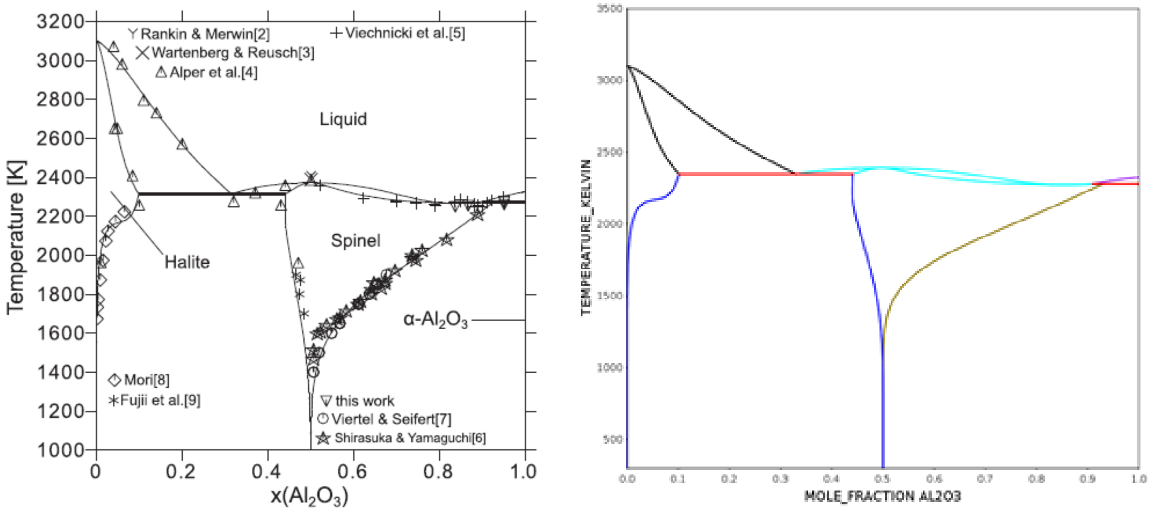

Figure 174 – Al_2O_3-MgO diagram phase published by Zienert [116] **(left) and used in this work (right)**

6.2.2.3 Al_2O_3-SiO_2

Mullite, the only intermediate stable phase at atmospheric pressure and high temperature in the Al_2O_3–SiO_2 system, has been the subject of numerous studies [167–169]. The thermodynamic assessment of the system has been published by Fabrichnaya et al.[122], and, in the following years by Mao et al.[170] and Lambotte and Chartrand [171], not considering the work of Fabrichnaya. In this work the optimization of Fabrichnaya (reported in Figure 175) has been adopted, because the phase models used are consistent with those adopted in the present work.

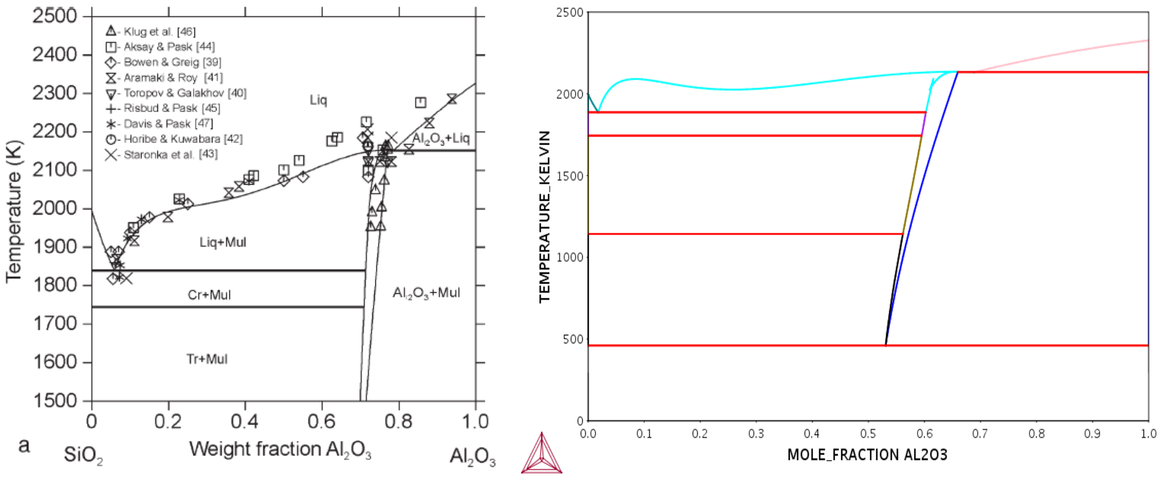

Figure 175 – Al_2O_3-SiO_2 diagram phase published by Fabrichnaya [122] (left) and used in this work (right)

6.2.2.4 Al_2O_3-Y_2O_3

In the Al_2O_3-Y_2O_3 system, there are three intermediate phases and it is not present any solubility. The three phases, called YAG, YAP and YAM are formed by congruent melting. In the system are present four eutectic reactions: Liquid ⇄ YAG + Al_2O_3 at 2084 K, Liquid ⇄ YAG + YAP at 2180 K, Liquid ⇄ YAP + YAM at temperature immediately above and Liquid ⇄ YAM + C-Y_2O_3 at 2220 K.

The description of the Al_2O_3-Y_2O_3system was modified by Fabrichnaya et al. [172] but a new reassessment was necessary because the Y–O description was changed by Swamy et al.[173].

Additionally, new calorimetric measurements became available and, for the consistency with other databases [174], the model of liquid needed to be changed by introducing a neutral species of AlO3/2 into the anion sublattice, published in the work about Al_2O_3-Y_2O_3-ZrO_2 ternary system[20]. These parameters have been used in this work, and the phase diagram is shown in Figure 176.

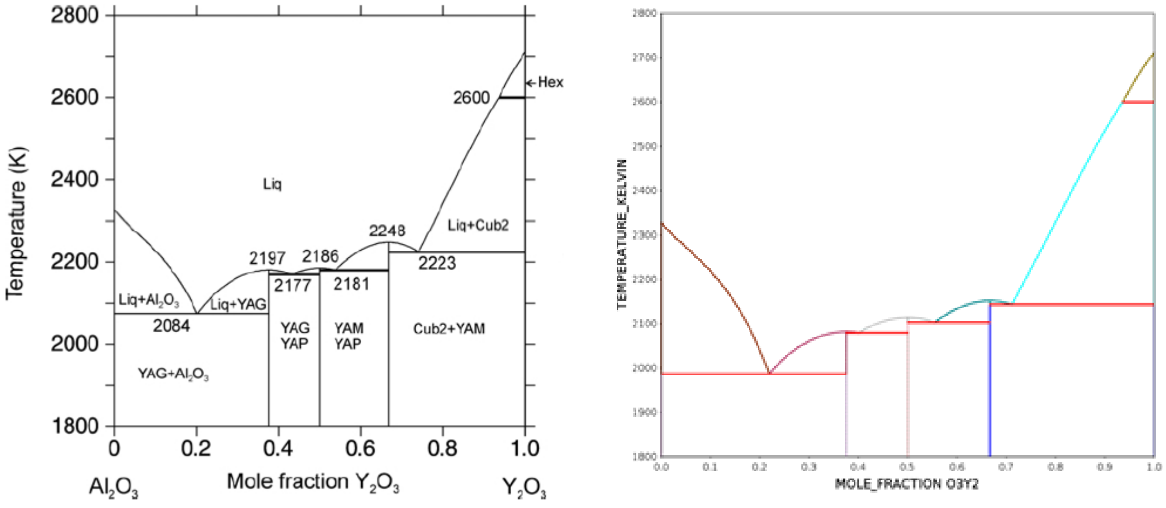

Figure 176 –Al_2O_3-Y_2O_3 diagram phase published by Fabrichnaya [20] (a) and used in this work (b)

6.2.2.5 Al_2O_3-ZrO_2

No intermediate compounds are stable in the Al_2O_3-ZrO_2 system. The T-ZrO_2 and C-ZrO_2 phases present a little solubility, but always less than 10 mol% of Al_2O_3 (around 4 mol% for cubic and 7 mol% for tetragonal phase). The invariant equilibrium are a eutectic reaction Liquid ⇄ T-ZrO2 + Al2O3 around 60 mol% of Al_2O_3 at 2140 K, the metatetic reactions C-ZrO_2 ⇄ T-ZrO_2 + Liquid at 2550 K and T-ZrO_2 ⇄ M-ZrO_2 + Al_2O_3 at 1400 K, as reported in Figure 177

The thermodynamic description of the ZrO_2–Al_2O_3 system was obtained by Dorner et al. [175] and Ball et al. [176], based on phase equilibria and the assumption that there is no solubility of Al_2O_3 in the solid phases. Wu [177] used a quasichemical model to describe the liquid phase in the ZrO_2–Al_2O_3 system.

Experimental investigations and thermodynamic modelling have been confirmed and reviewed by Fabrichnaya in 2004 [20]. Its assessment was adopted in the present work.

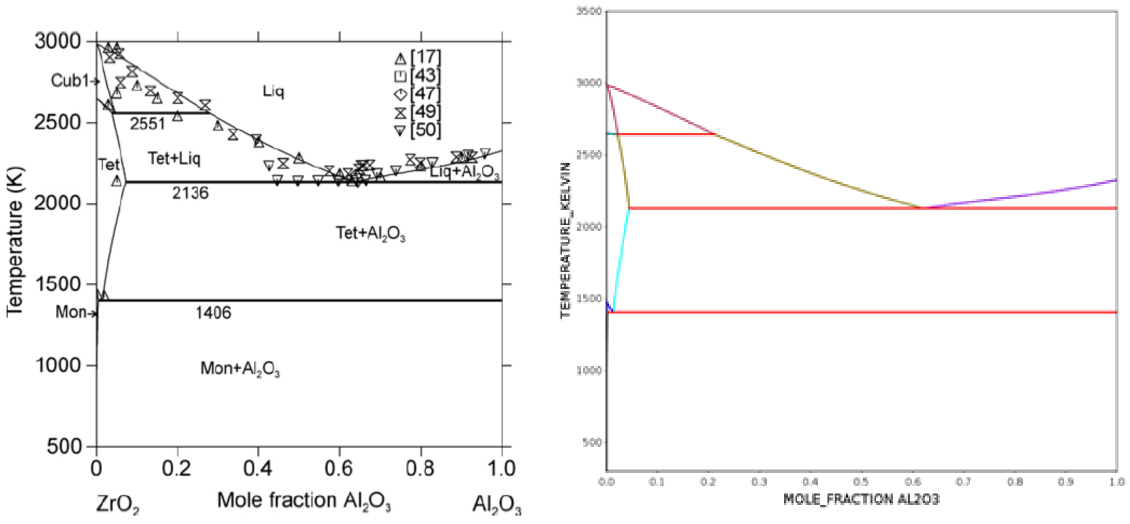

Figure 177 - Al_2O_3-ZrO_2 diagram phase published by Fabrichnaya [20] **(a) and used in this work (b)**

6.2.2.6 CaO-MgO

The CaO-MgO system is very simple, with only one eutectic reaction, Liquid ⇄ MgO + CaO at about 2650 K and two terminal solid solutions (both with halite structure), more exdended on the CaO side (CaO dissolves about 20 mol% of MgO, while on the MgO sideit is less than 10 mol%).

The assessment used in this work has been done by Hillert in 1989[178] (reported in Figure 178) , and substantially confirmed by Liang and Schmid-Fetzer in 2018 [179].

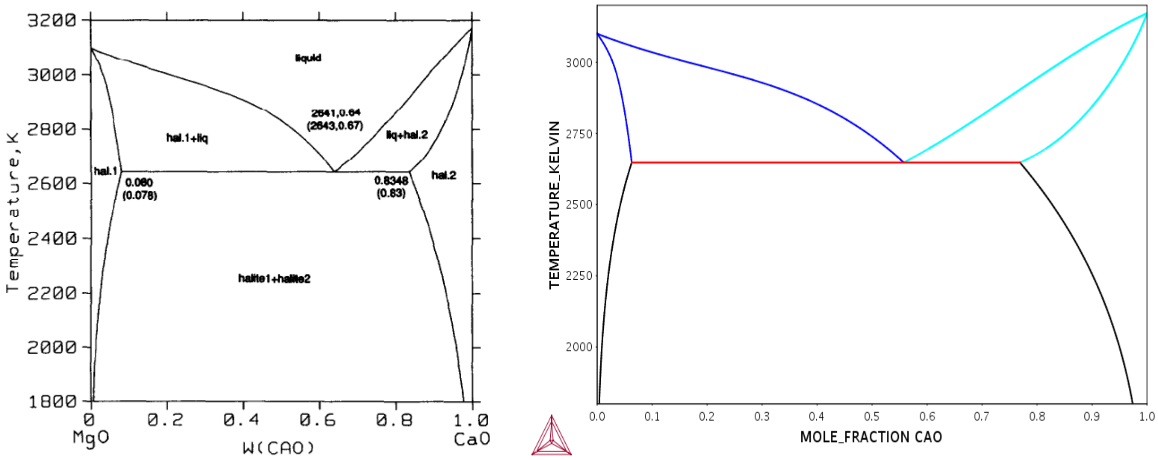

Figure 178 – CaO-MgO diagram phase published by Hillert [178] (left) and used in this work (right)

6.2.2.7 CaO-SiO$_2$

In the CaO-SiO$_2$ system there is no solid solubility, but four different stoichiometric compounds are stable.

The Ca_2SiO_4 has four polymorphic forms, olivine (below 1120 K), α'-Ca_2SiO_4 (1120 to 1710 K), α-Ca_2SiO_4 (up to 1710 K), and larnite (which forms as a metastable phase from α'-Ca_2SiO_4 below 970 K). α-Ca_2SiO_4 melts congruently at 2400 K. $CaSiO_3$ has two different polymorphic structure, wollastonite, below 1400 K and pseudo-wollastonite, stable up to the congruent melting at 1820K. The other two phases have peritectic decomposition: Hatrurite (Ca_3SiO_5) at 2700 K and Rankinite ($Ca_3Si_2O_7$) at 1740 K. Hatrurite decomposes at 1520 K.

The assessment of the system has been done by Hillert in 1990 [102] and it has been used in this work (Figure 179).

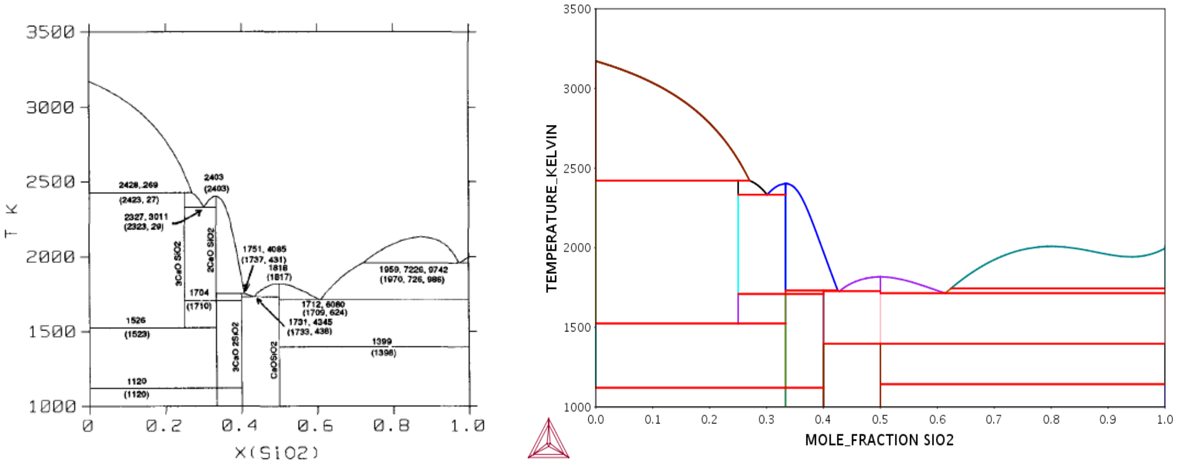

Figure 179 – CaO-SiO$_2$ diagram phase published by Hillert [102] (left) and used in this work (right)

6.2.2.8 $CaO-Y_2O_3$

The $CaO-Y_2O_3$ system has been studied by many experimental works [180–183], but the high temperatures and the proximity of the invariant reactions, made difficult to obtain an accurate knowledge of the phase diagram.

The first thermodynamic assessment has been published by Du and Jin in 1992[184].

The experimental and assessment works are summarized in the paper published by Li in 2018 [185] (Figure 180-a), which proposed a new modelling considering its own experimental results.

The phase models used by Li are not consistent with those adopted in the present work and a reassessment of the system was necessary. The phase diagram calculated according our new assessment is reported in Figure 180-b.

Terminal solid solutions are present on both sides: the CaO in Y_2O_3 is stable until a maximum of 8 mol% at 2400 K, while CaO dissolves a maximum of 13 mol% of Y_2O_3.

There are three intermediate compounds, all stable over 2000 K: $Ca_3Y_2O_6$ (stable in the range 2230-2430 K), CaY2O4 (stable between 2000 and 2400 K) and CaY_4O_7 (with stability range of 2400-2575 K).

The invariant equilibria are: $H-Y_2O_3 \rightleftarrows C-Y_2O_3 + Liquid$ at 2560 K, $Liquid \rightleftarrows CaY_4O_7 + C-Y_2O_3$ at 2550 K, $Liquid \rightleftarrows Ca_3Y_2O_6 + CaO$ at 2440K and $Liquid \rightleftarrows CaY_2O_4 + Ca_3Y_2O_6$ at 2430 K.

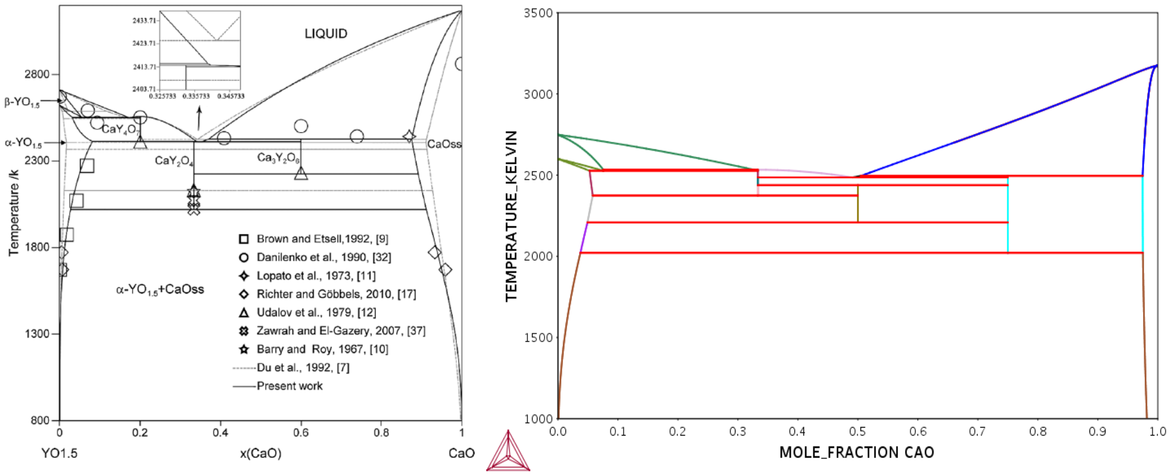

(a) *(b)*

Figure 180 - $CaO-Y_2O_3$ diagram phase published by Li[185] **(a) and assessed in this work (b)**

6.2.2.9 $CaO-ZrO_2$

In the $CaO-ZrO_2$ phase diagram all terminal phases, $C-ZrO_2$, $T-ZrO_2$, $M-ZrO_2$ and CaO (Halite), present some solubility. Among them only $C-ZrO_2$ dissolves CaO up to 20-25 mol%, while the solubility of the other phases is less than 10 mol%. Moreover in the system are three stable stoichiometric compounds: $CaZrO_3$, $CaZr_4O_9$ and $Ca_6Zr_{19}O_{44}$. The existence of $CaZr_4O_9$ and $Ca_6Zr_{19}O_{44}$ is controversial; although many research groups have investigated them, no general agreement has been reached about their existence. Another problem are their decomposition temperatures very close to eachother and thermodynamically unlikely. The $CaZrO_3$ phase has an allotropic transformation around 1250 K between orthorhombic and cubic structure.

The thermodynamic assessment has been done by Du et al. [186], Wang et al.[187] and Kwon and Jung [103]. In Figure 181-a is reported the phase diagram calculated by Kwon, where the experimental results are plotted.

Phase models used by these authors are not consistent with those adopted in the present work and a reassessment of the system was necessary. The phase diagram calculated in this work is compared with the previous version in Figure 181-b.

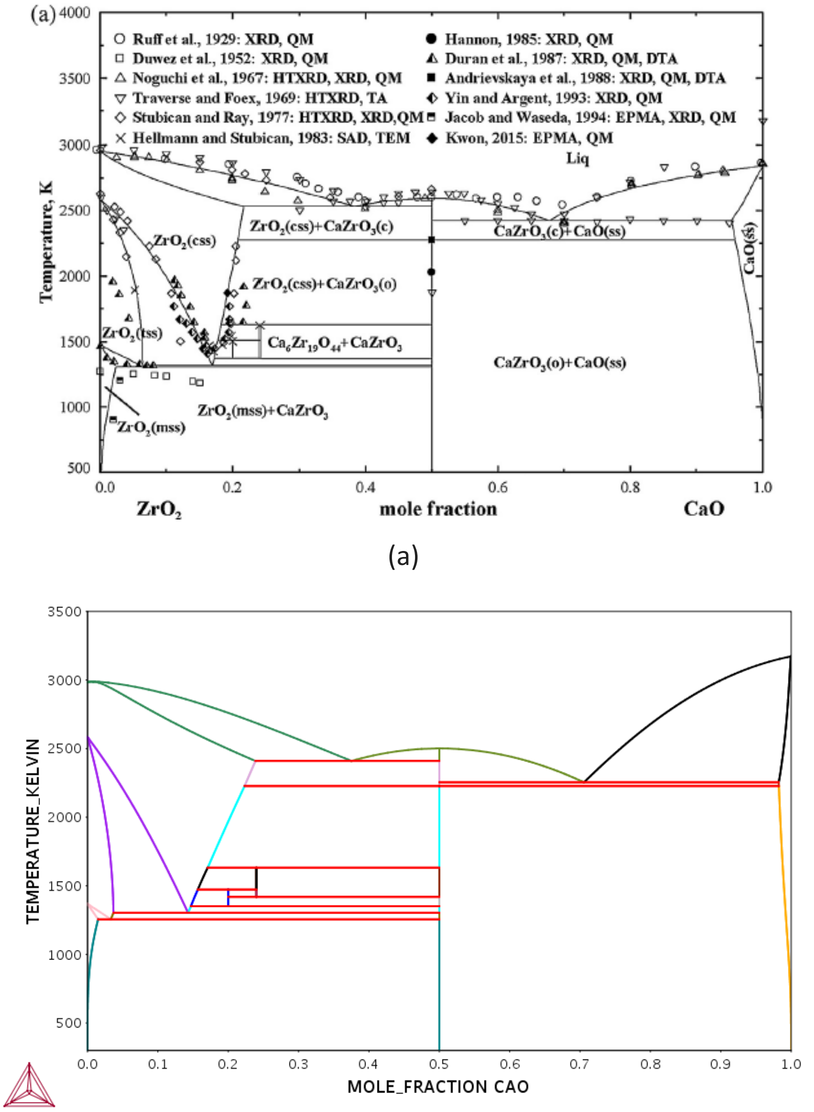

(a)

(b)

Figure 181 - CaO-ZrO_2 diagram phase published by Kwon[103]**(a) and obtained in this work (b)**

6.2.2.10 Al_2O_3 based ternary systems

The ternary systems based on alumina have not yet been included in the multicomponent database, but the critical review of the literature has been performed in this work.

The Al_2O_3-CaO-MgO system has been calculated by Hallstedt in 1995[188] with particular focus on liquid phase, while, thereafter, isothermal sections [189,190] and $CaAl_4O_7$-$MgAl_2O_4$ vertical section [191] have been experimentally investigated.

The Al_2O_3-CaO-SiO_2 system has been studied by Fabrichnaya and Nerad[192] using models compatible with those adopted in this work.

No thermodynamic assessment works have been founded about Al_2O_3-CaO-Y_2O_3, but the system has been experimentally studied by Udalov et al.[193] and Richter and Gobbels[194].

The system Al_2O_3-CaO-ZrO_2 has been also studied only experimentally in works performed in the 80s [195–197] of the last century.

The ternary systems Al_2O_3-MgO have not been studied in literature and no thermodynamic assessment has been found.

The Al_2O_3-SiO_2-Y_2O_3 has been optimized by Fabrichnaya et al. [172] considering many experimental works. It has been used and improved in subsequent papers [138,139]. The models used are compatible with database used in this work.

The Al_2O_3-SiO_2-ZrO_2 system has been calculated by CALPHAD method by Dorner et al in 1979 [175], while Al_2O_3- Y_2O_3 ZrO_2 system has been studied in detail by Fabrichnaya et al. in 2004 [20], a fundamental paper used in the present work to obtain phase models and thermodynamic functions.

6.2.2.11 CaO based ternary systems

The ternary systems formed by calcia have been partially considered in this work. The ternary systems formed by CaO and MgO have not been studied and should be considered for the completeness of the database.

The CaO-SiO_2-Y_2O_3 system has been investigated by Poerschke et al.[153]. This work has been used also to model the apatite phase in the MgO-SiO_2 Y_2O_3 system (see next chapter).

The system presents, in addition to apatite, three other intermediate phases that have been partially considered in this database. In particular, $Ca_3Y_2Si_6O_{18}$ phase is stable in the TBC-CMAS system studied experimentally in Ansaldo Energia laboratory.

CaO- SiO_2- ZrO_2 has been studied by Kwon et al. in 2017[198], using thermodynamic models not compatible with our database.

Finally, CaO- Y_2O_3- ZrO_2 has been modelled by Jin and Du[184], using phase models different from Kwon and our work.

The reassessment work of these systems, using experimental values reported in literature, is still in progress.

6.3 Discussion

The inter-oxide thermodynamic database for the simulation of the TBC-CMAS interactions was only defined in its initial phases and not all pseudo-binary and -ternary phase diagrams between ZrO_2, Y_2O_3, Al_2O_3, MgO, CaO and SiO_2 have been modeled and calculated.

The work was especially focused on the determination of the appropriate solution models for the terminal and intermediate solid phases with solubility in order to calculate solid solubility ranges in agreement with the results of the experimental investigations.

The determination of the models is particularly complicated in the case of multicomponent phases where several ions with different charge can mix, as described in chapter 6.1.2 where the model for the yttria-based mixed oxides is introduced.

One of the main problems is the proliferation end-members with the number of cationic species considered.

Once the models have been defined a critical analysis of all the literature about the systems is needed in order to reach a reliable evaluation of the interaction parameters required by models.

Moreover, thanks to the experimental study of the $MgO-Y_2O_3-ZrO_2$ ternary system, performed at the University of Freiberg in the group of Professor Olga Fabrichnaya, new information on this system has been obtained and its thermodynamic modeling improved.

This work, while not concluded, produced a useful basic structure of the inter-oxide database, which can be developed in the future by adding the assessments of the missing binary and ternary systems with calcium and aluminum.

Furthermore, the experimental data reported in chapter 5 show how the interaction between the thermal barrier and the oxide mixture is significant only at 1200° C. At that temperature the microstructure is significantly modified, but the formation of harmful phases is relevant only after long time. Furthermore, the quantities of secondary phases formed by the TBC-CMAS interaction are always lower than 5% and do not undergo compositional variation.

These findings allow us to state that the presence of CMAS partly influences the degradation of the material, but it seems more linked to kinetic than thermodynamic factors. Indeed, according to our results, the final amount of the monoclinic phase in the samples exposed with and without CMAS is the same, with the only difference that the latter forms the phase 1000-3000 hours before the former.

The evaluation of the t', t, c and m phase amounts in the samples without CMAS at 7 and 14 mol% Y_2O_3, gives us information about the ZrO_2-Y_2O_3 phase diagram in the area of greatest application interest, i.e. in the 0-20 wt% Y_2O_3 range.

According to the literature data, 7YSZ is the material where greater phase modifications occurs after exposure at high temperature.

At 1100 °C the matrix always remains t' for all exposure times, while the c phase tends to form after short times at 1200 °C, becoming the main phase always before 3000 h. At higher temperatures (1300 and 1400°C) the c phase is the only one detected.

Figure 182 shows the m phase evolution in the two 7YSZ batches for all the tested temperatures. The thermodynamic equilibrium is reached after 300h at 1400 °C and after 1000 h at 1300 °C. The effect of exposure time is mostly evident at 1200°C, where the m phase grows linearly respect other temperatures. Samples exposed at 1200°C show an amount of m phase after 10000 h, comparable to that measured at the highest temperatures. Finally, a temperature of 1100°C seems too low to detect important variations of phase amounts, also after 10000h.

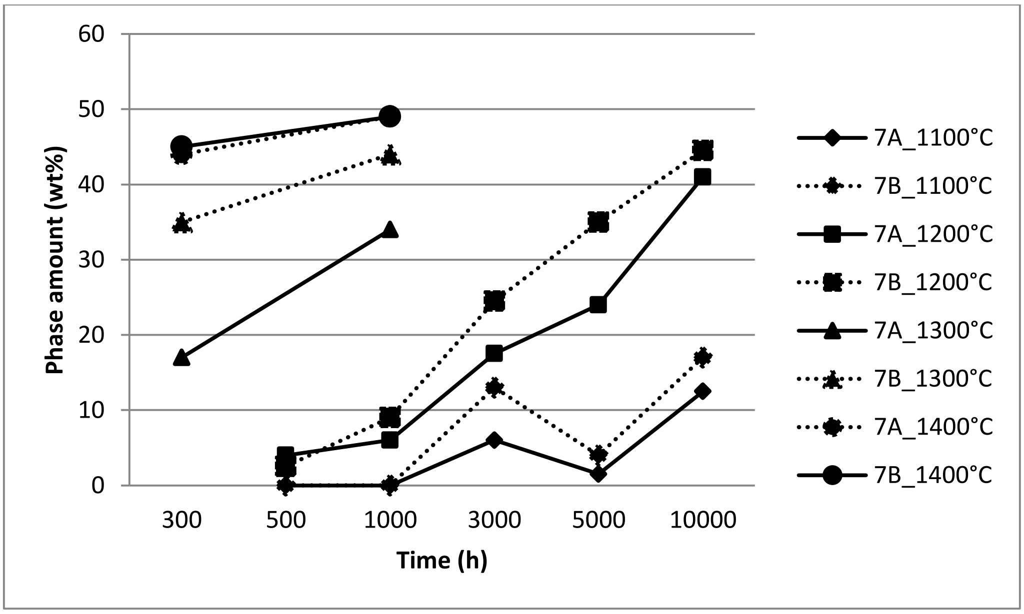

Figure 182 – Trend with time of m phase amount at all tested temperatures in a 7YSZ samples

In Figure 183 the evolution of t, t' and c phases at 1200°C has been reported. In both batches, the inversion (increasing/decreasing) of the t→c matrix occurs after 2000-3000h of exposure time.

Moreover, while the tetragonal phases tend to decrease with time, until it disappears after 10000h, the c phase remains constant after increasing during the first 3000h.

In Figure 183-b the different behavior of t' and t phases is reported. The t' phase, stable in as delivered samples, is the only phase measured after 500h, but it tends to disappear after 3000-5000h. The t phase however, missing at short time appears after 1000h, reaches a maximum around 3000h and after that to vanishes again after 10000h. The two phases are stable at the same time only at 1000h. Finally, no significant variation in the samples obtained with different batches has been observed.

The 14YSZ samples maintain the c structure at all the tested temperatures, regardless of the type of batch. Only at 1200°C, m phase has been identified with a quantity which could be the equilibrium amount. Samples exposed show the presence of small quantity of m phase only after 5000 h. This quantity is within the limits of the measurement uncertainty. Samples exposed for longer aging times confirm the presence of this phase, with a better definition of its quantity (around 6%).

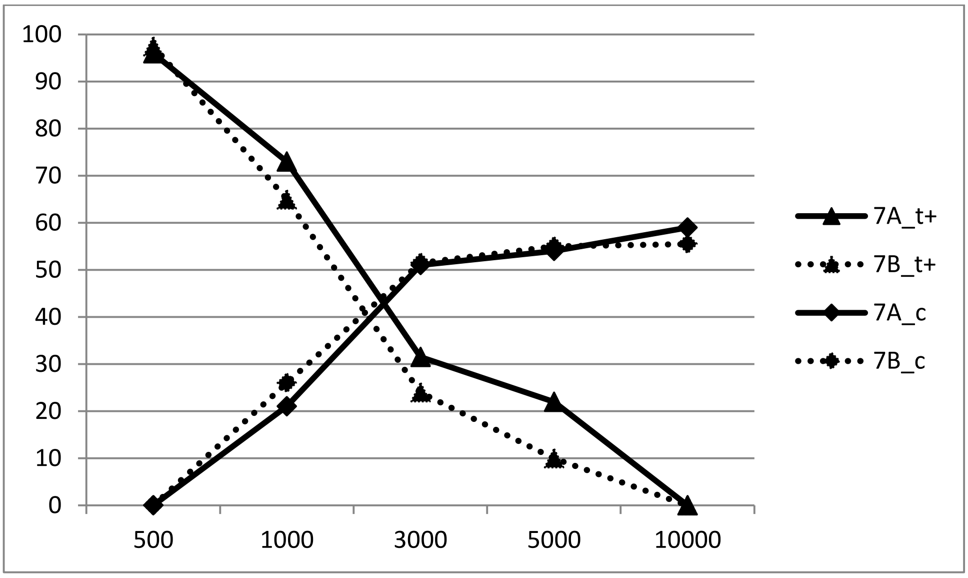

(a)

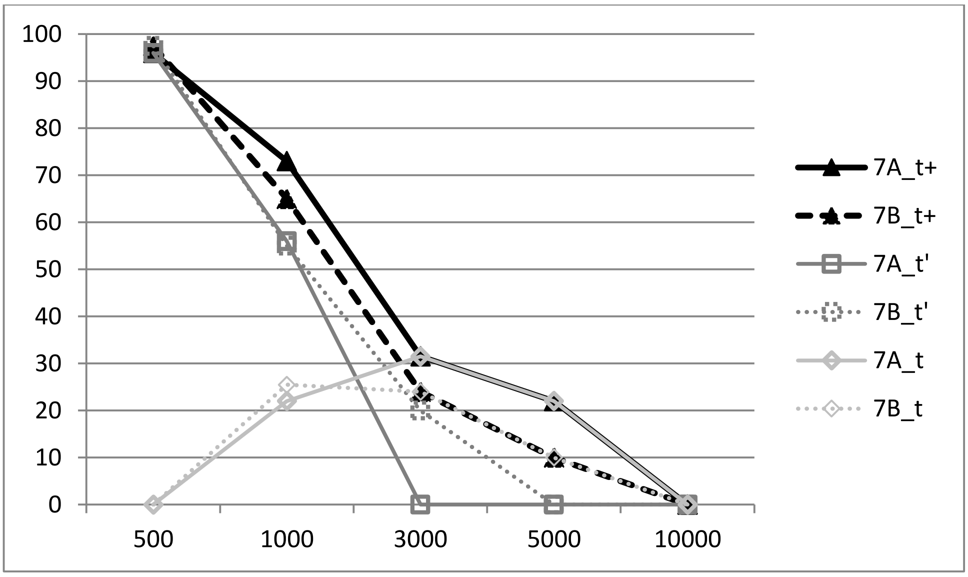

(b)

Figure 183 - Amount of c and t^+ phases in all samples exposed at 1200°C as a function of the exposure time (a), effect of t and t' phases in the total tetragonal trend (b)

The collection of these data allowed to slightly modify the ZrO_2-Y_2O_3 diagram in the zirconia rich area. The new phase equilibria are shown in Figure 184 by dotted lines and are compared to the literature data (continuous lines) already shown at the beginning of the thesis.

The behavior of the monoclinic phase at 1100°C suggests that the invariant equilibrium t → m + c is around that temperature, probably slightly higher. The presence of the t' phase in the samples, even after 10000h, underlines that the thermodynamic transformations have not yet come to an end. Similarly, the behavior of 14YSZ after a long exposure time at 1200°C, with the formation of the monoclinic phase, suggests that, at that temperature, the chosen composition lies inside the biphasic field t + c. During cooling, the tetragonal phase formed at high temperature evolves into the monoclinic phase.

The new version of the proposed diagram also foresees an increase of the t→m transition temperature in pure zirconia. Such transition temperatures have already investigated in literature with discordant results: The invariant temperatures proposed in this thesis have been used in the literature, for example by Kwon and Jung [103,198] in the assessment of binary and ternary systems containing zirconium oxide. The proposed changes will have to be confirmed by specific experimental and computational phase diagram studies, for example by investigating other compositions in addition to the two tested in this work.

If the present results will be confirmed, it will be necessary to slightly modify the assessment of pure zirconia in order to optimize higher order systems.

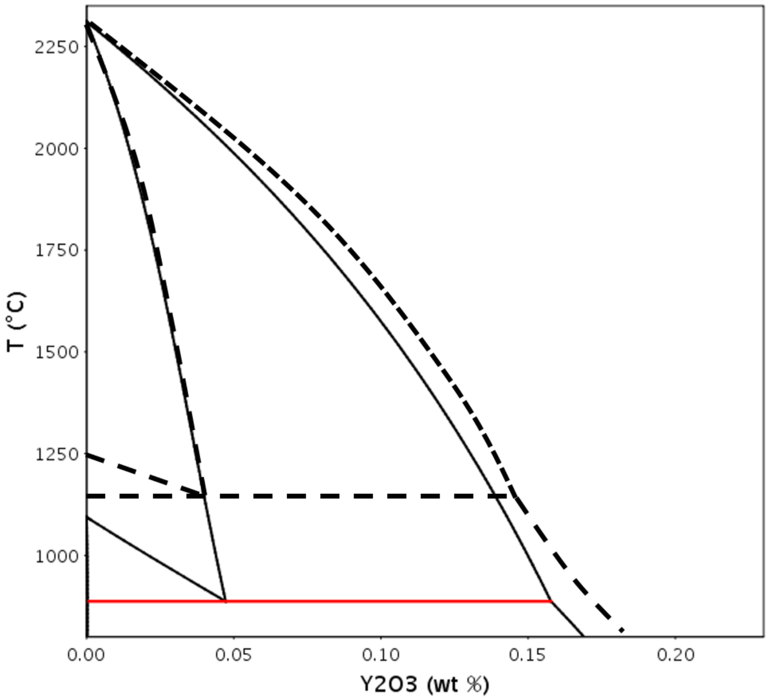

Figure 184 – New ZrO_2-Y_2O_3 phase diagram proposed by experimental results obtain in this thesis

7 Conclusion

The research activity reported in this thesis was carried out in the framework of a collaboration between Ansaldo Energia and the Department of Chemistry and Industrial Chemistry of the University of Genoa. The aim was to study and characterize the materials used in the ceramic coatings of gas turbine blades, by themselves and in contact with silicate powders known as CMAS. Our approach included experimental investigations and thermodynamic modeling according to the CALPHAD approach of inter-oxide interactions whit the aim of creating a tool which will enable future researchers to predict the evolution of such materials during service and in contact with corrosive substances.

Results reported in this thesis have been obtained also thanks to the collaboration with different research groups. In particular, phase models used for the implementation of the thermodynamic database were developed with the help of Prof. Olga Fabrichnaya and its group (University of Freiberg, Germany), while thermophysical properties were measured with the help of the group of Dr. Bison and Dr. Farrarini (CNR-ITC, Padova).

The experimental study considered different types of ceramic materials, from 7YSZ (zirconia partially stabilized with 7% yttria), regularly used in gas turbines, to new materials such as 14YSZ (zirconia with 14% yttria) and a double layer coating formed by the superposition of the two mentioned materials.

Several samples have been exposed to different high temperature treatments, with and without addition of CMAS, to evaluate how the applied conditions modify constitution and properties of the tested materials. Samples have been characterized by the classical materials investigation techniques. In particular, by XRD for phase identification and quantification, and SEM (with EDS and EBSD probes) for microstructural study.

In the first part of the thesis, phase evolution of 7YSZ due to high temperature treatments between 1100 and 1400°C has been studied in depth, with particular attention to the formation of the monoclinic phase, which is harmful to this type of material.

The study at different temperatures is also carried out to simulate the temperature gradient present inside the components in service. In fact, if the upper layer of the material exerts at a very high temperature (about 1400°C) the underlying layer see a significantly lower temperature (1100°C). Not being possible to simulate this gradient in static ovens, samples have been tested at different temperatures.

The study started from the evaluation of TBC obtained by APS deposition from different precursor powders. This allowed us to verify that the TBC performance is strongly affected by the characteristics of the starting material. In fact, an excess of monoclinic phase in the powders leads to a massive material with a constitution not suitable for use.

7YSZ powder has been exposed to high temperature with a batch of 14YSZ powder, to evaluate differences in the evolution of phases. It resulted that the monoclinic phase, present in the as delivered powders, tends to increase in the 7YSZ samples with increasing time and temperature, while it decreases in the 14YSZ samples. This suggests that the new 14YSZ material can be used in more extreme conditions than 7YSZ, as its composition lowers the amount of the monoclinic phase.

The effect of the different cooling rates from high-temperature on the evolution of the monoclinic phase has been evaluated in the 7YSZ material. This test has been designed to simulate the effect of start-up and shutdown cycles that the gas turbine undergoes in service.

Indeed, the monoclinic formation is inhibited/hindered by fast cooling from high temperature, but short aging at relatively low temperatures is sufficient to significantly increase its quantity in the material.

Actually, a treatment at a very low temperature (250°C) for 24h is enough for the phase to increase by about 10%, regardless of the deposition method used to obtain the material.

This phenomenon demonstrates that the operating temperature is not the only parameter for evaluating the degradation of the material used in gas turbines, but cycling and cooling processes must be taken into consideration.

Using samples exposed between 1100 and 1400°C, the variation of the material constitution was studied both from the kinetic (short exposure times) and the thermodynamic point of view (exposure times up to 10000h) by measuring the variation of the t, t' c and m phases after exposure to high temperature.

We found that:

- The **tetragonal prime phase** tends to decrease steadily with temperature; long-term studies show that beyond 1200°C it disappears after 3000h.
- The **tetragonal phase** tends to reach a maximum in the first hours of high temperature exposure (1300 and 1400°C), but it is no longer stable at 1200°C after 10000h. It is never stable at 1100°C, even after 10000h.
- The **cubic phase** is the high temperature matrix. At 1200°C the cubic phase becomes the predominant phase within 3000h, and, after that, it tends to remain constant. At 1100°C, 10% of this phase forms only after long exposure time.
- The **monoclinic phase** begins to grow slowly at 1100°C approaching an amount around 20% only after 10000h. At 1200°C it tends to grow steadily with time up to about 40%. At higher temperatures the increase is less pronounced, and it is not particularly visible with the

increasing exposure time at 1400°C, probably because the material reached quickly the thermodynamic equilibrium.

The good agreement of 7YSZ results with literature for each phase confirms that the phase evolution is similar regardless of the batch of precursor powders used, if the deposition technique is the same (in this case air plasma spray).

In conclusion, the 7YSZ material cannot be used at temperatures higher than 1200°C because the microstructural degradation is too fast at higher temperature.

The study of the evolution of the phases made it possible to use the quantity of tetragonal prime phase to evaluate the service temperature of the material in the gas turbine. This method is applicable If the turbine has operated within 1100 °C: However, if the material operates close to 1200°C for long times (e.g. life of the gas turbine about 25000 hours), this method is not applicable because the tetragonal prime phase is no longer stable. In these conditions, identifiable by the absence of the tetragonal phases and by a very high quantity of monoclinic phase, the material temperature can be derived from the amount of monoclinic phase, because at 1200°C it tends to increase linearly with the exposure time.

In the second part of the thesis, the degradation of the ceramic material due to the interaction with external corrosive agents such as CMAS mixtures, was studied. For this study, the classical 7YSZ material has been mainly considered, but innovative materials such as 14YSZ and 7+14YSZ bilayer have been also investigated.

The samples were exposed to four different temperatures for long times up to 10000h. The analysis by X-ray diffraction allowed to evaluate the evolution of the present phases in the samples and the micrographic analyzes the occurred microstructural modifications.

The amount of the monoclinic phase is higher in all materials in the samples with the presence of the corrosive at 1200°C. At higher temperature, this is confirmed only for 7YSZ and double layer materials (7YSZ + 14YSZ). The effect of both types of CMAS is to accelerate this transformation, with a stronger reactivity of ANS composition.

The effect of CMAS is very limited at 1100°C, due to low temperature, and small amount of secondary phases has been found. The evolution of the phases is very similar to that observed in the samples without CMAS. The presence of CMAS does not clearly modify the microstructural aspect.

At 1300°C and 1400°C the effect of CMAS is limited as it is liquid at this temperature and in all samples it penetrates through the samples without appreciable interaction. The equilibrium situation predicted by thermodynamics is reached: at 1400°C, even for the shortest aging time, while, at 1300°C, small evolution with time is observed between the two analyzed aging exposure (7YSZ and DL).

Exposure to these temperature leads to a sintering effect in the tested samples, as already observed in the CMAS-free samples, and an increase in grain size, especially the cubic ones (more evident in the 14YSZ samples).

The most interesting temperature for CMAS-TBC interaction is 1200°C where phase evolution and microstructural modifications are strongly accelerated by the presence of CMAS. In particular, ANS composition behaves as the most reactive one and for the longest aging time the difference between samples with and without CMAS is large and cannot be justified only by kinetic effects. In fact, at this temperature some interaction phases are observed.

Our investigations demonstrate that in the new 14YSZ material the monoclinic phase formation is inhibited at all tested temperatures except 1200°C after long time, or in the presence of CMAS.

It can be concluded that the 14YSZ material does not form dangerous m phase not only in highly demanding engines with very high inlet temperature, but also in conventional gas turbines, where pollution from external compressed air is possible. Then, the applicability of 14YSZ is wider than 7YSZ.

In the last chapter the thermodynamic models used for the oxide phases and the assessment procedure adopted for the implementation of a thermodynamic database for the simulation of the complex interactions occurring in CMAS-TBC systems under different thermodynamic conditions have been described.

Special attention was given to the definition of suitable phase models for the oxide solution phases, where several cations with different charge can share the same sublattice. This allowed us to create a well-structured database, which can be easily extended in the future to new components. Once completed, it will allow us to calculate not only the stable oxide phases in classical and new TBC in different working conditions, but also their interactions with other materials such as CMAS. In this way it will be possible to predict materials behavior during service in gas turbines.

Finally, the constitutional study of the main phases (namely tetragonal, cubic and monoclinic phases) stable after very long time equilibration at high temperature in TBC at two different compositions (7 and 14%) made it possible to propose some modification to the ZrO_2-Y_2O_3 phase diagram, which is crucial for the application of TBC. If our modifications will be confirmed by further experimental investigations, a thermodynamic reassessment of the ZrO_2-Y_2O_3 system will be necessary.

This thesis work allowed to clarify the properties and implementation limits of materials already used in gas turbines and to characterize new materials in order to determine the best usable temperature ranges. The in-depth knowledge of thermal barriers and their properties as a function of exposure to high temperatures and with the presence of corrosive agents can help to optimize the performance of the gas turbine, in particular the efficiency strictly correlated to the working temperature.

References

[1] M.P. Boyce, Gas Turbine Engineering Handbook, Fourth Edi, 2012.

[2] T. Giampaolo, Gas Turbine Handbook: Principles and Practices, 3rd Editio, 2006.

[3] S. Langston, G. Opdyke, Introduction to Gas Turbines for Non- Engineers, Glob. Gas Turbine News. 37 (1997).

[4] N.P. Padture, M. Gell, E.H. Jordan, Thermal Barrier Coatings for Gas-Turbine Engine Applications, Sci. Compass. 296 (2002) 280–285.

[5] I. Uda, Studio dell’evoluzione della microstruttura di una superlega a base cobalto allo scopo di individuare una metodologia per la stima della temperatura e della vita residua da applicare ai componenti caldi delle turbine a gas, University of Genoa, 2012.

[6] R.C. Reed, The superalloys: Fundamentals and Applications, 2006.

[7] Y. Wang, G. Cacciamani, Experimental investigation and thermodynamic assessment of the Al-Co-Ni system, Calphad Comput. Coupling Phase Diagrams Thermochem. 61 (2018) 198–210. https://doi.org/10.1016/j.calphad.2018.03.008.

[8] J. Sato, T. Omori, K. Oikawa, I. Ohnuma, R. Kainuma, K. Ishida, No Title, Science (80-.). 312 (2006). https://doi.org/10.1126/science.1121738.

[9] G. Roncallo, Studio della stabilità delle fasi in una lega a base cobalto utilizzata per i componenti delle turbine a gas, University of Genoa, 2016.

[10] S.R.J. Saunders, Coatings and surface treatments for high temperature oxidation resistance, 5 (1989) 780–798.

[11] G.W. Goward, Progress in coatings for gas turbine airfoils, 109 (1998) 73–79.

[12] M.J. Pomeroy, Materials & Design Coatings for gas turbine materials and long term stability issues, 26 (2005) 223–231. https://doi.org/10.1016/j.matdes.2004.02.005.

[13] Report Ansaldo Energia: Review of coatings and deposition processes for turbine blades, n.d.

[14] J.-M. Joubert, Crystal chemistry and Calphad modeling of the σ phase, Prog. Mater. Sci. 53 (2008) 528–583. https://doi.org/10.1016/j.pmatsci.2007.04.001.

[15] Report Ansaldo Energia, 2005.

[16] S. Sitzia, Studio dell’evoluzione nel tempo di un rivestimento metallico per componenti di turbine a gas, University of Genoa, 2018.

[17] L.Y. Liu, R. Shankar, P. Howard, Surface & Coatings Technology High sintering resistance of a novel thermal barrier coating, Surf. Coat. Technol. 204 (2010) 3154–3160. https://doi.org/10.1016/j.surfcoat.2010.02.072.

[18] D.R. Clarke, S.R. Phillpot, Thermal barrier coating materials, Mater. Today. 8 (2005) 22–29. https://doi.org/10.1016/S1369-7021(05)70934-2.

[19] E. Vacchieri, Degrado microstrutturale di superleghe dovuto all’esposizione ad alta

temperatura, anche in presenza di carichi meccanici, statici e ciclici, University of Genoa, 2008.

[20] O. Fabrichnaya, F. Aldinger, Assessment of thermodynamic parameters in the system ZrO_2–Y_2O_3–Al_2O_3, Zeitschrift Für Met. 95 (2004) 27–39. https://doi.org/10.3139/146.017909.

[21] K.A. Khor, J. Yang, Transformability of t-ZrO2 and lattice parameters in plasma sprayed rare-earth oxides stabilized zirconia coatings, 37 (1997) 1279–1286.

[22] G. Witz, V. Shklover, W. Steurer, S. Bachegowda, H.P. Bossmann, Phase evolution in yttria-stabilized zirconia thermal barrier coatings studied by rietveld refinement of X-ray powder diffraction patterns, J. Am. Ceram. Soc. 90 (2007) 2935–2940. https://doi.org/10.1111/j.1551-2916.2007.01785.x.

[23] J.R. Brandon, R. Taylor, Phase stability of zirconia-based thermal barrier coatings part I. Zirconia-yttria alloys, Surf. Coatings Technol. 46 (1991) 75–90. https://doi.org/10.1016/0257-8972(91)90151-L.

[24] J. Ilavsky, J. Wallace, J.K. Stalick, Thermal-Spray Yttria-Stabilized Zirconia Phase Changes During Annealing, Proc. Int. Therm. Spray Conf. 10 (2000) 1185–1189.

[25] U. Schulz, Phase Transformation in EB-PVD Yttria Partially Stabilized Zirconia Thermal Barrier Coatings during Annealing, J. Am. Ceram. Soc. 83 (2004) 904–910. https://doi.org/10.1111/j.1151-2916.2000.tb01292.x.

[26] R.A. Miller, Phase Stability in Plasma Sprayed, Partially Stabilized Zirconia- Yttria, Sci. Technol. Zirconia I. (1981) 241–253.

[27] H. Zhao, C.G. Levi, H.N.G. Wadley, Molten silicate interactions with thermal barrier coatings, Surf. Coatings Technol. 251 (2014) 74–86. https://doi.org/10.1016/j.surfcoat.2014.04.007.

[28] P. Mechnich, W. Braue, Volcanic Ash-Induced Decomposition of EB-PVD Gd 2 Zr 2 O 7 Thermal Barrier Coatings to Gd-Oxyapatite, Zircon, and Gd, Fe-Zirconolite, 1965 (2013) 1958–1965. https://doi.org/10.1111/jace.12251.

[29] C.S. Ramachandran, V. Balasubramanian, P. V. Ananthapadmanabhan, Thermal cycling behaviour of plasma sprayed lanthanum zirconate based coatings under concurrent infiltration by a molten glass concoction, Ceram. Int. 39 (2013) 1413–1431. https://doi.org/10.1016/j.ceramint.2012.07.084.

[30] D.L. Poerschke, C.G. Levi, Effects of cation substitution and temperature on the interaction between thermal barrier oxides and molten CMAS, J. Eur. Ceram. Soc. 35 (2015) 681–691. https://doi.org/10.1016/j.jeurceramsoc.2014.09.006.

[31] G. Moskal, L. Swad, M. Hetma, B. Witala, B. Mendala, J. Mendala, P. Sosnowy, Characterisation of the microstructure and thermal properties of Nd 2 Zr 2 O 7 and Nd 2 Zr 2 O 7 / YSZ thermal barrier coatings, 32 (2012) 2035–2042. https://doi.org/10.1016/j.jeurceramsoc.2011.12.004.

[32] H.P. Bossmann, G.C. Gualco, Ansaldo Report, n.d.

[33] G. Mauer, M.O. Jarligo, S. Rezanka, A. Hospach, R. Vaßen, Novel Opportunities for Thermal Spray by PS-PVD, Surf. Coat. Technol. (2014). https://doi.org/10.1016/j.surfcoat.2014.06.002.

[34] G. Mauer, A. Hospach, R. Vaßen, Surface & Coatings Technology Process development and coating characteristics of plasma spray-PVD, Surf. Coat. Technol. 220 (2013) 219–224. https://doi.org/10.1016/j.surfcoat.2012.08.067.

[35] X. Ma, F. Wu, J. Roth, M. Gell, E.H. Jordan, Low thermal conductivity thermal barrier coating deposited by the solution plasma spray process, 201 (2006) 4447–4452. https://doi.org/10.1016/j.surfcoat.2006.08.095.

[36] A.D. Jadhav, N.P. Padture, E.H. Jordan, M. Gell, P. Miranzo, E.R. Fuller, Low-thermal-conductivity plasma-sprayed thermal barrier coatings with engineered microstructures, 54 (2006) 3343–3349. https://doi.org/10.1016/j.actamat.2006.03.024.

[37] P. Blazdell, S. Kuroda, Plasma spraying of submicron ceramic suspensions using a continuous ink jet printer, 123 (2000) 239–246.

[38] H. Kassner, R. Siegert, D. Hathiramani, R. Vassen, D. Stoever, Application of Suspension Plasma Spraying (SPS) for Manufacture of Ceramic Coatings, 17 (2008) 115–123. https://doi.org/10.1007/s11666-007-9144-2.

[39] S. Sampath, U. Schulz, M.O. Jarligo, Processing science of advanced thermal-barrier systems, 37 (2012) 903–910. https://doi.org/10.1557/mrs.2012.233.

[40] X. Chen, T. Ohnuki, S. Kuroda, M. Gizynski, H. Araki, H. Murakami, M. Watanabe, Y. Sakka, Columnar and DVC-structured thermal barrier coatings deposited by suspension plasma spray : high-temperature stability and their corrosion resistance to the molten salt, Ceram. Int. 42 (2016) 16822–16832. https://doi.org/10.1016/j.ceramint.2016.07.174.

[41] S. Kim, D. Lee, J. Koo, C. Seok, Evaluation of Influence of Cracks on DVC Coating Using Finite Element Analysis, 467 (2014) 24–28. https://doi.org/10.4028/www.scientific.net/AMM.467.24.

[42] J.A. Haynes, M.K. Ferber, W.D. Porter, Characterization of Alumina Scales Formed During Isothermal and Cyclic Oxidation of Plasma-Sprayed TBC Systems at 1150 ° C, 52 (1999).

[43] W.J. Quadakkers, V. Shemet, D. Sebold, R. Anton, E. Wessel, L. Singheiser, Oxidation characteristics of a platinized MCrAlY bond coat for TBC systems during cyclic oxidation at 1000 8 C, 199 (2005) 77–82. https://doi.org/10.1016/j.surfcoat.2004.11.038.

[44] C.G. Levi, J.W. Hutchinson, M.H. Vidal-Sétif, C.A. Johnson, Environmental degradation of thermal-barrier coatings by molten deposits, MRS Bull. 37 (2012) 932–941. https://doi.org/10.1557/mrs.2012.230.

[45] R. Wellman, W. G., N. J.R., CMAS corrosion of EB PVD TBCs: Identifying the minimum level to initiate damage, Int. J. Refract. Met. Hard Mater. 28 (2010) 124–132.

[46] X. Chen, Calcium-magnesium-alumina-silicate (CMAS) delamination mechanisms in EB-PVD thermal barrier coatings, Surf. Coatings Technol. 200 (2006) 3418–3427. https://doi.org/10.1016/j.surfcoat.2004.12.029.

[47] S. Krämer, J. Yang, C.G. Levi, C.A. Johnson, Thermochemical interaction of thermal barrier coatings with molten CaO-MgO-Al 2O 3-SiO 2 (CMAS) deposits, J. Am. Ceram. Soc. 89 (2006) 3167–3175. https://doi.org/10.1111/j.1551-2916.2006.01209.x.

[48] J.M. Drexler, A.L. Ortiz, N.P. Padture, Composition effects of thermal barrier coating ceramics on their interaction with molten Ca-Mg-Al-silicate (CMAS) glass, Acta Mater. 60 (2012) 5437–5447. https://doi.org/10.1016/j.actamat.2012.06.053.

[49] Y.X. Kang, Y. Bai, C.G. Bao, Y. Wang, H.Y. Chen, Y. Gao, B.Q. Li, Defects/CMAS corrosion resistance relationship in plasma sprayed YPSZ coating, J. Alloys Compd. 694 (2017) 1320–1330. https://doi.org/10.1016/j.jallcom.2016.10.074.

[50] A.R. Krause, H.F. Garces, G. Dwivedi, A.L. Ortiz, S. Sampath, N.P. Padture, Calcia-magnesia-alumino-silicate (CMAS)-induced degradation and failure of air plasma sprayed yttria-stabilized zirconia thermal barrier coatings, Acta Mater. 105 (2016) 355–366. https://doi.org/10.1016/j.actamat.2015.12.044.

[51] R. Kumar, E. Jordan, M. Gell, J. Roth, C. Jiang, J. Wang, S. Rommel, CMAS behavior of yttrium aluminum garnet (YAG) and yttria-stabilized zirconia (YSZ) thermal barrier coatings, Surf. Coatings Technol. 327 (2017) 126–138. https://doi.org/10.1016/j.surfcoat.2017.08.023.

[52] L. Li, N. Hitchman, J. Knapp, Failure of thermal barrier coatings subjected to CMAS attack, J. Therm. Spray Technol. 19 (2010) 148–155. https://doi.org/10.1007/s11666-009-9356-8.

[53] P. Mohan, B. Yuan, T. Patterson, V. Desai, Y. Sohn, Degradation of yttria stabilized zirconia thermal barrier coatings by molten CMAS (CaO-MgO-Al2O3-SiO2) deposits, Mater. Sci. Forum. 595-598 PA (2008) 207–212. https://doi.org/10.4028/www.scientific.net/MSF.595-598.207.

[54] Y. Wu, H. Luo, C. Cai, Y. Wang, Y. Zhou, L. Yang, G. Zhou, Comparison of CMAS corrosion and sintering induced microstructural characteristics of APS thermal barrier coatings, J. Mater. Sci. Technol. 35 (2019) 440–447. https://doi.org/10.1016/j.jmst.2018.09.046.

[55] M. Firpo, Characterization of ceramic coating with function of thermal barrier after Calcium-Magnesium-Alumino-Silicates attack, University of Genoa, 2015.

[56] A. Bonadei, G.C. Gualco, H.P. Bossmann, Ansaldo Energia, 2015.

[57] A.K. Rai, R.S. Bhattacharya, D.E. Wolfe, T.J. Eden, CMAS-resistant thermal barrier coatings (TBC), Int. J. Appl. Ceram. Technol. 7 (2010) 662–674. https://doi.org/10.1111/j.1744-7402.2009.02373.x.

[58] W.D. Callister, Materials science and engineering An introduction, 9th Editio, 2000.

[59] H.M. Rietveld, A profile refinement method for nuclear and magnetic structures, J. Appl.

Crystallogr. 2 (1969) 65–71. https://doi.org/10.1107/s0021889869006558.

[60] B.A. Hunter, C.J. Howard, D.J. Kim, Neutron Diffraction Study of Tetragonal Zirconias containing Tetravalent Dopants, Aust. J. Phys. 51 (1998) 539–545.

[61] D.G. Lamas, N.E. Walsoe de Reca, X-ray diffraction study of compositionally homogeneous , nanocrystalline yttria-doped zirconia powders, 35 (2000) 5563–5567.

[62] X. Xia, R. Oldman, R. Catlow, Computational Modeling Study of Bulk and Surface of Yttria-Stabilized Cubic Zirconia, (2009) 3576–3585. https://doi.org/10.1021/cm900417g.

[63] L.M.D. Cranswick, R.J. Hill, Golden Book of Phase Transitions, 1st ed., Wroclaw, 2002.

[64] L.B. McCusker, R.B. Von Dreele, D.E. Cox, D. Douer, P. Scardi, Rietveld refinement guidelines, J. Appl. Cryst. 32 (1999) 36–50.

[65] M. Davidson, M. Abramowitz, Optical Microscopy, 2002.

[66] A.J. Schwartz, M. Kumar, B.L. Adams, D.P. Field, Electron Backscatter Diffraction in Materials Science, 2009.

[67] J.A. Cape, G.W. Lehman, Temperature and Finite PulseTime Effects in the Flash Method for Measuring Thermal Diffusivity, 1909 (1963) 1–6. https://doi.org/10.1063/1.1729711.

[68] R.D. Cowan, Pulse Method of Measuring Thermal Diffusivity at High Temperatures, 926 (1963) 34–36. https://doi.org/10.1063/1.1729564.

[69] R.E. Taylor, K.D. Maglic, Pulse method for thermal diffusivity measurement, Plenum Press, 1984.

[70] A. Technical Report C714-72, Standard test method for thermal diffusivity of carbon and graphite by a thermal pulse method., 1972.

[71] W.J. Parker, R.J. Jenkins, C.P. Butler, G.L. Abbott, Flash Method of Determining Thermal Diffusivity, Heat Capacity, and Thermal Conductivity, 1679 (1961). https://doi.org/10.1063/1.1728417.

[72] T. Nishizawa, Progress of CALPHAD, Mater. Trans. JIM. 33 (1992) 713–722. https://doi.org/10.2320/matertrans1989.33.713.

[73] Lukas. H.L., E.T. Henig, B. Zimmermann, Optimization of phase diagrams by a least squares method using simultaneously different types of data, Calphad. 1 (1977) 225–236.

[74] B. Sundman, B. Jansson, J.-O. Andersson, The thermo-calc databank system, Calp. (1985) 153–190.

[75] H.J. Seifert, F. Aldinger, Applied Phase Studies, Z. Met. 87 (1996) 841–853.

[76] O. Redlich, A.T. Kister, Algebraic Representation of Thermodynamic Properties and the Classification of Solutions, Ind. Eng. Chem. 40 (1948) 345–348. https://doi.org/10.1021/ie50458a036.

[77] M. Hillert, The compound energy formalism, J. Alloys Compd. 320 (2001) 161–176.

[78] H.L. Lukas, S.G. Fries, B. Sundman, Computationl thermodynamics: The CALPHAD method, Cambridge University Press, 2007.

[79] M. Hillert, Phase equilibria, phase diagrams and phase transformations, their thermodynamic basis, 1998.

[80] V. Lughi, D.R. Clarke, Low-temperature transformation kinetics of electron-beam deposited 5 wt.% yttria-stabilized zirconia, Acta Mater. 55 (2007) 2049–2055. https://doi.org/10.1016/j.actamat.2006.11.007.

[81] M. Yashima, M. Kakihana, M. Yoshimura, Metastable-stable phase diagrams in the zirconia-containing systems utilized in solid-oxide fuel cell application, Solid State Ionics. (1996) 1131–1149.

[82] B. E, G.C. Gualco, Ansaldo Energia - powders studies, 2008.

[83] J.H. Pee, T. Akao, S. Ohtsuka, M. Hayakawa, The Kinetics of Isothermal Martensitic Transformation of Zirconia Containing a Small Amount of Yttria, Mater. Trans. 44 (2003) 1783–1789. https://doi.org/10.2320/matertrans.44.1783.

[84] J. Chevalier, L. Gremillard, A. V. Virkar, D.R. Clarke, The tetragonal-monoclinic transformation in zirconia: Lessons learned and future trends, J. Am. Ceram. Soc. 92 (2009) 1901–1920. https://doi.org/10.1111/j.1551-2916.2009.03278.x.

[85] J. Lefevre, De Differenetes Modifications Structurales des Phases de Type Fluorine Dans les Systemses a Base de Zircone ou D'Oxyde de Hafnium (Various Structural Modifications of the Fluorite Type Phases in Systems Zirconium or Hafnium Oxide), Ann. Chim. 8 (1963) 117–149.

[86] H.G. Scott, Phase relationships in the zirconia-yttria system, J. Mater. Sci. 10 (1975) 1527–1535. https://doi.org/10.1007/BF01031853.

[87] G. Roncallo, E. Barbareschi, G. Cacciamani, E. Vacchieri, Effect of cooling rate on phase transformation in 6–8 wt% YSZ APS TBCs, Surf. Coatings Technol. 412 (2021).

[88] G. Witz, H.P. Bossmann, Determination of Thermal Barrier Coatings Average Surface Temperature After Engine Operation for Lifetime Validation, J. Eng. Gas Turbines Power. 134 (2012). https://doi.org/10.1115/1.4007343.

[89] E. Dow Whitney, Kinetics and Mechanism of the Transition of Metastable Tetragonal to Monoclinic Zirconia, Trans. Faraday Soc. 61 (165AD) 1991–2000.

[90] C. Wang, M. Zinkevich, F. Aldinger, The Zirconia-Hafnia system: DTA measurements and thermodynamic calculations, J. Am. Ceram. Soc. 89 (2006) 3751–3758. https://doi.org/10.1111/j.1551-2916.2006.01286.x.

[91] B. E, DG00015304, 2017.

[92] H. Chang, C. Cai, Y. Wang, Y. Zhou, L. Yang, G. Zhou, Calcium-rich CMAS corrosion induced microstructure development of thermal barrier coatings, Surf. Coatings Technol. 324 (2017)

577–584. https://doi.org/10.1016/j.surfcoat.2017.05.076.

[93] Z. Stein, R. Naraparaju, U. Schulz, P. Kenesei, J.-S. Park, J. Almer, S. Raghavan, Synchrotron X-Ray Diffraction Study of Phase Transformation in CMAS Ingressed EB-PVD Thermal Barrier Coatings, (2020) 1–8. https://doi.org/10.2514/6.2020-0400.

[94] G. Pujol, F. Ansart, J.P. Bonino, A. Malié, S. Hamadi, Step-by-step investigation of degradation mechanisms induced by CMAS attack on YSZ materials for TBC applications, Surf. Coatings Technol. 237 (2013) 71–78. https://doi.org/10.1016/j.surfcoat.2013.08.055.

[95] P. Scardi, L. Lutterotti, E. Galvanetto, Microstructural characterization of plasma-sprayed zirconia thermal barrier coatings by X-ray diffraction full pattern analysis, Surf. Coatings Technol. 61 (1993) 52–59. https://doi.org/10.1016/0257-8972(93)90202-Y.

[96] N.R. Shankar, H. Herman, S.P. Singhal, C.C. Berndt, Neutron and X-ray diffraction of plasma-sprayed zirconia-yttria thermal barrier coatings, Thin Solid Films. 119 (1984) 159–171. https://doi.org/10.1016/0040-6090(84)90531-5.

[97] J.D. Ballard, J. Davenport, C. Lewis, W. Nelson, R.H. Doremus, L.S. Schadler, Phase stability of thermal barrier coatings made from 8 wt.% yttria stabilized zirconia: A technical note, J. Therm. Spray Technol. 12 (2003) 34–37. https://doi.org/10.1361/105996303770348474.

[98] F. Cernuschi, P. Bison, D.E. Mack, M. Merlini, S. Boldrini, S. Marchionna, S. Capelli, S. Concari, A. Famengo, A. Moscatelli, W. Stamm, Thermo-physical properties of as deposited and aged thermal barrier coatings (TBC) for gas turbines: State-of-the art and advanced TBCs, J. Eur. Ceram. Soc. 38 (2018) 3945–3961. https://doi.org/10.1016/j.jeurceramsoc.2018.04.044.

[99] J.E. Saal, D.W. Shin, A.J. Stevenson, G.L. Messing, Z.K. Liu, J. O. Andersson, T. Helander, L. H. Hoeglund, P. S. Shi, and B. Sundman, 312 (2010).

[100] G. Di Girolamo, C. Blasi, L. Pagnotta, M. Schioppa, Phase evolution and thermophysical properties of plasma sprayed thick zirconia coatings after annealing, Ceram. Int. 36 (2010) 2273–2280. https://doi.org/10.1016/j.ceramint.2010.07.035.

[101] D.M. Lipkin, J.A. Krogstad, Y. Gao, C.A. Johnson, W.A. Nelson, C.G. Levi, Phase evolution upon aging of air-plasma sprayed t′-zirconia coatings: I - Synchrotron X-ray diffraction, J. Am. Ceram. Soc. 96 (2013) 290–298. https://doi.org/10.1111/j.1551-2916.2012.05451.x.

[102] M. Hillert, B. Sundman, X. Wang, An assessment of the CaO-SiO2 system, Metall. Trans. B. 21 (1990) 303–312. https://doi.org/10.1007/BF02664198.

[103] S.Y. Kwon, I.H. Jung, Critical evaluation and thermodynamic optimization of the CaO-ZrO2and SiO2-ZrO2systems, J. Eur. Ceram. Soc. 37 (2017) 1105–1116. https://doi.org/10.1016/j.jeurceramsoc.2016.10.008.

[104] A. Azzopardi, R. Mévrel, B. Saint-Ramond, E. Olson, K. Stiller, Influence of aging on structure and thermal conductivity of Y-PSZ and Y-FSZ EB-PVD coatings, Surf. Coatings Technol. 177–178

(2004) 131–139. https://doi.org/10.1016/j.surfcoat.2003.08.073.

[105] V. Lughi, D.R. Clarke, Transformation of electron-beam physical vapor-deposited 8 wt% yttria-stabilized zirconia thermal barrier coatings, J. Am. Ceram. Soc. 88 (2005) 2552–2558. https://doi.org/10.1111/j.1551-2916.2005.00452.x.

[106] J.A. Krogstad, M. Lepple, Y. Gao, D.M. Lipkin, C.G. Levi, Effect of yttria content on the zirconia unit cell parameters, J. Am. Ceram. Soc. 94 (2011) 4548–4555. https://doi.org/10.1111/j.1551-2916.2011.04862.x.

[107] H. Toraya, Effect of YO1.5 Dopant on Unit-Cell Parameters of ZrO2 at Low Contents of YO1.5, J. Am. Ceram. Soc. 72 (1989) 662–664. https://doi.org/10.1111/j.1151-2916.1989.tb06191.x.

[108] R.P. Ingel, L.I. D., Lattice Parameters and Density for Y2O3-Stabilized ZrO2, J. Am. Ceram. Soc. 69 (1986) 325–332. https://doi.org/10.1111/j.1151-2916.1986.tb04741.x.

[109] C. Wang, Experimental and Computational Phase Studies of the ZrO 2 -based Systems for Thermal Barrier Coatings Chong Wang, 2006.

[110] C. Artini, G.A. Costa, M. Pani, A. Lausi, J. Plaisier, Journal of Solid State Chemistry Structural characterization of the CeO 2 / Gd 2 O 3 mixed system by synchrotron X-ray diffraction, J. Solid State Chem. 190 (2012) 24–28. https://doi.org/10.1016/j.jssc.2012.01.056.

[111] M. Chen, B. Hallstedt, L.J. Gauckler, Thermodynamic modeling of the ZrO2-YO1.5system, Solid State Ionics. 170 (2004) 255–274. https://doi.org/10.1016/j.ssi.2004.02.017.

[112] S. Katagiri, N. Ishizawa, A new high temperature modification of face-centered cubic Y 2 O 3, 8 (1993) 10060.

[113] V. Swamy, N.A. Dubrovinskaya, L.S. Dubrovinsky, I. Introduction, melting point, (1999) 456–459.

[114] A. Navrotsky, L. Benoist, H. Lefebvre, Direct Calorimetric Measurement of Enthalpies of Phase Transitions at 2000 1 –2400 1 C in Yttria and Zirconia, 2944 (2005) 2942–2944. https://doi.org/10.1111/j.1551-2916.2005.00506.x.

[115] S. V Ushakov, A. Navrotsky, Experimental Approaches to the Thermodynamics of Ceramics above 1500 ° C, 20 (2012) 1–20. https://doi.org/10.1111/j.1551-2916.2012.05102.x.

[116] T. Zienert, O. Fabrichnaya, Thermodynamic assessment and experiments in the system MgO-Al2O3, Calphad Comput. Coupling Phase Diagrams Thermochem. 40 (2013) 1–9. https://doi.org/10.1016/j.calphad.2012.10.001.

[117] G. Roncallo, G. Cacciamani, E. Vacchieri, M. Ilatovskaia, I. Saenko, O. Fabrichnaya, Thermodynamic modeling and experimental investigation of the MgO-Y2O3-ZrO2 system, J. Am. Ceram. Soc. (2020) 1–17. https://doi.org/10.1111/jace.17224.

[118] V. Swamy, S.K. Saxena, B. Sundman, An assessment of the one-bar liquidus phase relations in the MgO-SiO2 system, Calphad. 18 (1994) 157–164.

[119] S.K. Saxena, Earth mineralogical model: Gibbs free minimization computation in the system

MgO-FeO-SiO2, Geochim. Cosmochim. Acta. 60 (1996) 2379–2395.

[120] O.B. Fabrichnaya, Themodynamic modelling of melting in the system FeO-MgO-SiO2-02 at pressure of 1 bar, Calphad. 24 (2000) 113–131.

[121] V.B.M. Hageman, H.A.J. Oonk, No Title, Phys. Chem. Glas. 27 (1986) 194–198.

[122] O.B. Fabrichnaya, A. Costa e Silva, F. Aldinger, Assessment of thermodynamic functions in the MgO–Al2O3–SiO2 system, Zeitschrift Für Met. 95 (2004) 793–805.

[123] L.M. Lopato, Tresvyatskii S.G., Phase diagram of the system Y2O3-MgO, Ov. Powder Matall. Met. Ceram. 6 (1963) 454–457.

[124] Tresvyatskii S.G., L.M. Lopato, O.A. A., S.A. V., Phase diagram of systems formed by Yttrium, Erbium and Ytterbium Oxides with Magnesium Oxide, Inorg. Mater. 7 (1971) 1798–1801.

[125] Y. Du, Z. Jin, Thermodynamic assessment of the YO1.5MgO system, J. Alloys Compd. 176 (1991) 3–6. https://doi.org/10.1016/0925-8388(91)90003-E.

[126] A.V. Shevchenko, L.M. Lopato, Y.M. Karpenko, G.I. Gerasimyuk, A.K. Ruban, Liquidus surface and polythermal sections of the system ZrO2-Y2O3-MgO, Inorg. Mater. 27 (1991) 830–833.

[127] N. Bochvar, L. Rokhlin, Ternary Alloys. A Comprehensive Compendium of Evaluated Constitutional Data and Phase Diagrams, Wiley-VCH, Weinheim, 2001.

[128] Y. Du, Z. Jin, P. Huang, Thermodynamic Calculation of the Z r 0 2 -YO .5 -MgO System, 12 (1991).

[129] Y. Du, Z. Jin, P. Huang, Thermodynamic Assessment of the ZrO2–YO1.5 System, J. Am. Ceram. Soc. 74 (1991) 1569–1577. https://doi.org/10.1111/j.1151-2916.1991.tb07142.x.

[130] Y. Yin, B.B. Argent, Phase diagrams and thermodynamics of the systems ZrO2-CaO and ZrO2-MgO, J. Phase Equilibria. 14 (1993) 439–450. https://doi.org/10.1007/BF02671962.

[131] S. Serena, M.A. Sainz, S. de Aza, A. Caballero, Thermodynamic assessment of the system ZrO2-CaO-MgO using new experimental results Calculation of the isoplethal section MgO·CaO-ZrO2, J. Eur. Ceram. Soc. 25 (2005) 681–693. https://doi.org/10.1016/j.jeurceramsoc.2004.02.011.

[132] D. Pavlyuchkov, G. Savinykh, O. Fabrichnaya, Experimental Investigation and Thermodynamic Modeling of the ZrO2 -MgO System, Adv. Eng. Mater. 15 (2013) 618–626. https://doi.org/10.1002/adem.201200316.

[133] N.A. Toropov, I.A. Bondar, Silicates of rare-earth elements, Izv. Akad. Nauk SSSR, Otd. Khim. Nauk. (1961) 547–550.

[134] I.A. Bondar, Rare-earth silicates, Izv. Acad. Nauk SSSR, Ser. Khim. (1964) 1921–1925.

[135] C.H. Drummond, W.E. Lee, W.A. Sanders, J.D. Kiser, Crystallization and characterization of Y2O3-SiO2 glasses, Ceram. Eng. Sci. Proc. 9 (1988) 1343–1354.

[136] I. Warsaw, R. Roy, Progress in the Science and Technology of the Rare Earth, vol. 1, Pergamon Press, 1964.

[137] D.M. Cupid, H.J. Seifert, Thermodynamic calculations and phase stabilities in the Y-Si-C-O

system, J. Phase Equilibria Diffus. 28 (2007) 90–100. https://doi.org/10.1007/s11669-006-9014-5.

[138] H. Mao, M. Selleby, O. Fabrichnaya, Thermodynamic reassessment of the Y 2O3-Al2O3-SiO2 system and its subsystems, Calphad Comput. Coupling Phase Diagrams Thermochem. 32 (2008) 399–412. https://doi.org/10.1016/j.calphad.2008.03.003.

[139] Z. Pan, O. Fabrichnaya, H.J. Seifert, R. Neher, K. Brandt, M. Herrmann, Thermodynamic evaluation of the Si-C-Al-Y-O system for LPS-SiC application, J. Phase Equilibria Diffus. 31 (2010) 238–249. https://doi.org/10.1007/s11669-010-9695-7.

[140] D.N. Kamaev, S.A. Archugov, G.G. Mikhailov, Study and thermodynamic analysis of the ZrO2-SiO2 system, Russ. J. Appl. Chem. 78 (2005) 200–203. https://doi.org/10.1007/s11167-005-0259-2.

[141] C.E. Curtis, H.G. Sowman, investigation of the Thermal Dissociation , Reassociation , and Synthesis of Zircon, J. Am. Ceram. Soc. 36 (1953) 190–193.

[142] W.C. Butterman, W.R. Foster, Zircon stability and the zirconium oxide-silicaphase diagram, Am. Miner. 52 (1967) 880–885.

[143] M.R. Anseau, J.P. Biloque, P. Fierens, Some studies on the thermal solid statestability of zircon, J. Mater. Sci. 11 (1976) 578–582.

[144] A. Kaiser, M. Lobert, R. Telle, Thermal stability of zircon (ZrSiO4), J. Eur. Ceram. Soc. 28 (2008) 2199–2211. https://doi.org/10.1016/j.jeurceramsoc.2007.12.040.

[145] H.B. Barlett, X-Ray and Microscopic studies of silicate melts containing ZrO2, J. Am. Ceram. Soc. 14 (1931) 837–843.

[146] N.A. Toropov, F.Y.A. Galakhov, Liquidation in the system ZrO2-SiO2, Izv.Akad. Nauk SSSR, Ser. Khim. (1956) 158–161.

[147] R. Telle, F. Greffrath, R. Prieler, Direct observation of the liquid miscibility gap in the zirconia-silica system, J. Eur. Ceram. Soc. 35 (2015) 3995–4004. https://doi.org/10.1016/j.jeurceramsoc.2015.07.015.

[148] N. Zhirnova, Melting-point diagram of the system: ZrO2-SiO2, Obshch.Khim. 4 (1934) 1464–1470.

[149] O. Fabrichnaya, C. Wang, M. Zinkevich, C.G. Levi, F. Aldinger, Phase Equilibria and Thermodynamic Properties of the ZrO2-GdO1.5-YO1.5 System, J. Phase Equilibria Diffus. 26 (2005) 591–604. https://doi.org/10.1361/154770305X74395.

[150] M. Zinkevich, Thermodynamics of rare earth sesquioxides, Prog. Mater. Sci. 52 (2007) 597–647. https://doi.org/10.1016/j.pmatsci.2006.09.002.

[151] O. Fabrichnaya, G. Savinykh, G. Schreiber, M. Dopita, H.J. Seifert, Experimental investigation and thermodynamic modelling in the ZrO2-La2O3-Y2O3 system, J. Alloys Compd. 493 (2010)

263–271. https://doi.org/10.1016/j.jallcom.2009.12.076.

[152] S. Kuang, M.J. Hoffmann, H.L. Lukas, G. Petzow, Experimental Study and Thermodynamic Calculations of the MgO-Y2O3-SiO2 System, Key Eng. Mater. 89–91 (1993) 399–404. https://doi.org/10.4028/www.scientific.net/KEM.89-91.399.

[153] D.L. Poerschke, T.L. Barth, O. Fabrichnaya, C.G. Levi, Phase equilibria and crystal chemistry in the calcia-silica-yttria system, J. Eur. Ceram. Soc. 36 (2016) 1743–1754. https://doi.org/10.1016/j.jeurceramsoc.2016.01.046.

[154] H.G. Scott, Phase relationships in the magnesia-yttria-zirconia system, J. Aust. Ceram. Soc. 17 (1981) 16–20.

[155] J.R. Hallmenn, V.S. Stubican, Phase Relations and Ordering in the Systems MgO-Y2O3-ZrO2 and CaO-MgO-ZrO2, J. Am. Ceram. Soc. 66 (1983) 265–267.

[156] L.M. Lopato, G.I. Gerasimyuk, A.V. Shevchenko, Y.M. Karpenko, Interaction in the system ZrO2-Y2O3-MgO at 1300-1900°C, Inorg. Mater. (Engl. Transl.). 27 (1991) 827–830.

[157] Z. Jin, Y. Du, A reassessment of the ZrO2YO1·5MgO system, Ceram. Int. 20 (1994) 17–25. https://doi.org/10.1016/0272-8842(94)90004-3.

[158] S.S. Pandit, K.T. Jacob, Phase relations in the system MgO-SiO2-ZrO2 at 1700 K, Metall. Mater. Trans. B. 26 (1995) 397–399. https://doi.org/10.1007/BF02660981.

[159] B. Hallstedt, Assessment of the CaO-Al2O3 System, J. Am. Ceram. Soc. Ociety. 73 (1990) 15–23.

[160] B. Hallstedt, Thermodynamic calculation of some subsystems of the Al-Ca-Mg-Si-O system, J. Phase Equilibria. 14 (1993) 662–675. https://doi.org/10.1007/BF02667878.

[161] H. Mao, M. Selleby, B. Sundman, A re-evaluation of the liquid phases in the CaO-Al2O3and MgO-Al2O3systems, Calphad Comput. Coupling Phase Diagrams Thermochem. 28 (2004) 307–312. https://doi.org/10.1016/j.calphad.2004.09.001.

[162] C. Guo, S. Shang, Z. Du, P.D. Jablonski, M.C. Gao, Z.-K. Liu, Thermodynamic modeling of the CaO–CaF2–Al2O3 system aided by first-principles calculations, Calphad. 48 (2015) 113–122. https://doi.org/10.1016/j.calphad.2014.12.002.

[163] K. Shirasuka, G. Yamaguchi, Precise measurement of the crystal data and the solid solution range of the defective spinel, MgO . nAl2O3, Yogyo-Kyokai-Shi. 82 (1974) 650–653.

[164] H. Viertel, F. Seifert, Thermal stability of defect spinels in the system MgAl2O4-Al2O4, Neues Jahrb. Miner. Abh. 140 (1980) 89–101.

[165] B. Hallstedt, Thermodynamic Assessment of the System MgO-Al2O3, J. Am. Ceram. Soc. 75 (1992) 1497–1507. https://doi.org/10.1111/j.1151-2916.1992.tb04216.x.

[166] I.H. Jung, S.A. Decterov, A.D. Pelton, Critical thermodynamic evaluation and optimization of the MgO–Al2O3, CaO–MgO–Al2O3 and MgO2-Al2O3-2SiO2 systems, J. Phase Equilibria Diffus. 25 (2004) 329–345.

[167] W.E. Cameron, Mullite: A Substituted Alumina, Am. Mineral. 62 (1977) 747–755.

[168] Y. Nakajima, P.H. Ribbe, Twinning and Superstructure of Aluminum- Rich Mullite, Am. Mineral. 66 (1981) 142–147.

[169] M. Tokonami, Y. Nakajima, N. Morimoto, The Diffraction Aspect and a Structural Model of Mullite, Al(Al1+2xSi1-2x)O5-x, Acta Crystallogr. Sect. A Cryst. Physics, Diffraction, Theor. Gen. Crystallogr. 36 (1980) 270–276.

[170] H. Mao, M. Selleby, B. Sundman, Phase equilibria and thermodynamics in the Al2O 3-SiO2 system - Modeling of mullite and liquid, J. Am. Ceram. Soc. 88 (2005) 2544–2551. https://doi.org/10.1111/j.1551-2916.2005.00440.x.

[171] G. Lambotte, P. Chartrand, Thermodynamic evaluation and optimization of the Al2O 3-SiO2-AlF3-SiF4 reciprocal system using the modified quasichemical model, J. Am. Ceram. Soc. 94 (2011) 4000–4008. https://doi.org/10.1111/j.1551-2916.2011.04656.x.

[172] O. Fabrichnaya, H. Jürgen Seifert, R. Weiland, T. Ludwig, F. Aldinger, A. Navrotsky, Phase equilibria and thermodynamics in the Y2O3-Al2O3-SiO2 system, Zeitschrift Fuer Met. Res. Adv. Tech. 92 (2001) 1083–1097.

[173] V. Swamy, H.J. Seifert, F. Aldinger, Thermodynamic properties of Y 2 O 3 phases and the yttrium–oxygen phase diagram, 269 (1998) 201–207.

[174] B. Hallstedt, M. Hillert, M. Selleby, B. Sundman, Modelling of acid and basic slags Divieion of Physical, Calphad. 18 (1994) 31–37.

[175] P. Dörner, L.J. Gauckler, H. Krieg, H.L. Lukas, G. Petzow, J. Weiss, On the calculation and representation of multicomponent systems, Calphad. 3 (1979) 241–257. https://doi.org/10.1016/0364-5916(79)90023-3.

[176] R.G.J. Ball, M.A. Mignanelli, T.I. Barry, J.A. Gisby, The calculation of phase equilibria of oxide core-concrete systems, J. Nucl. Mater. 201 (1993) 238–249. https://doi.org/10.1016/0022-3115(93)90179-3.

[177] P. Wu, Ph.D. Thesis, Ecole Polytechnique, Montreal, 1992.

[178] M. Hillert, X. Wang, Solid Cao Liquid CaO Solid MgO Liquid MgO, 13 (1989) 267–271.

[179] S.M. Liang, R. Schmid-Fetzer, Complete thermodynamic description of the Mg-Ca-O phase diagram including the Ca-O, Mg-O and CaO-MgO subsystems, J. Eur. Ceram. Soc. 38 (2018) 4768–4785. https://doi.org/10.1016/j.jeurceramsoc.2018.06.015.

[180] L.M. Lopato, G.I. Gerasimyuk, A.V. Shevchenko, S.G. Tresvyatskii, Phase equilibria in the systems Dy2O3-CaO, Y2O3-CaO, Yb2O3-CaO, Izv. Akad. Nauk SSSR Ser. Neorg. Mater. 9 (1973) 380–383.

[181] W. Wongng, The ICDD/PDF coverage of the high Tc superconductor and related compounds in the A-R-Cu-O systems (A = Ba, Sr and Ca, and R =Lanthanides and Y), Powder Diffr. 7 (1992) 125–133.

[182] Y. Kaminaga, H. Yamane, T. Yamada, Quaternary compounds prepared in a CaO–Y2O3–SnO2 system, J. Am. Ceram. Soc. 90 (2007) 1917–1920.

[183] V.S. Derevschikov, A.I. Lysikov, A.G. Okunev, High temperature CaO/Y2O3 carbon dioxide absorbent with enhanced stability for sorption-enhanced reforming applications, Ind. Eng. Chem. Res. 50 (2011) 12741–12749.

[184] Z. Jin, Y. Du, Thermodynamic calculation of the ZrO2-YO1.5-CaO phase diagram, Calphad. 16 (1992) 355–362. https://doi.org/10.1016/0364-5916(92)90011-L.

[185] Z. Li, J. Wang, B. Li, S. Wang, W. Ali, S. Wang, X. Wang, X. Lu, C. Li, K. Wang, Thermodynamic evaluation of the BaO-CaO-YO1.5system, J. Eur. Ceram. Soc. 38 (2018) 323–332. https://doi.org/10.1016/j.jeurceramsoc.2017.08.025.

[186] Y. Du, Z. Jin, P. Huang, Thermodynamic Calculation of the Zirconia–Calcia System, J. Am. Ceram. Soc. 75 (1992) 3040–3048. https://doi.org/10.1111/j.1151-2916.1992.tb04384.x.

[187] K. Wang, C.H. Li, Y.H. Gao, X.G. Lu, W.Z. Ding, Thermodynamic reassessment of ZrO2-CaO system, J. Am. Ceram. Soc. 92 (2009) 1098–1104. https://doi.org/10.1111/j.1551-2916.2009.02942.x.

[188] B. Hallstedt, Thermodynamic assessment of the Cao-MgO-Al2O3 system, J. Am. Ceram. Soc. 78 (1995) 193–198.

[189] A.H. De Aza, J.E. Iglesias, P. Pena, S. De Aza, Ternary System Al 2 O 3 – MgO – CaO : Part II , Phase Relationships in the, J. Am. Ceram. Soc. 83 (2000) 919–927.

[190] M. Gobbels, E. Woermann, J. Jung, The Al-Rich of the system CaO-Al2O3-MgO, J. Solid State Chem. 120 (1995) 358–363.

[191] I.H. Jung, S.A. Decterov, A.D. Pelton, MgO-Al2O3, 345 (2004) 551–552.

[192] O.B. Fabrichnaya, I. Nerad, Thermodynamic properties of liquid phase in the CaO·SiO2–CaO·Al2O3·2SiO2–2CaO·Al2O3·SiO2 system, J. Eur. Ceram. Soc. 20 (2000) 505–515.

[193] Y. Udalov, Z. Appen, V. Parshina, The Al2O3-CaO-Y2O3 system, Inorg. Chem. 24 (1979) 1549–1553.

[194] A. Richter, M. Gobbels, Phase Equilibria and Crystal Chemistry in the System CaO-Al2O3-Y2O3, J. Phase Equilibria Diffus. 31 (2010) 157–163. https://doi.org/10.1007/s11669-010-9672-1.

[195] T. Muromura, Y. Hinatsu, No Title, Mater. Res. Bull. 21 (1986) 61–67.

[196] M. J. Bannister, No Title, J. Aust. Ceram. Soc. 17 (1981) 21–24.

[197] J. Liddle, N.H. Brett, No Title, Ceram. Trans. J. 84 (1985) 128–134.

[198] S.Y. Kwon, W.Y. Kim, P. Hudon, I.H. Jung, Thermodynamic modeling of the CaO-SiO2-ZrO2 system coupled with key phase diagram experiments, J. Eur. Ceram. Soc. 37 (2017) 1095–1104. https://doi.org/10.1016/j.jeurceramsoc.2016.10.011.